

**Global-Scale, Nonlinearly-Generated Waves in the  
Space-Atmosphere Interaction Region**

by

**Vu Anh Nguyen**

B.S., University of Colorado, 2011

M.S., University of Colorado, 2011

A thesis submitted to the  
Faculty of the Graduate School of the  
University of Colorado in partial fulfillment  
of the requirements for the degree of  
Doctor of Philosophy  
Department of Aerospace Engineering Sciences

2016

This thesis entitled:  
Global-Scale, Nonlinearly-Generated Waves in the Space-Atmosphere Interaction Region  
written by Vu Anh Nguyen  
has been approved for the Department of Aerospace Engineering Sciences

---

Prof. Scott E. Palo

---

Dr. Ruth S. Lieberman

Date \_\_\_\_\_

The final copy of this thesis has been examined by the signatories, and we find that both the content and the form meet acceptable presentation standards of scholarly work in the above mentioned discipline.

Nguyen, Vu Anh (Ph.D., Aerospace Engineering Sciences)

Global-Scale, Nonlinearly-Generated Waves in the Space-Atmosphere Interaction Region

Thesis directed by Prof. Scott E. Palo

Understanding of the space-atmosphere interaction region spanning from 60 km to 500 km altitude is becoming increasingly important for satellite operations. Significant variability in this region is induced by global-scale atmospheric tides and planetary waves generated in the lower atmosphere, which can vertically propagate with increasing amplitude. Past studies have suggested that these global scale waves may nonlinearly interact to produce additional secondary waves and thus, introduce further variability in the region

This dissertation investigates the secondary waves that are produced during a nonlinear interaction between the quasi two-day wave and the migrating diurnal tide, two of the largest global-scale waves in the upper atmosphere. Theoretically, this nonlinear interaction should produce the 16hrW4 and 2dayE2 secondary waves. The main goal is to characterize the secondary wave forcing region and understand how this relates to their manifestation throughout the atmosphere. The first portion of this dissertation applies the Fast Fourier Synoptic Mapping technique to present new observational evidence of secondary waves in the mesosphere-lower thermosphere region. The results demonstrate that the secondary waves are significant at altitudes above 80 km, and do not necessarily coincide with the regions where the interacting primary waves are largest.

In order to further understand the secondary wave generation process, numerical experiments with a linearized tidal model are conducted. First, short-term primary wave estimates are extracted from the NOGAPS-ALPHA reanalysis model and are utilized to derive observationally-based nonlinear forcing quantities for the 16hrW4 and 2dayE2 secondary waves. The nonlinear forcing values are then implemented in a linear tidal model that is modified to compute secondary wave responses from the surface to the upper thermosphere. Numerical experimental results demonstrate that the magnitude of the secondary wave response in the mesosphere-lower thermosphere region is depen-

dent on factors such as the spatial distribution and location of the forcing, and the secondary wave frequency and vertical wavelength. Additional experiments simulating the interaction between the quasi two-day wave and the migrating semidiurnal tide suggest that certain secondary waves may be able to propagate far into the thermosphere and hence, introduce significant variability within the space-atmosphere interaction region.

## Dedication

To my parents, for your unconditional guidance, support and love.

## Acknowledgements

The completion of this dissertation would not have been possible without the guidance and support of several individuals. Some of these names are listed here, but are by no means a complete list.

I wish to thank my advisor Prof. Scott Palo for giving me the opportunity to conduct research under his wing even though I first walked into his office six years ago without ever hearing the word “atmospheric tide” before. I am grateful for his timely advice which has allowed me to develop into a critically-thinking, independent researcher. I also wish to thank Dr. Ruth Lieberman who saw enough potential in me to agree to support my Ph.D. This dissertation would not have been possible without her mentoring and knowledge of middle/upper atmospheric dynamics. I am appreciative of Prof. Jeff Forbes who kindly granted me permission to modify the GSWM for this study. His class on atmospheric tides and planetary waves was also one of the most valuable classes that I have taken at CU. Additionally, I would like to thank my other committee members, Dr. Han-li Liu and Prof. John Cassano, for the educational discussions both inside and outside of our committee meetings. I have also stood on the shoulders of many other experts in the field to be where I am today. I would like to specifically acknowledge Dr. Loren Chang for his insight and support during my summer stint at National Central University in Taiwan.

I am also appreciative of all the students and other faculty members who I’ve been fortunate to interact with over the last 10 years. To my professors, thank you for being an inspiration to me and helping the CU Aerospace Engineering Department become a world-class environment for education and research. To all of my past and current colleagues who I’ve been fortunate enough

to connect with, thank you for making my CU experience such a wonderful and unforgettable one. I wish everyone here the same joy that you have given me over the years.

This work was supported by JPL subcontract 1483557 through GATS, Inc. and the JPL Strategic University Research Partners (SURP) award.

## Contents

<b>Chapter</b>		
<b>1</b>	<b>INTRODUCTION</b>	<b>1</b>
1.1	The Space-Atmosphere Interaction Region . . . . .	1
1.2	Atmospheric Tides and Planetary Waves . . . . .	4
1.3	Limited Understanding of Nonlinearly Generated Waves . . . . .	7
1.4	Objectives . . . . .	9
<b>2</b>	<b>BACKGROUND</b>	<b>12</b>
2.1	Classical Tidal Theory . . . . .	12
2.1.1	Mathematical Formulation . . . . .	12
2.1.2	Tidal Sources and Theory Limitations . . . . .	19
2.2	Migrating Diurnal Tide . . . . .	20
2.3	Planetary Waves and the Quasi Two-Day Wave . . . . .	25
2.4	Secondary Waves from Quasi Two-Day Wave and Migrating Diurnal Tide Interaction	28
2.5	Potential Impacts of Nonlinearly Generated Waves . . . . .	32
<b>3</b>	<b>METHODOLOGY &amp; DATA SOURCES</b>	<b>38</b>
3.1	Methodology . . . . .	38
3.2	Data Sources . . . . .	40
3.2.1	Satellite Instruments . . . . .	40
3.2.2	NOGAPS Reanalysis . . . . .	43

3.2.3	Global Scale Wave Model . . . . .	43
<b>4</b>	<b>SECONDARY WAVES FROM OBSERVATIONS</b>	<b>47</b>
4.1	Technique for Extracting Secondary Wave Evidence . . . . .	47
4.1.1	Estimating Waves from Satellite Instruments . . . . .	47
4.1.2	Fast Fourier Synoptic Mapping Method . . . . .	51
4.2	Quasi Two-Day Wave and Secondary Waves from SABER Observations . . . . .	57
4.3	Secondary Wave Comparison to NOGAPS-ALPHA . . . . .	67
<b>5</b>	<b>COMPUTATION OF SECONDARY WAVE FORCING</b>	<b>72</b>
5.1	Origin of Nonlinear Forcing . . . . .	72
5.2	Primary Wave Estimates . . . . .	73
5.2.1	Estimating from Only Observations . . . . .	73
5.2.2	Chosen Method: NOGAPS-ALPHA . . . . .	90
5.3	Nonlinear Forcing Results . . . . .	97
<b>6</b>	<b>SECONDARY WAVE RESPONSES</b>	<b>107</b>
6.1	Secondary Wave Response in Zero-Wind Background . . . . .	107
6.2	Dissipation Effects on Secondary Wave Hough Modes . . . . .	113
6.3	Efficient Projection of Forcing on Propagating Hough Modes . . . . .	118
6.4	Importance of Altitude Location . . . . .	123
6.5	Impact of Primary Wave Phase on Secondary Wave Response . . . . .	128
6.6	Secondary Wave Response with Background Winds . . . . .	128
6.7	Shape Function . . . . .	135
6.8	Mean Wind Effects on the Nonlinear Forcing Projection Responses . . . . .	137
6.9	Time Evolution . . . . .	142
6.10	Comparison to NOGAPS . . . . .	147

<b>7</b>	<b>NONLINEAR INTERACTION BETWEEN QUASI-TWO DAY WAVE AND MIGRATING SEMIDIURNAL TIDE</b>	<b>151</b>
7.1	Introduction . . . . .	151
7.2	SW2-2dayW3 Amplitudes . . . . .	152
7.3	Nonlinear Forcing . . . . .	158
7.4	Secondary Wave Responses . . . . .	160
<b>8</b>	<b>CONCLUSIONS</b>	<b>173</b>
8.1	Summary . . . . .	173
8.2	Discussion and Future Work . . . . .	176
	<b>Bibliography</b>	<b>178</b>
	<b>Appendix</b>	
<b>A</b>	<b>GLOSSARY</b>	<b>187</b>
<b>B</b>	<b>WAVE NOMENCLATURE</b>	<b>188</b>
<b>C</b>	<b>DERIVATION OF NONLINEAR FORCING</b>	<b>189</b>
<b>D</b>	<b>FAST FOURIER SYNOPTIC MAPPING DETAILS</b>	<b>195</b>
D.1	FFSM Procedure . . . . .	195
D.2	Additional Aliasing Tests for Least Squares and FFSM methods . . . . .	199
<b>E</b>	<b>SUPPLEMENTAL FIGURES: PRIMARY WAVES AND NONLINEAR FORCING</b>	<b>202</b>
<b>F</b>	<b>SUPPLEMENTAL FIGURES: SECONDARY WAVES COMPUTED FROM THE LINEAR TIDAL MODEL</b>	<b>219</b>

## Figures

### Figure

1.1	Atmosphere-space coupling by waves . . . . .	3
1.2	Vertical propagation of migrating diurnal tide in observations . . . . .	5
1.3	Temperature perturbations seen in TIMED/SABER . . . . .	8
1.4	Forcing and generation of secondary waves . . . . .	11
2.1	Migrating diurnal tide hough modes and expansion functions . . . . .	22
2.2	Diurnal (1, 1) Hough mode in an eastward jet at 40° . . . . .	24
2.3	Daily estimates of the DW1 for 2009 at equator and 79 km . . . . .	25
2.4	QTDW geopotential height and circulation at 80 km . . . . .	27
2.5	Fourier power spectra of zonal wind fields in 2-day wave TIMEGCM experiment . . . . .	33
2.6	Planetary wave modulation of total electron content . . . . .	34
2.7	Response of the thermosphere to a varying eddy diffusion coefficient in the TIE-GCM . . . . .	36
3.1	SABER and MLS solar local time coverage . . . . .	42
3.2	NOGAPS-ALPHA 2-day wave comparison with MF radar . . . . .	44
4.1	MLS and SABER time/longitude sampling over multiple days . . . . .	49
4.2	MLS and SABER time/longitude sampling over multiple days in R-S coordinates . . . . .	52
4.3	Asynoptic Nyquist rectangle . . . . .	53
4.4	FFSM reconstruction of 2dayW3 signal . . . . .	54
4.5	Least squares method and FFSM aliasing from 2dayW3 to 2dayE2 . . . . .	56

4.6	FFSM reconstruction of 16hrW4 signal . . . . .	57
4.7	Evidence of 2dayE2 waves during 2dayW3 events . . . . .	58
4.8	Time evolution of 2dayW3 amplitude latitude structure for selected years . . . . .	61
4.9	2dayW3 latitude-altitude amplitude structure in temperature for selected years . . . . .	62
4.10	2dayW3 latitude-altitude amplitude structure in geopotential height for selected years . . . . .	63
4.11	2dayW3 phase progression with altitude at 30°S latitude . . . . .	64
4.12	2dayE2 latitude-altitude amplitude structure in temperature for selected years . . . . .	65
4.13	2dayE2 latitude-altitude amplitude structure in geopotential height for selected years . . . . .	66
4.14	2dayE2 phase progression with altitude at 10°S latitude . . . . .	67
4.15	2005 2dayW3 and secondary waves in NOGAPS-ALPHA . . . . .	69
4.16	2006 2dayW3 and secondary waves in NOGAPS-ALPHA . . . . .	70
4.17	2005 2dayE2 amplitude from NOGAPS sampled with SABER . . . . .	71
4.18	2006 2dayE2 amplitude from NOGAPS sampled with SABER . . . . .	71
5.1	Derived background zonal wind from WACCM model run . . . . .	76
5.2	Derived 2dayW3 zonal wind structure from WACCM model data . . . . .	78
5.3	Derived 2dayW3 meridional wind structure from WACCM model data . . . . .	79
5.4	Estimated 2dayW3 perturbation winds and background winds . . . . .	80
5.5	Examples of least squares fit to DW1 using MLS/SABER local time sampling . . . . .	83
5.6	MLS/SABER condition number as a function of time and latitude . . . . .	84
5.7	DW1 amplitude and phase estimates from MLS/SABER data . . . . .	85
5.8	Hough Mode Extension fits for the DW1 (1, 1) mode with MLS derived winds . . . . .	87
5.9	DW1 amplitude and phase estimates computed from generalized Hough mode fits . . . . .	89
5.10	2006 2dayW3 and DW1 time-latitude amplitude structure at 84 km . . . . .	91
5.11	2006 2dayW3 and DW1 latitude-altitude amplitude structure . . . . .	93
5.12	2006 2dayW3 and DW1 latitude-altitude phase structure . . . . .	94
5.13	2009 2dayW3 and DW1 time-latitude amplitude structure at 84 km . . . . .	95

5.14	2010 2dayW3 and DW1 time-latitude amplitude structure at 84 km . . . . .	96
5.15	2006 secondary wave forcing amplitude as a function of altitude and latitude . . . . .	98
5.16	2006 secondary wave forcing phase as a function of altitude and latitude . . . . .	99
5.17	2009 secondary wave forcing amplitude as a function of altitude and latitude . . . . .	101
5.18	2010 secondary wave forcing amplitude as a function of altitude and latitude . . . . .	102
5.19	2006 secondary wave forcing amplitude temporal evolution at 70 km . . . . .	103
5.20	2009 secondary wave forcing amplitude temporal evolution at 70 km . . . . .	105
5.21	2010 secondary wave forcing amplitude temporal evolution at 70 km . . . . .	106
6.1	2006 16hrW4-2dayE2 amplitude as a function of altitude and latitude . . . . .	109
6.2	2009 16hrW4-2dayE2 amplitude as a function of altitude and latitude . . . . .	110
6.3	2010 16hrW4-2dayE2 amplitude as a function of altitude and latitude . . . . .	111
6.4	2006 16hrW4-2dayE2 phase as a function of altitude and latitude . . . . .	112
6.5	16hrW4-2dayE2 Hough mode and wind expansion functions . . . . .	114
6.6	Amplitude and phase of primary 16hrW4-2dayE2 Hough modes for January 2006 . . . . .	115
6.7	Amplitude and phase of primary 16hrW4-2dayE2 Hough modes for January 2009 . . . . .	118
6.8	Amplitude and phase of primary 16hrW4-2dayE2 Hough modes for January 2010 . . . . .	119
6.9	2006 16hrW4-2dayE2 Hough mode projected forcing . . . . .	120
6.10	2006 16hrW4-2dayE2 zonal wind response to Hough mode projected forcing . . . . .	121
6.11	Vertical subsections of 16hrW4-2dayE2 thermal forcing centered at 70 km and 90 km . . . . .	123
6.12	2006 16hrW4-2dayE2 amplitude response to vertical subsections of forcing . . . . .	124
6.13	Maximum 16hrW4-2dayE2 amplitude vs. center altitude of forcing . . . . .	126
6.14	16hrW4-2dayE2 phase response to the 70 km and 90 km forcing subsections . . . . .	127
6.15	Background zonal wind configurations for each year . . . . .	130
6.16	2006 16hrW4-2dayE2 amplitude vs. altitude and latitude with background winds . . . . .	132
6.17	2009 16hrW4-2dayE2 amplitude vs. altitude and latitude with background winds . . . . .	133
6.18	2010 16hrW4-2dayE2 amplitude vs. altitude and latitude with background winds . . . . .	134

6.19	Primary 16hrW4-2dayE2 Hough modes for 2006 under background winds . . . . .	135
6.20	Effects of background winds on the shape function and 16hrW4 amplitude . . . . .	138
6.21	2006 16hrW4-2dayE2 zonal wind response to Hough mode projected forcing with background winds . . . . .	140
6.22	2006 16hrW4-2dayE2 amplitude response to vertical subsections of forcing with back- ground winds . . . . .	141
6.23	2006 16hrW4-2dayE2 amplitude temporal evolution at 90 km under background winds	143
6.24	2009 16hrW4-2dayE2 amplitude temporal evolution at 90 km under background winds	144
6.25	2010 16hrW4-2dayE2 amplitude temporal evolution at 90 km under background winds	145
6.26	Background zonal wind temporal-latitudinal evolution at 72 km for all years . . . . .	146
6.27	Vertical-latitudinal comparison of 16hrW4-2dayE2 amplitude results to NOGAPS- ALPHA . . . . .	148
6.28	Temporal-latitudinal comparison of 16hrW4-2dayE2 amplitude results to NOGAPS- ALPHA . . . . .	149
7.1	Ground-based evidence of 2dayW3-SW2 nonlinear interaction . . . . .	153
7.2	2006 2dayW3 and SW2 latitude-altitude amplitude structure . . . . .	154
7.3	2006 2dayW3 and SW2 latitude-altitude amplitude structure . . . . .	155
7.4	2006 2dayW3 and SW2 time-latitude amplitude structure at 90 km . . . . .	156
7.5	2006 9.6hrW5 and 16.0hrE1 forcing amplitude as a function of altitude and latitude	159
7.6	2006 9.6hrW5-16.0hrE1 amplitude as a function of altitude and latitude . . . . .	161
7.7	2006 9.6hrW5-16.0hrE1 phase as a function of altitude and latitude . . . . .	162
7.8	9.6hrW5-16.0hrE1 Hough mode and wind expansion functions . . . . .	164
7.9	2006 9.6hrW5-16.0hrE1 Hough mode projected forcing . . . . .	165
7.10	Amplitude and phase of primary 9.6hrW5-16.0hrE1 Hough modes for January 2006	166
7.11	2006 9.6hrW5-16hrE1 amplitude vs. altitude and latitude with background winds . .	168
7.12	2009 9.6hrW5-16hrE1 amplitude vs. altitude and latitude with background winds . .	169

7.13	2010 9.6hrW5-16hrE1 amplitude vs. altitude and latitude with background winds . . .	170
7.14	Vertical-latitudinal comparison of 9.6hrW5-16.0hrE1 amplitude results to NOGAPS- ALPHA . . . . .	172
D.1	Least squares method and FFSM aliasing from 16hrW4 to 2-dayE2 for SABER . . .	199
D.2	FFSM reconstruction of 2dayW3 signal using MLS sampling . . . . .	200
D.3	Least squares method and FFSM aliasing from 2dayW3 to 2dayE2 for MLS . . . . .	201
D.4	Least squares method and FFSM aliasing from 16hrW4 to 2dayE2 for MLS . . . . .	201
E.1	MLS 2dayW3 latitude-altitude amplitude structure from 2005 to 2010 . . . . .	202
E.2	MLS 2dayE2 latitude-altitude amplitude structure from 2005 to 2010 . . . . .	203
E.3	2009 NOGAPS 2dayW3 and DW1 latitude-altitude amplitude structure . . . . .	204
E.4	2009 NOGAPS 2dayW3 and DW1 latitude-altitude phase structure . . . . .	205
E.5	2010 2dayW3 and DW1 latitude-altitude amplitude structure . . . . .	206
E.6	2010 NOGAPS 2dayW3 and DW1 latitude-altitude phase structure . . . . .	207
E.7	2009 secondary wave forcing phase as a function of altitude and latitude . . . . .	208
E.8	2010 secondary wave forcing phase as a function of altitude and latitude . . . . .	209
E.9	2006 secondary wave forcing amplitude temporal evolution at 90 km . . . . .	210
E.10	2009 secondary wave forcing amplitude temporal evolution at 90 km . . . . .	211
E.11	2010 secondary wave forcing amplitude temporal evolution at 90 km . . . . .	212
E.12	2009 NOGAPS 2dayW3 and SW2 latitude-altitude amplitude structure . . . . .	213
E.13	2009 NOGAPS 2dayW3 and SW2 latitude-altitude phase structure . . . . .	214
E.14	2010 NOGAPS 2dayW3 and SW2 latitude-altitude amplitude structure . . . . .	215
E.15	2010 NOGAPS 2dayW3 and SW2 latitude-altitude phase structure . . . . .	216
E.16	2009 secondary wave forcing amplitude as a function of altitude and latitude . . . .	217
E.17	2010 secondary wave forcing amplitude as a function of altitude and latitude . . . .	218
F.1	2009 16hrW4-2dayE2 phase as a function of altitude and latitude . . . . .	219

F.2	2010 16hrW4-2dayE2 phase as a function of altitude and latitude . . . . .	220
F.3	2009 Maximum 16hrW4-2dayE2 amplitude vs. center altitude of forcing . . . . .	221
F.4	2010 Maximum 16hrW4-2dayE2 amplitude vs. center altitude of forcing . . . . .	221
F.5	2009 16hrW4-2dayE2 Hough mode projected forcing . . . . .	222
F.6	2010 16hrW4-2dayE2 Hough mode projected forcing . . . . .	223
F.7	2009 16hrW4-2dayE2 zonal wind response to Hough mode projected forcing . . . . .	224
F.8	2010 16hrW4-2dayE2 zonal wind response to Hough mode projected forcing . . . . .	225
F.9	2006 16hrW4-2dayE2 response to 2dayW3 shifted phase . . . . .	226
F.10	2006 16hrW4-2dayE2 phase as a function of altitude and latitude under background winds . . . . .	227
F.11	2009 16hrW4-2dayE2 phase as a function of altitude and latitude under background winds . . . . .	228
F.12	2010 16hrW4-2dayE2 phase as a function of altitude and latitude under background winds . . . . .	229
F.13	Primary 16hrW4-2dayE2 Hough modes for 2009 under background winds . . . . .	230
F.14	Primary 16hrW4-2dayE2 Hough modes for 2010 under background winds . . . . .	231
F.15	Vertical-latitudinal comparison of 16hrW4-2dayE2 amplitude results to NOGAPS- ALPHA for 2009 . . . . .	231
F.16	Vertical-latitudinal comparison of 16hrW4-2dayE2 amplitude results to NOGAPS- ALPHA for 2010 . . . . .	232

## Chapter 1

### INTRODUCTION

This Ph.D. dissertation focuses on the nonlinear interaction between the quasi two-day wave and the migrating diurnal tide, two of the largest global scale waves in the atmosphere. Past theoretical studies have suggested that the interaction between these waves produces additional secondary waves in the atmosphere. However, the generation and overall manifestation of secondary atmospheric waves is not well understood. The research herein elucidates this topic by analyzing the generation and manifestation of secondary nonlinear waves in the atmosphere by applying innovative techniques to estimate wave spectra on short time scales in conjunction with numerical modeling. The results of this research improves our fundamental understanding of nonlinear interactions between global scale waves in the stratosphere/mesosphere/thermosphere and provides new insights regarding the potential impacts of these waves on the space-atmosphere interaction region.

#### 1.1 The Space-Atmosphere Interaction Region

Since the dawn of the space age in the late 1950s, nations around the globe have become increasingly dependent on space-based technology to meet the daily needs of society. As a result, comprehension of the environment where many of our satellites reside and operate has never been more crucial. For instance, satellite orbit maintenance and deorbiting trajectory predictions rely on the accurate description of neutral atmospheric density over time and space (Leonard et al., 2012 [45]). Similarly, satellite communication links and GPS-based navigation depend on an accurate

characterization of electrically-charged particle density in the upper atmosphere. However, the detailed characterization of the satellite environment is difficult to achieve because it lies within the complex space-atmosphere interaction region (CEDAR Strategic Vision [5]). Broadly defined as the boundary between the lower atmosphere and interplanetary space, the space-atmosphere interaction region encompasses the mesosphere (60-100 km), the thermosphere ( $\sim$ 100-500 km) and the electrically-charged ionosphere ( $\sim$ 90-500 km). It is widely recognized that the composition and dynamics of this region are simultaneously affected by direct solar and geomagnetic forcing from above and meteorological processes from below. Consequently, a complete description of the satellite environment involves disentangling multiple complex processes.

Lower atmospheric processes affecting the space-atmosphere interaction region are mainly driven by waves of varying temporal frequencies. As depicted in Figure 1.1, the three main classes of waves that can vertically couple different atmospheric regions are gravity waves, planetary waves and atmospheric tides. Gravity waves arise from disturbances to the general stratification of the atmosphere. As air parcels are displaced downward or upward to regions of different densities, a restoring buoyancy force causes the parcels to oscillate in a wave-like motion. Some of these waves may propagate away from their source regions depending on the characteristics of the wave and the state of the background atmosphere. Gravity waves range on scales from tens to thousands of kilometers horizontally and have periods from minutes to hours. In contrast, planetary waves and atmospheric tides are global scale waves with periods on the order of hours to days. While some planetary-scale waves and atmospheric tides may dynamically resemble large-scale gravity waves, their motion may also be modified by the rotational motion of the earth. The forcing, dynamics and impact of planetary waves and atmospheric tides on the space-atmosphere interaction region is the subject of this dissertation and hence, more detail will be provided in the upcoming chapters.

The energy sources of gravity waves, planetary waves and atmospheric tides largely originate from the solar-driven processes in the troposphere (0-20 km) and stratosphere (20-60 km) where most of the mass of the atmosphere is contained. The mean background atmosphere acts as a waveguide, permitting certain waves to propagate upward. Wave oscillations typically increase in

amplitude with altitude as a consequence of exponentially decreasing density and conservation of energy. As a result, waves typically reach maximum amplitudes between 80 and 120 km where the induced perturbation values can be as large as the mean background state. These waves can transport a significant amount of heat, momentum and mass having a measurable impact on the mean state and variability of the mesosphere and lower thermosphere (MLT) region. Furthermore, because the MLT region lies within the strongly-coupled space-atmosphere interaction region, the effects of these waves can be transmitted to higher altitudes in the thermosphere and ionosphere. Thus, the characterization of the coupled space-atmosphere interaction region, and ultimately our ability to sustain our space-dependent lifestyle, is dependent on understanding atmospheric waves at all temporal and spatial scales.

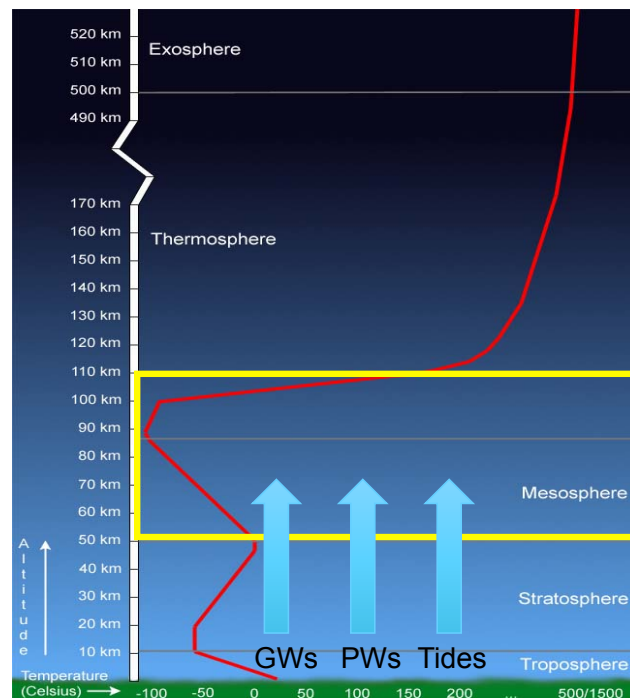


Figure 1.1: A diagram illustrating the vertical propagation of gravity waves (GWs), planetary waves (PWs) and atmospheric tides originating in the lower atmosphere. The Mesosphere-Lower Thermosphere (MLT) region highlighted in yellow. An approximate atmospheric temperature profile is shown in red. Figure modified from Russell, 2010 [94].

## 1.2 Atmospheric Tides and Planetary Waves

Atmospheric tides are global scale oscillations of atmospheric field variables with periods that are subharmonics of a solar or lunar day. They are forced primarily by atmospheric solar absorption or the lunar gravitational force, but can also be generated from nonlinear interactions between global scale waves (Forbes and Wu, 2006 [18]). Many tidal components are forced in the lower atmosphere where they are either confined to their source region or free to propagate vertically as shown in Figure 1.2. Vertically propagating tides from the lower atmosphere reach maximum values in the MLT region where dissipative forces such as molecular and turbulent diffusion begin to effectively dampen the tides. Tides also propagate horizontally across the globe and are commonly categorized by frequency and zonal wavenumber, which describes the number of perturbation maxima along a latitude circle. They can also be classified as migrating or nonmigrating. Migrating tides refer to components fixed in local time, propagating at the same phase speed as the apparent motion of the sun. Because they represent the largest components of solar forcing, migrating tides are usually the most prominent tidal components in the MLT region. Nonmigrating tides refer to components whose phase speed differs from the apparent motion of the sun, but can still be significant in portions of the atmosphere.

In contrast, planetary waves generally encompass all global scale oscillations that have periods greater than a solar day. Like atmospheric tides, planetary waves can propagate horizontally with varying wavenumber and frequency, as well as vertically, carrying momentum and energy. Planetary waves incorporate a broad range of wave types including Rossby waves and Kelvin waves that arise due to the rotational effects of the Earth's atmosphere. Some forcing mechanisms for planetary waves include mean flow instability, land-sea boundaries, topography and tropical convection. Planetary waves may also arise as manifestations of the unforced, resonant modes of the atmosphere. One of the most dominant manifestations of a resonant mode in the MLT region is the quasi two-day wave, which propagates westward with zonal wavenumber 3 (2dayW3). The quasi two-day is most prominent in the summer hemisphere shortly after solstice and remains one

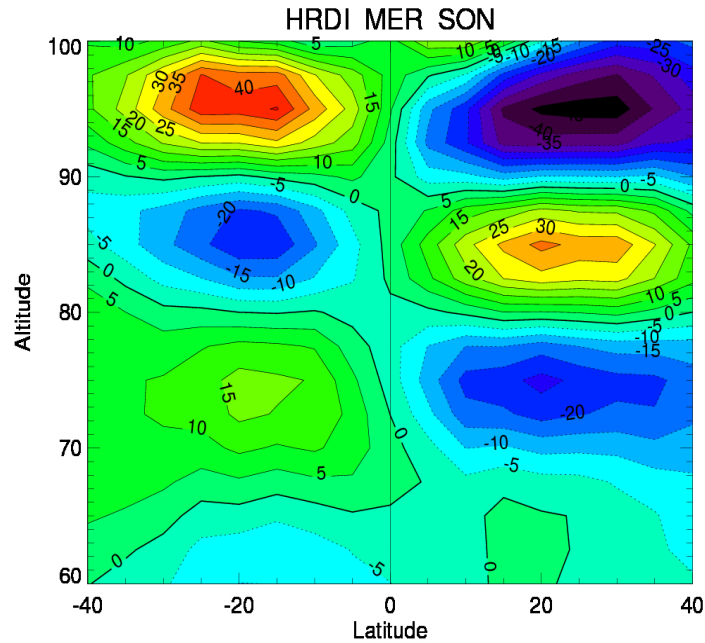


Figure 1.2: Meridional wind perturbations (zonal mean removed) measured at fixed local time by the High Resolution Doppler Imager (HRDI) satellite on the Upper Atmospheric Research Satellite (UARS). Figure taken from Lieberman, 2010.

of the most dominant global waves in the MLT region.

The existence of atmospheric tides and planetary waves in the atmosphere has been quantitatively predicted by classical tidal theory (Chapman and Lindzen, 1970 [8]). By linearizing the conservation laws for mass, momentum and energy along with the simplifying assumptions that the background atmosphere is windless, inviscid and horizontally uniform, the responses of specific atmospheric tides and planetary waves to a given forcing profile can be calculated. Studies over the past decades have eliminated some of the simplifying assumptions adopted by classical tidal theory, which has narrowed the gap between theory and observation. However, past studies have shown that there exists atmospheric waves that do not conform to the results of linear tidal theory. Teitelbaum and Vial, 1991 [107] showed that the nonlinear terms in the governing conservation laws can serve as a pathway for planetary waves and tides propagating in the same region to interact with each other. In this scenario, two primary planetary waves or tides can nonlinearly force

secondary waves whose frequencies and zonal wavenumbers are the sum and difference of those of the interacting waves. Moreover, the magnitudes of secondary waves have been suggested to be significant when the interacting waves are of moderate to large amplitude.

There has been some observational evidence supporting the existence of nonlinearly generated waves in the atmosphere. In many of these studies, spectral analyses of ground-based observations have revealed the concurrent presence of two primary wave periodicities with one or both of the secondary wave periodicities predicted by nonlinear theory. Specifically, the studies by Manson and Meek, 1990 [60], Clark and Bergin, 1997 [9], and Beard et al., 1999 [3] detected 16 hour oscillations in ground-based data during a quasi two-day wave event, which suggests the nonlinear interaction between the quasi two-day wave and migrating diurnal/semidiurnal tides. Although ground-based measurements provide excellent temporal resolution, ground-based evidence of secondary waves is limited due to the fact that these measurements are confined locally and cannot provide global wavenumber information. More recently, the availability of satellites providing reliable measurements of the MLT region have yielded the potential for global scale observations of nonlinearly generated tides and planetary waves. In particular, Palo et al., 2007 [76] confirmed the existence of an eastward, two-day wave with wavenumber 2 (2dayE2) in the MLT region, which is theorized to be a product of a nonlinear interaction between the quasi two-day wave and the migrating diurnal tide.

The primary motivation for studying nonlinearly generated waves emerges from studies that suggest secondary waves from planetary-tidal wave nonlinear interactions can propagate vertically away from the region of excitation and have a significant impact on the space-atmosphere interaction region. The potential impact of the nonlinear products of a migrating diurnal tide and quasi two-day wave was highlighted by Pedatella and Forbes, 2012 [83] who observed that the low-latitude ionosphere at 360 km was dominated by 2dayW3 and 2dayE2 spectra in January 2006. It is not clear, however, how the effects of secondary waves or even primary waves can penetrate to high altitudes in the thermosphere and ionosphere. A modeling study by Pogoreltsev, 2001 [87] concluded that some secondary waves may have the appropriate propagating structure to be able

to directly penetrate into high altitudes in the thermosphere and ionosphere. Other modeling studies have suggested that secondary waves can modulate electrodynamic processes in the lower ionosphere (E-region) and drive the longitudinal variability in the upper ionosphere (Hagan et al., 2009 [29]; Pedatella et al., 2012 [84]). In addition to identifying the products of planetary-tidal wave nonlinear interaction, Teitelbaum and Vial, 1991 [107] theorized that the generated secondary waves can beat with the interacting tide and modulate the tidal amplitude with the period of the planetary wave. The modulation of atmospheric tidal amplitudes at planetary wave periodicities has been observed from both ground-based (Beard et al., 1999 [3]; Pancheva et al., 2006 [81]) and space-based platforms (Pedatella et al., 2012 [85]). Furthermore, Pancheva and Mukhtarov, 1994 [79] suggested that this modulation of atmospheric tides could be important for the transmission of planetary wave periodicities into the thermosphere and ionosphere. Nevertheless, the validity of these coupling mechanisms to the upper atmosphere cannot be fully investigated without first elucidating how nonlinear secondary waves are generated at lower atmospheric levels.

### 1.3 Limited Understanding of Nonlinearly Generated Waves

The physical nature and characteristics of nonlinearly generated secondary waves have not been thoroughly investigated due to the limited coverage of observational data available. Because nonlinear interactions between planetary waves and atmospheric tides appear to last on the order of days to weeks, global scale estimates on short time scales are necessary for conducting observational analyses of nonlinearly generated waves. Unfortunately, traditional methods of observation and analysis make it difficult to obtain short term wave spectra estimates on a global scale. Ground-based radar and lidar systems can only observe a small portion of the atmosphere but with high temporal accuracy, which prevents researchers from distinguishing global scale wave components in the observations. Satellite observations, in contrast, provide data over multiple locations and therefore, yields the potential to separate different wave components, but at limited time scales. As shown in Figure 1.3, satellites in sun-synchronous or near sun-synchronous orbits can observe global-scale perturbations representing the sum of different wave components at constant solar local

time. However, different wave components appear as the same perturbation in the solar local time frame. Past studies (Forbes et al., 1997 [17] and references therein) have produced reasonably accurate estimates of tidal components by accumulating observations over 24 hours of solar local time. By utilizing observations over a diurnal cycle, tidal aliases can be effectively removed from zonal mean effects and allow for the estimation of tidal amplitude and phase. For satellites in near sun-synchronous orbits, this process takes longer than 30 days, which means any shorter term tidal variations are averaged out. In contrast to tidal components, planetary waves with periods greater than one day lie within the Nyquist limits obtained from sun-synchronous satellite sampling of the atmosphere. Hence, they can be estimated within shorter temporal windows by using appropriate techniques such as the Fast Fourier Synoptic Mapping method developed by Salby, 1982 [97] and evaluating potential aliasing effects.

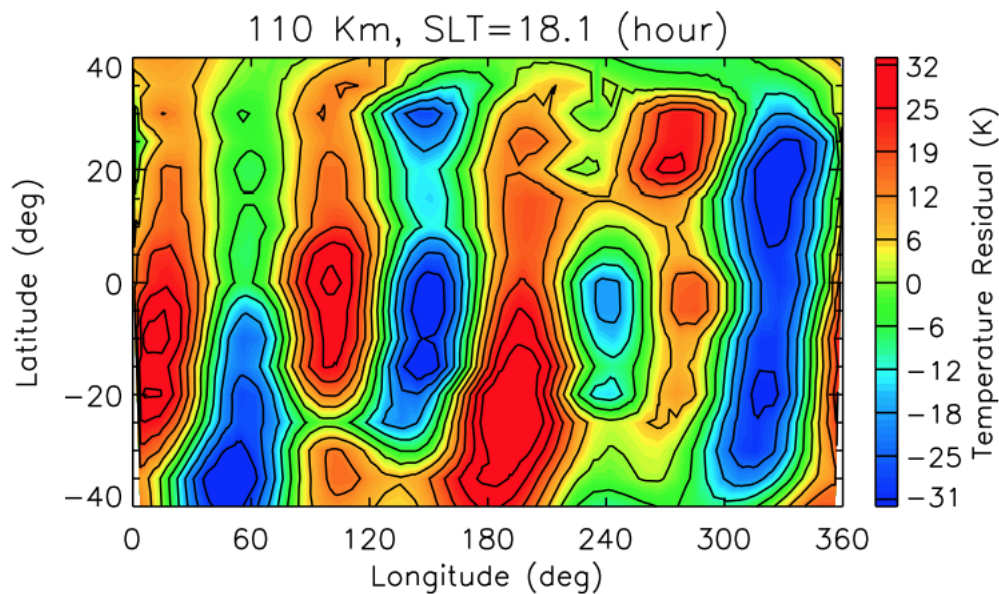


Figure 1.3: Temperature perturbations (5-day zonal mean removed) measured at constant local time by the SABER instrument on the TIMED satellite. Data are plotted as a function of latitude and longitude at 110km.

The absence of short term tidal observations on a global scale has prevented researchers from effectively investigating nonlinear interactions and the mechanisms of generating secondary

waves. Although there have been numerous studies that have analyzed the nonlinear interactions in numerical models, these studies have predominantly focused on providing evidence that secondary waves exist in different regions of the atmosphere (Angelats i Coll and Forbes, 2002 [1]; Lieberman et al., 2015 [50]) or how nonlinear interactions can induce tidal variability (Chang et al. [7]). One of the few studies which have investigated the nonlinear forcing and manifestation of secondary waves in the atmosphere was performed by Pogoreltsev, 2001 [87] who investigated the nonlinear products arising from an interaction between the quasi two-day wave and 16-day wave. Through the utilization of a two-dimensional, linearized numerical model, this study found that one of the nonlinearly generated waves from the 2dayW3-16dayW1 wave interaction was able to propagate away from the forcing region while the other secondary wave remained trapped near the excitation region (evanescent). However, the explanation and validation of these secondary wave results have not been provided to this date because more detailed studies on secondary waves from tidal-planetary wave interactions have not been conducted. Consequently, many questions remain about the factors that govern the secondary wave response in the MLT and the potential impacts on the entire space-atmosphere interaction region.

#### 1.4 Objectives

The focus of this dissertation centers on the forcing and response of the secondary waves arising from a nonlinear interaction between the migrating diurnal tide and quasi two-day wave (Figure 1.4) by utilizing a combination of observational data and numerical modeling. Novel observational techniques are used in conjunction with a two-dimensional, linear mechanistic model, to investigate the following questions:

- (1) **Where in the atmosphere are the migrating diurnal tide and quasi two-day wave interacting to nonlinearly force the secondary waves, and where do significant secondary wave responses occur?**

Secondary wave responses in the middle atmosphere are extracted from satellite observa-

tions using a Fast Fourier Synoptic Mapping (FFSM) method. These estimates provide clear global-scale evidence for the existence of secondary waves and also indicate where they are significantly large. In order to estimate the excitation region of the secondary waves, primary wave estimates are obtained through satellite and reanalysis observations. Primary wave estimates are used with the nonlinear advection terms found in the momentum and energy conservation equations to compute nonlinear momentum and thermal forcing terms for the 2dayE2 and 16hrW4 secondary waves and determine where the excitation region is predominantly located.

- (2) **How does the nonlinear forcing distribution arising from a migrating diurnal tide-quasi two-day wave interaction affect the structure and propagation of the resulting secondary waves?**

The computed nonlinear forcing distribution from observations are used as inputs to the linear mechanistic model to compute the modeled secondary wave responses and compare to the forcing region and the observational results. Numerical experiments are conducted to assess the secondary wave amplitude and propagation characteristics and its sensitivity to factors such as the spatial distribution of the forcing region and the background wind structure. The results are presented over multiple years to determine the role of secondary waves in inducing inter-annual variability within the SAIR. Finally, the secondary waves arising from the interaction between the 2dayW3 and the migrating semidiurnal tide (SW2) are analyzed within the linear model to provide further detail on the factors that govern the manifestation of secondary waves in the middle and upper atmosphere.

This dissertation is organized into eight chapters. Chapter 2 provides background information on classical tidal theory, planetary waves, nonlinear wave-wave interactions and possible impacts on coupling of the space-atmosphere interaction region. Chapter 3 describes the satellite data, estimation techniques and numerical models to be used and how they will be utilized to answer the dissertation science questions. New observational evidence of secondary waves arising

from 2dayW3-DW1 nonlinear interaction are presented in Chapter 4. In Chapter 5, techniques to estimate the primary waves from observational and reanalysis data sources and compute the nonlinear forcing quantities are discussed. These nonlinear forcing quantities are utilized as inputs to a linear tidal model in order to compute secondary wave responses. Results for the secondary wave responses to the 2dayW3-DW1 interaction along with numerical experiments that help elucidate their manifestation within the SAIR are presented in Chapter 6. To provide further context on the 2dayW3-DW1 nonlinear interaction, the secondary waves generated from the 2dayW3 and the SW2 are investigated in Chapter 7. Finally, the main conclusions of the dissertation are summarized in Chapter 8.

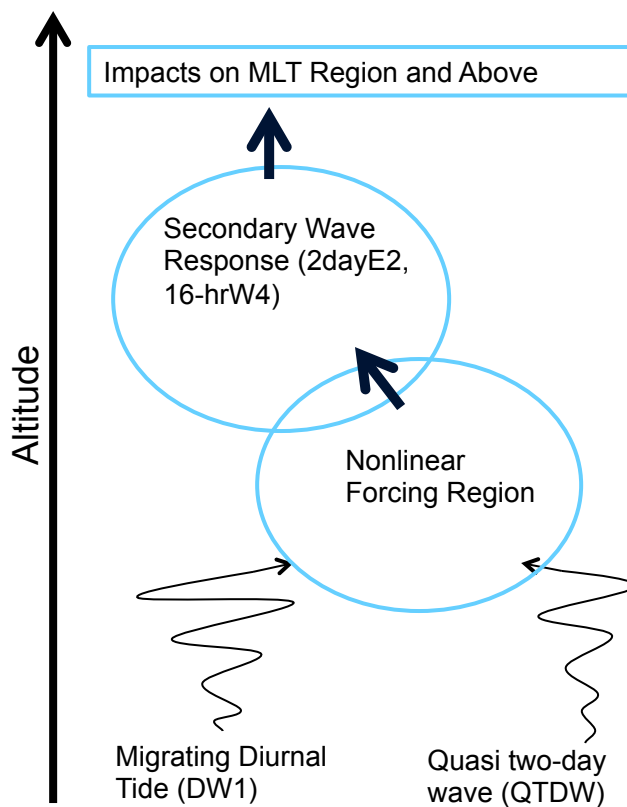


Figure 1.4: Diagram describing the generation and manifestation of secondary waves arising from DW1-2dayW3(QTDW) interaction. The main goal of this thesis is to understand the relationship between the nonlinear forcing region and the secondary wave response and the factors that govern the secondary wave response in the space-atmosphere interaction region.

## Chapter 2

### BACKGROUND

This chapter presents background information pertaining to the subject of this dissertation. A review of classical tidal theory is first presented to provide a theoretical basis for the observation of atmospheric tides and planetary waves in the atmosphere. Details on the migrating diurnal tide and the quasi two-day wave as well as information on how they can nonlinearly interact to generate secondary waves is also provided. Finally, possible mechanisms on how nonlinear interactions between tides and planetary waves can impact atmosphere-space weather coupling are discussed.

#### 2.1 Classical Tidal Theory

The classical theory of atmospheric tides as linearized perturbations on a background mean atmosphere driven by solar heating or lunar forcing is often attributed to Chapman and Lindzen, 1970 [8]. Since the theory has been extensively covered by Chapman and Lindzen, 1970 [8] and other works (Holton, 1975 [38]; Palo, 1994 [75]; Forbes, 1995 [12]), only information that is relevant to this dissertation is presented here. Many of the concepts and equations that are displayed in this section are revisited in subsequent chapters to help interpret the research results.

##### 2.1.1 Mathematical Formulation

Atmospheric tides can be theoretically derived as linearized solutions to the conservation principles governing atmospheric motion. For an ideal, thin, rotating and spherical atmosphere in hydrostatic equilibrium, the governing equations representing the conservation of momentum

(Equations 2.1-2.3), mass (Equation 2.4), energy (Equation 2.5) and the ideal gas law (Equation 2.6) can be written in spherical coordinates as follows (a glossary can be found in Appendix A):

$$\frac{\bar{D}u}{Dt} - \frac{uv \tan \phi}{a} + \frac{uw}{a} = 2\Omega(v \sin \phi - w \cos \phi) - \frac{1}{\rho a \cos \phi} \frac{\partial p}{\partial \lambda} - \frac{1}{\rho} F_x + M_x \quad (2.1)$$

$$\frac{\bar{D}v}{Dt} + \frac{u^2 \tan \phi}{a} + \frac{vw}{a} = -2u\Omega \sin \phi - \frac{1}{\rho a} \frac{\partial p}{\partial \phi} - \frac{1}{\rho} F_y + M_y \quad (2.2)$$

$$\frac{\partial p}{\partial z} = -\rho g \quad (2.3)$$

$$\frac{1}{\rho} \frac{\bar{D}\rho}{Dt} + \frac{1}{a \cos \phi} \frac{\partial u}{\partial \lambda} + \frac{1}{a \cos \phi} \frac{\partial}{\partial \phi} (v \cos \phi) + \frac{\partial w}{\partial z} = 0 \quad (2.4)$$

$$\rho c_v \frac{\bar{D}T}{Dt} = RT \frac{\bar{D}\rho}{Dt} + \rho J - \vartheta \quad (2.5)$$

$$p = \rho RT \quad (2.6)$$

Because the conservation principles are applied in a coordinate frame following the motion of the fluid (Lagrangian), the time rate of change in Equations 2.1, 2.2 and 2.4 is represented by  $\frac{\bar{D}}{Dt} = \frac{\partial}{\partial t} + \frac{u}{a \cos \phi} \frac{\partial}{\partial \lambda} + \frac{v}{a} \frac{\partial}{\partial \phi} + w \frac{\partial}{\partial z}$ . This term is called the material derivative and accounts for the local time rate of change and fluid advection into non-uniform spatial fields. It should be noted that the momentum equation in the vertical direction (Equation 2.3) has been replaced by the hydrostatic equation since the atmosphere is approximately balanced by the pressure gradient force and gravitational force. This implies that the equations only apply to motions where deviations from hydrostatic balance are small. Since this dissertation is not concerned with the lunar gravitational forcing of tides, the gravitational force in Equation 2.3 is assumed to be constant.

The full superposition of atmospheric tides and waves may be seen as a perturbation to the background zonal mean. Accordingly, each of the atmospheric field variables in Equations 2.1-2.6 may be decomposed into the following:

$$\begin{bmatrix} u(\lambda, \phi, z, t) \\ v(\lambda, \phi, z, t) \\ w(\lambda, \phi, z, t) \\ p(\lambda, \phi, z, t) \\ \rho(\lambda, \phi, z, t) \\ T(\lambda, \phi, z, t) \end{bmatrix} = \begin{bmatrix} \bar{u}(\phi, z, t) + u'(\lambda, \phi, z, t) \\ \bar{v}(\phi, z, t) + v'(\lambda, \phi, z, t) \\ \bar{w}(\phi, z, t) + w'(\lambda, \phi, z, t) \\ \bar{p}(\phi, z, t) + p'(\lambda, \phi, z, t) \\ \bar{\rho}(\phi, z, t) + \rho'(\lambda, \phi, z, t) \\ \bar{T}(\phi, z, t) + T'(\lambda, \phi, z, t) \end{bmatrix} \quad (2.7)$$

where the  $\bar{f}$  terms represent a zonal average of each atmospheric variable and the  $f'$  terms denote the perturbation quantities upon the zonal mean. The sum of the zonal average and perturbation terms produces the total atmospheric quantity.

In order to separate the linearized, governing equations for the zonal mean and perturbation quantities, further simplifications are made to the atmosphere:

- (1) The Coriolis force in the zonal momentum equation (Equation 2.1) is equal to  $2\Omega v \sin \phi$ .
- (2) Products of two perturbation quantities, which are nonlinear, are neglected. As a result, the equations are referred to as “linearized”.
- (3) Dissipation forces and momentum source terms are neglected ( $M_x = M_y = F_x = F_y = \vartheta = 0$ ).
- (4) The background zonal mean winds are equal to zero. This allows the equations to be separable and thus, can be solved analytically.
- (5) The background pressure, density and temperature are uniform in latitude and longitude.

From these assumptions, the linearized equations governing the perturbation motion can be written as:

$$\frac{\partial u'}{\partial t} - 2\Omega v' \sin \phi + \frac{1}{a \cos \phi} \frac{\partial}{\partial \lambda} \left( \frac{p'}{\rho_0} \right) = 0 \quad (2.8)$$

$$\frac{\partial v'}{\partial t} + 2\Omega u' \sin \phi + \frac{1}{a} \frac{\partial}{\partial \phi} \left( \frac{p'}{\rho_0} \right) = 0 \quad (2.9)$$

$$\frac{\partial p'}{\partial z} = -g\rho' \quad (2.10)$$

$$\frac{1}{\rho_0} \frac{\partial \rho'}{\partial t} + \frac{1}{a \cos \phi} \frac{\partial u'}{\partial \lambda} + \frac{1}{a \cos \phi} \frac{\partial}{\partial \phi} (v' \cos \phi) + \frac{\partial w'}{\partial z} = 0 \quad (2.11)$$

$$c_v \frac{\partial T'}{\partial t} = \left( \frac{RT_0}{\rho_0} \right) \frac{\partial \rho'}{\partial t} + J' \quad (2.12)$$

$$\frac{p'}{p_0} = \frac{\rho'}{\rho_0} + \frac{T'}{T_0} \quad (2.13)$$

Equations 2.8 and 2.9 represent the linearized momentum equations, which indicate that the acceleration, Coriolis and pressure gradient terms are in balance with each other. Neglecting lunar gravitational effects, atmospheric tides are mainly driven by the daily variation of atmospheric heating, represented by variable,  $J'$ , in Equation 2.12, representing the energy equation. Because the daily solar heating is predominantly periodic in both time and longitude, it can be assumed that the atmospheric tidal responses behave in a similar manner. Hence, each perturbation field is written as a superposition of all tidal components which vary in zonal wavenumber ( $s$ ) and associated frequency ( $\sigma\Omega$ , expressed as a multiple of the earth's rotation rate). Atmospheric tides, possessing periods of 24 hours or less, are associated with  $\sigma$  greater than or equal to 1 while planetary waves, defined by having periods greater than 24 hours, are described by  $\sigma$  less than 1.

$$\begin{bmatrix} u'(\lambda, \phi, z, t) \\ v'(\lambda, \phi, z, t) \\ w'(\lambda, \phi, z, t) \\ p'(\lambda, \phi, z, t) \\ \rho'(\lambda, \phi, z, t) \\ T'(\lambda, \phi, z, t) \end{bmatrix} = \sum_s \sum_\sigma \begin{bmatrix} \hat{u}^{\sigma,s}(\phi, z) \\ \hat{v}^{\sigma,s}(\phi, z) \\ \hat{w}^{\sigma,s}(\phi, z) \\ \hat{p}^{\sigma,s}(\phi, z) \\ \hat{\rho}^{\sigma,s}(\phi, z) \\ \hat{T}^{\sigma,s}(\phi, z) \end{bmatrix} e^{j(s\lambda - \Omega\sigma t)} \quad (2.14)$$

In Equation 2.14, the terms within the brackets on the right hand side represent the complex amplitude of each tidal component classified by frequency ( $\sigma$ ) and wavenumber ( $s$ ). The exponential part on the right hand side indicates that each tidal component is periodic in time and longitude. The summation of components over all possible wavenumbers and frequencies results in the total atmospheric perturbation upon the zonal mean quantity.

The largest heating components are due to absorption of solar energy by water vapor in the troposphere and ozone in the stratosphere. Thus, in addition to being periodic in time and longitude, the daily heating of the atmosphere also varies with latitude and altitude. On the whole, the heating of the atmosphere is typically largest near the equator and in the troposphere and stratosphere. To account for this spatial variation, the heating is decomposed into a complete set of mutually orthogonal modes, where each is a product of a unique latitude-dependent function,  $\Theta_n^{\sigma,s}(\phi)$  and a unique altitude-dependent function,  $J_n^{\sigma,s}(z)$ . Each mode is commonly referred to as a ‘‘Hough’’ mode due to the fact that each latitudinal function,  $\Theta_n^{\sigma,s}$ , in Equation 2.15 is a Hough function (Hough [41]) and a solution to Laplace’s tidal equation discussed later. For a given frequency, each Hough mode is often denoted by absolute zonal wavenumber ( $s$ ) and meridional index ( $n$ ).

$$J'(t, \lambda, \phi, z) = \sum_s \sum_\sigma \sum_n \Theta_n^{\sigma,s}(\phi) J_n^{\sigma,s}(z) e^{j(s\lambda - \Omega\sigma t)} \quad (2.15)$$

From the linearized thermodynamic energy equation (Equation 2.12) and the equation for

perturbation heating (Equation 2.15), it can be observed that the projection of heating amplitudes onto mutually orthogonal modes that are dependent in latitude and altitude causes a similar projection for tidal response amplitudes. Therefore, the tidal perturbation amplitudes can also be decomposed into a summation of mutually orthogonal Hough modes.

$$\begin{aligned}
\hat{u}(\phi, z) &= \sum_n U_n^{\sigma,s}(\phi) A_n^{\sigma,s}(L_n^{\sigma,s}(z)) \\
\hat{v}(\phi, z) &= \sum_n V_n^{\sigma,s}(\phi) B_n^{\sigma,s}(L_n^{\sigma,s}(z)) \\
\hat{w}(\phi, z) &= \sum_n \Theta_n^{\sigma,s}(\phi) C_n^{\sigma,s}(L_n^{\sigma,s}(z)) \\
\hat{p}(\phi, z) &= \sum_n \Theta_n^{\sigma,s}(\phi) D_n^{\sigma,s}(L_n^{\sigma,s}(z)) \\
\hat{\rho}(\phi, z) &= \sum_n \Theta_n^{\sigma,s}(\phi) E_n^{\sigma,s}(L_n^{\sigma,s}(z)) \\
\hat{T}(\phi, z) &= \sum_n \Theta_n^{\sigma,s}(\phi) F_n^{\sigma,s}(L_n^{\sigma,s}(z))
\end{aligned} \tag{2.16}$$

where  $U_n^{\sigma,s}$  and  $V_n^{\sigma,s}$  are related to the Hough function,  $\Theta_n^{s,n}$ , by the following expressions:

$$U_n^{\sigma,s}(\phi) = \frac{1}{2\Omega a[(\sigma/2)^2 - \sin^2 \phi]} \left[ \frac{s\sigma}{2 \cos \phi} + \sin \phi \frac{\partial}{\partial \phi} \right] \Theta_n^{\sigma,s}(\phi) \tag{2.17}$$

$$V_n^{\sigma,s}(\phi) = \frac{j}{2\Omega a[(\sigma/2)^2 - \sin^2 \phi]} \left[ s \tan \phi + \frac{\sigma}{2} \frac{\partial}{\partial \phi} \right] \Theta_n^{\sigma,s}(\phi) \tag{2.18}$$

The latitudinal functions in Equations 2.17 and 2.18 are known as the U and V expansion functions, respectively, and describe the latitudinal dependence of the horizontal wind fields. The latitudinal functions of the other variables ( $w'$ ,  $T'$ ,  $\rho'$  and  $p'$ ) are represented by the Hough function,  $\Theta_n$ .

The vertical dependence for each of the perturbation amplitudes is represented by the unique functions of  $L_n$ . Exact expressions for the full vertically-dependent functions for each perturbation field can be derived after algebraic manipulation of the linearized governing equations as presented in Chapman and Lindzen, 1970 [8].

Substituting the assumed solutions for each perturbation field ( $u'$ ,  $v'$ ,  $w'$ ,  $T'$ ,  $\rho'$ ,  $p'$ ) and forcing ( $J'$ ) into the linearized equations (Equations 2.8-2.13) and reducing the system of six equations

and six unknowns to one equation yields a single second-order partial differential equation that is separable in latitude and altitude. Two ordinary differential equations may be obtained after introducing a separation constant of  $-1/h_n$  where  $h_n$  is commonly referred to as the equivalent depth. The latitudinal dependent differential equation that is extracted is known as Laplace's tidal equation:

$$\frac{\partial}{\partial \mu} \frac{1 - \mu^2}{((\sigma/2)^2 - \mu^2)} \frac{\partial}{\partial \mu} \Theta_n^{\sigma,s} - \frac{1}{((\sigma/2)^2 - \mu^2)} \left( \frac{s^2}{1 - \mu^2} - \frac{s}{(\sigma/2)} \frac{((\sigma/2)^2 + \mu^2)}{((\sigma/2)^2 - \mu^2)} \right) \Theta_n^{\sigma,s} + \epsilon_n^{\sigma,s} \Theta_n^{\sigma,s} = 0 \quad (2.19)$$

where  $\mu = \sin \phi$  and  $\epsilon_n^{\sigma,s} = \frac{(2\Omega a)^2}{gh^{\sigma,s}}$

By applying the boundary condition of boundedness at the poles, solutions to Laplace's tidal equation for each tidal component denoted by  $(\sigma, s)$  can be found and form a complete set of eigenvalue-eigenfunction pairs. The eigenvalues ( $\epsilon_n$ ) are proportional to the equivalent depth and the eigenfunctions are the aforementioned Hough functions ( $\Theta_n$ ), which can be numerically solved by expanding  $\Theta_n$  into an expansion of associated Legendre Polynomials.

The other ordinary differential equation that is obtained from separation is referred to as the vertical structure equation:

$$H \frac{d^2 L_n}{dz^2} + \left( \frac{dH}{dz} - 1 \right) \frac{dL_n}{dz} + \frac{1}{h_n} \left( \frac{dH}{dz} + \kappa \right) L_n = \frac{\kappa}{\gamma g H h_n} J_n \quad (2.20)$$

The boundary conditions associated with the vertical structure equation are zero vertical velocity at  $z=0$  and upward energy propagation at  $z=\infty$ . By assuming these boundary conditions, solutions ( $L_n(z)$ ) to the vertical structure equation are found to be either sinusoidal (propagating) with some vertical wavelength or trapped within the excitation region, depending on the value of  $h_n$ . In general, positive values of  $h_n$  imply propagating Hough modes while negative values of  $h_n$  indicate evanescence.

Overall, the combination of Laplace's tidal equation and the vertical structure equation permits one to solve for all Hough functions ( $\Theta_n(\phi)$ ) of a specific tidal component and for each Hough mode, solve for the vertical structure ( $L_n(z)$ ) given the vertical, mode-specific heating profile.

Subsequently, the solutions for  $L_n(z)$  and  $\Theta_n(\phi)$  can be used in Equations 2.16-2.18 to determine the classical complex amplitudes for each tidal component. Finally, the superposition of all tidal components represents the total perturbation to the background zonal mean.

### 2.1.2 Tidal Sources and Theory Limitations

In classical tidal theory, the distribution of heating drives the generation of atmospheric tidal components. Most of the solar heating that excites atmospheric tides originates from infrared radiation absorption by water vapor in the troposphere, ultraviolet radiation absorption of ozone in the stratosphere and extreme-ultraviolet radiation by molecular oxygen in the lower thermosphere (Siebert, 1961 [103]; Chapman and Lindzen, 1970 [8]; Forbes and Garrett, 1978 [14]; Groves, 1982 [24]). Considering that atmospheric heating acts in accordance with the apparent westward motion of the sun across the Earth, it is expected that sun-synchronous (migrating) responses dominate the tidal spectrum. Although migrating tides are veritably the dominant components in the real atmosphere, a collection of nonmigrating tidal components exist as well. Nonmigrating components are forced by longitudinal variability in tidal sources, which can be introduced through land-sea differences topography, and latent heat release from tropical convection (Tsuda and Kato, 1989 [109]; Hamilton, 1981 [30]; Williams and Avery, 1996 [113]; Talaat and Lieberman, 1999 [105]). The mixture of migrating and nonmigrating tidal components that have been detected in the real atmosphere highlights the necessity of determining realistic solar heating distributions for the entire atmosphere.

Even with realistic distributions of atmospheric heating specified, the agreement of classical tidal theory with atmospheric tidal observations is limited due to the theoretical assumptions. While dissipation is not included in classical tidal theory, modeling and observational studies have concluded that dissipation from radiative cooling, friction, turbulence and diffusion of momentum and heat serve an important role in the damping of tidal amplitudes (Lindzen, 1972 [54]; Forbes and Hagan, 1979 [15]). Previous studies (Forbes, 1988 [16]) have also indicated that the effects of dissipation are greater for components with shorter vertical wavelengths and longer periods.

Subsequently, only few tides and waves are able to propagate above 100 km and directly penetrate the thermosphere and ionosphere.

Furthermore, the inclusion of realistic physical processes such as friction, mean winds and a nonuniform background atmosphere in the linearized perturbation equations (Equations 2.8-2.11) results in solutions that are not separable in latitude and altitude and thus, cannot be solved analytically. Hence, the latitudinal shape of each classical Hough modes is no longer independent with height (Richmond, 1975 [91]). In order to determine tidal solutions for a given forcing profile, the governing equations must be solved using numerical integration methods. A number of numerical studies conducted over the past four decades (Lindzen and Hong, 1974 [53]; Forbes and Hagan, 1988 [16]) have analyzed how mean winds can alter the latitudinal and vertical structure of tides from classical tidal theory. Spatial gradients in the background wind or temperature have also been observed to significantly enhance or suppress the propagation of waves (Walterscheid, 1980 [112]; McLandress, 2002 [64]). Additionally, large eastward or westward zonal winds can Doppler shift tides to smaller or larger frequencies, modifying the inherent propagation and dissipation characteristics of each wave (Forbes and Vincent, 1989 [19]).

Lastly, the interactions between atmospheric tides, planetary waves and gravity waves are not captured through the application of classical theory because nonlinear terms are neglected in the linearized governing equations. Studies have found that nonlinear interactions may have a large impact on the mean background state, short-term tidal variability and the generation of additional waves throughout the atmosphere (Teitelbaum and Vial, 1991 [107]; Angelats i Coll and Forbes, 2002 [1]; Chang et al., 2011 [7]). The generation of secondary waves is a key component in this dissertation and is discussed in subsequent chapters of this document.

## 2.2 Migrating Diurnal Tide

As predicted by tidal theory and shown in observations, the migrating diurnal tide is one of the principal responses to the solar heating of the atmosphere. Since it has a 24 hour period and propagates westward with one perturbation crest/trough along a latitude circle, it is commonly

referred to as DW1 (see Appendix B for nomenclature). The diurnal tide is primarily excited from the diurnal variation in infrared radiation absorption by water vapor in the troposphere and secondarily from ultraviolet radiation absorption in the the stratosphere and extreme ultraviolet radiation absorption in the lower thermosphere. Like many other tides and waves, the DW1 forced in the lower atmosphere assumes maximum amplitude values in the mesosphere-lower thermosphere (MLT) around 100 km before eddy and molecular diffusion forces suppresses the amplitude growth rate. The DW1 may also be re-excited in the lower thermosphere through extreme-ultraviolet absorption, but this component will not be discussed in further detail here.

Laplace's tidal equation from classical tidal theory predicts that the DW1 is composed of a series of Hough modes (Figure 2.1), which are commonly denoted by  $(|s|, n)$  where  $s$  is the zonal wavenumber and  $n$  is the meridional index representing the number of latitudinal nodes in the Northern or Southern Hemisphere. Because solar heating in the troposphere projects most efficiently on the DW1 (1, 1) Hough mode, the characteristics of the DW1 (1, 1) Hough mode dominates the latitudinal structure of the DW1 throughout the troposphere, stratosphere and mesosphere. As shown in Figure 2.1, the DW1 (1, 1) Hough function has a primary peak at the equator and secondary peaks that are anti-phase with the primary peak. From this result and Equation 2.16, it should be predicted that the DW1 (1, 1) mode in the temperature, pressure, density and vertical velocity fields be largest at the equator. In contrast, the U and V expansion functions show that the DW1 (1, 1) mode peaks around  $\pm 20^\circ$  latitude in the horizontal and meridional wind fields. During solstice periods or in the stratosphere, other Hough modes may be excited when the solar heating more efficiently projects onto the latitudinal structures of those respective modes.

The results of classical tidal theory also determine the propagation characteristics of each Hough mode. As previously mentioned, modes with negative equivalent depths (negative meridional index) are trapped near the excitation region while modes with positive equivalent depths (positive meridional index) are able to propagate vertically. Moreover, the modes with the largest vertical wavelengths are less susceptible to dissipation. This mechanism explains why the DW1 (1, 1) Hough mode with a long vertical wavelength (27.9 km) is able to penetrate higher into the atmosphere

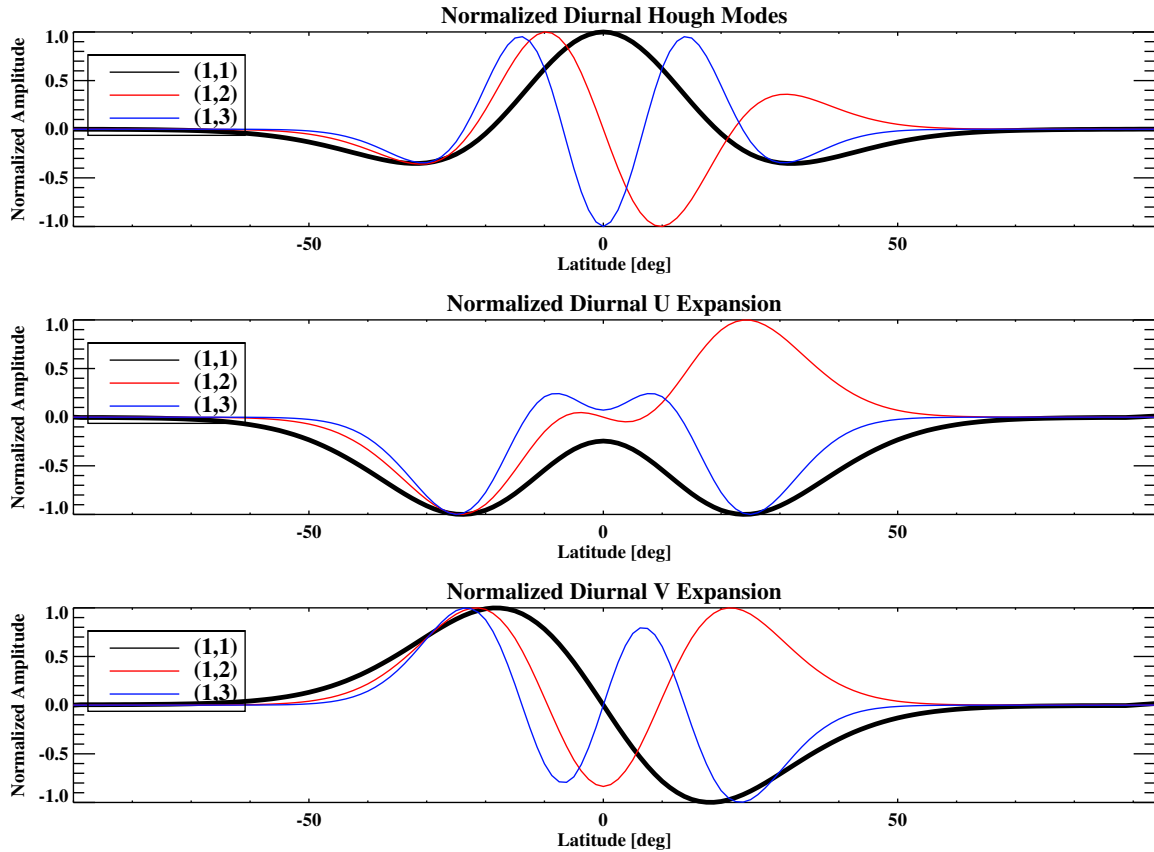


Figure 2.1: Latitudinal structure of the first 3 propagating modes of the migrating diurnal tide. The first 3 Hough modes (top, U expansion functions (middle) and V expansion functions (bottom) are displayed.

than other propagating DW1 modes ((1, 2), (1, 3), etc.) with shorter vertical wavelengths. In general, higher order modes have shorter vertical wavelengths and thus, are more susceptible to dissipation.

In reality, the presence of mean winds and nonuniform background fields may alter the Hough mode decomposition of the DW1 and other tides and planetary waves. There are several perspectives that can be used to describe these effects on the Hough modes. One perspective is the “mode coupling” approach (Forbes and Hagan, 1988 [16]. In this context, the tide is still assumed to be decomposed into a series of classical Hough modes and the main effect of zonal mean winds is to couple energy from one classical Hough mode to another. For example, Forbes and Hagan, 1988

[16] theoretically demonstrated that the background winds advect energy away from the dominant DW1 (1, 1) mode and to higher order modes, effectively changing the total latitudinal structure of the DW1. Other studies (Ortland, 2005 [72]; Svoboda et al., 2005 [104]) take the approach that each classical Hough mode structure undergoes changes in the presence of realistic parameters. By imposing a forcing profile resembling the DW1 (1, 1) mode from classical tidal theory at the lower boundary of a model, Ortland, 2005 [73] demonstrated how the latitudinal and vertical structure of the Hough mode evolves as it moves into regions where zonal wind effects and damping are significant. An example is shown in Figure 2.2, which shows the distortion of the classical DW1 (1, 1) Hough mode in a hypothetical atmosphere characterized by eastward winds centered at 40°N latitude. Because the shape of each Hough mode is altered, the modes using this approach are no longer orthonormal to each other and thus, cannot be superposed to form the total tide or wave.

Since classical tidal theory and subsequent modeling studies have indicated that the structure of the DW1 and other tidal components depends on a large number of factors, observations of DW1 amplitudes varying on different timescales are not surprising (Lieberman et al., 2007 [49]). By analyzing temperature data on the Upper Atmospheric Research Satellite (UARS) High Resolution Doppler Imager (HRDI) instrument, Burrage et al., 1995 [4] revealed semiannual and interannual amplitudes variations of the diurnal (1, 1) Hough mode in the stratosphere and mesosphere. Subsequent studies have suggested that the long term variations could be caused by a combination of variation in tidal heating, spatial gradients in the mean wind and wave momentum deposition (McLandress, 2002 [64]; Lieberman et al., 2007 [49]; Mayr and Mengel, 2005 [61]).

Until recently, definitive observations of short-term variability in the DW1 have been very limited due to the challenges of ground-based and satellite-based observations. Although ground-based studies have shown significant day-to-day changes in oscillations at diurnal periodicities, observations from only a single location do not allow one to separate the effects of the DW1 from other diurnal components with different zonal wavenumbers. In contrast, observations from a satellite-based platform are global in extent, but cannot distinguish between tidal components over time windows less than 30 days due to inadequate solar local time coverage. As a result, short-

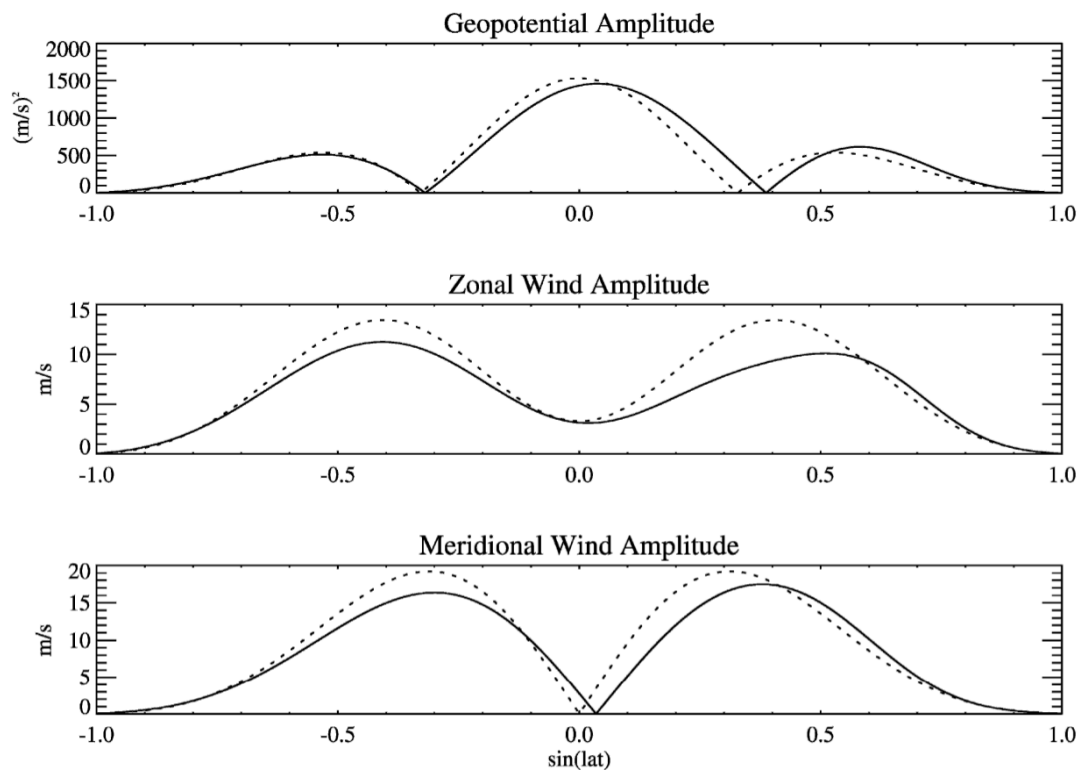


Figure 2.2: Diurnal (1, 1) Hough mode structure for geopotential height (top), zonal wind (middle) and meridional wind (bottom) fields under different mean wind configurations. Results for the zero wind case are represented by dashed lines while the results for an atmosphere characterized by an eastward Gaussian jet centered at  $40^\circ\text{N}$  latitude are represented by the solid lines. These results originate from a modeling study conducted by Ortland, 2005 [73].

term tidal changes cannot be captured from a single satellite. However, Nguyen and Palo, 2013 [69] recently validated a technique that provides estimates of the DW1 on a daily basis by combining data from two satellites. As shown in Figure 2.3, the DW1 amplitude can vary considerably on day-to-day basis. Details of this technique can be found in Chapter 5 of this dissertation and Nguyen and Palo, 2013 [69].

Despite the lack of short-term estimates of the DW1 until recently, several mechanisms driving short-term variability have been proposed. The leading theory is that tidal amplitudes can be altered on short time scales through nonlinear interactions with planetary waves (Teitelbaum and Vial, 1991 [107]). Chang et al., 2011 [7] investigated this mechanism by employing a general

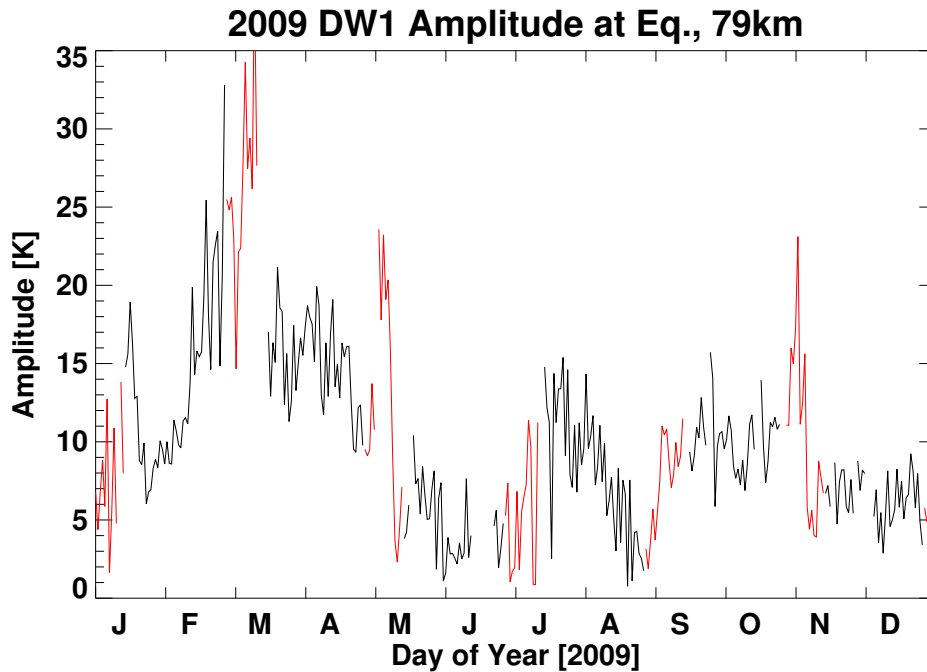


Figure 2.3: Daily estimates for the DW1 for 2009 at equator and 79 km. Results are obtained by combining MLS and SABER data as explained by Nguyen and Palo, 2013 [69]. Estimates obtained from poor MLS/SABER local time configurations (condition number greater than 20) are displayed in red. An explanation on local time sampling and condition number is provided in Chapter 5.

circulation model to analyze the variability of the DW1 in the presence of a quasi two-day wave. The study concluded that the DW1 amplitudes decreased in the presence of the quasi two-day wave through induced changes in the background wind and not through nonlinear forcing. As shown in Figure 2.3, however, large short-term changes in the DW1 amplitude occur throughout the year. Because planetary wave events are mainly transient, other mechanisms must exist to fully explain the day-to-day changes in the DW1.

### 2.3 Planetary Waves and the Quasi Two-Day Wave

In the middle and upper atmosphere research fields, planetary waves are generally defined as global scale oscillations with periods greater than a solar day (Forbes, 1995 [12]). Like atmospheric tides, planetary waves can propagate in the horizontal and vertical directions or remained trapped

near the excitation region. They are sometimes grouped by their dynamic behavior. Some planetary waves are classified as Rossby waves, which are mainly westward propagating with respect to the background flow and exist due to the variation of the Coriolis force with latitude. Others behave like inertia gravity waves, which are buoyancy waves that are modified by rotation. A special class of planetary waves is the Kelvin wave. These eastward propagating waves are strictly zonal wind perturbations that are confined to the equatorial region by the Coriolis force and have been observed to possess periods of 3-20 days (Salby et al., 1984, [100]; Riggin et al., 1997 [92]; Lieberman and Riggin, 1997 [47]).

While planetary waves may be forced by various processes such as topography, land-sea differences and convection, they can also act as manifestations of free, unforced, normal modes. These normal modes are predicted by classical tidal theory as solutions to Laplace's tidal equation in the case of zero forcing. Over the past half-century, researchers have provided normal mode evidence through observations of the 2day, 5day, 10day and 16day waves (Hirota, 1971 [35]; Madden and Julian, 1972 [57]; Madden, 1979 [56]; Salby, 1984 [98]; Forbes, 1996 [13]). These commonly observed waves assume periods and zonal wave numbers that are close to the values predicted by classical tidal theory. However, differences exist between the classical normal modes and the observed manifestations. For instance, unlike in classical tidal theory, the normal mode oscillations have been observed to display phase variation with altitude, which makes the normal modes susceptible to dissipative and mean wind effects (Salby, 1981 [96]).

Since the early 1970s, ground-based and space-based observations have revealed the quasi two-day wave (2dayW3) as one of the most dominant oscillations in the MLT region, achieving maximum amplitudes upwards of 50-60 m/s in the meridional wind field over some duration (Muller, 1972 [68]; Rodgers and Prata, 1981 [93]; Wu et al., 1993 [116]). Since significant 2dayW3 oscillations only last for about 20-30 days, the timeframes during which they are significant are often referred to as events. The largest events generally occur during late-January, which are characterized by large 2dayW3 amplitudes at mid-to-high latitudes in the southern summer hemisphere and weaker amplitudes at mid-to-high latitudes in the winter northern hemisphere. Events are also seen in

in the summer northern hemisphere in July, though these events are less prominent and generally have a longer lifetime.

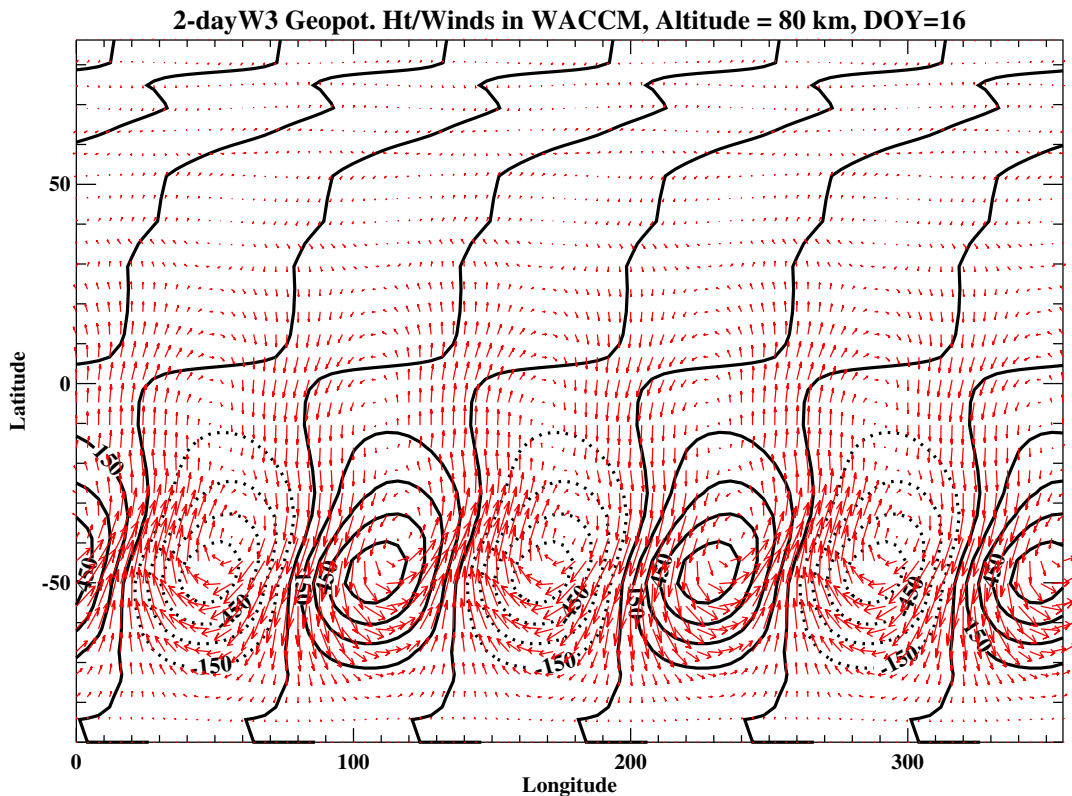


Figure 2.4: 2dayW3 geopotential height and wind vectors at 80 km as a function of latitude and longitude. Geopotential height perturbations are displayed as black contours while horizontal wind vectors are shown as red vectors. Results are output from WACCM experimental runs conducted by Nick Pedatella.

The 2dayW3 has exhibited wave periods of around 1.8-2.2 days (Harris and Vincent, 1993; [31]; Wu et al., 1993 [116]) with zonal wavenumbers 3 and 4 during the southern summer and zonal wavenumbers 2-4 during the northern summer. Due to similar period and zonal wavenumber, scientists have associated the 2dayW3 with the 2.1-day, (3, 3) mixed gravity-Rossby normal mode that is a solution to Laplace's tidal equation. It is sometimes referred to as the (3, 0) normal mode using a  $(|s|, |s| - n)$  notation (Salby, 1981 [95]). Because of its manifestation as a normal mode, the 2dayW3 is likely to be constantly forced by broadband forcing in the troposphere where most of the

turbulent processes in the atmosphere materializes (Salby, 1981 [95]). During post-solstice periods however, large westward zonal jets in the summer mesosphere often create large vertical shears and horizontal temperature gradients, creating baroclinically unstable regions. If the 2dayW3 is able to propagate into baroclinically unstable regions, the wave is significantly amplified by drawing energy from the mean flow (Plumb, 1983 [86]; Salby and Callaghan, 2000 [99]). From the amplification region, the 2dayW3 can further propagate vertically to about 100-120 km before it is dissipated by molecular and eddy diffusion. Along the way, it also imparts large westward momentum forcing onto the mean background flow (Lieberman, 1999 [46]). Consequently, the mean zonal flow shifts more westward and shuts off the growth rate of the 2dayW3 (Palo et al., 1999 [77]; Chang et al., 2011 [7]).

Since the 2dayW3 is a manifestation of a mixed gravity-Rossby mode, it behaves as an inertia gravity wave or Rossby wave depending on the period and horizontal scale of the wave. At mid-to-high latitudes, the quasi two-day wave dynamically behaves like a Rossby wave in quasi-geostrophic balance. This implies that the propagation and structure of the 2dayW3 is mainly determined from the balance between the Coriolis force and pressure gradient force. Figure 2.4 illustrates the relationship between the 2dayW3 winds and the geopotential height, which is representative of the perturbation pressure distribution. It is observed that the 2dayW3 winds are mostly parallel to geopotential height contours, indicating an approximate geostrophic balance. At lower latitudes, the quasi two-day wave is much smaller in amplitude and behaves more like an inertia-gravity wave due to the smaller Coriolis force near the equator.

## 2.4 Secondary Waves from Quasi Two-Day Wave and Migrating Diurnal Tide Interaction

As established by Teitelbaum and Vial [107], the simultaneous presence of two waves in the same region can force secondary waves through the nonlinear terms in the governing conservation laws. This is mathematically demonstrated here by expanding each atmospheric field variable ( $u, v, w, T, \rho, p$ ) in Equations 2.1-2.6, generally denoted here by  $f$ , into an asymptotic series of

power with small parameter,  $\epsilon$ .

$$f = f^{(0)} + \epsilon f^{(1)} + \epsilon^2 f^{(2)} + \dots \quad (2.21)$$

In Equation 2.21,  $f^{(0)}$ ,  $f^{(1)}$  and  $f^{(2)}$  represents the mean value, first-order perturbation and second-order perturbation values, respectively. The variables in the form expressed by Equation 2.21 are then substituted into the equations of motion (Equation 2.1-2.6). Separate sets of equations governing each order of motion can be obtained by collecting like powers of  $\epsilon$ . While linear terms such as the time derivative, Coriolis force, pressure gradient force, etc. are present in all sets of equations, the nonlinear terms in Equation 2.1-2.6 introduce more terms into the set of equations for increasing order of motion. For instance, substituting Equation 2.22 into the nonlinear advection term for arbitrary variable,  $f$ , results in the following:

$$\vec{u} \cdot \nabla f = \vec{u}^{(0)} \cdot \nabla f^{(0)} + \epsilon (\vec{u}^{(1)} \cdot \nabla f^{(0)} + \vec{u}^{(0)} \cdot \nabla f^{(1)}) + \epsilon^2 (\vec{u}^{(2)} \cdot \nabla f^{(0)} + \vec{u}^{(0)} \cdot \nabla f^{(2)} + \vec{u}^{(1)} \cdot \nabla f^{(1)}) + \dots \quad (2.22)$$

As shown in Equation 2.22, the sets of equations governing mean motion and perturbations of order  $n$  all contain mean advection terms of form  $\vec{u}_0 \cdot \nabla f^{(n)}$ . However, the first-order and second-order perturbation equations are also forced by an additional term  $(\vec{u}^{(n)} \cdot \nabla f_0)$  describing wave advection of the mean. Finally, the second-order equations are forced by an additional  $\vec{u}^{(1)} \cdot \nabla f^{(1)}$  term describing wave-wave advection.

If the mean state for all variables is defined, then a linearized set of equations is obtained for the first order perturbation as determined by classical tidal theory. Furthermore, if the first order perturbation is defined, then a set of linearized equations governing the motion of the second order perturbation is retrieved. In the linearized set of equations for the second order perturbations, the products of first order perturbations such as the wave-wave advection term become momentum and thermal source terms and are responsible for generating second order (secondary waves) at specific frequencies and wave numbers. This concept is demonstrated by decomposing each  $f^{(1)}$  into the sum of two primary waves,  $f_1$  and  $f_2$ . The wave-wave advection term may be expressed accordingly as:

$$\vec{u}' \cdot \nabla f' = \{(u'_1 + u'_2) \frac{\partial}{a \cos \phi \partial \lambda} + (v'_1 + v'_2) \frac{\partial}{a \partial \phi} + (w'_1 + w'_2) \frac{\partial}{\partial z}\} (f'_1 + f'_2) \quad (2.23)$$

Each perturbation in Equation 2.23 is assumed to be in the form  $\hat{f}\cos(s\lambda - \omega t + \theta_f)$ , where  $\hat{f}$  and  $\theta_f$  are the real-valued amplitude and phase values, respectively. Substituting this form into the wave-wave advection term (Equation 2.23) for each perturbation variable generates additional signals through trigonometric multiplication:

$$\begin{aligned} \cos(s_1\lambda - \omega_1 t + \theta_1) \cos(s_2\lambda - \omega_2 t + \theta_2) &= \frac{1}{2} \cos[(s_1 + s_2)\lambda - (\omega_1 + \omega_2)t + (\theta_1 + \theta_2)] \\ &+ \frac{1}{2} \cos[(s_1 - s_2)\lambda - (\omega_1 - \omega_2)t + (\theta_1 - \theta_2)] \end{aligned} \quad (2.24)$$

$$\begin{aligned} \cos(s_1\lambda - \omega_1 t + \theta_1) \sin(s_2\lambda - \omega_2 t + \theta_2) &= \frac{1}{2} \sin[(s_1 + s_2)\lambda - (\omega_1 + \omega_2)t + (\theta_1 + \theta_2)] \\ &- \frac{1}{2} \sin[(s_1 - s_2)\lambda - (\omega_1 - \omega_2)t + (\theta_1 - \theta_2)] \end{aligned} \quad (2.25)$$

As detailed in Appendix C, the multiplication of two primary waves described by zonal wave numbers,  $s_1$  and  $s_2$ , and frequencies,  $\omega_1$  and  $\omega_2$ , respectively, produces terms at the following wavenumber-frequency pairs:  $[(s_1 + s_2), (\omega_1 + \omega_2)]$ ,  $[(s_2 - s_1), (\omega_2 - \omega_1)]$ ,  $[(2s_1), (2\omega_1)]$ , and  $[(2s_2), (2\omega_2)]$ . Thus, the wave-wave advection term and other products of primary waves contained in the equations of motion theoretically generate secondary waves at the specified zonal wavenumber-frequency pairs by serving as momentum and thermal forcing terms in the linearized second-order perturbation equations. Past studies have found this generation mechanism is much more significant for the secondary waves at the sum and difference waves at  $[(s_1 + s_2), (\omega_1 + \omega_2)]$ ,  $[(s_2 - s_1), (\omega_2 - \omega_1)]$  than for the waves arising from self-interaction (Hines, 1960 [34]; Teitelbaum and Vial, 1991 [107]). Hence, this dissertation mainly focuses on the generation of the sum and difference secondary waves.

Applying this theory to the DW1 ( $s=-1$  and  $\omega=1$  cycles per day) and the quasi-two day wave ( $s=-3$  and  $\omega=0.5$  cycles per day) suggests the forcing of a westward propagating sum wave with a period of 16 hours and zonal wavenumber 4 ( $s=-4$  and  $\omega=1.5$  cycles per day) and an eastward difference wave with a period of 48 hours and zonal wavenumber 2 ( $s=2$  and  $\omega=0.5$  cycles per

day). In this scenario and throughout this dissertation, positive wavenumber refers to eastward propagating waves and negative wavenumber refers to westward propagating waves. For simplicity, these waves will be referred to as 16hrW4 and 2dayE2, respectively for the remainder of this document.

Several past studies have attempted to provide observational evidence of secondary waves from the nonlinear interaction between the DW1 and 2dayW3. According to Teitelbaum and Vial, 1991 [107], the linear superposition of the primary and secondary waves will result in an apparent modulation of the shorter period wave amplitude with the longer period wave. Many ground-based observational studies have applied this concept to identify nonlinear wave-wave interactions by observing tidal amplitude modulation at planetary wave periodicities (Manson and Meek, 1984 [59], Beard et al., 1999 [3]). Other studies have provided evidence of secondary waves by identifying secondary waves whose periods are distinct from the primary interacting waves. As an example, Pancheva, 2006 [81] used a meteor radar to identify a 16 hour periodicity in meridional wind data during a quasi-two day wave event. To verify that the 16 hour periodicity was a product of a DW1-2dayW3 nonlinear interaction, the observed vertical phase structure of the 16 hour periodicity was shown to match a hypothetical phase structure.

Although ground-based observations have provided circumstantial evidence of nonlinearly generated secondary waves at a single location, the origin of the generation cannot be understood without global measurements. Moreover, other secondary waves with similar periodicities (i.e. 2dayE2) to one of the primary interacting waves cannot be identified without multiple observations along a latitude circle to separate the wavenumbers. As explained previously, single satellite-based instruments can provide the necessary global measurements, but have poor temporal resolution for waves with periods less than 24 hours due to the long time windows that are required to eliminate aliasing from the measurements. Considering that 2dayW3 events and correspondingly, their nonlinear interactions with tides are short-lived, the generated secondary waves have been difficult to identify. However, secondary waves with periods longer than a day can be identified on short time scales using appropriate techniques. Recently, Palo, 2006 [76] applied the Fast Fourier

Synoptic Mapping (FFSM) method to satellite-measured temperatures to provide global evidence of secondary waves arising from DW1-2dayW3 interaction for the first time.

Due to the limitations of ground-based and satellite-based observations, other studies have turned to numerical models to investigate the DW1-QTDW nonlinear interaction. Using a self-consistent, time-dependent model with the complete conservation equations for momentum, mass and energy (National Center for Atmospheric Research Thermosphere-Ionosphere-Mesosphere-Electrodynamics General Circulation Model (NCAR TIME-GCM)), Palo et al., 1999 [77] showed that this nonlinear interaction could generate the 16hrW4 and 2dayE2 waves that are predicted from trigonometry. The study also found that these secondary waves can also interact with each other or the primary waves to produce smaller tertiary waves. Chang et al., 2011 [7] also used the NCAR TIME-GCM to investigate the interaction between 2dayW3 and the DW1 (as well as the SW2) and found similar secondary waves (Figure 2.5). While Palo et al., 1999 [77] and Chang et al., 2011 [7] demonstrated that secondary and tertiary waves may generated during nonlinear wave-wave interactions, they mainly focused on how the 2dayW3 interaction resulted in decreased DW1 amplitudes. Additionally, these studies did not investigate the forcing region of secondary waves and the reasons why secondary wave responses are significant. Thus, the overall forcing and manifestation of the secondary waves from the DW1-2dayW3 nonlinear interaction has yet to be explored in observations and numerical modeling.

## 2.5 Potential Impacts of Nonlinearly Generated Waves

The main motivation for understanding the generation mechanism of secondary waves is that these waves may assume an important role in the coupling of the space-atmosphere interaction region. Although some of the possible impacts are briefly mentioned in Chapter 1, more detailed information is presented in this section.

A recent study by Pedatella and Forbes, 2012 [83] highlights the potential impacts of nonlinearly generated waves in coupling the MLT to the F-region ionosphere. Spanning 150 km to 500 km in co-location with the neutral thermosphere, the F-region ionosphere contains the highest

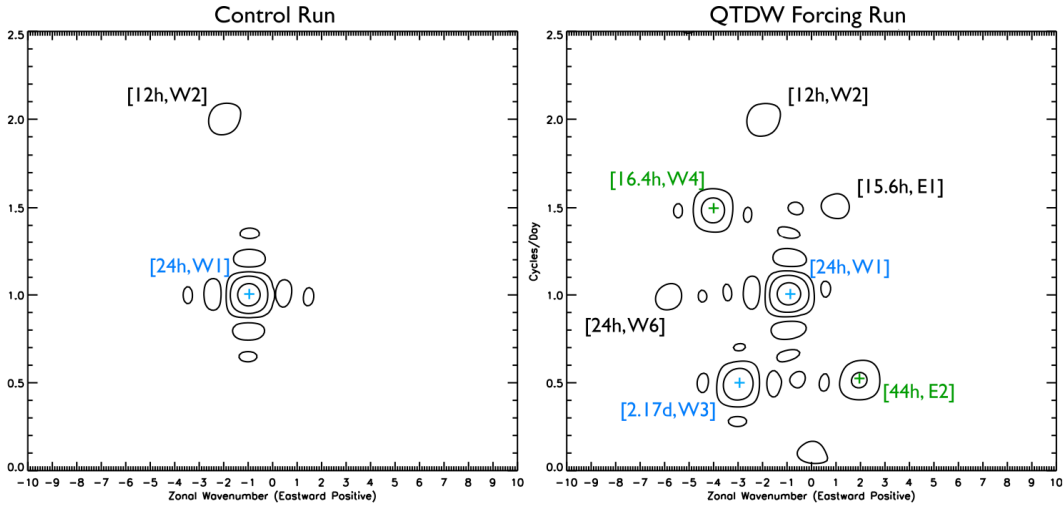


Figure 2.5: Fourier power of zonal wind fields in TIME-GCM control run (left) with no forcing and (right) with 2-dayW3 forcing at  $7.5^\circ$  S, 90 km altitude. Figure taken from Chang et al., 2011 [7].

concentration of ions and electrons in the atmosphere. In this study, temperatures and OH airglow emissions in the MLT region measured from the Sounding of the Atmosphere using Broadband Emission Radiometry (SABER) instrument on the Thermosphere Ionosphere Mesosphere Energetics and Dynamics (TIMED) satellite were spectrally analyzed along with electron density measured at around 350 km by the Challenging Minisatellite Payload (CHAMP) satellite during late January 2006 when the 2dayW3 is most prominent. As displayed in Figure 2.6, a westward-propagating, 2-day, zonal wavenumber 3 periodicity and eastward propagating, 2-day, zonal wavenumber 2 periodicity dominates the spectra in both the MLT and ionospheric observations. Pedatella and Forbes, 2012 [85] concluded that these spectral peaks represented the 2dayW3 and 2-dayE2 respectively and thus, represented the majority of the longitudinal variability observed in the MLT and F-region ionosphere during this period.

Despite the correlation between perturbations observed in the MLT and ionosphere, it is still not clear how the effects of atmospheric tides and planetary waves and their nonlinearly generated components can be transmitted to the ionospheric altitudes that are over 150 km above most source regions. Most scientists have suggested that the main pathway for this process to occur is through

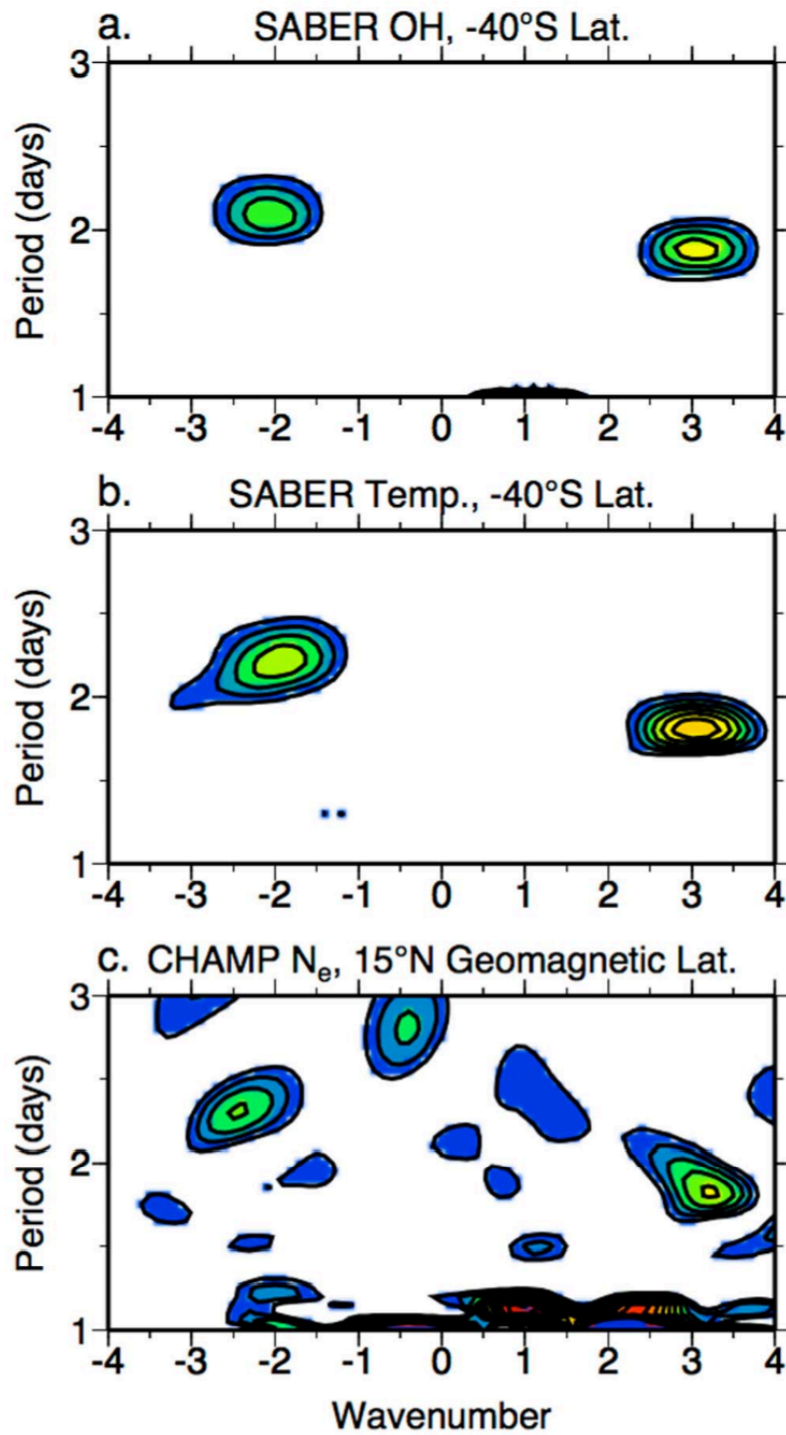


Figure 2.6: Residual total electron content (TEC) observed by the CHAMP satellite at 22:00 local time and 350km. Residual TEC were passed through a bandpass filter centered at 15 days. Figure taken from Pedatella and Forbes, 2012 [83].

the E-region ionosphere, which is beneath the F-region and spans 100 to 150 km altitude. Unlike the F-region ionosphere at higher altitudes, the E-region is characterized by frequent collisions between charged-particles and neutral species due to a denser neutral atmosphere. Since neutral collisions are more effective in dislodging ions than electrons from their equilibrium positions on Earth's magnetic field lines, neutral winds induced by tides or planetary waves can cause smaller electrons to separate from larger ions. These perturbation winds induce changes in the polarization electric field, which are subsequently mapped along Earth's magnetic field lines to induce changes in the electron and ion densities at higher altitudes in the ionosphere. This entire process is known as the E-region dynamo (Appleton, 1946 [2]; Tarpley, 1970 [106]; Immel et al., 2006 [42]).

Most long period waves however have been observed to dissipate below the E-region, but yet long period wave periodicities still exist at high altitudes in the upper atmosphere. Thus, other mechanisms must also exist for these effects to be transmitted beyond the wave dissipation region. Scientists have suggested that the effects of nonlinear interactions on atmospheric tides may play a role in transmitting the effects of longer-period planetary waves to the upper atmosphere (Pancheva and Mukhtarov, 2003 [78]; Mitchell et al., 1996 [65]). In this mechanism, the superposition of nonlinearly generated secondary waves and the interacting atmospheric tide causes tidal amplitude modulation at the interacting planetary wave period. Because atmospheric tides are characterized by shorter periods, they are less susceptible to dissipation and may propagate to higher altitudes in the upper atmosphere.

Another suggested mechanism through which planetary waves and tides can influence the region above their dissipation region involves the modulation of breaking gravity waves. This mechanism is initiated in the stratosphere and mesosphere where the direction and magnitude of the background zonal wind largely determines the vertical propagation of small-scale gravity waves (Garcia and Solomon, 1985 [21]). Since global-scale waves essentially induce large-scale oscillations in the background zonal wind, the amount of vertically propagating gravity waves may be modulated at planetary wave or tidal periods. This process may have a significant impact on the thermosphere and ionosphere because the amount of breaking gravity waves in the MLT region

determines the amount of turbulent mixing. To demonstrate the variability induced in the upper atmosphere by turbulent mixing modulation at planetary wave periods, Nguyen and Palo, 2014 [70] employed the National Center for Atmospheric Research Thermosphere Ionosphere Electrodynamics General Circulation Model (NCAR TIE-GCM). As shown in Figure 2.7, this study found that the modulation of turbulent mixing at planetary wave periods may induce similar periodicities in thermospheric density and composition by affecting the molecular diffusion of different species. The study also concluded that changes in neutral composition may also induce changes in ionospheric density by affecting electron recombination rates. Overall, this mechanism was found to be more effective for long period planetary waves than shorter period waves.

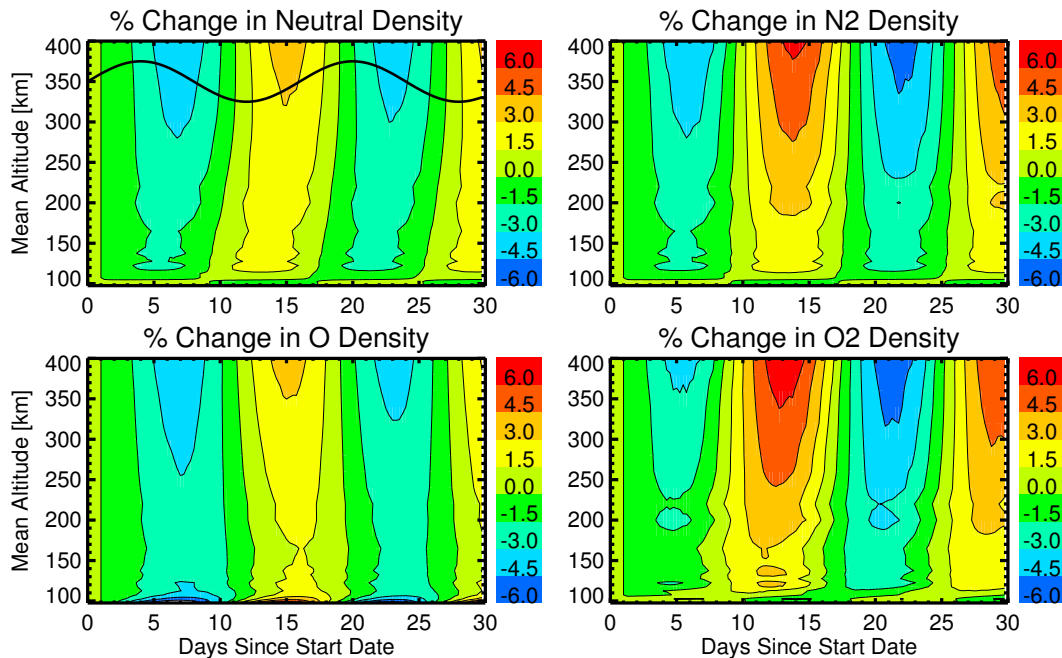


Figure 2.7: TIE-GCM globally averaged percent change in overall neutral density (upper-left),  $[N_2]$  density (upper-right),  $[O]$  density (lower-left), and  $[O_2]$  density (lower-right) induced by varying the eddy diffusion coefficient at the lower boundary of the model (97km). The variation of the eddy diffusion coefficient over time is represented by the thick black line shown in the upper-left plot at approximately 350 km. Results for all plots are displayed on a constant altitude grid.

While many mechanisms have been suggested to explain the presence of atmospheric tides and planetary waves in the upper atmosphere, this process cannot be completely disentangled

without understanding the behavior of waves in the regions closer to their source. Currently, the nature of nonlinearly generated secondary waves in particular has not been thoroughly investigated and thus, many questions remain about how these waves can couple different atmospheric regions together. For instance, it is not known whether secondary waves arising from nonlinear interactions can effectively penetrate into the E-region ionosphere and beyond. Additionally, it is not clear why certain interactions give rise to more significant secondary waves than others. The research presented in this dissertation addresses these questions by elucidating the relationship between the forcing and response of secondary waves in the MLT region.

## Chapter 3

### METHODOLOGY & DATA SOURCES

The chapter herein provides a summary of the methodology used to address the dissertation questions and a detailed description of the data sources used.

#### 3.1 Methodology

As presented in Chapter 1, the main goals of this dissertation are to determine the relationship between the nonlinear forcing region and secondary wave response, and to elucidate the factors that govern the secondary wave manifestation in the SAIR. The science questions to be addressed are restated here for clarity:

- (1) **Where in the atmosphere is the migrating diurnal tide and quasi two-day wave interacting to nonlinearly force the secondary waves, and where do significant secondary wave responses occur?**
- (2) **How does the nonlinear forcing distribution arising from a migrating diurnal tide-quasi two-day wave interaction affect the structure and propagation of the resulting secondary waves?**

The goals of the dissertation are achieved by employing a combination of satellite-based observations and numerical models. An outline of the procedure employed to accomplish the dissertation objectives is presented below.

- (1) **The Fast Fourier Synoptic Mapping (FFSM) method is applied to satellite observations to extract new evidence of secondary waves in the middle and upper atmosphere.**

As explained in detail in Chapter 4, the FFSM method has the capability of presenting global-scale evidence of secondary waves arising from nonlinear interaction between the 2dayW3 and migrating tides (DW1, SW2). Thus, this method is used to locate where significant 2dayW3-tidal secondary wave responses are occurring in the atmosphere. In the dissertation, the FFSM is applied to satellite observations from TIMED-SABER and AURA-MLS, which provide global, asynoptic measurements of stratospheric and mesospheric temperatures. Results for the 2dayW3 and secondary wave activity over multiple years of satellite observations as well as a comparison to NOGAPS-ALPHA reanalysis model output are presented in Chapter 4.

- (2) **Determine the nonlinear forcing region of each secondary wave by computing estimates of primary wave amplitude and phase.**

Accurate nonlinear forcing values for each secondary waves require accurate estimates of primary waves in the temperature and horizontal wind fields. Because nonlinear interaction events involving the 2dayW3 are expected to occur over only several weeks, the primary estimates must be described by sufficiently small temporal resolution. Options to extract primary wave estimates from satellite observations and reanalysis model model output are presented and detailed in Chapter 5.

The primary wave estimates are used in conjunction with the governing, linearized perturbation equations to compute the nonlinear forcing for each secondary wave. Analysis of the spatial distribution and location of the secondary wave forcing and a comparison to the secondary wave response is presented in Chapter 6.

- (3) **Implement the computed nonlinear forcing profiles in a linear tidal model to determine the relationship between the secondary wave forcing and response.**

The computed nonlinear forcing distribution for the secondary waves are implemented as momentum and thermal source terms within a linear mechanistic model derived from the Global Scale Wave Model (GSWM) in order to excite the 2dayE2 and 16hrW4 secondary waves. In order to isolate the effects of the nonlinear forcing on the secondary wave response, initial experiments are performed for the case when zero background winds are present. Numerical experiments are performed to understand the most important region of secondary wave forcing. These experiments include background winds derived from observations to assess the effects of background winds on the secondary wave response.

## **3.2 Data Sources**

The aforementioned methodology employs data from a wide variety of observational instruments and numerical models. The remainder of this chapter provides a detailed description of the primary sources of data used in the dissertation.

### **3.2.1 Satellite Instruments**

#### **3.2.1.1 AURA-MLS**

Launched onboard the Earth Observing System (EOS) Aura satellite in 2004, the Microwave Limb Sounder (MLS) instrument currently observes the limb of the atmosphere to provide global measurements of composition, pressure, cloud water vapor, temperature and geopotential height throughout the upper troposphere, stratosphere and mesosphere (Schwartz et al., 2008 [102]; Livesey et al., 2011 [55]). EOS Aura-MLS orbits the globe fifteen times over a solar day with each orbit being characterized by an altitude of 705 km and an inclination of  $98.2^\circ$ . These parameters correspond to a sun-synchronous orbit, which is defined by the orbital plane being fixed with respect to a vector pointing from the Earth to the Sun. Accordingly, EOS Aura-MLS crosses a latitude circle at the same solar local time on the ascending or descending legs of the orbit.

To produce estimates of each atmospheric parameter, the MLS instrument remotely measures

atmospheric limb emissions from spectral regions within the microwave regime, specifically at 188 GHz and 234 GHz. Retrieval algorithms then convert the observed emissions assuming an a priori atmospheric state to derive vertical profiles of atmospheric parameters at each location along the satellite orbit. The vertical resolution of each profile ranges from  $\sim 4$  km in the stratosphere to  $\sim 10$  km in the upper mesosphere as a consequence of the averaging kernel that is utilized in the retrieval algorithm (Livesey et al., 2011 [55]).

For this dissertation, the MLS Version 3.3 Level 2 data set (Version 3.3) is used, which contains vertical profiles of temperature and geopotential height at each location defined by the EOS Aura orbital track. Each vertical profile contains scientifically useful measurements between 261 and 0.001 hPa. MLS Level 2 measurements are almost continuously available between its launch date in 2004 and 2016. Small time gaps in the dataset correspond to timeframes when there are operational issues or when geophysical phenomena such as extensive cloud cover prevent the accurate estimation of atmospheric fields from the measured radiances.

### **3.2.1.2 TIMED-SABER**

The Sounding of the Atmosphere using Broadband Emission Radiometry (SABER) instrument, launched aboard the Thermosphere Ionosphere Mesosphere Energetics and Dynamics (TIMED) satellite in 2001, measures infrared emissions near  $15\mu m$  from the limb of the atmosphere to derive vertical profiles of temperature, pressure, geopotential height, volume mixing ratios, volume emission rates, cooling and heating rates and chemical heating rates. The SABER instrument monitors the atmosphere from a nearly circular 625 km orbit with  $74^\circ$  inclination. Unlike true sun-synchronous satellites such as EOS Aura, the TIMED orbital plane slowly precesses at a rate such that 22 hours of solar local time (SABER data are not provided near noon time due to sun-viewing restrictions) are acquired in about 60 days.

The differences between the MLS and SABER solar local time coverage are illustrated in Figure 3.1, which shows each satellite's local time coverage at different latitudes throughout the course of the year. Because it is in a true sun-synchronous satellite, MLS observes a latitude

circle at approximately two solar local times throughout the year, corresponding to the ascending and descending portions of the orbit. Whereas the difference between the MLS ascending and descending local times are about 12 hours apart at low latitudes, the local time difference at higher latitudes is much smaller due to the orbit track. In contrast to MLS, SABER measurements slowly precess in local time throughout the year. Abrupt changes in the SABER local time coverage also occur every 60 days. Changes of about 3 hours correspond to instrument yaw maneuvers, which changes the SABER viewing angle from one hemisphere to another. These are executed to keep the SABER instrument on the cold side of the spacecraft and ensure it remains within operational temperature limits.

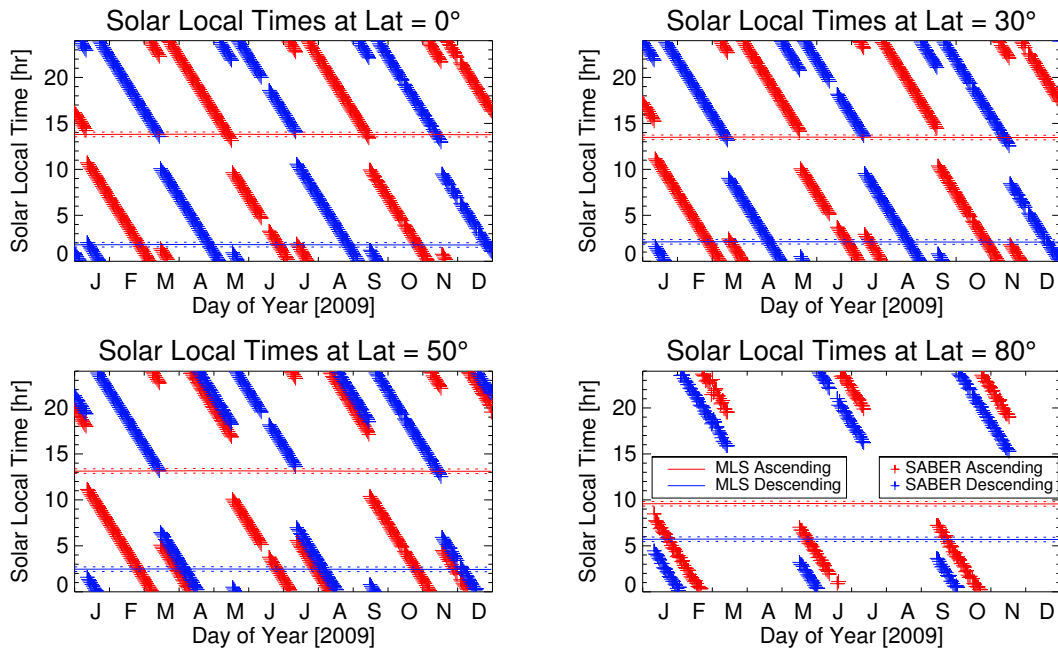


Figure 3.1: SABER and MLS local time coverage for 2009 at  $0^\circ$  (upper-left),  $30^\circ$  (upper-right),  $50^\circ$  (lower-left),  $80^\circ$  (lower-right). SABER local times are denoted as '+' symbols while MLS measurements are represented by solid lines. Ascending measurements are colored in red and descending measurements are colored in blue.

Similar to MLS, SABER employs retrieval algorithms assuming a priori state variables to convert measured atmospheric limb emissions to vertical profiles of atmospheric parameters (Remsberg et al., 2008 [90]). In this dissertation, vertical profiles of temperature and geopotential height in-

cluded in the Version 2.0 SABER dataset will be analyzed. Each profile in this dataset contains scientifically valid measurements between 10 km and 110 km with 2 km vertical resolution.

### 3.2.2 NOGAPS Reanalysis

NOGAPS-ALPHA couples the Naval Research Laboratory (NRL) Atmospheric Variational Data Assimilation System (NAVDAS) with the operational NOGAPS global forecast model to produce model output throughout the stratosphere and mesosphere (Hoppel et al. [40]). The version of the model used here contains 68 model layers from the surface to the model top at 0.0005 hPa ( $\sim 96$  km). The top two layers of the model (0.0005 hPa and 0.00089 hPa) form the "sponge" layer", where additional damping is applied to the potential temperature that nudges the temperature towards isothermal values. The operational NOGAPS forecast model includes parameterizations of middle atmospheric radiative heating and cooling and middle atmospheric drag obtained from the Whole Atmosphere Community Climate Model (WACCM) (Garcia et al., 2007 [20]). The NOGAPS forecast model is coupled with NAVDAS to assimilate temperature data from the Microwave Limb Sounder (MLS) and SABER instruments, and provide output on an hourly basis. The model output at hourly temporal resolution allows for accurate short-term, observationally-based, estimates of tides and planetary waves.

Validation of the NOGAPS-ALPHA model has come in the form of numerous middle atmospheric studies including several focusing on the 2dayW3 wave (McCormack et al., 2009, 2010 [62, 63]). As shown in Figure 3.2, the 2dayW3 computed in the NOGAPS-ALPHA agrees favorably with ground-based medium frequency radar observations during the same period and location. This study performed by McCormack et al., 2009 [62] provides confidence that NOGAPS-ALPHA effectively captures the physical processes observed.

### 3.2.3 Global Scale Wave Model

Past numerical investigations of atmospheric tides and planetary waves have primarily involved the use of general circulation models or linear tidal models. General circulation models such

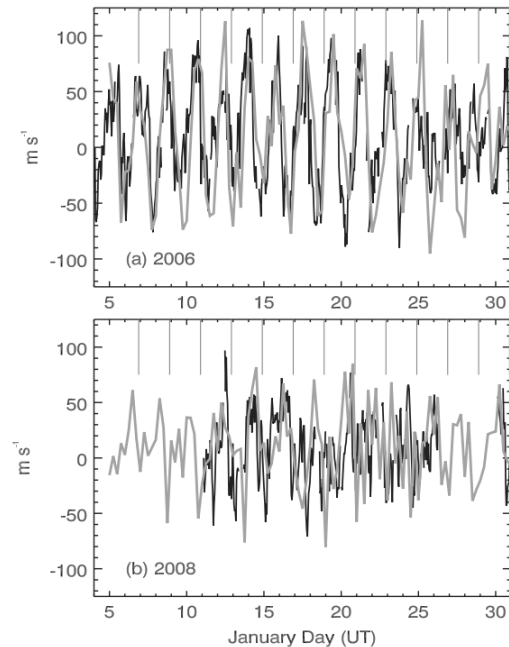


Figure 3.2: Time series of meridional winds over Adelaide, Australia during a) January 2006 and b) January 2008. Black curve represents ground-based MF radar observations at 88 km. Gray curve represents NOGAPS-ALPHA meteorological analyses at the 0.0036 hPa level (88 km in log-pressure altitude).

as the NCAR TIME-GCM solve the first principle continuity, momentum, and energy equations for a spherical Earth. Atmospheric tides and planetary wave investigations using general circulation models have typically involved forcing the model with specific tidal components and analyzing the response of the atmosphere above. Investigations using general circulation models provide valuable insight into wave-wave interactions and wave-mean flow interactions (Hagan et al., 1995 [28]) because these models are driven by governing equations that include both nonlinear and linear terms. However, the complex and nonlinear nature of these models makes it difficult to disentangle the effects of different mechanisms from each other.

Since the main goal of this dissertation is to analyze the response of secondary waves solely due to nonlinear tidal-planetary wave interaction forcing, the majority of the numerical investigations herein employs a linear tidal model, the Global Scale Wave Model (GSWM). Although linear tidal

models cannot directly simulate nonlinear interactions between atmospheric tides and planetary waves, the effects of nonlinear forcing can be analyzed by providing it as known momentum and thermal source terms in the model. Unlike general circulation models, linear tidal models allow for the direct effects of specified forcing inputs to be easily isolated since nonlinear processes are not included in these models. Furthermore, linear tidal models are often more flexible, allowing for forcing input to be applied to regions away from the model lower boundary.

Developed by Hagan et al., 1995 [28], the GSWM is a two-dimensional, linearized, steady-state model that extends globally in latitude and from 0 km to 400 km in altitude. The GSWM solves the linearized perturbation equations under realistic atmospheric conditions (Forbes, 1982 [11]) to compute the atmospheric response for a particular oscillation. An atmospheric tide or planetary wave is excited in the model by specifying an altitude-latitude dependent distribution of atmospheric heating for the given frequency and zonal wave number of the particular oscillation. In past GSWM investigations, heating distributions have been obtained from direct observations and observationally-based models (Groves, 1982 [24], Kalnay et al., 1996 [43], Williams and Avery, 1996 [113], Zhang et al., 2010 [119]), which include the effects of infrared absorption by water vapor in the troposphere, ultraviolet absorption by ozone in the stratosphere and latent heat release. The response of the excited oscillations throughout the atmosphere are simulated under the effects of a non-uniform background atmosphere, zonal mean winds and dissipative processes such as ion drag, molecular and eddy viscosity and conductivity, radiative damping and gravity wave drag (Hagan and Forbes, 2002 [26]).

Due to the inclusion of realistic processes, the linearized perturbation equations cannot be separated in latitude and altitude as performed in classical tidal theory. Therefore, numerical integration techniques must be applied to compute the solutions under different forcing profiles. As explained by Forbes, 1982 [11], the GSWM expresses the linearized perturbation equations as a system of four coupled, partial differential equations in altitude and latitude describing the perturbation zonal velocity, meridional velocity, vertical velocity and temperature. For each wave component defined by frequency and wavenumber, the four equations are discretized with respect

to  $K$  number of latitude grid points using finite-difference approximations to obtain a system of ordinary differential equations:

$$\hat{A} \frac{d^2}{dZ^2} \vec{\Phi} + \hat{B} \frac{d}{dZ} \vec{\Phi} + \hat{C} \vec{\Phi} = \vec{D} \quad (3.1)$$

where  $\hat{A}$ ,  $\hat{B}$ ,  $\hat{C}$  are  $4K \times 4K$  matrices,  $\hat{D}$  is a  $4K$  vector and  $\Phi$  is the solution vector of complex amplitudes given by  $[u_1, v_1, w_1, T_1, \dots, u_k, v_k, w_k, T_k]$ .

The algorithm by Linzden and Kuo, 1969 [52] may be applied to Equation 3.11 in order to obtain the solutions for each wave component at all latitude and altitude grid points within the model.

In this dissertation, the GSWM-09 version of the model is employed to investigate the generation of secondary waves from nonlinear forcing. Currently, the GSWM-09 is set up so that only thermal forcing from tropospheric and stratospheric heating can excite atmospheric tides and planetary waves within the model. To investigate the response of nonlinearly generated secondary waves, a distribution of momentum and thermal forcing arising from a nonlinear generation of the primary waves must be specified within the model. Thus, modifications were implemented within the model source code in order to investigate the nonlinear forcing of secondary waves arising from the 2dayW3-DW1 nonlinear interactions.

## Chapter 4

### SECONDARY WAVES FROM OBSERVATIONS

The following chapter presents new observational results of secondary waves arising from 2dayW3-DW1 nonlinear interaction. Although there have been past studies that have presented evidence of secondary waves from this interaction (Palo et al., 2007 [76]; Moudden et al., 2014 [66]), their conclusions are limited by analysis of potential aliasing on the observations. In this dissertation research, the Fast Fourier Synoptic Mapping method is utilized to provide new evidence of secondary waves from global satellite observations. Details of this method as well as an overview of estimating global scale waves from satellite observations are presented at the beginning of this chapter. Satellite observations of secondary waves are then interpreted and compared to reanalysis output from NOGAPS-ALPHA.

#### 4.1 Technique for Extracting Secondary Wave Evidence

##### 4.1.1 Estimating Waves from Satellite Instruments

Because atmospheric tides and planetary waves are global scale oscillations that are periodic in time and longitude, each wave component may be specified by a unique temporal frequency and zonal wavenumber describing the oscillation in time and longitude, respectively. The summation of atmospheric tides and planetary waves over all frequencies and integer zonal wavenumbers represents the perturbation imposed upon the background zonal mean quantity. This may be

mathematically represented by the following expression for a generic atmospheric field,  $f$ .

$$f'(\lambda, \phi, z, t) = \sum_k \sum_i A_{s_k, \sigma_i}(\phi, z) \cos(s_k \lambda - \Omega \sigma_i t + \Theta_{s_k, \sigma_i}(\phi, z)) \quad (4.1)$$

In order to extract wave components from observations, an atmospheric field must be sufficiently sampled in longitude and time. While ground-based instruments can only observe the atmosphere at one longitude, space-based instruments sample the atmosphere over multiple locations across the globe, which yields the potential to estimate amplitude and phase of each wave component. Most techniques to extract global-scale waves from satellite-based observations begin by grouping observations into particular latitude and altitude bins. In an ideal scenario, the observations in each latitude-altitude bin are evenly-spaced along independent longitude and time axes with high resolution. Regular sampling along longitude and time would allow for two-dimensional Discrete Fourier Transforms (DFT) to transform the data into the frequency-wavenumber domain and derive estimates of the amplitude and phase of each tidal component over the latitude and altitude range being observed.

Unfortunately, ideal sampling of the atmosphere in time and longitude is not obtained from satellites instruments that monitor the middle and upper atmosphere. As illustrated in Figure 4.1, MLS and SABER observations only provide an asynoptic sampling of the atmosphere, which is defined by observing the Earth at one longitude at one point in time. For sun-synchronous or near-sun-synchronous satellites such as MLS and SABER, the observed longitude for the ascending or descending legs of the orbit is linearly dependent on the time of the observations and may be expressed by:

$$\lambda_i = \lambda_a - ct_i \quad (4.2)$$

In Equation 4.2,  $\lambda_a$  represents an initial longitude and the rate constant ( $c$ ) is dependent on the satellite orbit. The rate constant for sun-synchronous satellites such as MLS is 360/24 degrees per hour, which means that a global range of longitude is sampled in exactly 24 hours. The SABER instrument, located in a near-sun-synchronous orbit, is described by a rate constant that is slightly larger than 360/24 degrees per hour.

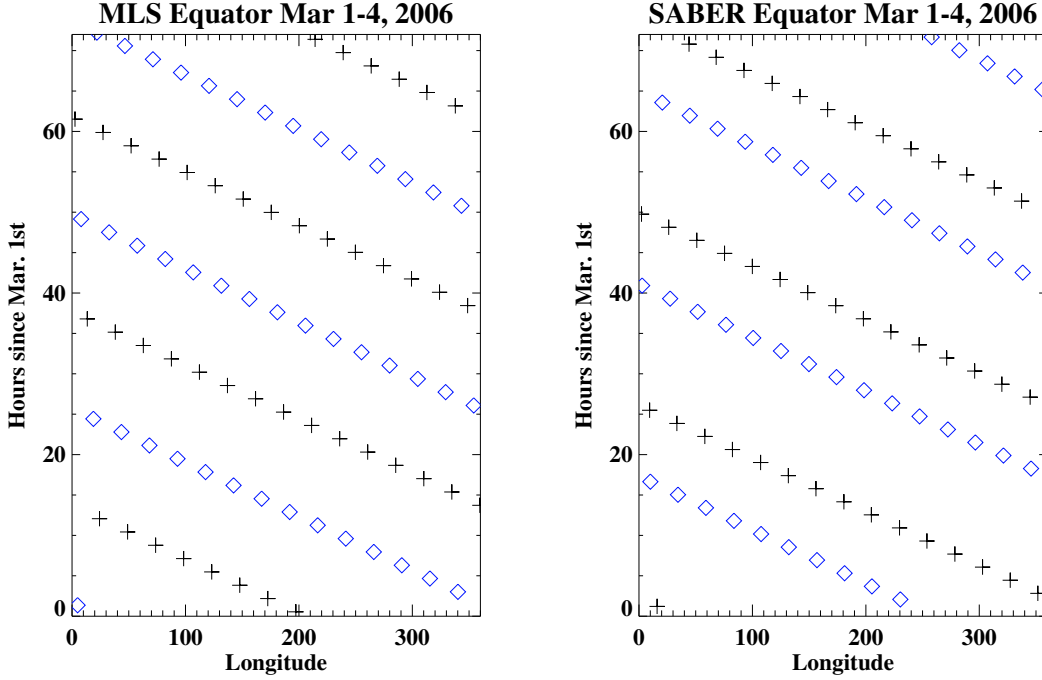


Figure 4.1: MLS (left) and SABER (right) time/longitude sampling at the equator over multiple days. ‘+’ symbols represent ascending measurements while ‘◇’ symbols represent descending measurements. Longitude units are in degrees.

Since the longitude sampling obtained from satellite instruments is not independent of the temporal sampling, DFT methods cannot be directly applied to extract the atmospheric wave spectrum at each location. Most observational analyses have circumvented this problem by least squares fitting functions representing individual wave components to the observations at each latitude and altitude grid point (Wu et al., 1995 [114]). The least squares problem is constructed by modeling each observation  $y_i$  at each time ( $t_i$ ) and longitude ( $\lambda_i$ ) as a summation of the zonal mean ( $A_0$ ) and cosine and sine basis functions representing a wave with a particular wavenumber and frequency:

$$y_i = A_0 + A \cos(\theta) \cos(s\lambda_i - \sigma t_i) - A \sin(\theta) \sin(s\lambda_i - \sigma t_i) \quad (4.3)$$

By compiling observations at each latitude and altitude grid point over a finite time interval, a linear system  $\hat{y} = H\hat{x}$  can be created where  $y$  is a  $n \times 1$  vector of observations,  $H$  is a  $n \times 3$  matrix where each row contains the cosine and sine basis functions and  $x$  is the solution vector.

Expressions for  $H$  and  $\hat{x}$  may be expressed as:

$$H_i = \begin{bmatrix} 1 & \cos(s\lambda_i - \sigma t_i) & -\sin(s\lambda_i - \sigma t_i) \end{bmatrix} \quad (4.4)$$

$$\hat{x} = \begin{bmatrix} A_0 \\ A \cos \theta \\ A \sin \theta \end{bmatrix} \quad (4.5)$$

The least squares solution for  $\hat{x}$  is one that minimizes the error between the observations and the wave fitting functions contained in matrix  $H$  and is computed from  $\hat{x} = (H^T H)^{-1} H^T \hat{y}$ . Subsequently, the amplitude ( $A$ ) and phase ( $\theta$ ) for an individual wave component are estimated by

$$\begin{aligned} \text{Amplitude} &= \sqrt{A \cos^2 \theta + A \sin^2 \theta} \\ \text{Phase} &= \tan^{-1} \left( \frac{A \sin \theta}{A \cos \theta} \right) \end{aligned} \quad (4.6)$$

Although the least squares method has been utilized extensively to estimate global-scale waves from space, this method does not prevent leakage between waves located within the Nyquist limits, which results from the non-uniform sampling in time and longitude. To evaluate the effect of aliasing, the longitude-time sampling for each orbital leg (Equation 4.2) is substituted into Equation 4.3:

$$y_i = A_1 \cos [-(\sigma + cs)t_i + s\lambda_a] + A_2 \sin [-(\sigma + cs)t_i + s\lambda_a] \quad (4.7)$$

Equation 4.7 shows that a wave with zonal wavenumber ( $s$ ) and frequency ( $\sigma$ ) appear as a wave with frequency  $(\sigma - cs)$  cycles per day from samples of a given latitude obtained from a single portion of the orbit. This circumstance can be problematic because waves with different zonal wavenumber and frequency can appear as identical signals from this sampling. For instance, the 2dayW3 ( $\sigma = 0.5$ ,  $s = -3$ ) and the 2dayE2 ( $\sigma = 0.5$ ,  $s = 2$ ) both appear as waves with frequency 2.5 cycles per day from each orbital leg of a sun-synchronous satellite or constant local time perspective. Equivalently, the least squares fitting functions displayed in Equation 4.7 are

exactly equal for both the 2dayE2 and the 2dayW3 when atmospheric measurements are acquired at constant local time. It follows that the estimated amplitude and phase of both waves are identical regardless of the actual amplitude and phase of the waves. This particular example is troublesome for investigating nonlinear interactions between the 2dayW3 and migrating diurnal tide because the effects of the secondary wave (2dayE2) are not separated from the 2dayW3 when least squares methods are applied at constant local time. The effects of aliasing between certain waves are mitigated if the least squares method incorporates observations from both legs of the orbit and hence, at two different local times. However, aliasing effects are still present in least squares methods for cases where the ascending and descending local times are separated by less than 12 hours apart (Wu et al., 1995 [114]).

Due to the limitations of least squares methods, another technique is utilized to estimate planetary waves from satellite data. As explained in the following section, this technique, unlike least squares methods, successfully prevents coupling between planetary waves within the sampling Nyquist limits for MLS and SABER observations.

#### **4.1.2 Fast Fourier Synoptic Mapping Method**

Originally developed by Salby, 1982 [97] and Hayashi, 1982 [32] in the early 1980s, the Fast Fourier Synoptic Mapping (FFSM) method can be utilized to compute the space-time Fourier transform within the satellite sampling Nyquist limits. Additionally, the FFSM method prevents coupling between waves within the Nyquist limits although waves lying outside of the Nyquist limits can still alias into the spectrum. The method initially groups satellite-based observations over multiple days into latitude and altitude grid points and ascending/descending orbital legs. For each latitude and altitude grid point, the ascending and descending sequences, originally placed on a time-longitude grid, are unwrapped in longitude and then placed on a set of axes defined by  $s$  which is parallel to the orbit sampling and  $r$  which is orthogonal to  $s$  (Figure 4.2). The rotation angle between the  $r$ - $s$  coordinate system from the original longitude-time system is dependent on the satellite orbital parameters and can be estimated from the rate constant ( $c$ ) shown in Equation

4.2.

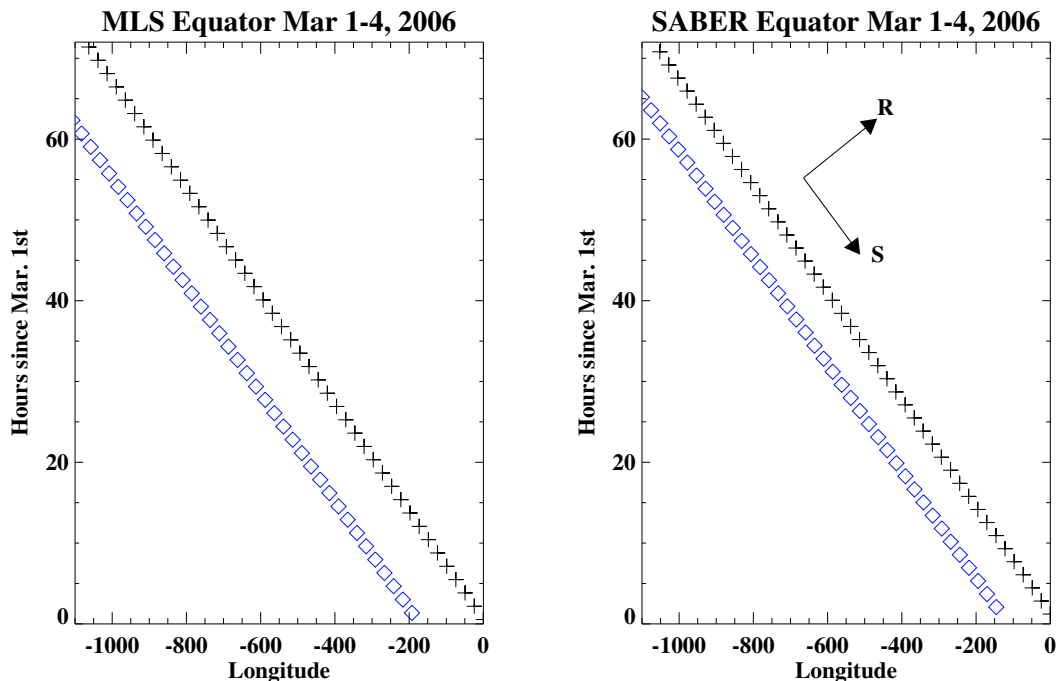


Figure 4.2: Same as Figure 4.1 except longitude is now referenced from the longitude of the first sample.

Since the ascending and descending sequences are equally spaced along the  $s$ -axis, a DFT can be applied to each sequence to compute the complex amplitude at each  $k_s$  frequency. The observed frequency spectrum along  $k_s$  is determined by a satellite's asymptotic sampling of the atmosphere and therefore, does not represent the actual frequency spectrum of the atmosphere. Waves with different zonal wavenumber and frequency can be shifted to the same  $k_s$  frequency as explained in the previous section. Salby, 1982 [97] determined that only two waves with integer zonal wave number can appear at any value of  $k_s$  within the satellite sampling Nyquist limits, which is approximately  $\sim \pm 1$  day and  $\sim \pm 7$  zonal wave number. The waves in each pair have identical  $\sigma + cs$  and are separated by one in zonal wavenumber ( $s$ ). An example of the location of a  $k_s$  pair in the frequency-wavenumber spectrum is shown in Figure 4.3.

The waves in each pair can be completely separated from each other by quantitatively assess-

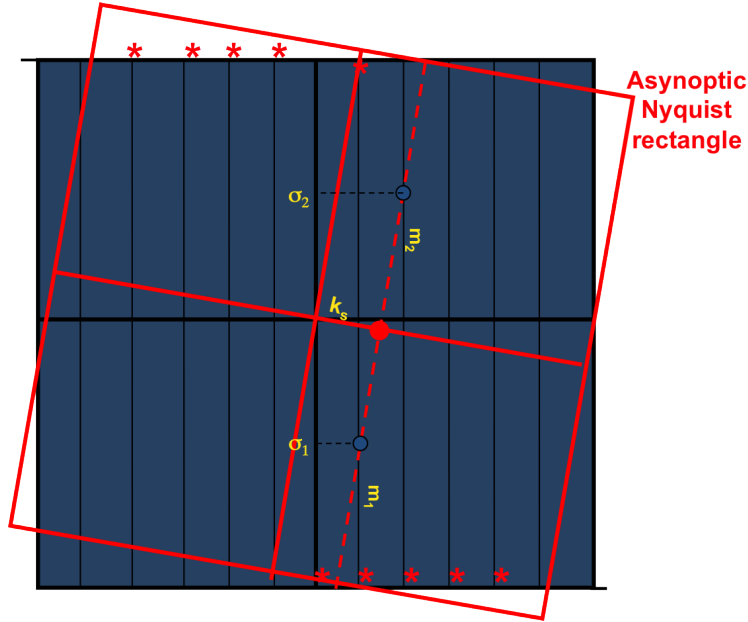


Figure 4.3: Asynoptic Nyquist rectangle in relation to the frequency-wavenumber spectrum. The dark blue rectangle represents the frequency-wavenumber spectrum where frequency is the vertical axis and wavenumber is the horizontal axis. The tilted red rectangle represents the asynoptic Nyquist rectangle where  $k_r$  frequency is the vertical axis and  $k_s$  frequency is the horizontal axis. Two possible frequency-wavenumber pairs,  $(\sigma_1, m_1)$  and  $(\sigma_2, m_2)$ , within the asynoptic Nyquist rectangle can appear at the same  $k_s$  when sampled along the satellite orbit.

ing the phase difference between the  $k_s$  spectrum on the ascending and descending portions of the orbit based on the time and longitude separation between each orbital leg. By resolving the wave pair at each  $k_s$  frequency and rotating the spectra back into the frequency-wavenumber coordinate frame, the complex amplitude for all waves within the satellite Nyquist limits can be computed.

It should be mentioned the FFSM method uses several pieces of information that are not utilized in least squares method, which explains the advantage of the FFSM method. Unlike the least squares method, the FFSM assumes that only two waves with integer zonal wavenumber within the Nyquist limits can contribute to a spectral point in the  $k_s$  domain. Moreover, the FFSM uses the phase difference between the ascending and descending portions of the orbit to completely separate the wave pair. Least squares methods do not utilize this orbital phase information in contrast to the FFSM method. Hence, least squares methods are unable to completely resolve the

wave pairs within the Nyquist limits when the ascending and descending local times do not differ by 12 hours.

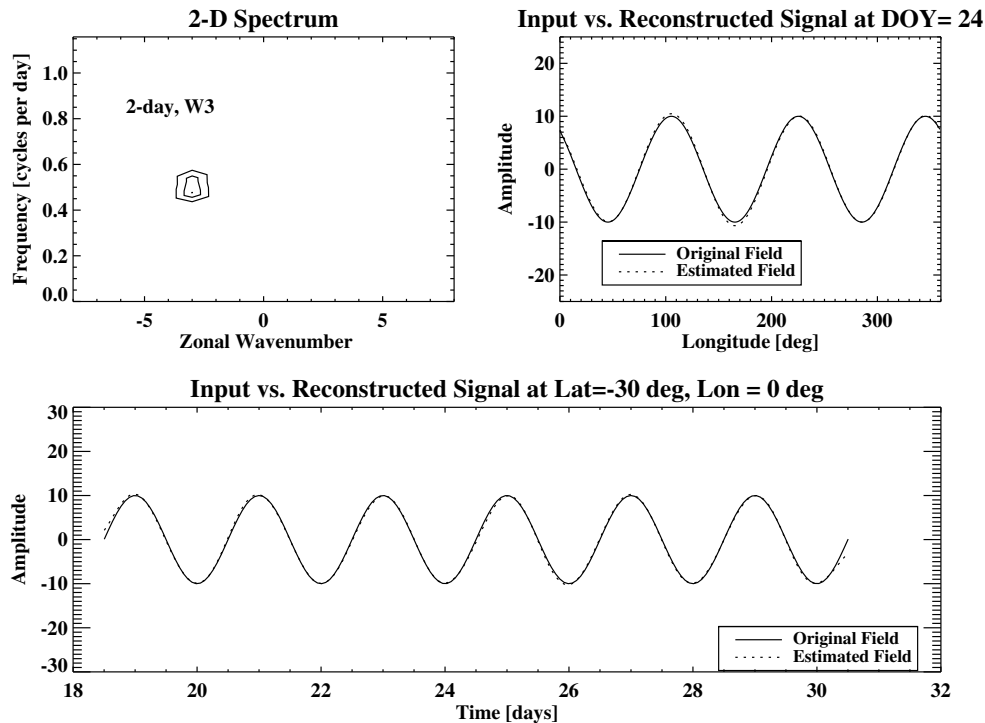


Figure 4.4: Reconstruction of a westward-propagating sinusoid described by a period of 2 days, zonal wavenumber 3 and amplitude of 10 K from FFSM spectral coefficients obtained for SABER time/longitude sampling of the equator over 12 days. The top left plot shows the FFSM frequency-wavenumber spectrum. The top right plot compares the FFSM reconstructed signal (dashed) to the true sinusoid signal (solid) at constant time and the bottom plot compares the signals at constant longitude.

The accuracy of the FFSM method in estimating the frequency-wavenumber spectrum from satellite observations is tested by first constructing a simple, two-dimensional atmosphere in time and longitude containing only a 2dayW3 ( $\sigma=0.5$ ,  $s=-3$ ) with 10 K amplitude. SABER sampling of the 30°N latitude circle in time and longitude over 12 days is then applied to the model atmosphere to construct ascending and descending orbital sequences for the application of the FFSM method. As presented in Figure 4.4, the derived frequency-wavenumber spectrum for the test displays only on spectral peak centered at 0.5 cycles per day in frequency and -3 in zonal wavenumber, which

corresponds to the 2dayW3. Although the 2dayE2 wave is observed at the same frequency as the 2dayW3 from an ascending or descending orbital sampling viewpoint, the 2dayW3 does not alias into the energy observed at the 2dayE2 frequency-wavenumber band. Additionally, the 2dayW3 does not alias into any other frequency-wavenumber band. Consequently, the estimated frequency-wavenumber spectrum can be used to reconstruct the model atmosphere almost exactly.

For the results contained in this chapter, 2dayW3 and 2dayE2 amplitudes and phases are computed with the use of the FFSM method. However, estimates for the amplitude and phase cannot be reliably determined directly from the FFSM frequency-wavenumber spectrum. Since the time interval between the first and last orbits used in the FFSM do not necessarily line up with an integer number of 2dayW3 wave cycles, minor spectral leakage to adjacent frequency bands can occur as illustrated in Figure 4.4. Thus, the complex amplitude at the exact 2dayW3 frequency and wavenumber is not an accurate representation of the amplitude and phase. To produce accurate estimates of the amplitude and phase for a specific planetary wave, observations are reconstructed using only the spectral coefficients corresponding to the desired zonal wavenumber. The filtered observations at the desired zonal wavenumber are free from any possible leakage from components within the Nyquist limits. Because potential coupling between components within the Nyquist limits has been eliminated by filtering the observations at the desired wavenumber, the main disadvantage of least squares methods has been removed. Thus, the least squares method is then applied to the filtered reconstruction to obtain accurate estimates for the amplitude and phase of the desired waves.

The accuracy of this procedure in estimating planetary wave amplitudes is compared to the least squares method in Figure 4.5. A comparison is performed by estimating the 2dayE2 amplitude from SABER sampling of a model atmosphere containing only the 2dayW3 using the FFSM-least squares method and the traditional least squares method. While the FFSM-least squares method correctly estimates zero amplitude for the 2dayE2, the least squares method estimates significant amplitudes at this band due to aliasing from the 2dayW3. As shown in the comparison and noted by Wu et al., 1995 [114], the aliasing from the 2dayW3 to the 2dayE2 signal is present whenever the

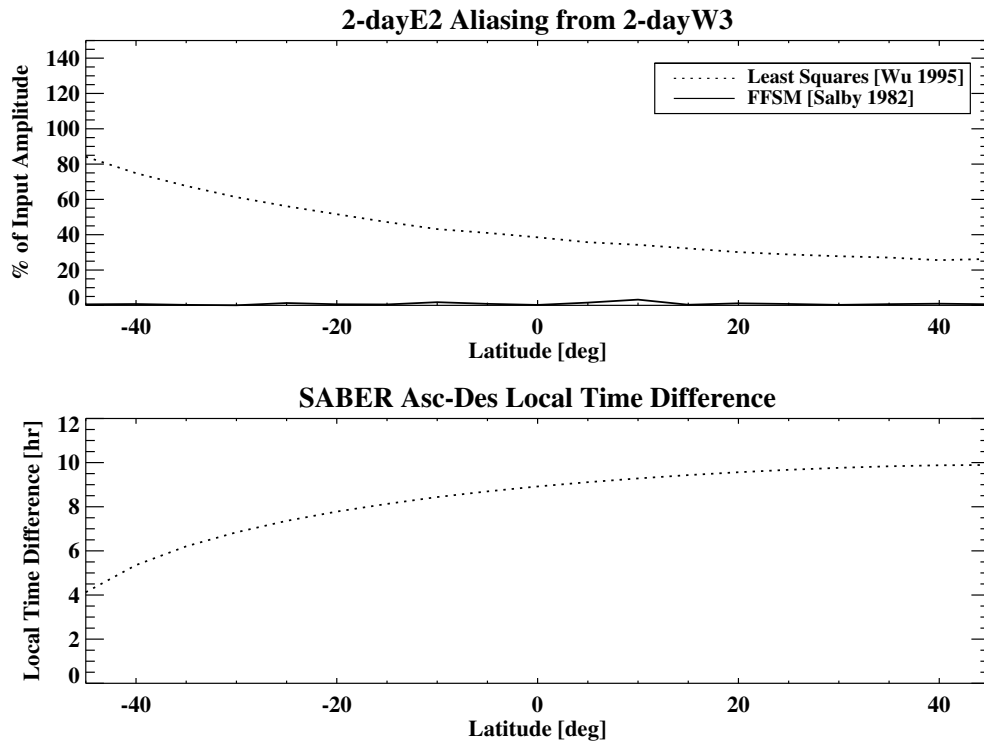


Figure 4.5: A comparison of the 2dayE2 amplitude estimated when only a 2dayW3 is present using SABER ascending/descending sampling for the traditional least squares method and the FFSM-least squares method used in this dissertation. The top plot shows the estimated amplitude of the 2dayE2 in terms of the percent 2dayW3 amplitude as a function of latitude. The bottom plot shows the difference between the ascending and descending local times as a function of latitude.

ascending and descending local times are less than 12 hours apart, which is the case for SABER.

Energy present at frequency-wavenumber bands outside of the satellite Nyquist limits, however, can alias into the FFSM-derived frequency-wavenumber spectrum. For instance, the 16hrW4, 16hrE1, 9.6hrW5 etc. in addition to the 2dayW3 and 2dayE2 all appear as a wave with frequency 2.5 cycles per day from a satellite sampling viewpoint. Because waves with periods less than a day cannot be resolved from observations from a single satellite, these waves will contribute spectral energy to its aliasing components within the Nyquist frequency limits as shown in Figure 4.6. Thus, special attention must be paid to the aliasing effects caused by signals lying outside the Nyquist limits when interpreting the results.

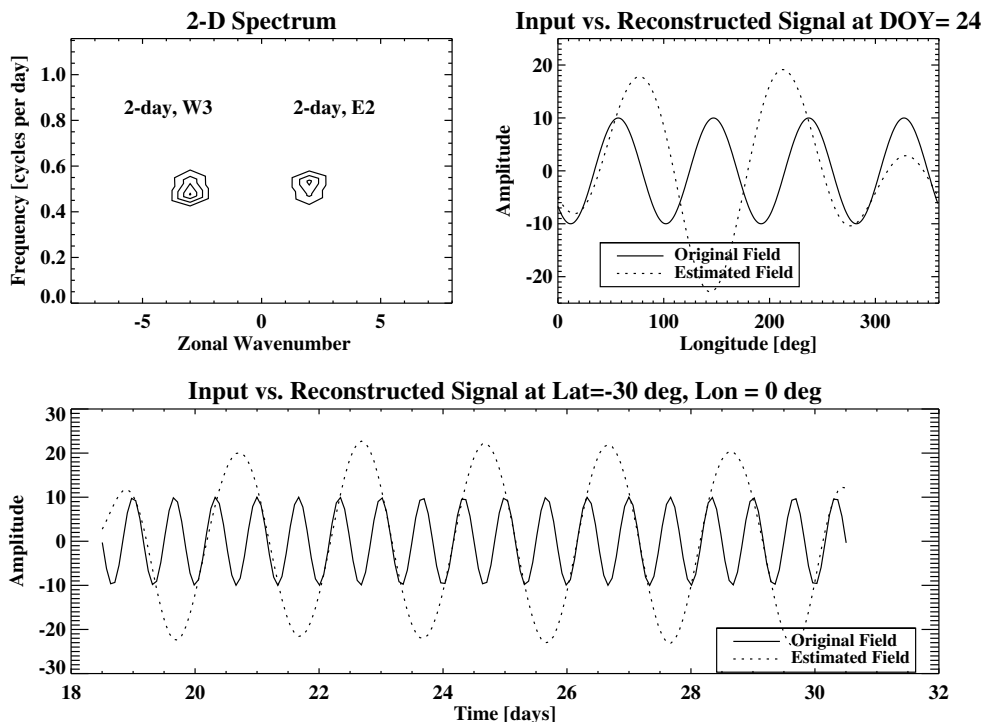


Figure 4.6: Same as Figure 4.4 except for a 16hrW4 signal. Since 16hrW4 lies outside of the Nyquist limits, it projects energy into the 2dayW3 and 2dayE2 spectra.

## 4.2 Quasi Two-Day Wave and Secondary Waves from SABER Observations

Evidence of secondary waves generated from the 2dayW3-DW1 nonlinear interaction are sought by applying the FFSM method to the SABER and MLS observations separately. The FFSM method computes the frequency-wavenumber spectrum of observations at each altitude-latitude grid point over a specified time interval, which can be used to locate the spectral peaks corresponding to the dominant waves at that location. The spectrum shown in Figure 4.7 is computed for SABER temperature data within a 12-day window in late-January at various latitude-altitude grid points in the Southern Hemisphere upper mesosphere. Only spectral peaks with significant power above the noise floor are presented in the results. In order to estimate the noise floor, the mean of the spectral power values contained within the 25th and 75th percentiles is calculated. A chi-square test is then conducted to determine the significant spectral peaks that lie below the  $\alpha = 0.05$  level.

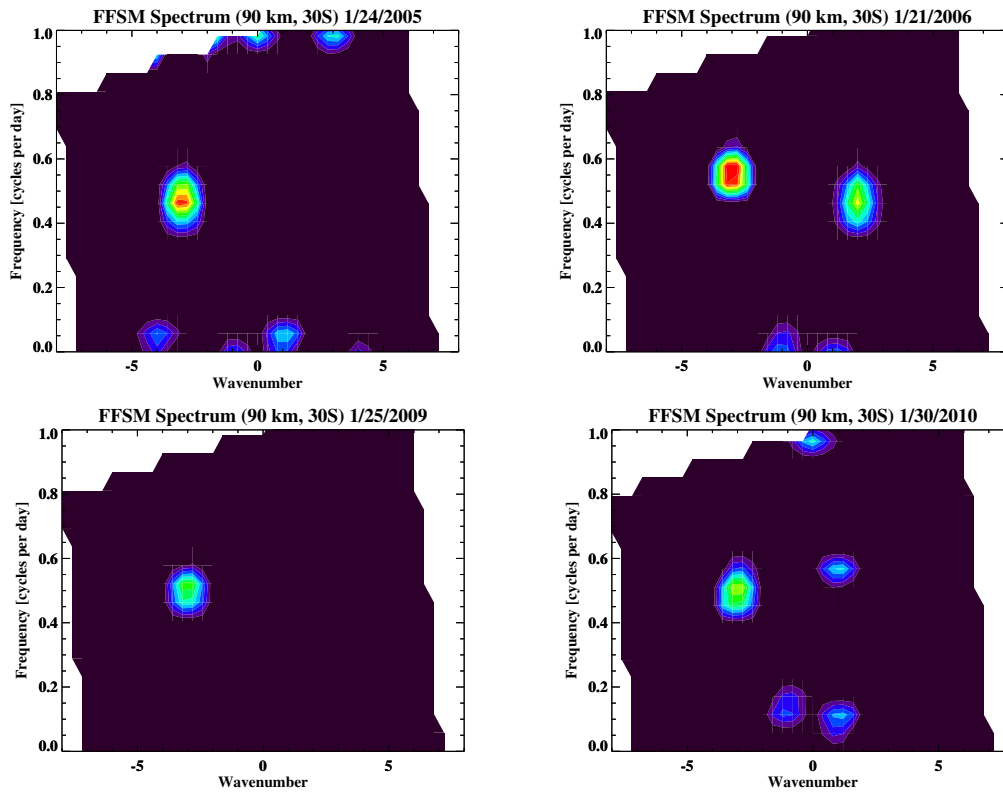


Figure 4.7: Frequency-wavenumber plots for SABER temperature observations of the S. Hemisphere MLT region during the peak of 2dayW3 events for 2006, 2007, 2011 and 2012. Plots are shown for 2006, 2007, 2011, and 2012 at different latitude and altitude locations. Only significant peaks below  $\alpha = 0.05$  are displayed on the plots.

Thus, the probability of each significant peak being a result of random noise in the data is less than 5%.

From Figure 4.7, a dominant spectral peak at about 0.5 cycles per day ( $f=0.5$  cpd) and zonal wavenumber -3 ( $s=-3$ ) is observed during late-January in all four years presented. This corresponds to the westward-propagating 2dayW3. A smaller peak at ( $f=0.5$  cpd,  $s=+2$ ) corresponding to the 2dayE2 wave also appears in the results displayed for two out of the four years. Analysis presented earlier in this chapter showed that the spectral values computed from the FFSM method do not contain aliasing effects from spectra within the Nyquist limits for a single satellite ( $f=\pm 1$  day,  $s=\sim \pm 7$ ). Therefore, the spectral energy observed at ( $f=0.5$  cpd,  $s=+2$ ) does not contain any aliasing effects from the 2dayW3.

However, the spectral peak at ( $f=0.5$  cpd,  $s=+2$ ) may also contain energy from waves that lie outside the Nyquist limits and alias to the same frequency and zonal wavenumber. As previously explained, waves characterized by the same  $|\sigma + s|$  appear as the same wave from a sun-synchronous sampling perspective. Thus, the 16hrW4 ( $f=1.5$  cpd,  $s=-4$ ), 16hrE1 ( $f=1.5$  cpd,  $s=+1$ ), and 9.6hrW5 ( $f=2.5$  cpd,  $s=+5$ ) waves will appear at the same frequency as the 2dayE2 and 2dayW3 waves from the MLS or SABER sampling perspective. Because waves with frequency greater than 1 cpd are not resolved by the FFSM, the spectral energy from these high frequency waves will alias to the spectral points within the Nyquist limits at ( $f=0.5$  cpd and  $s=+2$ ) as well as ( $f=0.5$  cpd and  $s=-3$ ). Coincidentally, the 2dayE2, 16hrW4, 16hrE1 and 9.6hrW5 waves are all secondary waves that are theoretically generated from the nonlinear interaction between the 2dayW3 and the DW1 or the SW2 (migrating semidiurnal tide). Therefore, any spectral energy contained at ( $f=0.5$  cpd,  $s=+2$ ) is most likely dominated by secondary waves generated from the 2dayW3-DW1 interaction or 2dayW3-SW2 interaction. The presence of the 2dayE2 can thus be viewed as a proxy of nonlinear interaction between these atmospheric tides and the 2dayW3.

While the simultaneous presence of the ( $f=0.5$  cpd,  $s=-3$ ) and ( $f=0.5$ ,  $s=+2$ ) peaks are presented in two of the cases (2006, 2010) in Figure 4.7 to present evidence of nonlinear interaction activity during 2dayW3 events, the other cases (2005, 2009) are also presented to show that the

presence of the 2dayW3 does not necessarily imply the presence of secondary waves. An explanation of this result is presented throughout subsequent chapters of this dissertation, which describe the numerical experiments results conducted with a linearized tidal model.

The amplitude and phase of the 2dayW3 and the 2dayE2 signal are estimated by applying the least squares method to reconstructed observations at the desired wave number using the spectral coefficients from the FFSM method. This procedure eliminates aliasing between the 2dayW3 and the 2dayE2 signal while accounting for the spectral leakage to adjacent frequencies resulting from the FFSM method application. The amplitude structure of the 2dayW3 observed from MLS temperatures at 80 km in time and longitude for years between 2005 and 2010 is displayed in Figure 4.8. The results show that the 2dayW3 maximizes in the Southern Hemisphere at around 30°S and 40°S latitude. As concluded by past studies (Salby, 1981 [95]; Plumb, 1983 [86]), the amplification of the 2dayW3 at these latitudes is likely due to the wave extraction of energy from the mean flow in baroclinically unstable regions. Each 2dayW3 event peaks around late-January and lasts for about 20-30 days, which is consistent with past studies.

From Figure 4.8, it can also be observed that the 2dayW3 exhibits large interannual variability. The largest 2dayW3 amplitudes are observed during 2005 and 2006 while weak 2dayW3 amplitudes are observed in 2008 and 2009. Furthermore, the peak day of the 2dayW3 varies from mid-January (2009) to the end of the January (2010). Interannual differences in the 2dayW3 structure have the potential to induce interannual differences in the nonlinear interaction with the DW1 and are explored in subsequent sections of this dissertation.

Figure 4.9 shows the vertical-latitudinal structure of the 2dayW3 amplitude extracted from SABER temperature on the peak day for each of the same years presented in the previous figure. The SABER 2dayW3 results are presented here instead of the MLS results to show the amplitude structure above 90 km, which is approximately equivalent to the upper limit of the MLS measurements. Because of the SABER observational constraints during this period, 2dayW3 results are only presented between 50°S and 80°N. While biases exist between the MLS and SABER data sets, the relative structure of the 2dayW3 extracted from each data set are similar (see Appendix E for

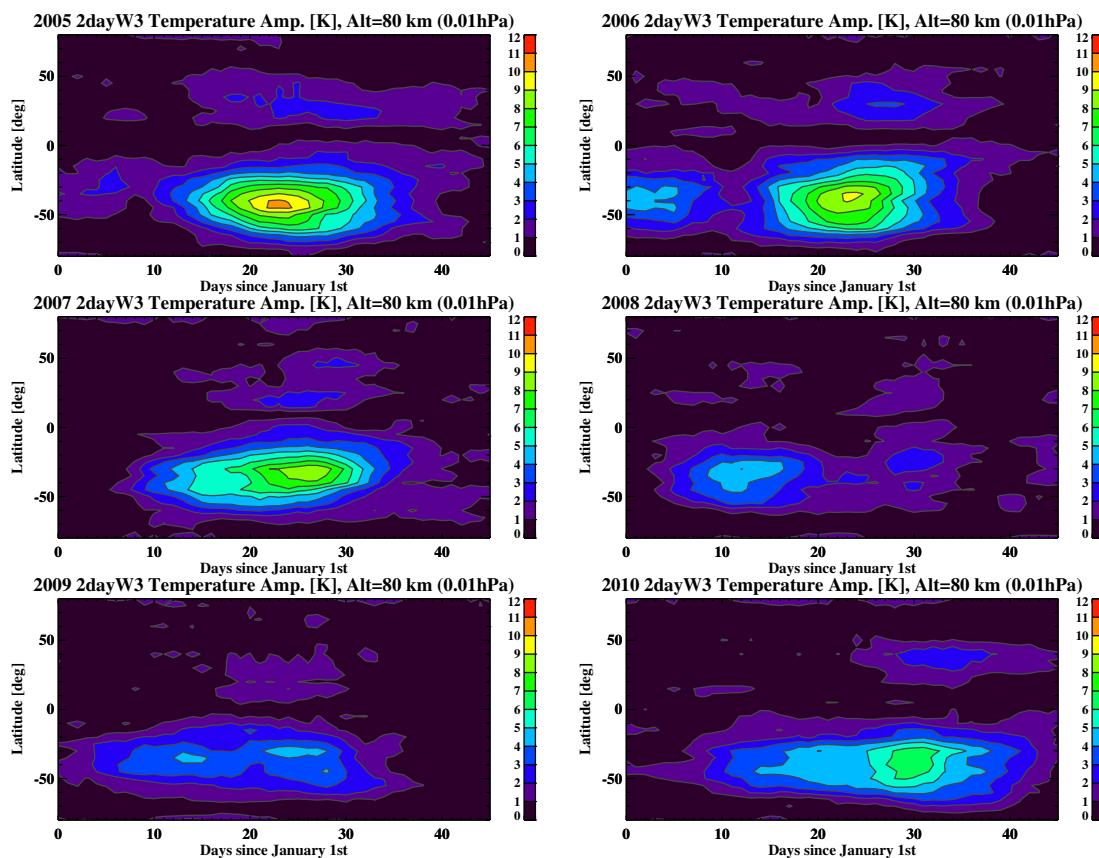


Figure 4.8: Time evolution of 2dayW3 amplitude latitude structure for six selected years between 2005 and 2012 during January and February. Estimates are derived from MLS observations.

MLS results).

The 2dayW3 amplitude structures as a function of altitude and latitude depicted in Figure 4.9 show that that the 2dayW3 begins to achieve significant amplitudes at the stratopause around 50 km where baroclinically unstable regions are likely located. Hence, 50 km is chosen to be the bottom boundary of the plots contained in Figure 4.9. The 2dayW3 amplitudes increase with altitude and reach a peak around 80 km in the Southern Hemisphere. From 80 km altitude, the 2dayW3 slightly decreases with altitude before increasing and reaching a second peak above 100km. The approximate bimodal structure in temperature is related to the 2dayW3 structure in geopotential height, which is shown in Figure 4.10. In contrast to the 2dayW3 temperature structure, the geopotential height structure of the 2dayW3 amplitude is described by only one

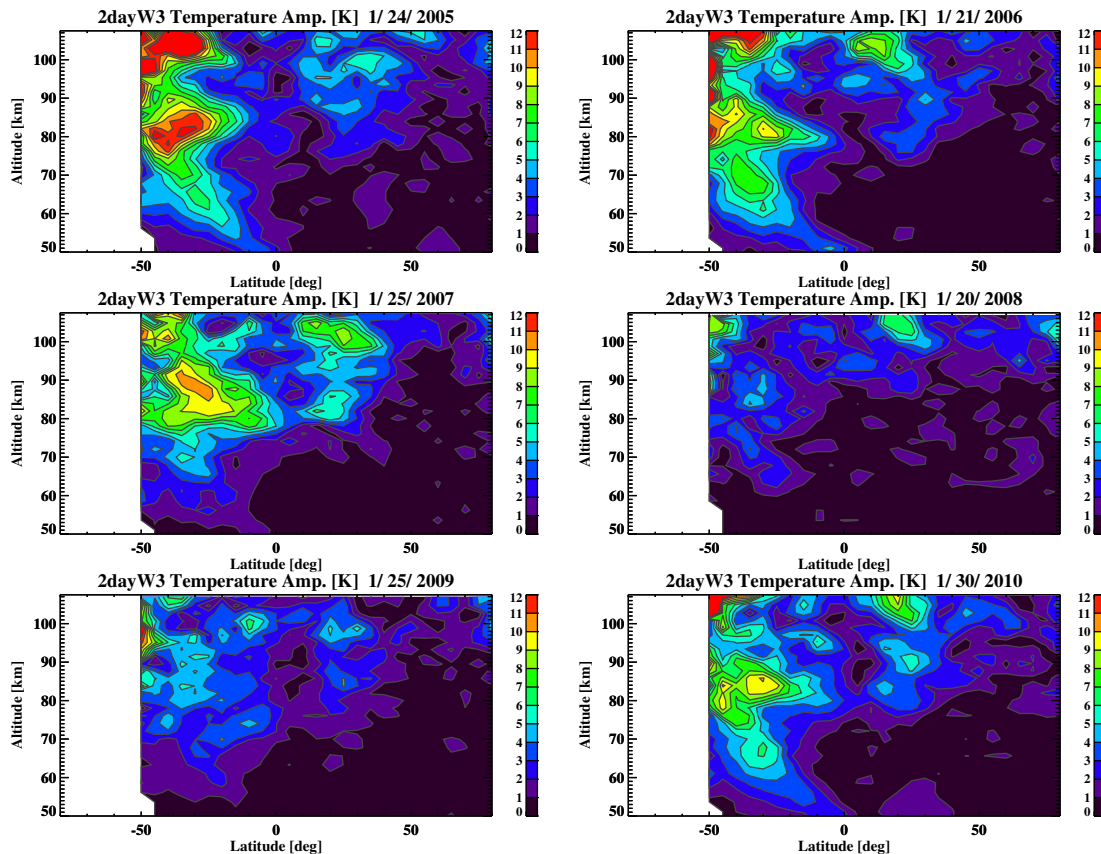


Figure 4.9: 2dayW3 latitude-altitude amplitude structure during late-January for selected years. 2dayW3 estimates are determined from 12 days of SABER temperature data centered near the peak of the 2dayW3 event.

peak at 90 km during most 2dayW3 events. Since perturbation temperature is approximately proportional to the vertical gradient in perturbation geopotential height (Sassi et al., 2002 [101]), small perturbation temperatures should be observed at the altitude where the geopotential height maximizes and large perturbation temperatures should be observed where geopotential height is increasing or decreasing. This relationship is apparent by comparing Figure 4.9 to Figure 4.10. Furthermore, since the vertical gradient of the 2dayW3 geopotential height changes sign from positive to negative at around 90 km (Figure 4.10), the temperature perturbation should be out of phase above and below the geopotential height maximum.

As illustrated in Figure 4.11, the 2dayW3 phase shows a clear progression with altitude near

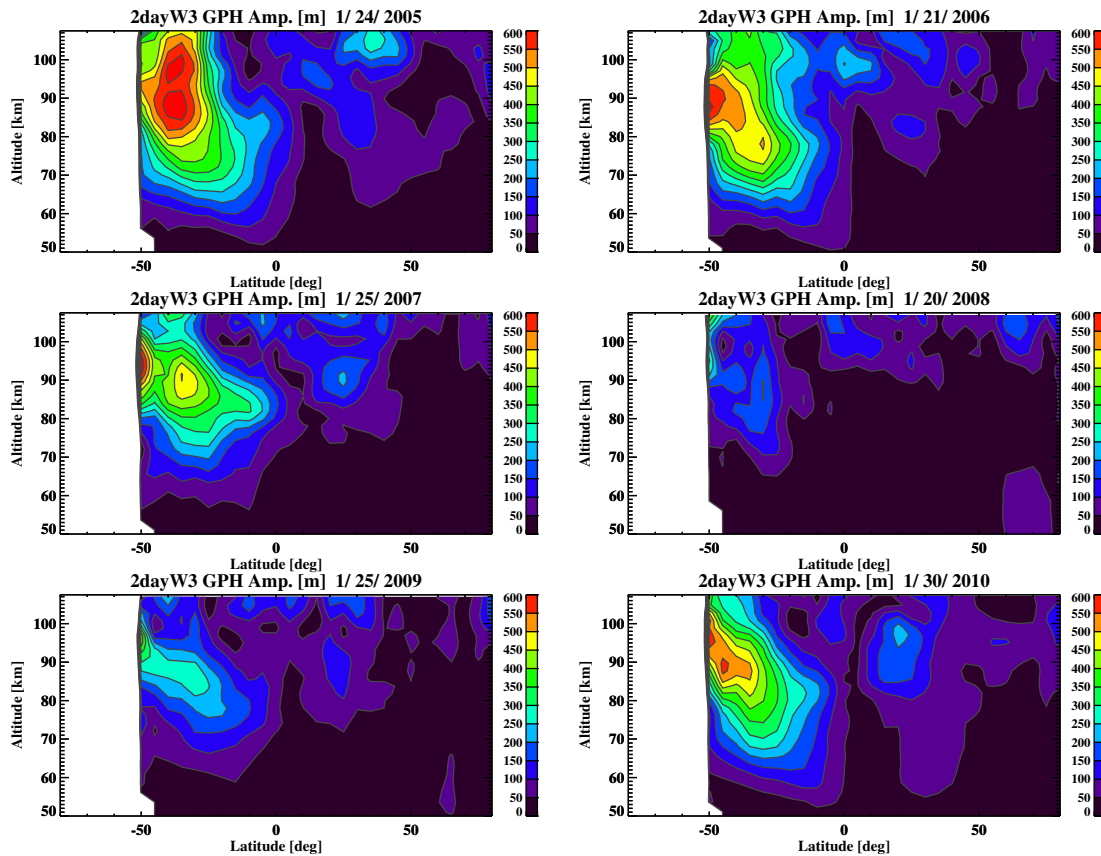


Figure 4.10: Same as Figure 4.9 except for geopotential height.

the latitude of peak amplitude at  $30^{\circ}\text{S}$ . The downward phase progression with altitude indicates upward energy propagation, which is consistent with the theory and observation of the 2dayW3. Vertical wavelengths of 50-60 km are observed in the 2dayW3 phase estimates throughout each year, which are consistent with previous studies. The long vertical wavelength of the 2dayW3 implies that the 2dayW3 is less susceptible to dissipation and may effectively penetrate into the lower thermosphere.

Figures 4.12 and 4.13 show the amplitude structure of the 2dayE2 wave as a function of latitude and altitude in the temperature and geopotential height fields, respectively. The estimated amplitude of the 2dayE2 wave, as explained earlier, likely contains aliased contributions from other 2dayW3-migrating tide nonlinear secondary waves such as the 16hrW4, 16hrE1 and 9.6hrW5.

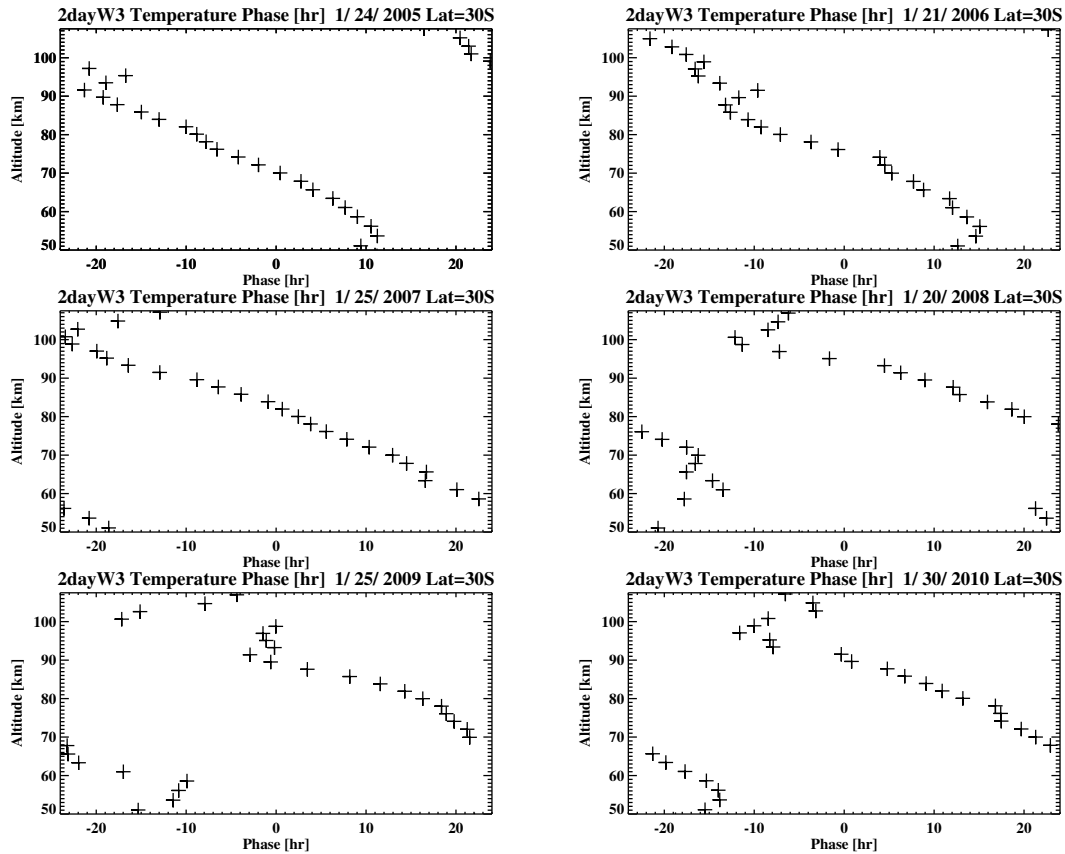


Figure 4.11: 2dayW3 phase as a function of altitude at 30°S latitude. Downward phase progression indicates upward energy propagation.

Hence, the amplitude of the 2dayE2 wave may be interpreted as some combination of all nonlinearly generated components that arise during an interaction between the 2dayW3 and a migrating tide.

As depicted in Figure 4.12, the 2dayE2 amplitude structure does not resemble the 2dayW3 amplitude structure in altitude and latitude. While the 2dayW3 is significant throughout the range from 50 km and 110 km and peaks around 40°S, the majority of the 2dayE2 significant amplitudes is only observed above 80 km altitude and closer to the equator. The independence of the 2dayE2 amplitude structure from the 2dayW3 structure provides strong evidence that the 2dayW3 is not aliasing into the 2dayE2 results. If 2dayW3 aliasing effects were present, large 2dayE2 amplitudes would coincide with large 2dayW3 amplitudes.

Unlike the 2dayW3, the 2dayE2 amplitude does not exhibit a clear amplitude structure with

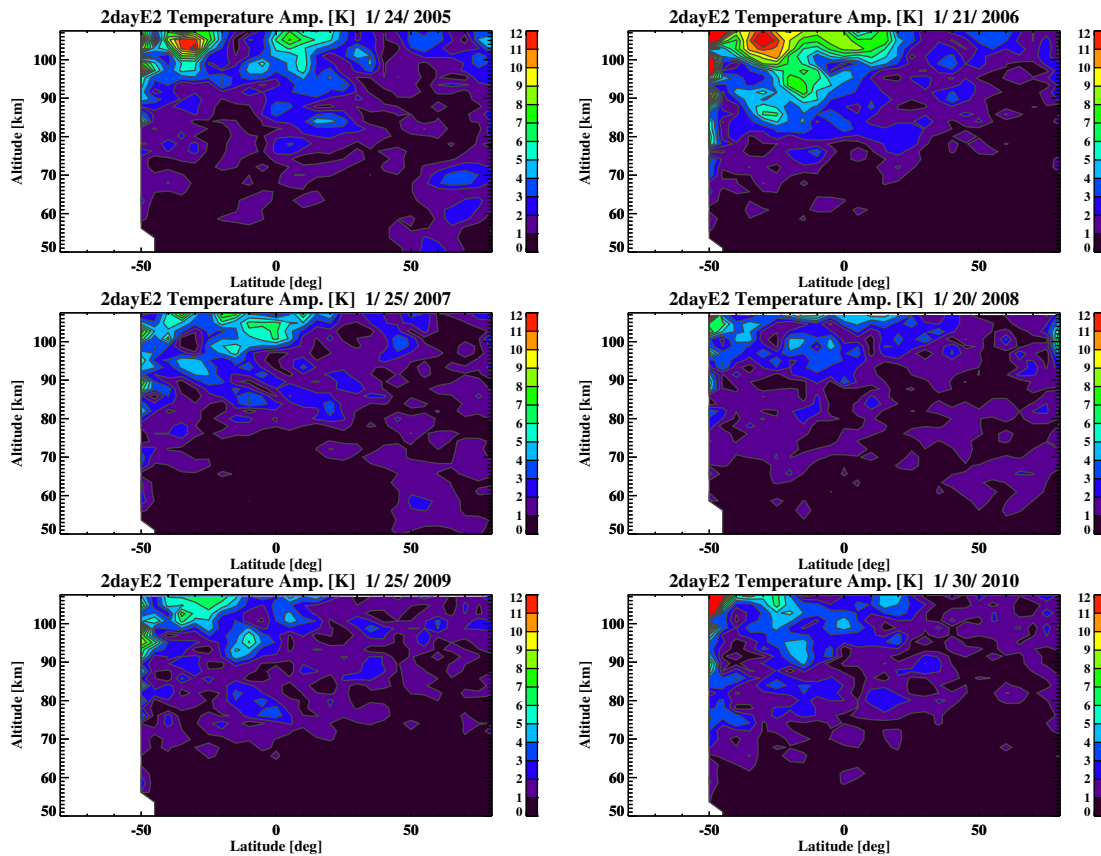


Figure 4.12: Same as Figure 4.9 except for 2dayE2 temperature.

altitude other than being significant above 80 km. The 2dayE2 amplitude may be significant at one altitude level and then insignificant at a level merely several kilometers above. This result may be partially interpreted as the aliasing of different secondary waves to the 2dayE2 frequency and wavenumber. While the aliased components of secondary waves with periods less than a day may constructively add with the 2dayE2 wave to produce large 2dayE2 amplitudes at one altitude, the waves may destructively add to produce small amplitudes at another. The presence of multiple secondary waves in the same region may be further supported by Figure 4.14, which shows the lack of 2dayE2 phase progression with altitude at low latitudes. The observed lack of phase progression may indicate that the presence of aliasing secondary waves at the same location as the 2dayE2 wave, which can lead to erroneous estimates for the 2dayE2 phase. It should also be noted that low

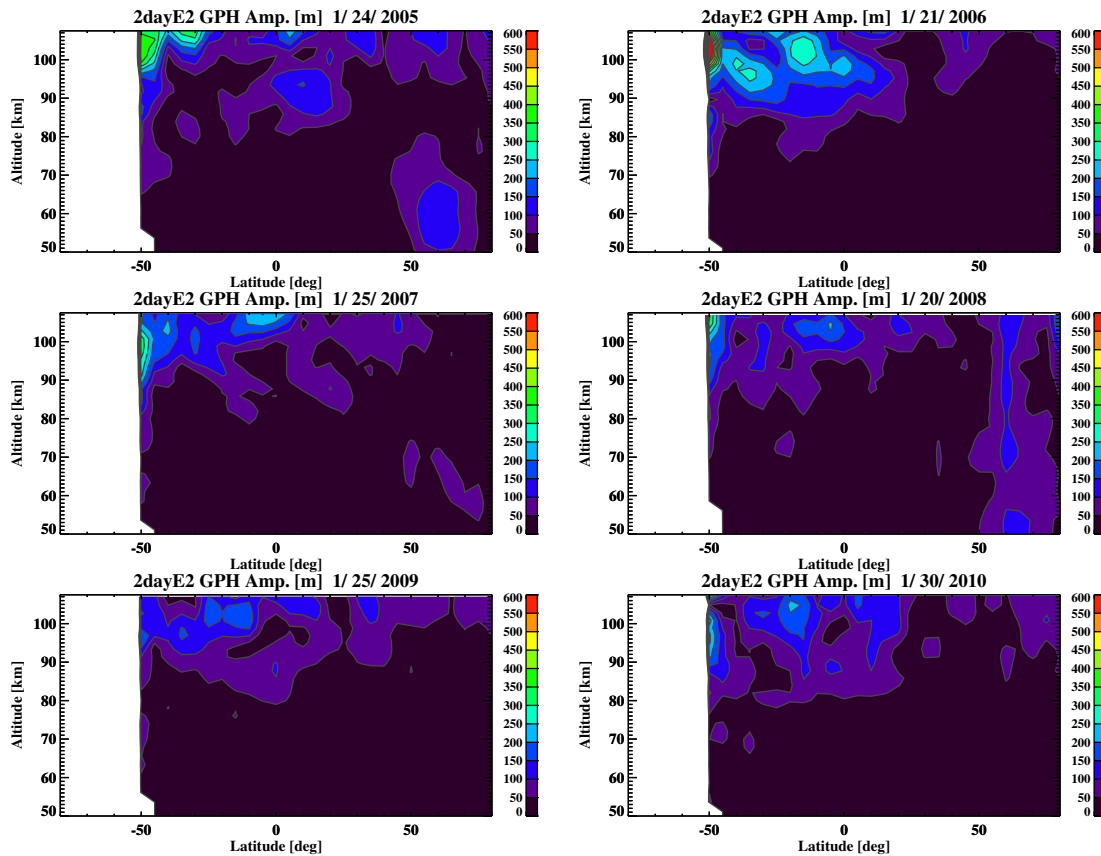


Figure 4.13: Same as Figure 4.9 except for 2dayE2 geopotential height.

secondary wave amplitudes below 90 km may also contribute to erroneous 2dayE2 phase estimates.

The results displayed in 4.12 and 4.13 also show that the 2dayE2 amplitude representing the secondary waves from the 2dayW3-migrating tide interaction exhibits large year-to-year variation. The 2dayE2 amplitude is largest during 2006, which coincides with one of the largest 2dayW3 events. However, a clear correlation between peak 2dayW3 amplitude and significant 2dayE2 amplitude is not observed on a year-to-year basis. For instance, the 2dayE2 amplitude during 2009 is similar to the the 2dayE2 observed during 2005 even though the 2dayW3 during 2009 is small in magnitude. The factors explaining the the year-to-year variation in the 2dayE2 amplitude representing the secondary waves originating from the 2dayW3-migrating tide have not been studied by past analyses. The results contained in Chapter 6 of this dissertation serve to help explain the

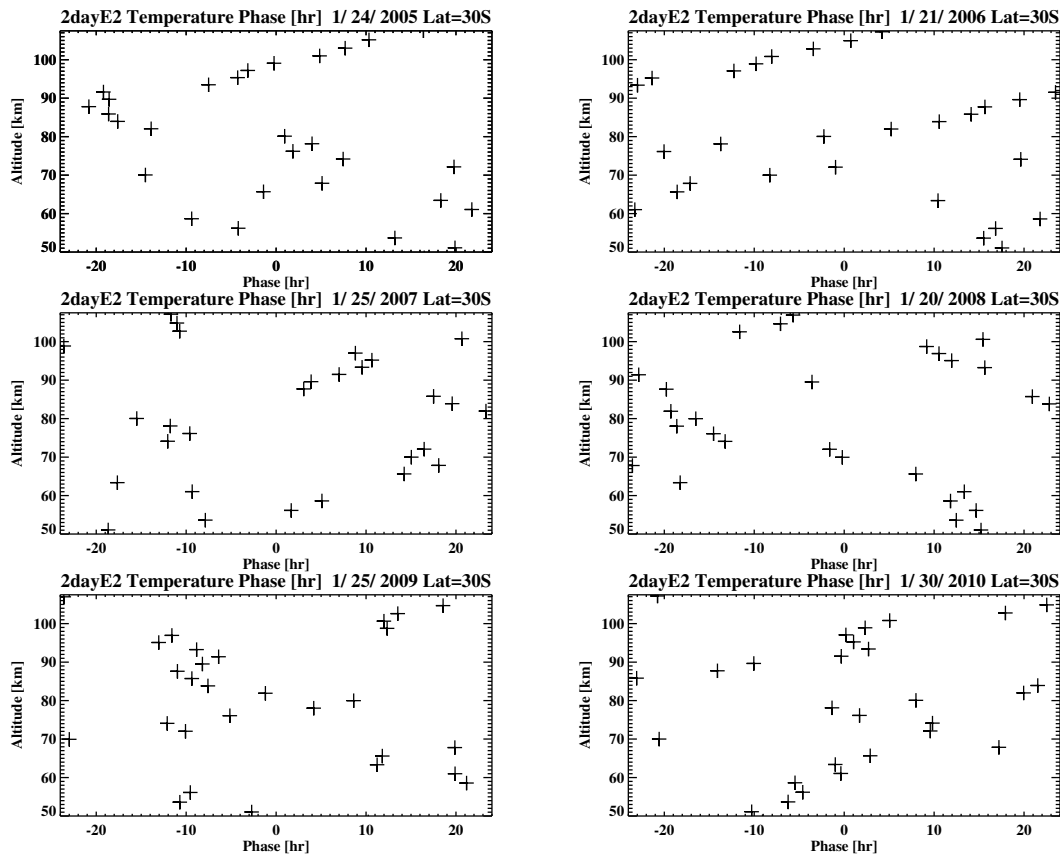


Figure 4.14: 2dayE2 phase as a function of altitude at  $10^{\circ}\text{S}$  latitude. Downward phase progression indicates upward energy propagation.

observed interannual variability.

### 4.3 Secondary Wave Comparison to NOGAPS-ALPHA

The content contained in the previous section demonstrated that the evidence of secondary waves extracted from satellite observations is somewhat limited because the contributions of each secondary wave to the 2dayE2 signal cannot be deduced. In order to analyze the likely composition of the observed 2dayE2 signal, NOGAPS-ALPHA reanalysis output is employed. Since NOGAPS-ALPHA outputs data on a synoptic grid with hourly temporal resolution, the amplitude and phase of waves with periods as small as 2 hours can be estimated using a two-dimensional Fourier transform. The secondary waves extracted from NOGAPS-ALPHA are expected to be

similar to the observed waves because the model assimilates temperature data from both TIMED-SABER and Aura-MLS. Hence, NOGAPS-ALPHA provides a powerful tool to assess secondary wave observations up to its upper boundary of about 95 km.

The amplitude and phase of the 2dayW3 and each secondary wave arising from nonlinear interaction with migrating diurnal/semidiurnal tides (2dayE2, 16hrW4, 16hrE1 and 9.6hrW5) are extracted from model output within a 6-day length window centered on a particular day. The Fourier transform in time and longitude is then applied to the data at each altitude and latitude location. Results for the temporal window centered on January 24th, 2005 are shown in Figure 4.15. The 2dayW3 reaches maximum amplitudes of about 10 K at middle southern latitudes, which is similar to the 2dayW3 amplitude observed in SABER and MLS shown previously. The majority of secondary wave amplitudes are only significant above 80 km and reach maximum amplitudes near the upper boundary of NOGAPS-ALPHA around 95 km. The largest secondary wave between 80 and 95 km is the 16hrW4, which peaks around 35°N and attains amplitudes between 4 K and 5 K. It should be noted that the 2dayE2 observed at high latitudes in the Northern hemisphere is not likely a product of nonlinear interaction. Past studies (Manney and Randel, 1993 [58]) have shown that the 2dayE2 in this region is likely a product of the polar night jet stream instability, which gives rise to the 4dayE1 and 2dayE2 wave packet.

Figure 4.16 displays results for the NOGAPS-ALPHA 2dayW3 and secondary waves during late-January 2006. As expected, the 2dayW3 amplitude is large and displays a similar structure to the 2dayW3 observed in SABER and MLS. Like the 2005 results, the secondary waves are only significant above 80 km. However, there are small differences between the amplitude structure of each secondary wave during each year. For example, the 16hrW4 wave during 2006 shows amplitude in both hemispheres whereas the 2005 16hrW4 wave is only present in the northern hemisphere.

To directly compare the NOGAPS-ALPHA secondary waves to the SABER observations, the atmospheric temperature field is reconstructed from the NOGAPS-ALPHA 2dayW3 and secondary waves shown in Figures 4.15 and 4.16. The FFSM technique is then utilized to estimate the 2dayE2 amplitude from the SABER sampling of the reconstructed temperature field. As shown

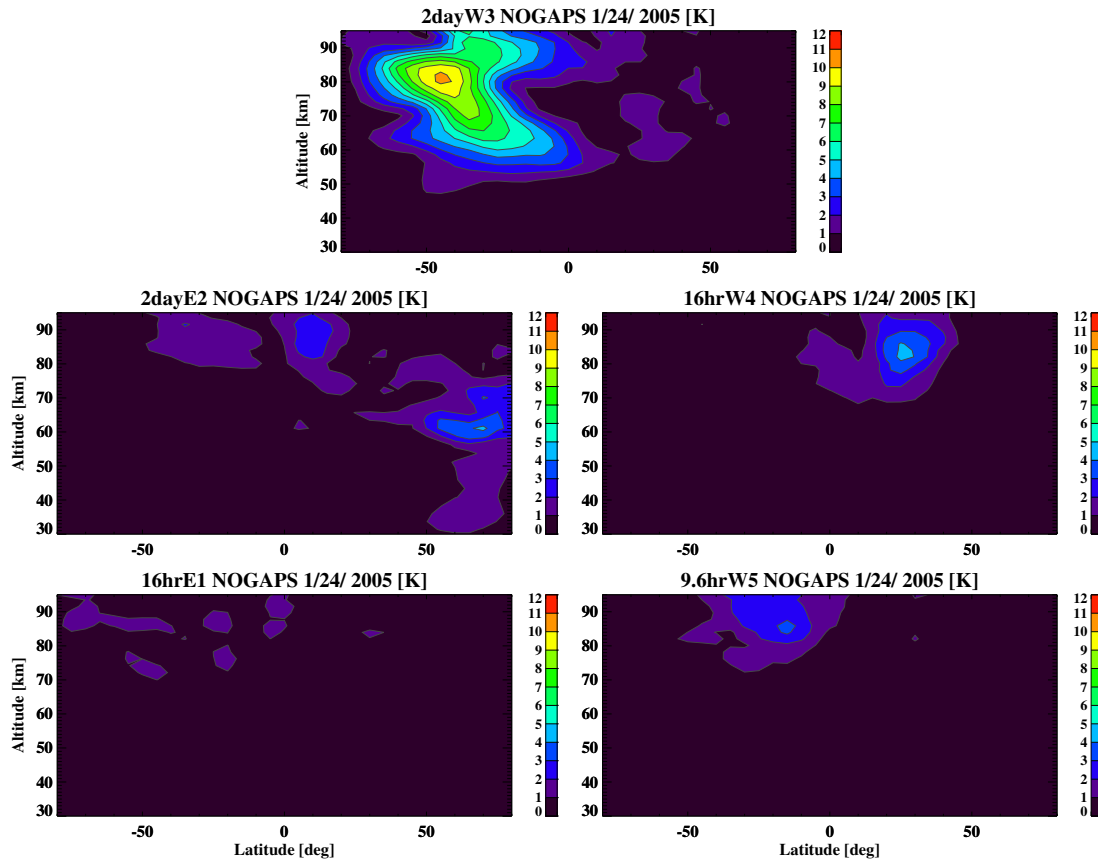


Figure 4.15: 2dayW3 , 2dayE2, 16hrW4, 16hrE1, and 9.6hrW5 amplitude structure extracted using a 6-day window of NOGAPS-ALPHA hourly output centered on January 24th, 2005.

in Figure 4.17, the 2dayE2 altitude-latitude structure estimated from SABER sampling of the NOGAPS-ALPHA reconstructed atmosphere exhibits largest amplitudes at low latitudes above 75 km and high Northern latitudes below. By comparing to 4.15, it is observed that the sampled 2dayE2 amplitude during 2005 contains contributions from all the secondary waves arising from nonlinear interaction between the 2dayW3 and migrating tides. During 2006 (Figure 4.16), the sampled 2dayE2 amplitude from NOGAPS is largely aliased by the 16hrW4 appearing at low Southern latitudes above 80 km. Additionally, the resemblance of the sampled 2dayE2 amplitude structures to the 2dayE2 structures extracted from SABER temperatures (Figure 4.12) implies that the SABER 2dayE2 estimates likely contain additional contributions from the 16hrW4, 16hrE1 and 9.6 hrW5 waves. It is concluded that the FFSM-derived 2dayE2 amplitude structure observed

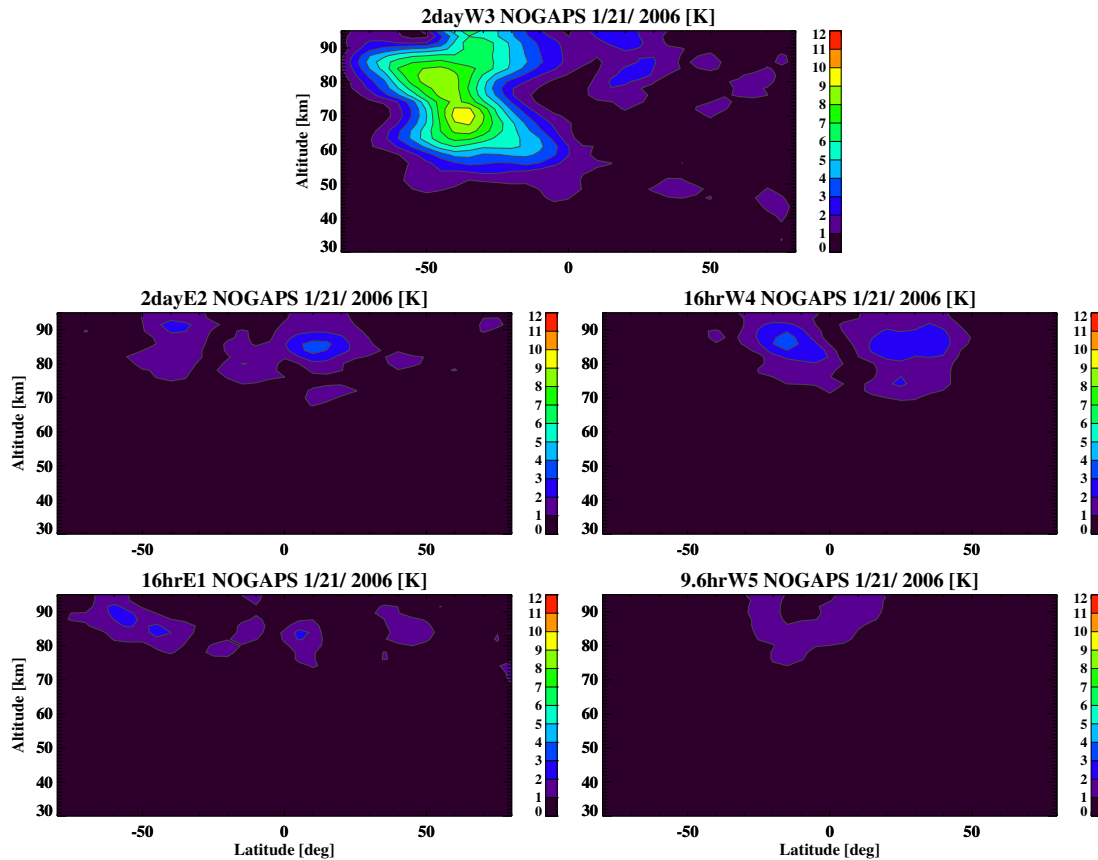


Figure 4.16: Same as Figure 4.15 except for January 21st 2006.

from SABER is dominated by the secondary waves arising from nonlinear interaction between the 2dayW3 and migrating tides.

The exercise of extracting the 2dayE2 amplitude from SABER samples of the reconstructed NOGAPS field is repeated by applying the least squares method. The reconstructed NOGAPS field was least squares fit to the 2dayE2 signal to estimate the wave amplitude and phase. These results displayed in Figures 4.15 and 4.16 show that least-squares method does not effectively remove the 2dayW3 signal from the 2dayE2. Thus, the 2dayE2 amplitude estimated from the least squares method does not necessarily imply that a nonlinear interaction between the 2dayW3 and atmospheric tides is occurring. This serves as another piece of evidence that the FFSM is a superior technique in providing evidence of 2dayW3-tidal interactions.

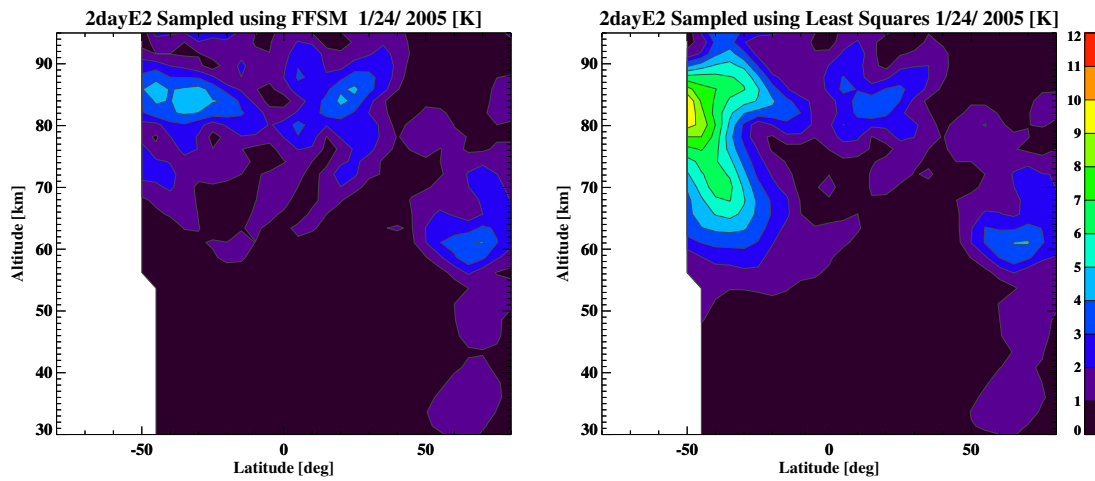


Figure 4.17: 2dayE2 signal amplitude estimated by applying SABER sampling to the reconstructed field formed from the 2dayW3, 2dayE2, 16hrW4, 16hrE1, and 9.6hrW5 waves for January 24th, 2005 and subsequently, implementing the FFSM method (left) and the least squares method (right). Results show that the FFSM method eliminates aliasing from the 2dayW3 while the least squares method does not.

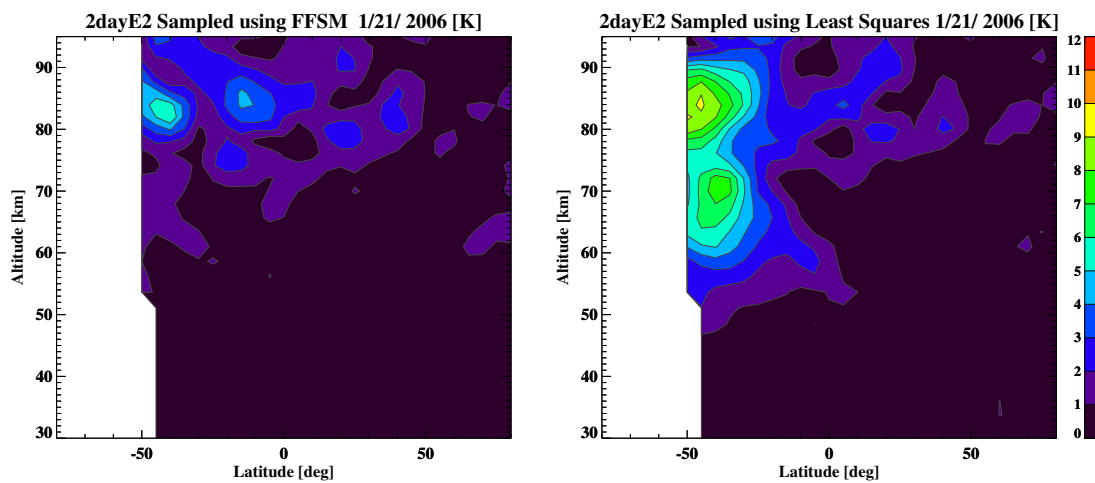


Figure 4.18: Same as Figure 4.17 except for January 21st 2006.

## Chapter 5

### COMPUTATION OF SECONDARY WAVE FORCING

The following chapter presents a discussion on how short-term primary estimates can be computed and utilized for deriving the nonlinear forcing quantities for each secondary wave. First, a variety of techniques are presented to derive global, short-term estimates of the 2dayW3 and DW1 in temperature and horizontal wind from satellite observations. While the primary wave estimates derived purely from observations are ideal because they are minimally impacted by physical assumptions, they are limited by the spatial and temporal resolution and coverage of satellite-based observations. Hence, it was eventually chosen to use reanalysis output from the NOGAPS-ALPHA model to extract short-term estimates for the DW1 and 2dayW3. Analyses in this chapter demonstrate that the primary wave estimates extracted from the NOGAPS-ALPHA model agree quite well with satellite observations and consequently, may be used to compute accurate distributions of nonlinear forcing quantities. The final portion of this chapter presents the nonlinear forcing quantities for the 16hrW4 and 2dayE2 secondary waves derived from the primary waves estimates.

#### 5.1 Origin of Nonlinear Forcing

The theory presented in Chapter 2 demonstrated that the existence of secondary waves in the atmosphere originates from the nonlinear terms contained in the zonal momentum, meridional momentum, and energy primitive equations (Teitelbaum and Vial, 1991 [107]). The nonlinear forcing for each secondary wave can be computed by assuming that each perturbation field variable ( $f'$ ) is a summation of two primary waves ( $f'_1$  and  $f'_2$ ). By substituting this form into the generalized

advection term, the largest nonlinear term in the primitive equations, the following expression is obtained:

$$\vec{u}' \cdot \nabla f' = \{(u'_1 + u'_2) \frac{\partial}{a \cos \phi \partial \lambda} + (v'_1 + v'_2) \frac{\partial}{a \partial \phi}\} (f'_1 + f'_2) \quad (5.1)$$

In the preceding equation,  $u'$ , and  $v'$  denote the perturbation zonal and meridional wind, respectively. The variable,  $f'$ , represents either the perturbation zonal wind or meridional wind in the momentum equations and the perturbation temperature in the thermal energy equation. Since the perturbation vertical wind is typically much smaller than the horizontal wind components, this term is neglected in the nonlinear forcing computation. Each perturbation field in Equation 5.1 is assumed to be in the form  $\hat{A} \cos(s\lambda - \omega t + \theta_f)$ , where  $s$  represents zonal wavenumber,  $\omega$  denotes wave frequency, and  $\hat{A}$  and  $\theta_f$  are the real-valued amplitude and phase values, respectively. Substituting this form into the advection term and other nonlinear terms in the primitive equations results in trigonometric multiplication of primary waves and subsequently produces forcing at the following wavenumber-frequency pairs:  $[(s_1 + s_2), (\omega_1 + \omega_2)]$ ,  $[(s_2 - s_1), (\omega_2 - \omega_1)]$ ,  $[(2s_1), (2\omega_1)]$ , and  $[(2s_2), (2\omega_2)]$ . Thus, the forcing for each secondary wave can be computed by inserting the primary wave amplitude and phase definitions into the nonlinear terms contained in the primitive equations, which include the advection of momentum and temperature, and smaller order curvature terms. Details of computing the nonlinear forcing terms for each secondary wave from primary wave amplitude and phase values are given in Appendix C.

## 5.2 Primary Wave Estimates

### 5.2.1 Estimating from Only Observations

Primary wave estimates used in the nonlinear forcing are ideally extracted from the raw observational data because the estimates are not impacted by model simplifications and/or unrealistic physical assumptions. However, obtaining accurate, global estimates of each primary wave in all required fields (temperature, meridional wind and zonal wind) is a major challenge. While satellite instruments such as TIMED-SABER provide near-global observations of temperature from the up-

per troposphere to lower thermosphere where tides and planetary waves are most significant, there are only sparse wind observations throughout this range. The only current satellite instrument capable of providing wind measurements in the MLT region is the TIMED Doppler interferometer (TIDI) on the TIMED satellite, which functions by monitoring the Doppler shift of airglow emissions using a limb-scan Fabry Perot interferometer (Killeen et al., 2006 [44]). Unfortunately, TIDI wind measurements can only be provided over a narrow range between 85 km and 105 km and consequently, are not sufficient for extracting the complete 2dayW3 structure. As a result, extracting primary wave estimates from raw horizontal wind measurements is currently not possible with the existing suite of observational instruments.

For the interaction between DW1 and 2dayW3, primary wave amplitude and phase should additionally be estimated over short temporal windows because 2dayW3 events only last for a few weeks. Although lower frequency spectra such as the 2dayW3 can be easily resolved on time scales of a few days using satellite temperature data, higher frequency tides such as the DW1 can only be estimated with 60-day resolution by traditional least squares methods applied to temperature data from a single (near) sun-synchronous satellite. These long-term estimates of the DW1 do not sufficiently capture short-term changes and are likely not sufficient for computing nonlinear forcing that are only valid over short time scales.

In this section, several techniques to overcome the aforementioned challenges are described and applied to satellite observations. First, a balanced wind approach is applied to MLS observations to derive 2dayW3 estimates in the horizontal wind fields. Afterward, techniques to derive short-term estimates of the DW1 from satellite observations are explored. The approaches explained in this section are desirable because they only make a small number of assumptions about the physical dynamics of the atmosphere. However, the results presented in the rest of this section show that the accuracy limitations that accompany these techniques outweigh their benefits. Consequently, it is chosen to extract primary waves estimates from NOGAPS reanalysis data, which is later explained in section 5.2.2.

### 5.2.1.1 Quasi-Two-Day Wave Balanced Winds

Despite the paucity of satellite wind observations in the MLT region, it is still possible to derive 2dayW3 winds by applying a balanced wind approach to existing observations of geopotential height. In this balanced wind approach, scale analyses of the governing equations for background and perturbation motion are performed to derive a one-to-one relationship between horizontal winds and geopotential height. An overview of this technique and balanced wind results for the 2dayW3 are provided in this section.

As explained in Chapter 2, equations governing background and perturbation motion are derived by linearizing about a zonally-averaged basic state. While classical tidal theory assumes a zero wind basic state, the analyses presented here assume a nonzero zonal wind basic state for more accuracy. By assuming that the zonally averaged wind in the meridional and vertical directions are zero and the basic state changes slowly over time, the time tendency, advection and most of the curvature terms contained in the background momentum equations may be eliminated. A scale analysis of the remaining terms in the momentum equations shows that the dominant terms are the Coriolis force, the pressure gradient force and the  $\frac{\bar{u}^2 \tan \phi}{a}$  curvature term for the stratosphere and mesosphere. Thus, the momentum equation for background motion in the meridional direction may be expressed as the following.

$$\bar{u} \left( f + \bar{u} \frac{\tan \phi}{a} \right) = - \frac{\partial \bar{\Phi}}{\partial y} \quad (5.2)$$

In Equation 5.2, the pressure gradient force is expressed in terms of geopotential height ( $\partial p = \rho \partial \Phi$ ), which can be derived for an atmosphere in approximate hydrostatic balance. Solving for  $\bar{u}$  in Equation 5.2 produces the following expression for the zonally averaged zonal wind in terms of the zonally averaged geopotential height (Hitchman and Leovy [36]).

$$\bar{u} = - \frac{1}{f} \frac{\partial \bar{\Phi}}{\partial y} \left[ 1 - \frac{(1/f)(\partial \bar{\Phi} / \partial y)}{2\Omega a \cos \phi} \right]^{-1} \quad (5.3)$$

The preceding equation shows that observations of geopotential height may be used to approximate the zonally averaged zonal wind. The approximated winds, often referred to as the

gradient zonal mean wind, has been demonstrated in past studies to be an accurate representation of the actual zonal mean wind throughout most of the stratosphere and mesosphere (Hitchman and Leovy, 1986 [36]; Randel [88]). The only exception occurs near the equator where the zero Coriolis parameter ( $f$ ) leads to undefined solutions. Most studies have solved this problem by interpolating the gradient winds across the equator, which is adopted here.

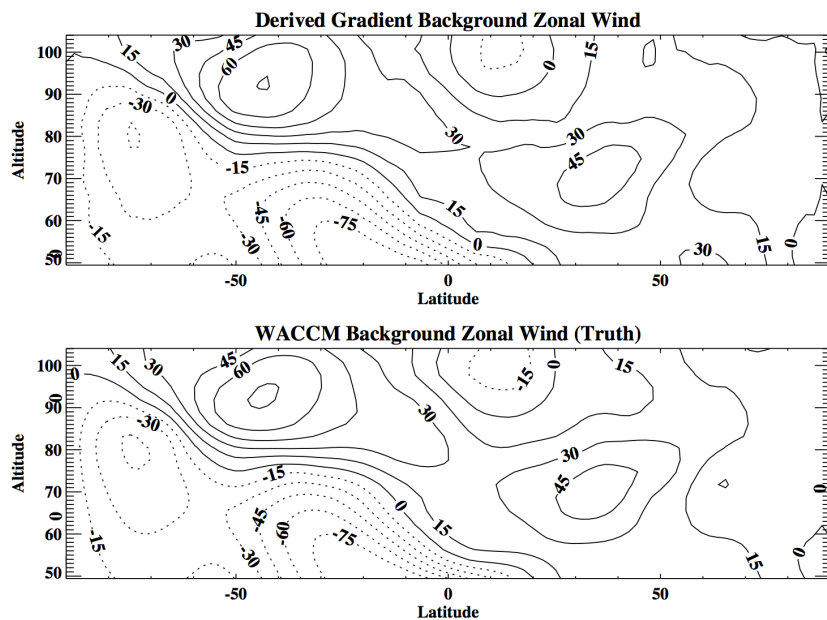


Figure 5.1: Background zonal wind structure derived by applying balanced wind approach to WACCM model data. The top plot shows the derived background zonal wind structure while the bottom plot shows the true WACCM background zonal wind structure. Contour levels are spaced 15 m/s apart.

The assumption that atmospheric motion is in approximate gradient wind balance is validated here by employing the Whole Atmosphere Community Climate Model (WACCM), which is a numerical model spanning from the surface to the thermosphere (Garcia, 2007 [20]). Since WACCM has been shown to accurately portray the dynamics of the real atmosphere, the validity of the gradient wind approximation can be tested by extracting the gradient wind and comparing it with the actual winds in the model. The comparison displayed in Figure 5.1 shows that the derived gradient wind with interpolated winds across the equator is a good approximation to

the zonally averaged zonal wind solved by a particular WACCM run (courtesy of Nick Pedatella). Thus, it is concluded that the gradient wind derived from geopotential height observations is a good representation of the observed background zonal wind in the stratosphere and mesosphere.

Similarly, the 2dayW3 winds can be derived from geopotential height observations by applying a scale analysis of the perturbation momentum equations. By neglecting meridional and vertical background motion, friction and the products of perturbation quantities, the linearized momentum equations governing 2dayW3 motion may be expressed as:

$$\frac{\partial u'}{\partial t} + \frac{\bar{u}}{a \cos \phi} \frac{\partial u'}{\partial \lambda} - \hat{f}v' = -\frac{1}{a \cos \phi} \frac{\partial \Phi'}{\partial \lambda} \quad (5.4)$$

$$\frac{\partial v'}{\partial t} + \frac{\bar{u}}{a \cos \phi} \frac{\partial v'}{\partial \lambda} + \tilde{f}u' = -\frac{1}{a} \frac{\partial \Phi'}{\partial \phi} \quad (5.5)$$

where  $\hat{f} = \left[ 2\Omega \sin \phi - \frac{1}{a \cos \phi} \frac{\partial}{\partial \phi} (\bar{u} \cos \phi) \right]$  and  $\tilde{f} = \left[ 2\Omega \sin \phi - \frac{2\bar{u}}{a} \tan \phi \right]$

Solutions for  $u'$  and  $v'$  representing the 2dayW3 zonal and meridional wind perturbation respectively may be derived from Equations 5.4-5.5 by assuming solutions of the form  $e^{i(s\lambda - \Omega\sigma t)}$ . As a result,  $\frac{\partial}{\partial t} \rightarrow -i\Omega\sigma$  and  $\frac{\partial}{\partial \lambda} \rightarrow is$ . After approximating the background zonal wind ( $\bar{u}$ ) by the gradient wind (Equation 5.2), a linear system of two equations is created relating the perturbation horizontal winds to perturbation geopotential height. Thus, the 2dayW3 winds can be calculated from Equations 5.4-5.5 using observations of geopotential height.

However, unique solutions for  $u'$  and  $v'$  cannot be computed when the determinant of the system is equal to or close to zero. The locations of zero determinant system is dependent on the background zonal wind structure. Mathematically, these cases occur when:

$$\delta = \frac{\left( \bar{u} \frac{s}{a \cos \phi} - \Omega\sigma \right)^2}{\hat{f}\tilde{f}} \rightarrow 1 \quad (5.6)$$

In order to compute solutions for  $u'$  and  $v'$  at the zero determinant cases, the approach by Hitchman and Leovy, 1987 [37] is adopted. In this approach, Rayleigh friction force terms are added to the right hand side of Equations 5.4 and 5.5 in the form of  $-\mu_0 u'$  and  $-\mu_0 v'$  for cases

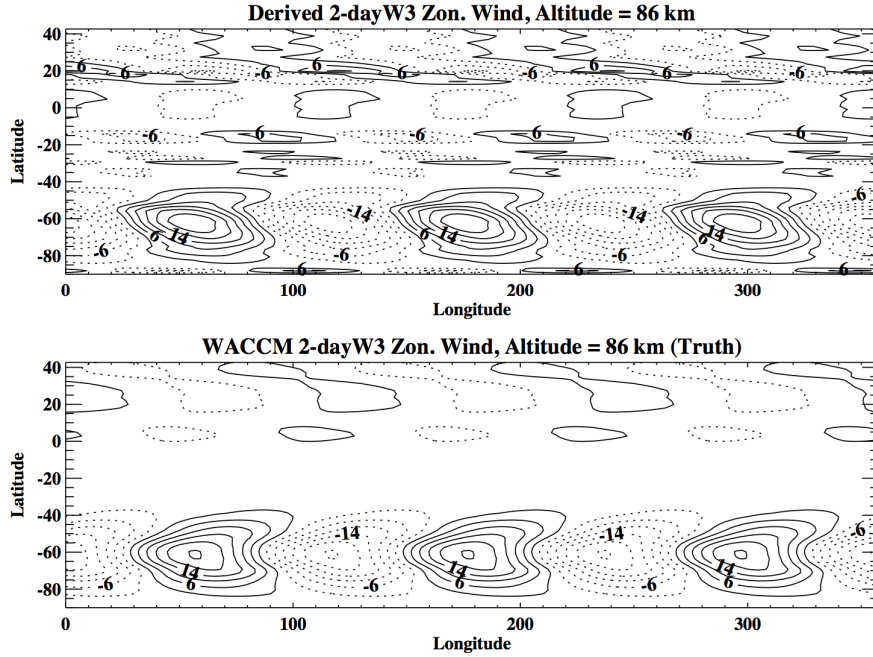


Figure 5.2: The 2dayW3 zonal wind structure derived by applying balanced wind approach to WACCM model data. The top plot shows the derived 2dayW3 zonal wind perturbation reconstructed in latitude and longitude while the bottom plot shows the true WACCM QTDW zonal wind perturbation. Contour levels are spaced 4 m/s apart.

where  $0.8 < \delta < 1.2$ . The inclusion of friction in the perturbation momentum equations causes the system determinant to be nonzero and thus, allows for the computation of unique solutions.

Like the gradient wind approach, the method to derive the 2dayW3 winds from geopotential height observations is tested with WACCM output. The 2dayW3 winds and geopotential height are initially extracted from a WACCM run where the wave is significant using a two-dimensional discrete Fourier transform. The 2dayW3 geopotential height is then utilized with Equations 5.4 and 5.5 to estimate the 2dayW3 zonal and meridional winds. Figures 5.2 and 5.3 compare the 2dayW3 wind quantities derived from geopotential height to the 2dayW3 winds extracted directly from the model at the same altitude level. It is observed that the derived 2dayW3 winds approximates the actual 2dayW3 winds in WACCM most accurately at southern latitudes where the 2dayW3 is large. Larger differences can be observed at latitudes around  $20^\circ\text{N}$  and  $20^\circ\text{S}$ , which correspond to locations where the system of equations represented by Equations 5.4 and 5.5 is indeterminate.

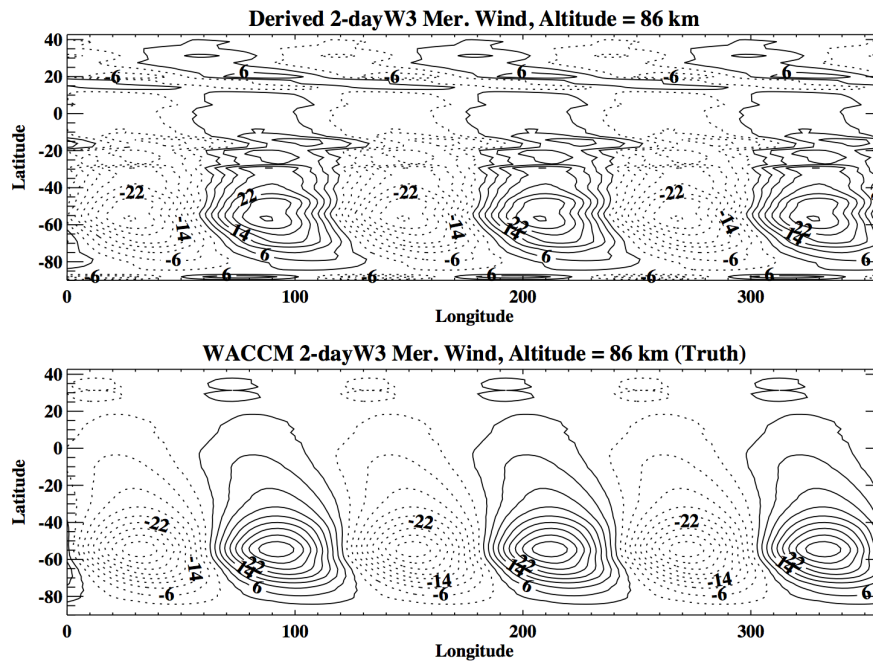


Figure 5.3: Same as Figure 5.2 except for QTDW meridional wind.

This balanced wind technique is applied to MLS geopotential height estimates of the 2dayW3 in order to derive 2dayW3 horizontal wind estimates. Figure 5.4 displays derived 2dayW3 horizontal wind amplitudes and phases along with derived background winds for a late-January time period. The results reveal that the 2dayW3 wind amplitude is most dominant at mid-latitudes in the Southern Hemisphere as expected. Merdional wind amplitudes of up to 48 m/s are observed in the upper mesosphere, which is within the range of values shown in past observational and modeling studies (Gu et al., 2013 [25]; Palo et al., 1999 [77]). Also consistent with past studies is the observed the 2dayW3 downward phase progression and vertical wavelength of about 50 km. Sharp latitudinal gradients in the wind amplitude, however, are observed at low-latitudes, which imply that singular solutions are likely affecting the wind estimates. These singular solutions at low-latitudes would subsequently lead to erroneous nonlinear forcing at low latitudes and perhaps invalid conclusions about the manifestation of secondary waves in the MLT region.

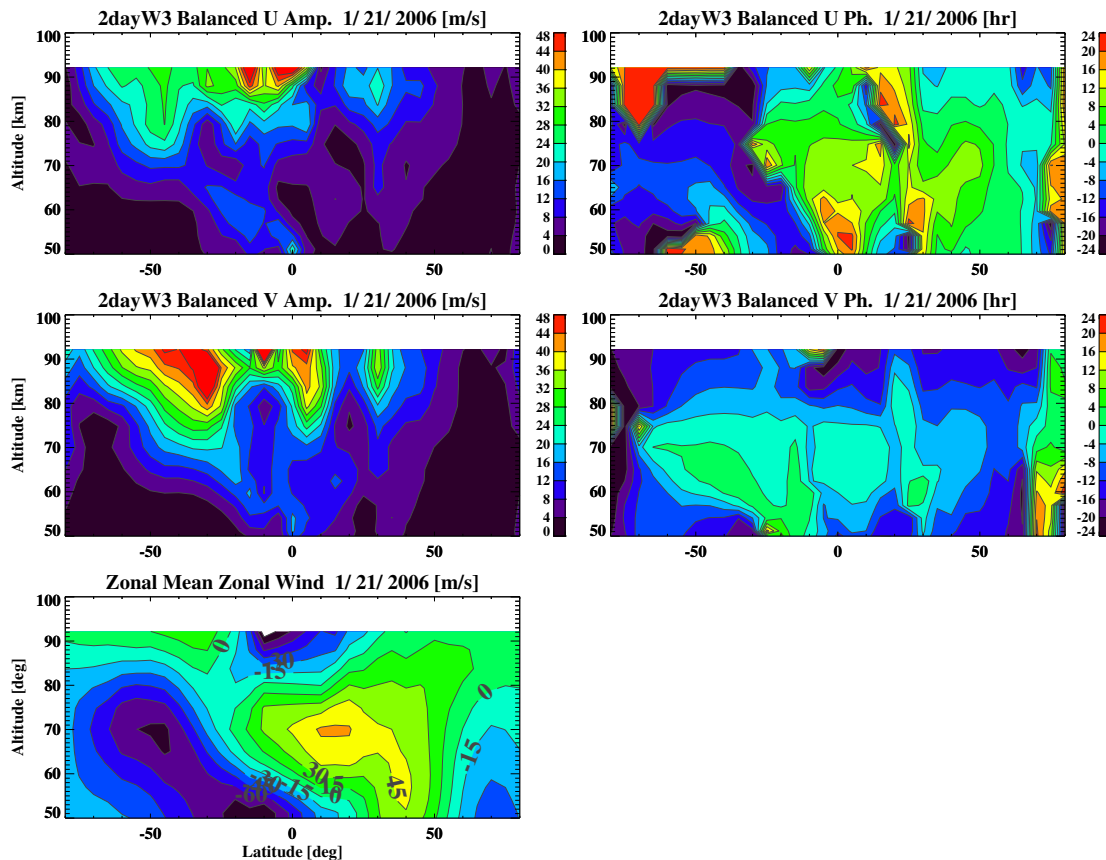


Figure 5.4: Estimated 2dayW3 perturbation wind amplitudes, phases and background zonal winds derived by applying balanced wind approach to MLS geopotential height data. The 2dayW3 amplitude for zonal wind (top-left) meridional wind (middle-left) and 2dayW3 phase for zonal wind (top right) and meridional wind (middle right) are displayed. The bottom plot shows the derived background zonal wind.

### 5.2.1.2 Short-term DW1 Estimates

Unlike planetary waves, atmospheric tides possess periods with less than a day, which lie outside the Nyquist limits obtained from MLS and SABER sampling. Thus, the FFSM method cannot be applied to estimate the amplitude and phase of atmospheric tides. Many past studies analyzing tides from space have addressed this problem by taking advantage of satellites such as SABER that precess in local time (Zhang et al., 2006 [120], Xu et al., 2007 [118], Mukhtarov et al., 2009 [67]). By utilizing such satellites, a diurnal range of local times can be obtained over a global range in longitude. With full sampling in both solar local time and longitude, estimates

for amplitude and phase for each tidal component can be computed using DFT or least squares methods. However, the time resolution of these estimates is dependent on the time required to obtain full solar local time coverage, which often exceeds 30 days. Short-term estimates for a full tidal spectrum cannot be achieved through the use of a single satellite, which is necessary to accurately investigate nonlinear interactions that occur over short time periods.

One possible method of obtaining shorter-term estimates of the migrating diurnal tide is through the technique recently developed by Nguyen and Palo, 2013 [69]. They showed that a combination of temperature measurements from MLS and SABER produces the observational coverage necessary to compute the amplitude and phase of the migrating diurnal tide (DW1) on a short-term basis. Since the MLS and SABER instruments are located in true or near-sun-synchronous orbits, each instrument observes a latitude circle at constant local time over a given day on the ascending or descending portions of the orbit. As a result, measurements at four solar local times are obtained on a given day by accounting for observations from both instruments, which is sufficient to estimate estimate the amplitude and phase of the DW1.

The technique demonstrated by Nguyen and Palo, 2013 [69] is initiated by placing MLS and SABER temperatures over a single day on a common grid defined by latitude, altitude, orbit and orbital leg and then averaging each bin. The latitude grid is chosen to be defined by  $5^\circ$  bins ranging between  $-82.5^\circ$  and  $82.5^\circ$  while the vertical grid is chosen to be the MLS pressure level grid. As recommended by the MLS team (Schwartz et al., 2008 [102]), each SABER profile is least squares fit to the vertical grid by assuming that the MLS grid is piecewise linear. After placing the temperatures on a common grid and averaging, the temperatures are zonally averaged along orbit at each altitude and latitude to attenuate the effects due to non-migrating tides and other sources of longitudinal variability. Consequently, four zonal temperature profiles are obtained at four different solar local times over a single day. To eliminate potential error due to systematic differences between instruments, the mean temperature differences are applied to the MLS zonal temperature profiles.

Because the DW1 is a migrating tide, the same phase of the DW1 is observed on each orbital

revolution at a constant local time. As a result, the effects of the DW1 are not attenuated after zonal averaging process. Moreover, the DW1 with  $s=-1$  and  $\sigma=1$  can be assumed to be sinusoidal in local time and independent of longitude from Equation 3.2. From this assumption, the zonally averaged temperature due to the influence of the DW1 and daily zonal mean can be represented by the following equation:

$$T(t_{LT}) = A_0 + A_1 \cos \frac{2\pi t_{LT}}{24} + A_2 \sin \frac{2\pi t_{LT}}{24} \quad (5.7)$$

where  $T$  is the zonally averaged temperature,  $t_{SLT}$  denotes solar time,  $A_0$  denotes the daily zonal mean and  $A_{1,2}$  represents the amplitude coefficients. From zonally averaged temperatures at four solar local times, a linear system of four equations and three unknowns can be created:

$$\begin{bmatrix} T_1 \\ T_2 \\ T_3 \\ T_4 \end{bmatrix} = \begin{bmatrix} 1 & \cos \frac{2\pi t_{LT,1}}{24} & \sin \frac{2\pi t_{LT,1}}{24} \\ 1 & \cos \frac{2\pi t_{LT,2}}{24} & \sin \frac{2\pi t_{LT,2}}{24} \\ 1 & \cos \frac{2\pi t_{LT,3}}{24} & \sin \frac{2\pi t_{LT,3}}{24} \\ 1 & \cos \frac{2\pi t_{LT,4}}{24} & \sin \frac{2\pi t_{LT,4}}{24} \end{bmatrix} \begin{bmatrix} A_0 \\ A_1 \\ A_2 \end{bmatrix} \quad (5.8)$$

Least squares estimates for  $A_0$ ,  $A_1$ , and  $A_2$  may be obtained from Equation 3.4, which are subsequently used to calculate the amplitude and phase of the DW1.

$$\begin{aligned} \text{Amplitude} &= \sqrt{A_1^2 + A_2^2} \\ \text{Phase} &= \tan^{-1}(A_2/A_1) \end{aligned} \quad (5.9)$$

Figure 5.5 shows examples of how a sinusoid representing the DW1 are least squares fit to four zonal temperature averages in local time. Error bars displayed in each of the figure subplots represent the standard deviation of the samples used in the zonal temperature averages. The magnitude of the error bars is dictated by the magnitude of the longitudinal variability that is attenuated through zonal averaging. Chi-squared values are also displayed in each example to quantify how well the least squares solution for the DW1 fits the zonal temperature averages. The

chi-squared values can be large when the effects of instrument measurement error or the presence of other tides and waves leak into the zonal temperature averages.

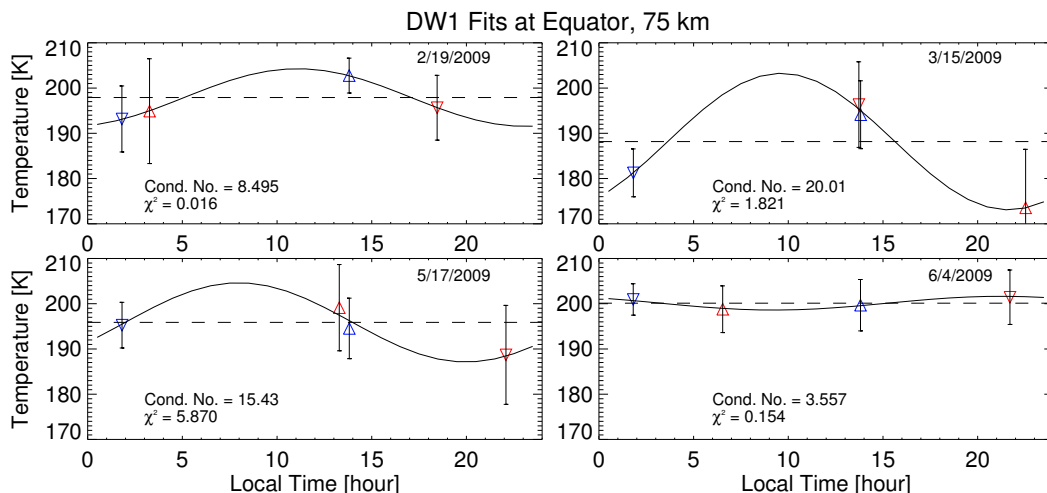


Figure 5.5: Least squares fits to four zonal temperature averages (equator, 75 km altitude) for different days in 2009. Blue and red triangles symbolize MLS and SABER zonal temperature averages, respectively. Upward and downward triangles denote ascending and descending measurements, respectively. Condition number is displayed to describe the local time sampling while the  $\chi^2$  value is presented to show the goodness of fit. Lower values indicate better local time sampling and quality of fit. The daily mean temperatures are indicated by the dashed line.

As shown in Figure 5.5, the local time sampling of the zonal temperature average varies throughout the year due to SABER being located in orbit that slowly precesses in local time. The local time sampling of each fit is quantified by the condition number (Olver and Shakiban, 2006 [71]). Small condition numbers appear when the local time samples are close to evenly-spaced while large condition numbers arise when the local time sampling is poor, leading to an almost linearly dependent systems. Consequently, systems characterized by large condition numbers are not as robust to measurement error and un-modeled effects. Figure 5.6 displays the variation of condition number from late-2005 to early-2006. The condition number varies at a period close to 60 days due to the SABER local time precession rate. It is also observed that the condition number can be large away from the equator, particularly in the southern hemisphere during this timeframe.

A major source of error for the DW1 estimates originates from the presence of the migrating

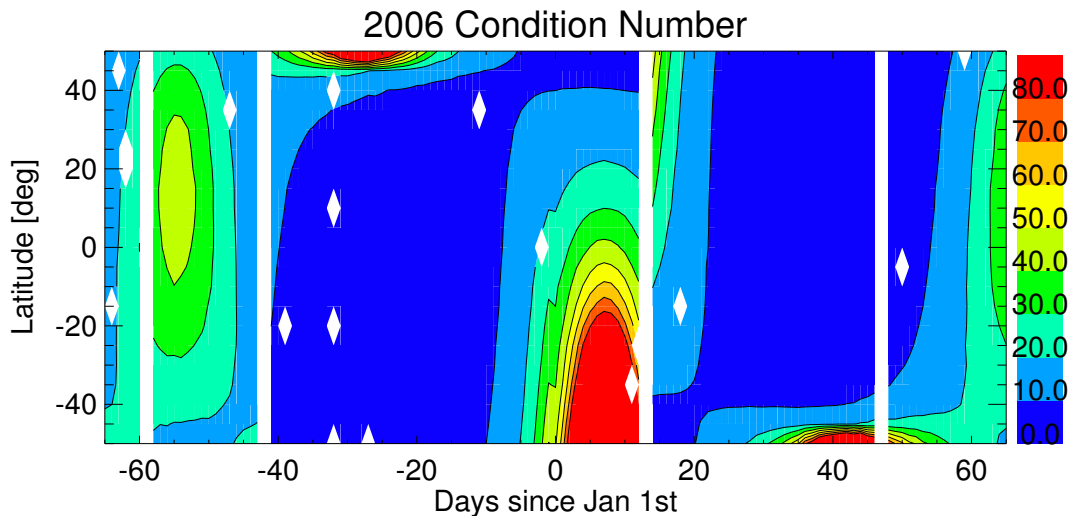


Figure 5.6: Condition number resulting from MLS/SABER local time sampling as a function of day and latitude. Smaller (larger) condition numbers indicate good (poor) local time sampling.

semidiurnal tide (SW2). Although the averaging at constant local time attenuates non-migrating effects, migrating effects such as the DW1 and SW2 are not. Analysis from Nguyen and Palo, 2013 [69] show that the effects of the SW2 introduce error in the DW1 estimates during periods when the SW2 amplitude is significant and when the local time sampling is not evenly spaced. Since SW2 can achieve non-negligible amplitudes at altitudes above 85 km, the DW1 estimates are confined to the region below that level. Furthermore, estimates obtained from condition number greater than 20 are not scientifically analyzed because they are more likely to be affected by error sources such as the SW2 and remaining systematic differences between the instruments. Finally, non-migrating effects may leak into the DW1 estimates if temperatures along a given latitude circle are not well-sampled in longitude. Thus, DW1 estimates obtained from zonal temperature averages using 8 orbits of data or less are excluded from scientific analysis.

An example of short-term amplitude and phase estimates of the DW1 produced by this technique is shown in Figure 5.7. The estimated DW1 amplitude increases with altitude as expected and achieves a primary peak of about 10 K at the equatorial mesosphere. Amplitude peaks of up to 6 K are observed over a wide range of latitudes at 50 km, which are likely manifestations of

evanescent modes forced by ozone heating in the stratosphere. The phase structure of the DW1 mainly exhibits downward phase progression at the equator with a vertical wavelength of about 25 km. This result reveals the dominance of the first propagating Hough mode of the DW1, especially in the equatorial mesosphere.

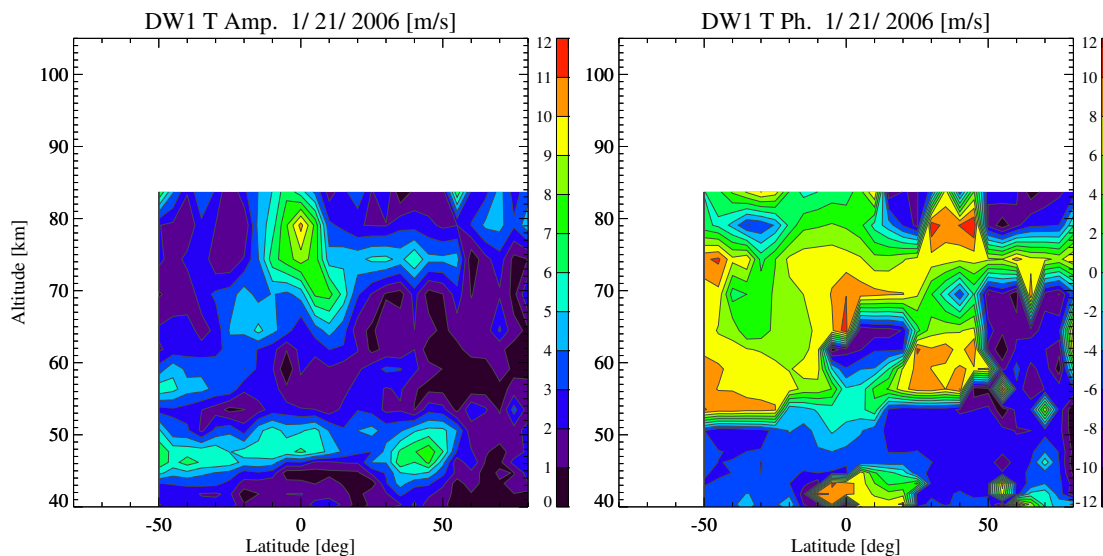


Figure 5.7: DW1 amplitude (top) and phase (bottom) estimates from combined MLS and SABER data as a function of altitude and latitude.

From Figure 5.7, it is apparent that the main disadvantage of this technique is the lack of full global coverage. SABER does not observe latitudes poleward of  $-50^{\circ}\text{S}$  during this time period, which prevents estimates from being produced in this region. Additionally, this technique can only be utilized to generate DW1 estimates up to 85 km due to the potential introduction of aliasing from the SW2 and larger systematic differences between MLS and SABER. Because DW1 and 2dayW3 are expected to achieve considerable amplitude above 85 km, it is expected that the nonlinear forcing produced from their interaction be large and thus, should not be ignored.

In order to obtain DW1 estimates in these regions, Hough Mode Extensions (HMEs) can be employed. This method not only fills in the observational temperature gaps, but also produces DW1 estimates in the horizontal wind fields for the full nonlinear forcing computation. Computed

from the Global Scale Wave Model (GSWM), a HME is a representation of a classical Hough mode under realistic atmospheric conditions (Svoboda et al., 2005 [104]). Each HME is computed by implementing a heat source near the lower boundary of the model with a latitudinal structure identical to the corresponding Hough mode. Subsequently, the GSWM computes the amplitudes and phases of each perturbation field ( $u$ ,  $w$ ,  $v$ ,  $T$ ,  $\rho$ ) at each altitude-latitude grid point. The tabulation of amplitudes and phases for each Hough mode is referred to as the HME and is internally consistent relative to each perturbation field.

In past studies, HMEs are computed from the GSWM assuming a windless, dissipative background atmosphere described by equatorial profiles of temperature and density obtained from the MSISE90 empirical model (Hedin, 1991 [33]). In this study, more realistic background temperature and zonal winds are included in the model by using values estimated from the MLS observations and derived gradient wind. Background material presented in Chapter 2 demonstrated that the presence of a non-zero background zonal wind and background temperature gradients causes the (1,1) Hough Mode to couple into other modes and produce a DW1 that is more representative of reality. The HME produced from MLS-derived background configurations during January 21st, 2006 is displayed in the leftmost plots of Figure 5.8. As expected, a dominant (1,1) Hough mode that increases in amplitude with altitude is observed in the results. There are, however, some deviations from the (1,1) Hough mode structure which indicate that the background causes coupling to higher order Hough modes.

Since the velocity and temperature perturbation fields for each HME maintain internally self-consistent relative amplitude and phase relationships, observations of one perturbation field allow for the estimation of the rest of the fields. Thus, the short-term estimates of DW1 in the temperature field can be least squares fit to the HME for the (1, 1) Hough mode and used to produce a complex normalizing coefficient. This coefficient can then be used to reconstruct the (1, 1) Hough mode velocity fields and serve as estimates for the DW1 horizontal wind. HME fits to the DW1 temperature estimates for late-January 2006 (Figure 5.7) are displayed in the rightmost plots in Figure 5.8. The altitude-latitude structure of the HME fits are identical to the HMEs on

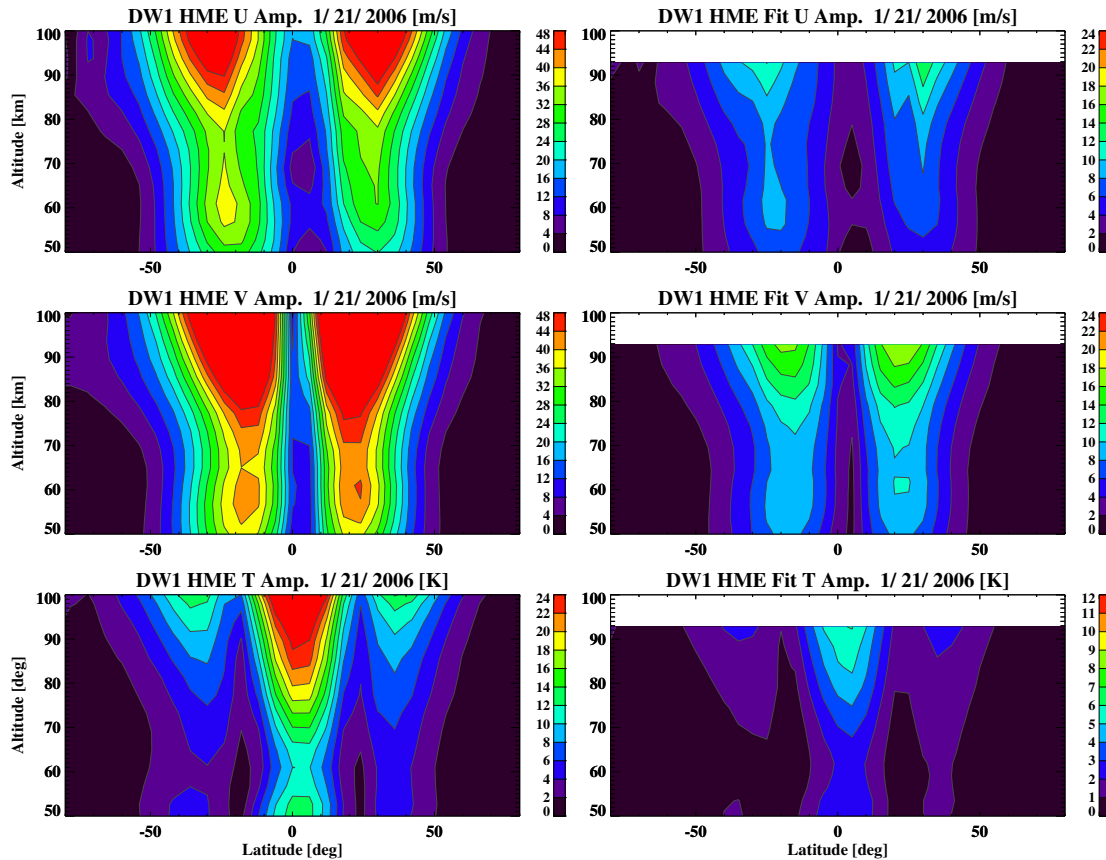


Figure 5.8: Amplitude of the Hough Mode Extension for the DW1 (1, 1) mode in the temperature (top), zonal wind (middle) and meridional wind (bottom) fields for atmosphere with zonal winds derived from MLS observations in late-January 2011.

the left side of the figure except scaled by a complex coefficient determined by the fitting to the observed DW1 temperature estimates.

The accuracy of this method in deriving the DW1 perturbation wind fields is dependent on how well the DW1 HME fit in the temperature field is representative of the observed DW1 temperature estimates. Above 50 km, the DW1 HME fit captures the general observed features of the DW1 temperature amplitude structure. Both structures display a primary peak at the equator with smaller secondary peaks near  $30^\circ$  latitude in both hemispheres. Furthermore, both amplitude structures exhibit approximate exponential growth with altitude.

However, there are some noticeable differences between the DW1 temperature HME fit and

observed DW1 estimates. Observations show moderate DW1 estimates around 45-50 km altitude over a wide latitudinal range, which is not exhibited by the HME structure. The observed DW1 activity near the stratopause is likely due to the excitation of other modes than DW1 (1, 1) mode by ozone heating. Classical tidal theory and observations have shown that most of these modes are confined to excitation region and consequently, do not propagate far into the mesosphere region.

Smaller differences between the latitudinal symmetry of the observed and HME-fit amplitude structures are also observed. While the HME amplitude structure is mainly symmetric about the equator, the observed DW1 amplitude structure exhibits more asymmetry with primary and secondary peaks that are skewed towards the northern hemisphere. This result implies generated HMEs do not sufficiently capture the manifestation of higher order DW1 Hough Modes that are seen in the observations. Finally, the magnitude of the observed and HME-fit DW1 amplitudes differ by several degrees K, which further indicate that there are differences between the HME and observed DW1 structure. These differences between the observations and HMEs are significant because they suggest that the full DW1 amplitude and phase structure in the temperature and horizontal wind fields are not captured by the HME technique. Hence, the nonlinear forcing produced from these DW1 estimates may not be accurate.

Another possible option for deriving short-term DW1 estimates is a recently developed method by Ortland et al., 2016 [74]. In this method, generalized Hough modes are fitted to one day of SABER temperatures and superimposed to produce daily DW1 estimates. Generalized Hough modes for DW1 are computed by first projecting heating from the Modern-Era Retrospective Analysis For Research for Applications (MERRA) reanalysis model onto classical Hough modes. Each classical Hough mode heating projection is used to force a linearized primitive equation model with specified monthly climatology winds and realistic dissipation. The tabulation of amplitudes and phases representing the model response to an individual Hough mode heating profile represents a generalized Hough mode, which is analogous to a HME..

As detailed by Ortland et al. [74], the first four propagating and two evanescent generalized hough modes are fit to SABER raw temperature observations in order to acquire daily DW1

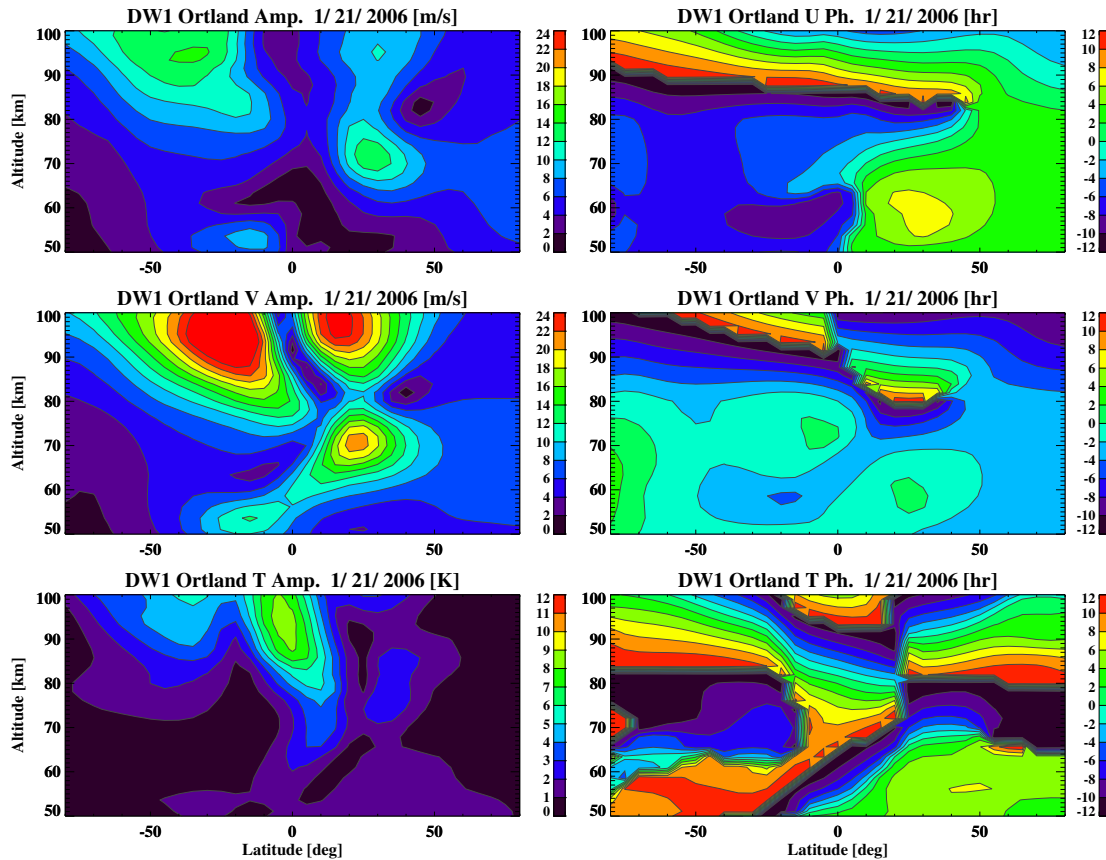


Figure 5.9: Amplitude of the Hough Mode Extension for the DW1 (1, 1) mode in the temperature (top), zonal wind (middle) and meridional wind (bottom) fields for atmosphere with zonal winds derived from MLS observations in late-January 2011.

estimates. Because the relationships between temperature and horizontal wind are self-consistent for each generalized Hough mode, this procedure allows for the daily estimation of DW1 horizontal winds as well as temperature. The daily estimates for the DW1 are then vector averaged over a 12 day window. As shown in Figure 5.9, this method produces a DW1 amplitude structure that is dominated by a (1, 1) Hough mode as expected. The Ortland generalized Hough mode technique also produces DW1 amplitude estimates that more closely resemble the MLS-SABER observed DW1 than the HME method. The Ortland method captures more higher-order features and latitudinal asymmetry than the HME method that are also present in the MLS-SABER DW1 estimates. This is expected because more Hough modes are used in the fitting process, which results

in a more accurate representation of the DW1.

### 5.2.2 Chosen Method: NOGAPS-ALPHA

However, due to the limitations of the aforementioned techniques, NOGAPS-ALPHA reanalysis output is chosen to produce primary wave estimates for the dissertation. The main advantage of using NOGAPS-ALPHA is that it provides atmospheric field variables on a regular, global, hourly grid up to approximately 95 km. High temporal and spatial resolution output allows for simple and accurate extraction of planetary waves and tidal spectra over short temporal windows. Although the model relies on some physical assumptions about the atmosphere, it also assimilates observational data from both the TIMED-SABER and Aura-MLS satellite instruments. Hence, it is expected that the model captures the majority of the wave dynamics occurring in the real atmosphere. This hypothesis is supported by the results presented in this section.

To extract 2dayW3 and DW1 amplitude and phase in temperature and horizontal wind from NOGAPS-ALPHA, a sliding 6-day length window is employed to compute the two-dimensional Fourier transform in time and longitude at each altitude and latitude location. The plots contained in Figure 5.10 show that the largest 2dayW3 amplitudes during January 2006 are observed in the upper mesosphere at around 40°S. Past studies have shown that the 2dayW3 is likely a manifestation of a resonant mode of the atmosphere (Salby, 1981 [95]; Hagan et al., 1993 [27]; Randel, 1994 [89]). During post-solstice periods, large westward zonal jets in the summer mesosphere create baroclinically unstable regions that serve as amplification sources for the 2dayW3. The results show that the 2dayW3 increases in early January 2006, peaks around January 21st, and then decreases afterward. The rapid decrease in the 2dayW3 amplitude during late January is well-known and has been analyzed in numerous studies (Wu et al., 1996 [115]; Limpasuvan and Wu, 2003 [51]; Tunbridge et al., 2011 [110]). The current understanding is that 2dayW3 imparts large westward momentum forcing onto the mean background (Lieberman et al., 1999 [46]), which subsequently shifts the mean zonal flow more westward and shuts off the wave growth rate (Palo et al., 1999 [77]; Chang et al., 2011 [7]).

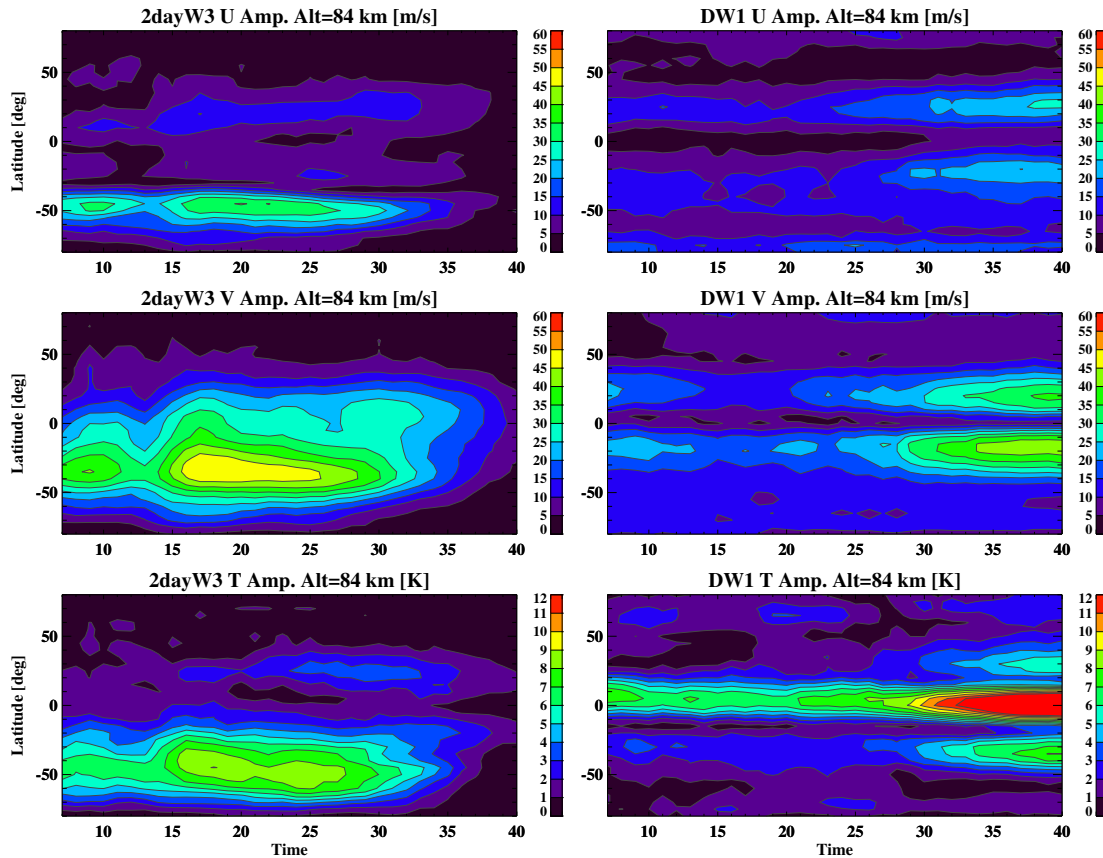


Figure 5.10: Amplitude of the 2dayW3 and DW1 as a function of time and latitude at 84 km during 2006. Estimates for the zonal wind field are shown on top, meridional wind in the middle and temperature on the bottom.

The plots on the right side of Figure 5.10 illustrate the temporal-latitude amplitude structure for DW1 in temperature and horizontal wind for early 2006 at 86 km, which is near the peak vertical location of 2dayW3. The DW1 amplitude structure obtained from NOGAPS-ALPHA is dominated by the first propagating Hough mode with a primary peak at the equator and two secondary peaks around  $\pm 30^\circ$  latitude in the temperature field. The prominence of the first propagating mode is well known and anticipated due to its associated long vertical wavelength. The DW1 amplitude also exhibits an anti-correlation with the 2dayW3 amplitude. The DW1 amplitude decreases around mid-January which is almost coincidental with the peak 2dayW3 amplitude. The decrease in the DW1 amplitude during a 2dayW3 event was evaluated most recently by Chang et

al., 2011 [7]. Using a generalized circulation model (NCAR TIME-GCM), Chang et al., 2011 [7] found that the decrease in the DW1 amplitude during a 2dayW3 event is mainly caused by 2dayW3 induced changes in the mean zonal background flow. The fact that this feature is captured in the NOGAPS-ALPHA model further supports the claim that the DW1 estimates presented here are suitable to evaluate the nonlinear forcing of secondary waves.

Figure 5.11 depicts the vertical-latitudinal amplitude structures of the 2dayW3 and DW1 for a 6-day window centered around January 21st, 2006, which is near the peak of the 2dayW3. The results show amplification of the 2dayW3 starting around 50-60 km and increasing amplitudes with altitude until 90 km where dissipation forces begin to dampen the wave. The largest 2dayW3 amplitudes are observed in the Southern Hemisphere although there is some 2dayW3 activity near the equator in the lower mesosphere and at Northern Hemisphere latitudes in the upper mesosphere. While the largest 2dayW3 amplitude values are concentrated in the Southern Hemisphere, the DW1 amplitude structure is symmetric about the equator. Like the 2dayW3, the DW1 amplitude increases with height until dissipation dominates in the lower thermosphere region. From Figure 5.11, it is concluded that the majority of the 2dayW3 response lies below 100 km and thus, captured by the NOGAPS-ALPHA model. Although residual 2dayW3 amplitude lying above the NOGAPS-ALPHA boundary contributes to the nonlinear forcing, the results from the linear model experiments presented later conclude that this region does not play an important role in the overall secondary wave response. Hence, solely utilizing NOGAPS-ALPHA to compute the nonlinear forcing is suitable for the dissertation goals.

The vertical-latitudinal phase structures of the 2dayW3 and DW1 are shown in Figure 5.12. The 2dayW3 phase structure exhibits downward progression in the horizontal wind and temperature fields throughout the mesosphere, which implies that the wave source originates from lower atmospheric regions. The vertical wavelength of the 2dayW3 in the upper mesosphere is approximately 50 km, while the vertical wavelength in the zonal and meridional wind fields appear to be slightly longer. Like the 2dayW3, DW1 also exhibits downward phase progression with altitude, which is consistent with the fact that DW1 is mainly generated from tropospheric and stratospheric

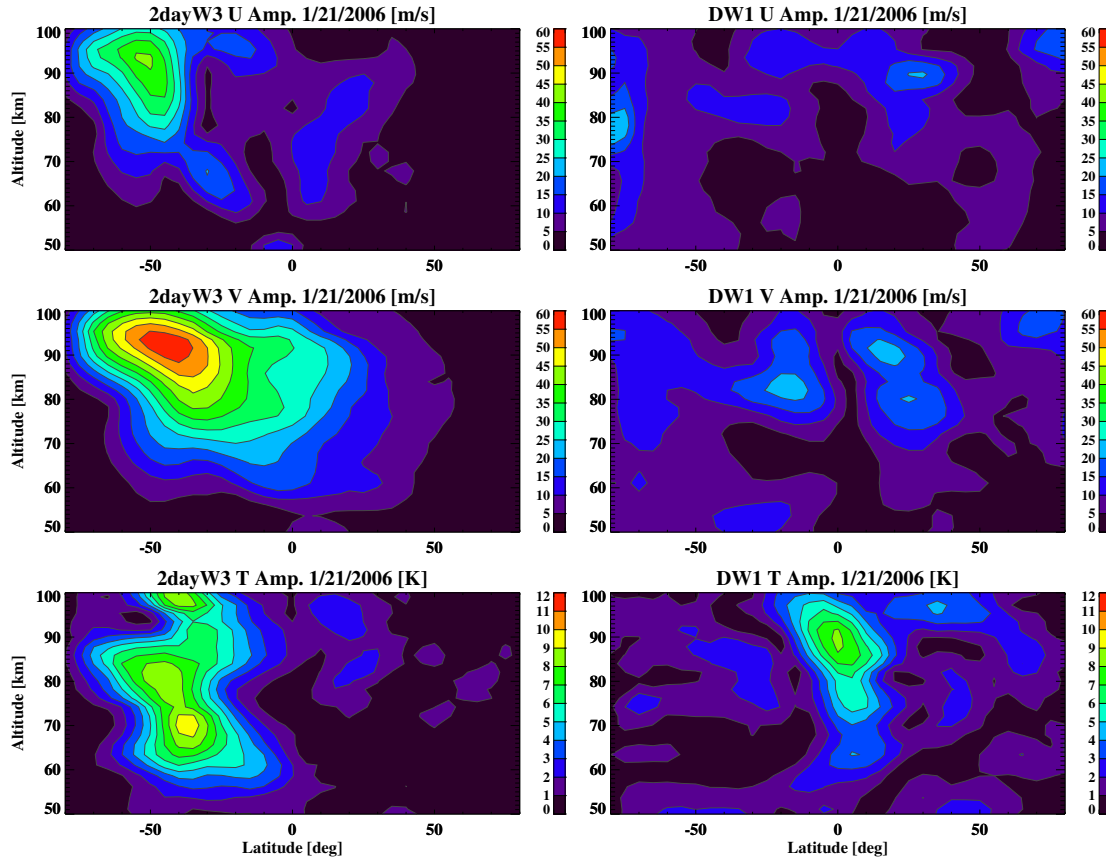


Figure 5.11: Amplitude of the 2dayW3 and DW1 as a function of latitude and altitude during 2006. Estimates for the zonal wind field are shown on top, meridional wind in the middle and temperature on the bottom.

heating sources. The phase structure is mainly latitudinally asymmetric in the meridional wind field and latitudinally symmetric in the zonal wind and temperature fields. This result, along with the observed vertical wavelength of approximately 25 km, again highlights the dominance of the (1, 1) Hough mode in the overall DW1 structure. Slight differences are observed between the vertical wavelength in each hemisphere. The results reveal that the DW1 vertical wavelength in the temperature and horizontal wind fields in the Northern Hemisphere is generally shorter than the vertical wavelength in the opposite hemisphere. This feature is mainly a result of the background wind structure during this time period. The eastward background zonal winds in the southern hemisphere result in an elongation of the DW1 vertical wavelength while the westward background

zonal winds in the northern hemisphere result in shorter DW1 vertical wavelengths (Forbes and Hagan, 1988 [16]).

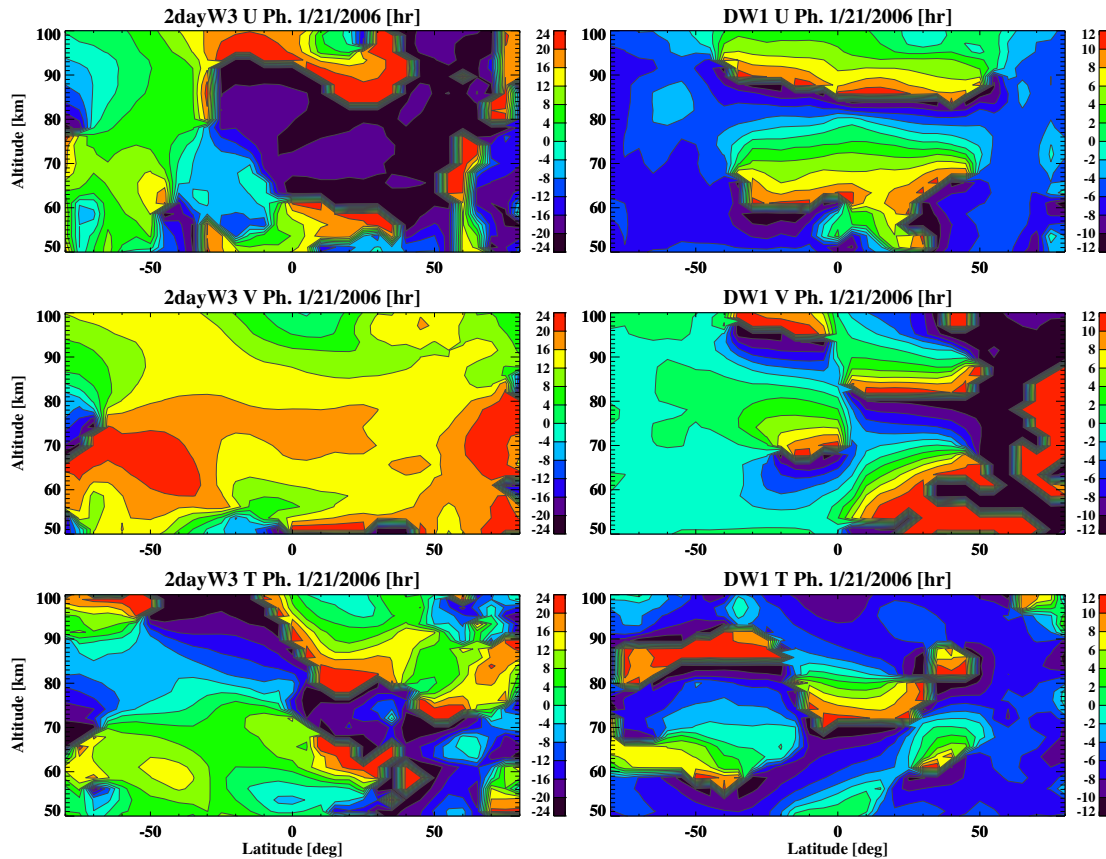


Figure 5.12: Phase of the 2dayW3 and DW1 as a function of latitude and altitude during 2006. Estimates for the zonal wind field are shown on top, meridional wind in the middle and temperature on the bottom.

NOGAPS-ALPHA estimates for the 2dayW3 and DW1 during January 2009 and 2010 are also produced to present a variety of 2dayW3-DW1 interaction cases. Similar to the 2dayW3 in 2006, the 2dayW3 in 2009 (Figure 5.13) increases throughout the early portion of January, reaches a peak at around January 20-25 and then quickly dissipates afterward. However, the 2dayW3 amplitude is much smaller, attaining peak values that were only half of the largest values observed during 2006. A moderate 2dayW3 event is observed in 2010 (Figure 5.13), which is characterized by peak 2dayW3 amplitude values that lie in between the values observed during 2006 and 2009.

The most striking difference about this event is that the 2dayW3 peaks around February 1st, which is approximately a week later than the 2dayW3 peak day for 2006 and 2009.

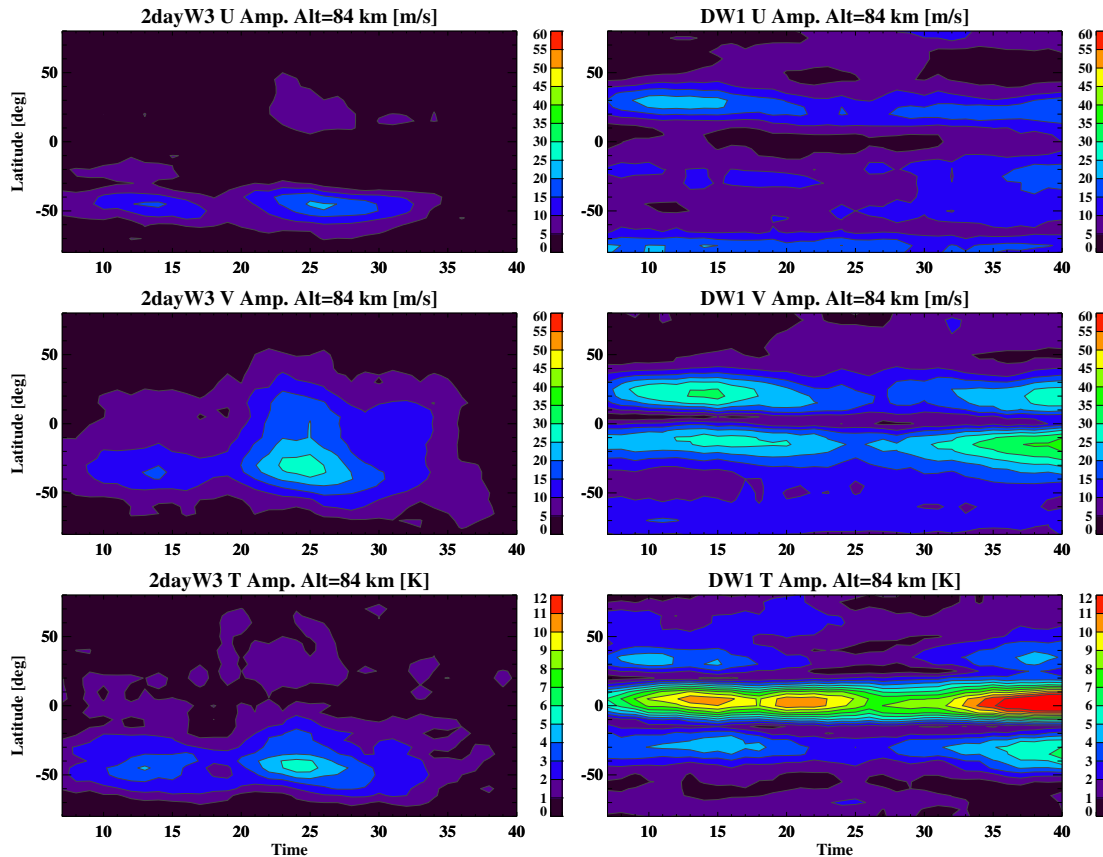


Figure 5.13: Amplitude of the 2dayW3 and DW1 as a function of time and latitude at 84 km during 2009. Estimates for the zonal wind field are shown on top, meridional wind in the middle and temperature on the bottom.

The results contained in Figure 5.13 and Figure 5.14 also serve to demonstrate that the DW1 exhibits significant interannual variability. In 2006 and 2009, the DW1 mainly increases throughout the month with the exception of the time period around the peak 2dayW3 day. In contrast, the DW1 in 2010 did not exhibit an increasing trend and did not show a remarkable decrease in amplitude during the peak 2dayW3 time period. Furthermore, the DW1 amplitude on a given day in January displayed year-to-year differences of about 5 K in temperature or 15 m/s in meridional wind.

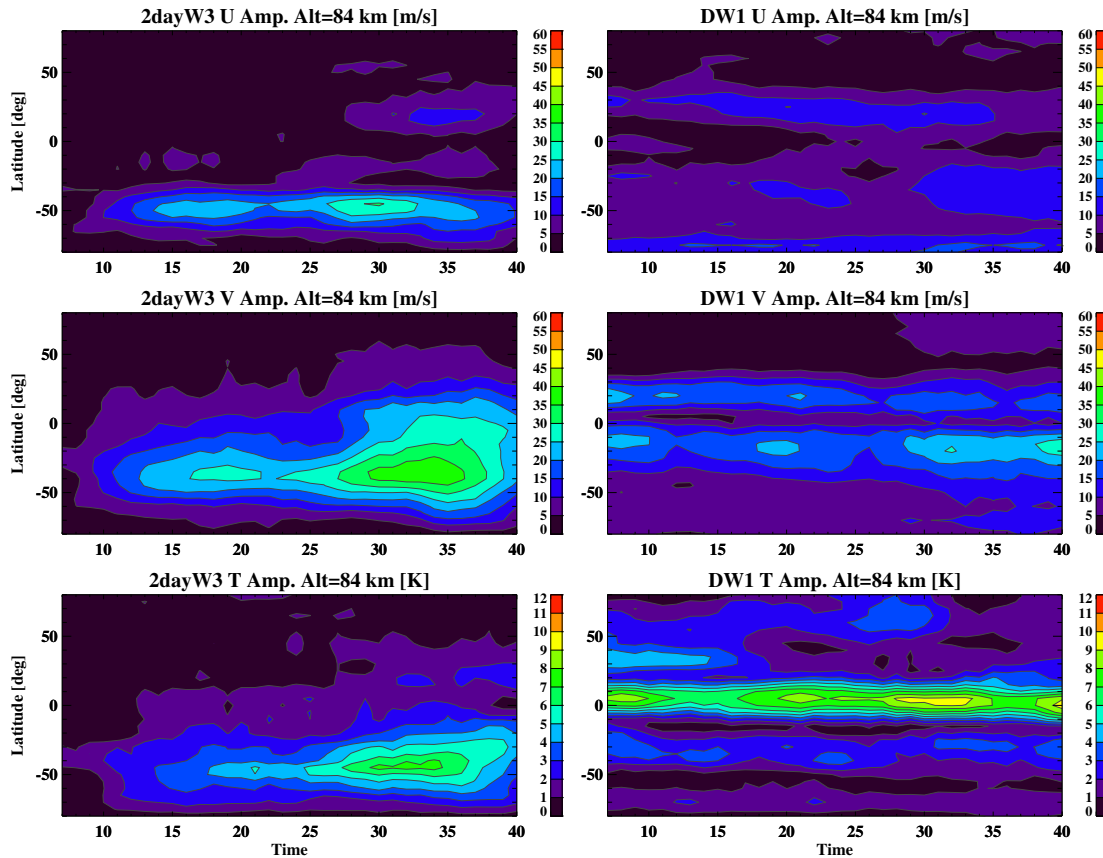


Figure 5.14: Amplitude of the 2dayW3 and DW1 as a function of time and latitude at 84 km during 2010. Estimates for the zonal wind field are shown on top, meridional wind in the middle and temperature on the bottom.

Finally, it is worth noting that the NOGAPS-ALPHA primary wave estimates displayed in this section compare favorably to the wave estimates obtained directly from observations. For example, the 2dayW3 extracted from TIMED-SABER (Chapter 4) show a similar temperature structure as the NOGAPS-ALPHA 2dayW3 shown here. The general agreement between the NOGAPS-ALPHA results and direct observations provide support that the NOGAPS-ALPHA is replicating the dynamics of the real atmosphere to an accurate degree. The model's agreement with observations along with its advantages of providing global data with high spatial and temporal resolution serve to validate the choice to use NOGAPS-ALPHA to determine primary wave values for the nonlinear forcing computation.

### 5.3 Nonlinear Forcing Results

NOGAPS-ALPHA estimates of the 2dayW3 and DW1 in the temperature and horizontal wind fields are utilized to compute the nonlinear forcing of each secondary wave generated through the interaction. The zonal, meridional and thermal forcing for the 16hrW4 and 2dayE2 secondary waves for a 6-day period centered around January 21st, 2006 are displayed in Figure 5.15. The results show that the largest nonlinear forcing amplitudes are represented at higher altitudes where the products of the primary wave amplitudes are the generally largest. Additionally, the largest nonlinear amplitude values are skewed towards southern latitudes, which is anticipated given the larger 2dayW3 amplitude observed in the southern hemisphere. The nonlinear forcing amplitude for both secondary waves is negligible below 50 km because the 2dayW3 does not undergo significant amplification until it is above the stratopause. At the altitudes above 90 km, the nonlinear forcing decreases due to increasing molecular and eddy diffusion which serve to decrease the primary wave amplitudes. It should also be noted that the nonlinear forcing is a vector product, which means that the relative phases of the contributing fields has an impact on the nonlinear forcing amplitude and phase structure.

Differences between the forcing for each secondary wave are also detected in Figure 5.15. While the meridional and thermal forcing amplitudes of both secondary waves are significant at low latitudes, the forcing amplitude of the 2dayE2 is more spread in latitude and attains significant values at higher latitudes. These differences are dictated by the phase relationships between the primary waves in temperature and horizontal wind. In most locations, the 16hrW4 nonlinear forcing is largest where the 2dayE2 nonlinear forcing is smallest and vice versa. Overall, however, the peak magnitude of the forcing for each secondary wave are quite similar.

The phase of the nonlinear forcing displays a clear vertical structure as depicted in Figure 5.16. The observed vertical wavelength of each nonlinear forcing can be predicted by assuming a constant vertical wavelength for each primary wave. As the previous primary wave results demonstrated, this is a valid assumption with the 2dayW3 exhibiting a vertical wavelength of about 50-60 km

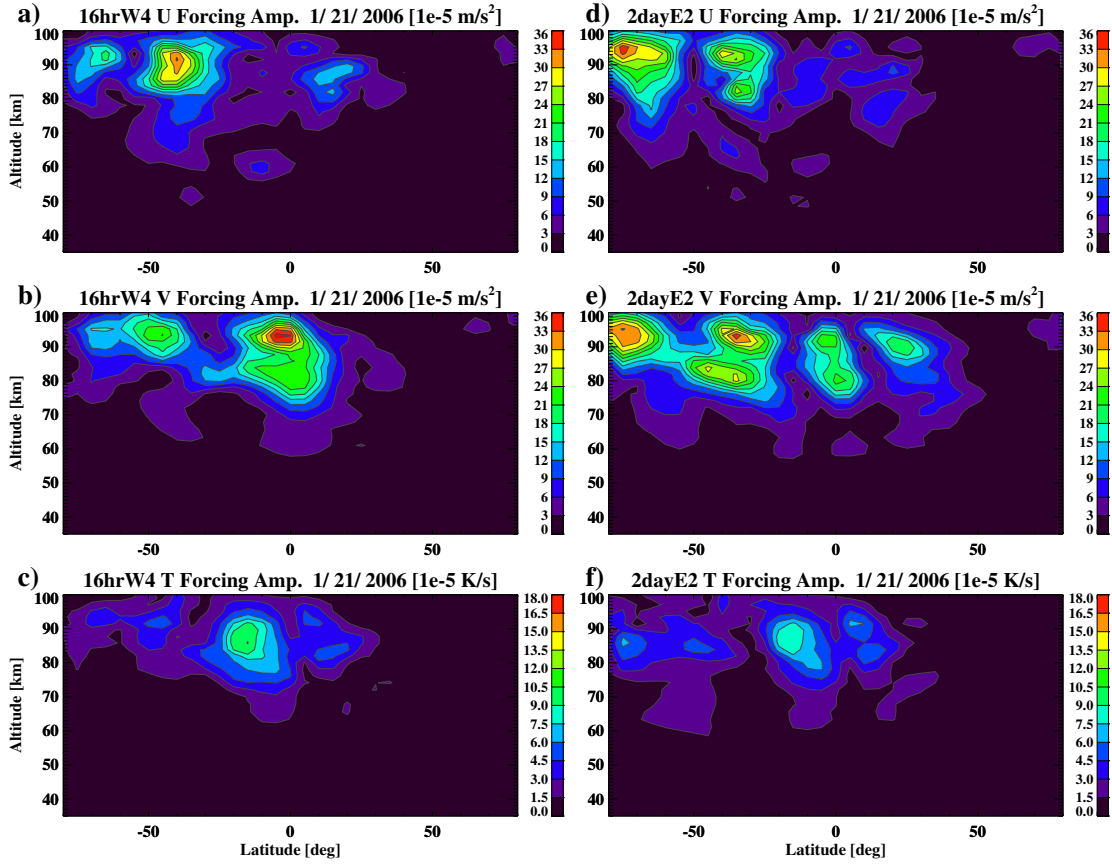


Figure 5.15: Vertical-latitude amplitude structure centered at January 21, 2006 for a) 16hrW4 zonal momentum forcing, b) 16hrW4 meridional momentum forcing, c) 16hrW4 thermal forcing, d) 2dayE2 zonal momentum forcing, e) 2dayE2 meridional momentum forcing, and f) 2dayE2 thermal forcing. Nonlinear forcing amplitude is derived from primary wave amplitude and phase estimates shown in section 5.2.2.

and the DW1 showing a vertical wavelength of about 25 km. By assuming a constant vertical wavelength, each primary wave can be written in terms of vertical wavenumber ( $k_z$ ) in addition to zonal wavenumber and frequency as  $\cos(s\lambda - \omega t + k_z z)$ . Multiplying primary waves in the preceding form together yields forcing that has a vertical structure dependent on the sum and difference of the primary vertical wave numbers as shown in Equation 5.10.

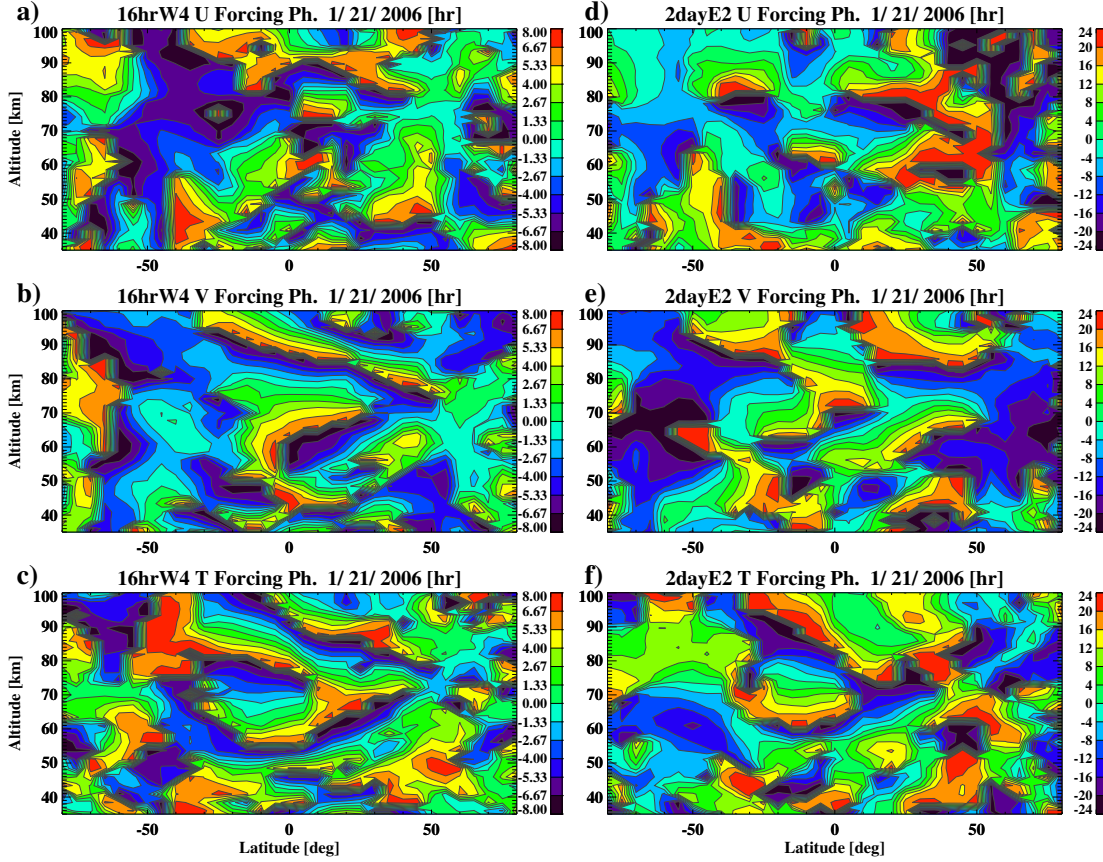


Figure 5.16: Vertical-latitude phase structure centered at January 21, 2006 for a) 16hrW4 zonal momentum forcing, b) 16hrW4 meridional momentum forcing, c) 16hrW4 thermal forcing, d) 2dayE2 zonal momentum forcing, e) 2dayE2 meridional momentum forcing, and f) 2dayE2 thermal forcing. Nonlinear forcing phase is derived from primary wave amplitude and phase estimates shown in section 5.2.2.

$$\begin{aligned}
 \cos(s_1\lambda - \omega_1 t + k_1 z) \cos(s_2\lambda - \omega_2 t + k_2 z) &= \frac{1}{2} \cos[(s_1 + s_2)\lambda - (\omega_1 + \omega_2)t + (k_1 + k_2)z] \\
 &+ \frac{1}{2} \cos[(s_1 - s_2)\lambda - (\omega_1 - \omega_2)t + (k_1 - k_2)z]
 \end{aligned}
 \tag{5.10}$$

By following the preceding equation and using the 2dayW3 and DW1 vertical wavelengths of 60 km and 25 km respectively, it is predicted that the 16hrW4 forcing has a vertical wavelength of 18 km and the 2dayE2 forcing has a vertical wavelength of 43 km. These predictions generally

approximate the vertical structure observed in the nonlinear forcing phase in temperature shown in Figure 5.16.

The nonlinear forcing produced during the peak day of the 2dayW3 event for 2009 and 2010 are shown in Figures 5.17 and 5.18 for comparison. For the 2009 case, the peak forcing amplitude is smaller than the 2006 peak forcing by about 25% in the meridional momentum field and up to 50% in the zonal momentum and thermal fields. This result is expected because the 2009 2dayW3 amplitude is about 50% smaller than the 2006 2dayW3 amplitude (section 5.2.2). Since the differences between the DW1 amplitude near the peak of the 2dayW3 during 2006 and 2009 are small, a larger 2dayW3 amplitude during 2006 should produce a stronger forcing as observed.

The nonlinear forcing produced during the 2010 interaction event (Figure 5.18) is approximately the same magnitude as the 2006 nonlinear forcing. Although the 2dayW3 during 2010 is smaller than the 2dayW3 during 2006, the DW1 is slightly larger. Unlike in the 2006 and 2009 cases, DW1 does not show a significant decrease near the peak of the 2dayW3 during 2010. Hence, the slightly larger DW1 amplitude compensates for the slightly smaller 2dayW3 to produce similar peak forcing to the 2006 interaction case.

Despite the differences in maximum forcing magnitudes, the latitudinal structure of the forcing for each wave is generally consistent throughout the years. In each case, the 16hrW4 forcing in temperature and meridional wind is mainly concentrated at low latitudes while the 2dayE2 forcing extends to higher southern latitudes. This trend is dictated by consistent dynamic behavior of the 2dayW3 and DW1 on a year-to-year basis. The 2dayW3 in each year is approximately in quasi-geostrophic balance at mid-to-high latitudes, which implies that the 2dayW3 horizontal wind vectors are generally rotational around geopotential height perturbations. As a result, the phase relationships among the 2dayW3 perturbation fields should not drastically change on a year-to-year basis as long as the 2dayW3 behaves like a quasi-geostrophic wave. Similarly, the DW1 in each year is approximated by an inertia gravity wave and also shows consistent phase relationships among the perturbation field variables. When multiplied together in the nonlinear forcing computation, these phase relationships tend to produce larger 16hrW4 nonlinear forcing at the low latitudes and

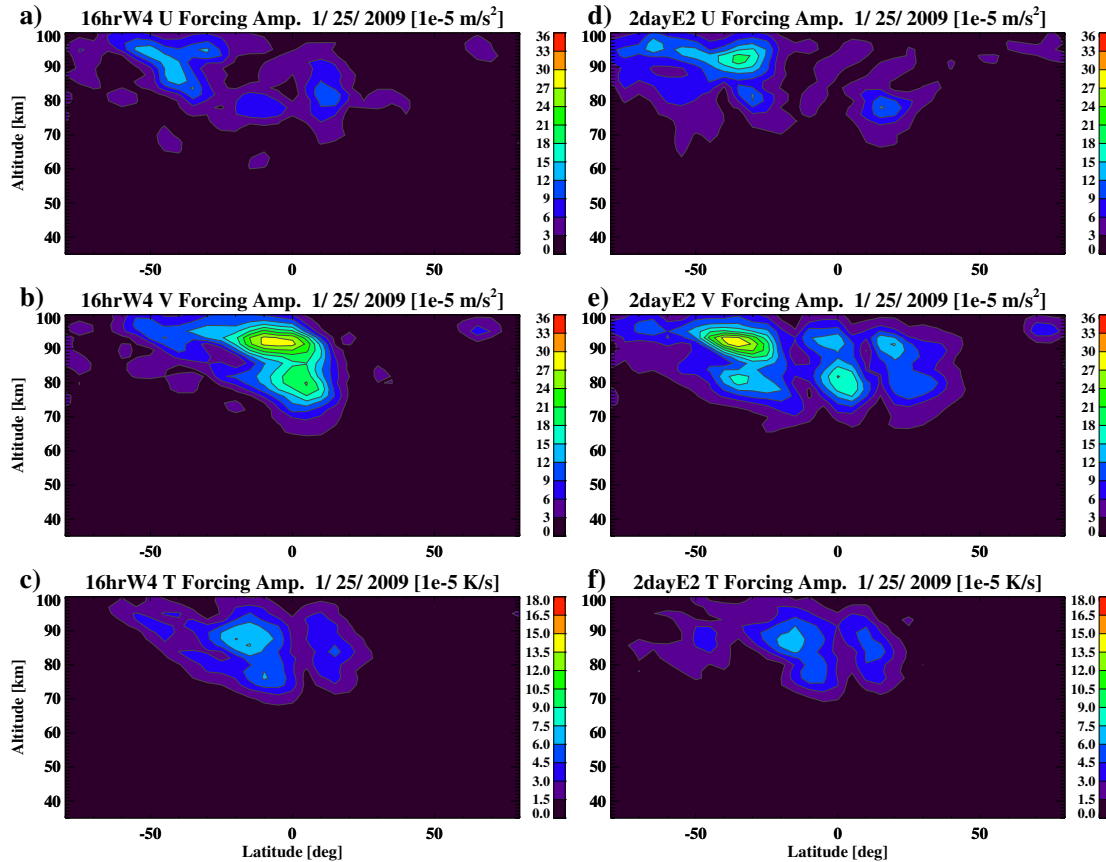


Figure 5.17: Vertical-latitude amplitude structure centered at January 25, 2009 for a) 16hrW4 zonal momentum forcing, b) 16hrW4 meridional momentum forcing, c) 16hrW4 thermal forcing, d) 2dayE2 zonal momentum forcing, e) 2dayE2 meridional momentum forcing, and f) 2dayE2 thermal forcing. Nonlinear forcing amplitude is derived from primary wave amplitude and phase estimates shown in section 5.2.2.

larger 2dayE2 at higher latitudes.

Small differences between the nonlinear forcing spatial structure are mainly driven by year-to-year variation in the primary wave amplitude spatial structure. For example, the the 2dayW3 and DW1 in 2006 extends further into the Southern Hemisphere than the other years. Consequently, larger nonlinear forcing amplitudes for both secondary waves are seen at high-Southern latitudes during 2006.

The temporal evolution of the nonlinear forcing at 70 km altitude for 2006, 2009 and 2010 are presented in Figures 5.19, 5.20 and 5.21, respectively. In all three cases, the nonlinear forcing

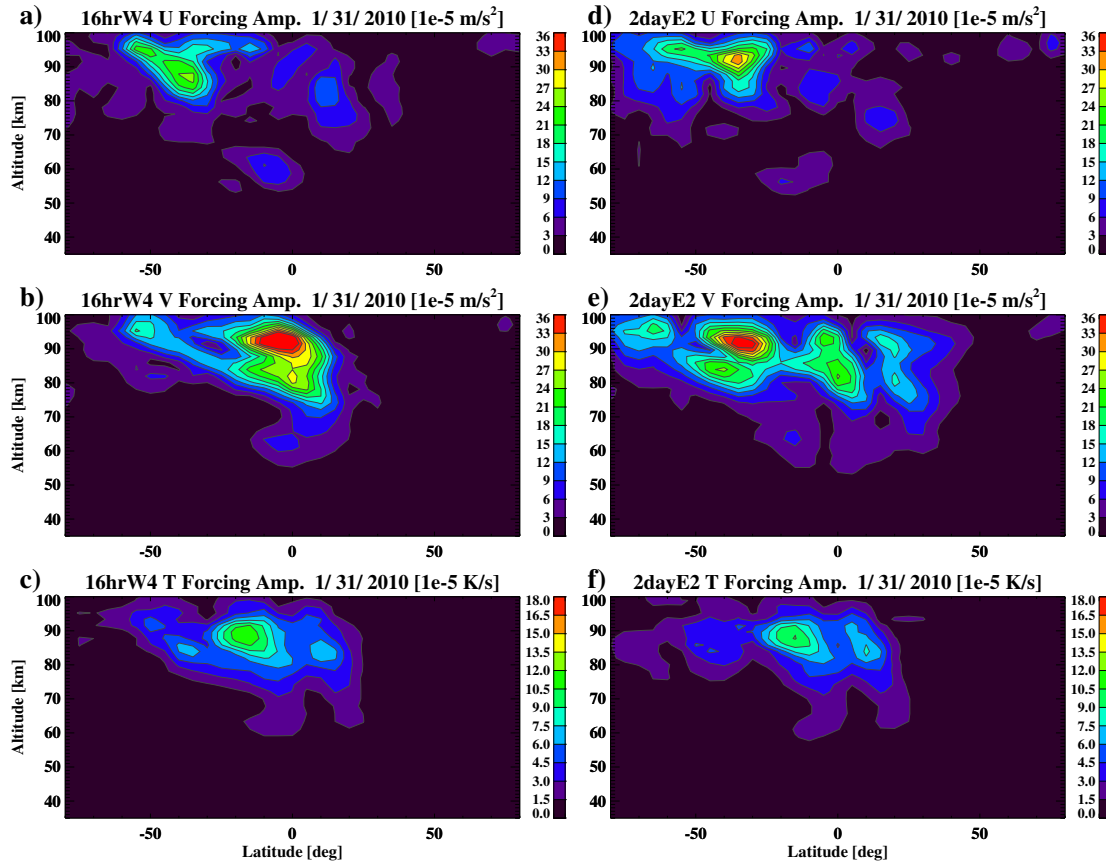


Figure 5.18: Vertical-latitude amplitude structure centered at January 30, 2010 for a) 16hrW4 zonal momentum forcing, b) 16hrW4 meridional momentum forcing, c) 16hrW4 thermal forcing, d) 2dayE2 zonal momentum forcing, e) 2dayE2 meridional momentum forcing, and f) 2dayE2 thermal forcing. Nonlinear forcing amplitude is derived from primary wave amplitude and phase estimates shown in section 5.2.2.

exhibits a strong correlation with the 2dayW3 amplitude. In 2006, the nonlinear forcing is significant for the majority of January and into early February, which mirrors the evolution of the 2dayW3. However, the peak of the nonlinear forcing for each secondary wave occurs a couple days later than the 2dayW3 peak amplitude day. Because the DW1 amplitude increases throughout the January time period, the maximum forcing values are seen closer to the end of January.

The nonlinear forcing produced during the 2009 and 2010 interaction events expectedly differ from the 2006 case. During 2009, the nonlinear forcing is only significant for a couple days, which reflects the short-lived nature of this particular 2dayW3 event. Although the nonlinear forcing

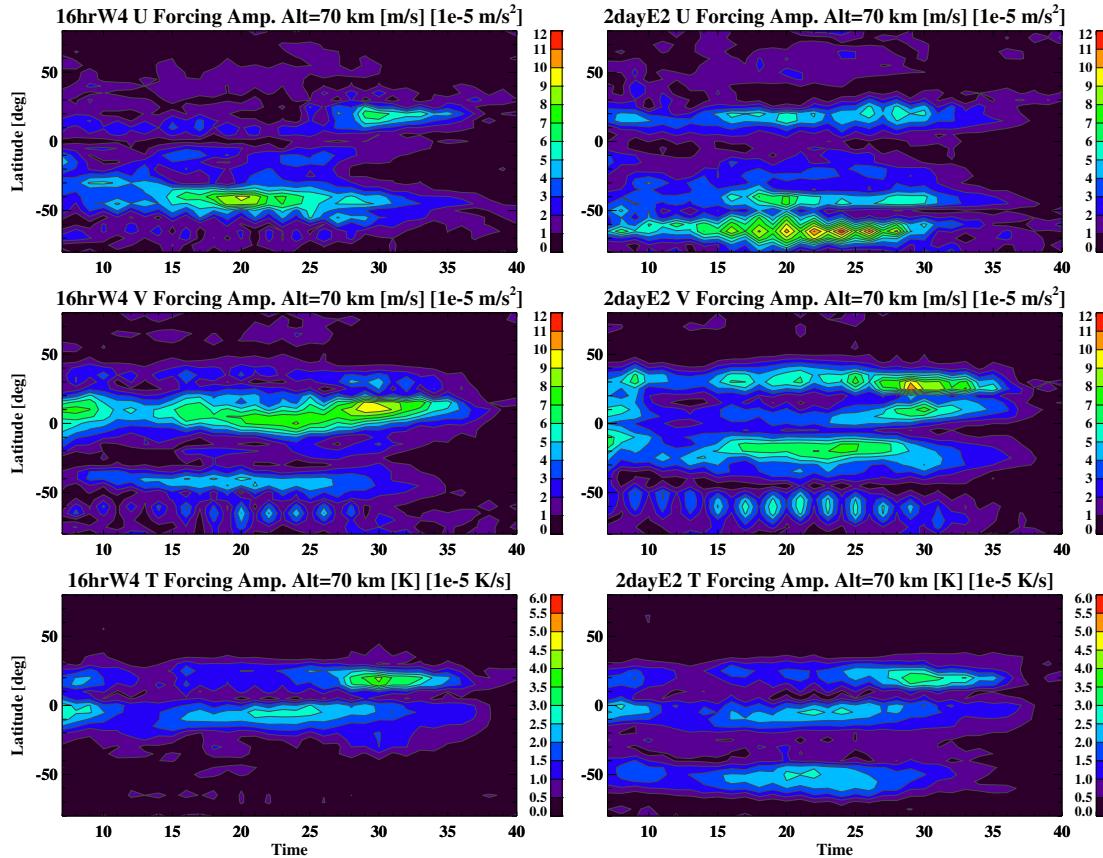


Figure 5.19: Temporal-latitude amplitude structure at 70 km during 2006 for a) 16hrW4 zonal momentum forcing, b) 16hrW4 meridional momentum forcing, c) 16hrW4 thermal forcing, d) 2dayE2 zonal momentum forcing, e) 2dayE2 meridional momentum forcing, and f) 2dayE2 thermal forcing. Nonlinear forcing amplitude is derived from primary wave amplitude and phase estimates shown in section 5.2.2.

for this case has a shorter duration than the 2006 case, the peak forcing amplitude at 70 km is similar, particularly in the meridional momentum field. Differences between the 2dayW3 and DW1 amplitudes are not as large in the lower mesosphere as in the upper mesosphere, which leads to smaller differences between the forcing at 70 km. A comparison of a similar plot at 90 km (Appendix E) reveals much larger nonlinear forcing in the 2006 case due to a greater 2dayW3 amplitude in the upper mesosphere. Similar to the 2006 and 2009 cases, the 2010 nonlinear forcing exhibits a strong correlation with the 2dayW3 amplitude. In 2010, the 2dayW3 peaks a week later than the other years, which results in nonlinear forcing peaking in early February instead of late January. The

peak amplitude of the nonlinear forcing however is comparable in magnitude to values observed during the other years.

In summary, this chapter showed how primary wave estimates in temperature and horizontal wind are used to compute the nonlinear forcing for each secondary wave. A variety of techniques were presented to show how primary wave estimates can be derived directly from observations over short time scales, which is necessary to study nonlinear wave-wave interactions. After detailed analysis, it was determined that NOGAPS-ALPHA was the best option to provide accurate primary wave estimates and nonlinear forcing for the secondary wave studies discussed in the remaining dissertation chapters. The nonlinear forcing derived from NOGAPS-ALPHA estimates of 2dayW3 and DW1 showed that the forcing is largest above 80 km and slightly skewed towards the southern hemisphere, which is expected due to the large primary waves present in these regions.

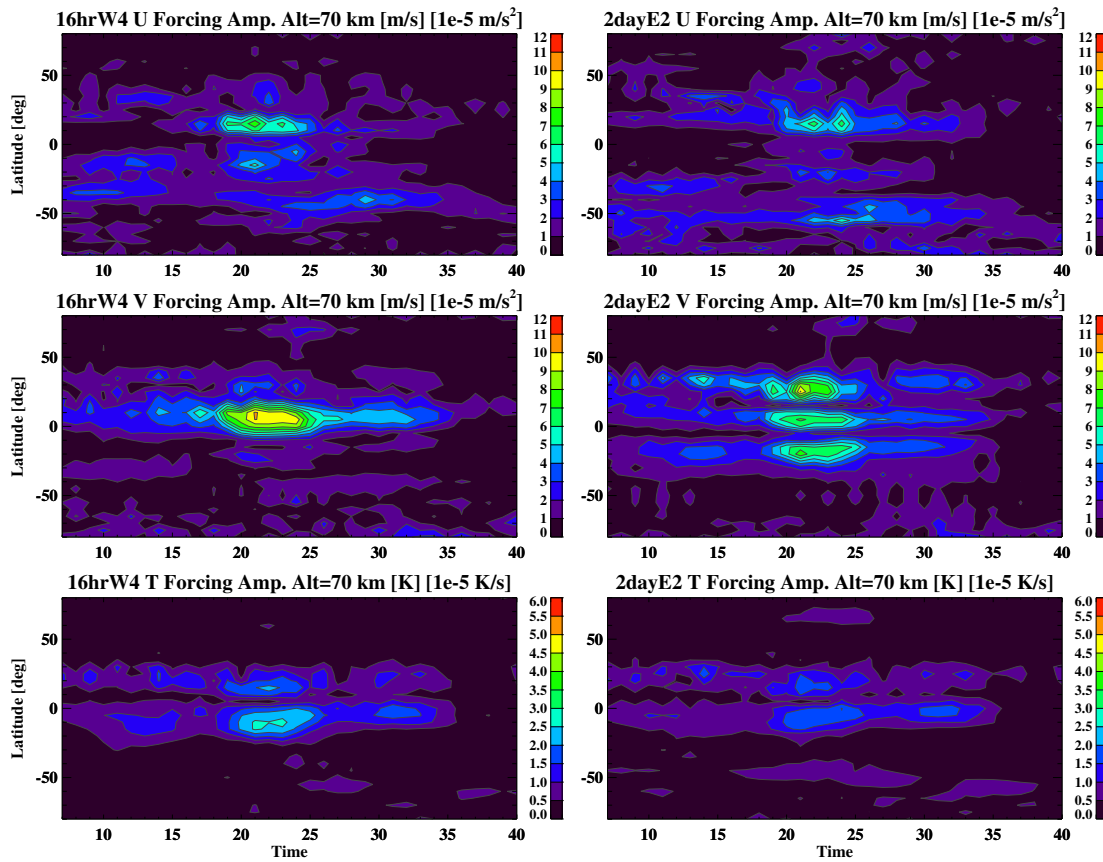


Figure 5.20: Temporal-latitude amplitude structure at 70 km during 2009 for a) 16hrW4 zonal momentum forcing, b) 16hrW4 meridional momentum forcing, c) 16hrW4 thermal forcing, d) 2dayE2 zonal momentum forcing, e) 2dayE2 meridional momentum forcing, and f) 2dayE2 thermal forcing. Nonlinear forcing amplitude is derived from primary wave amplitude and phase estimates shown in section 5.2.2.

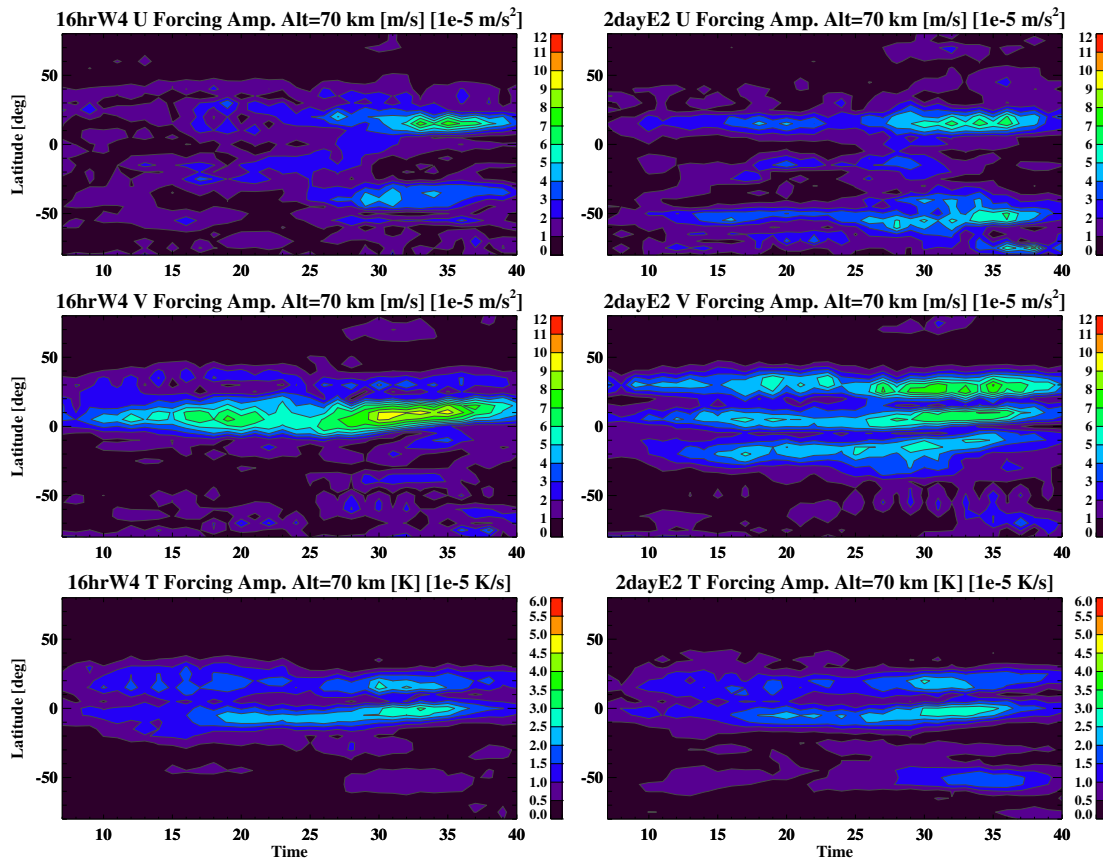


Figure 5.21: Temporal-latitude amplitude structure at 70 km during 2010 for a) 16hrW4 zonal momentum forcing, b) 16hrW4 meridional momentum forcing, c) 16hrW4 thermal forcing, d) 2dayE2 zonal momentum forcing, e) 2dayE2 meridional momentum forcing, and f) 2dayE2 thermal forcing. Nonlinear forcing amplitude is derived from primary wave amplitude and phase estimates shown in section 5.2.2.

## Chapter 6

### SECONDARY WAVE RESPONSES

In this chapter, 2dayW3-DW1 secondary wave responses to the nonlinear momentum and thermal forcing are presented and analyzed. As outlined in Chapter 3, the secondary wave responses are computed by introducing the derived nonlinear quantities as forcing inputs to the governing momentum and thermal perturbation equations. Solutions to these equations, which represent the secondary wave responses, are computed within a linearized model based on the Global Scale Wave Model (GSWM). The first portion of this chapter focuses on the case where the background zonal wind and temperature gradients are set to zero and only parameterized dissipation values are utilized. By analyzing secondary wave responses under this background model atmosphere configuration, the direct relationship between the nonlinear forcing and secondary wave response can be more easily disentangled. The latter portion of the chapter contains results for the case where realistic background winds and temperature gradients are added to the linearized tidal model, which allows for direct comparison with NOGAPS-ALPHA secondary wave results.

#### 6.1 Secondary Wave Response in Zero-Wind Background

In order to compute the responses for the 16hrW4 and 2dayE2 secondary waves, the GSWM source code is modified to accommodate thermal and momentum source terms other than the tidal heating terms nominally used in the model. Like the tidal heating term, the computed nonlinear thermal and momentum terms are placed on the right hand side of the linearized perturbation equations (Equation 2.8, 2.9, 2.12) and act as forcing terms. Each model run is initiated by

specifying the desired secondary wave periodicity and wavenumber, the wave forcing, and the background atmosphere configuration described by the zonal wind, temperature and dissipation. For the model results encompassed within this section, the following conditions are imposed:

- (1) Background zonal winds are set to zero.
- (2) Background temperatures are set to January climatological values at the equator. These values are obtained from the MSISE-90 model.
- (3) Eddy diffusion coefficients are set to January climatological values specified by Garcia and Solomon, 1985 [21].
- (4) Secondary wave forcing is computed from 6-day averaged DW1 and 2dayW3 NOGAPS-ALPHA results centered around the peak day of the 2dayW3 amplitude.

After specifying these conditions, the model numerically solves for the amplitude and phase of the desired secondary wave on a 3 degree resolution latitude grid and 4 km resolution altitude grid spanning from the surface to 400 km.

Figure 6.1 presents results for the 16hrW4 and 2dayE2 amplitude responses using the NOGAPS-ALPHA nonlinear momentum and thermal forcing centered around January 21st, 2006. The results reveal that the amplitudes for both waves increase with altitude throughout the mesosphere and achieve maximum amplitudes in the MLT region between 95 km and 120 km. Above this range, molecular dissipation dominates and acts to damp the wave amplitudes. A comparison of the secondary wave amplitude structure to the primary wave amplitudes and nonlinear forcing displayed in Figures 5.11 and 5.15, respectively, shows that the largest secondary amplitudes are not coincident with the regions of largest primary wave or nonlinear forcing amplitude. The analyses presented throughout the rest of this dissertation provide an explanation for this structure.

Results displayed in Figure 6.1 also reveal unexpected major differences between the amplitude structures for each secondary wave. While the 16hrW4 achieves maximum amplitudes of about 18 K in temperature and 18 m/s in the horizontal wind fields, the maximum 2dayE2 amplitudes

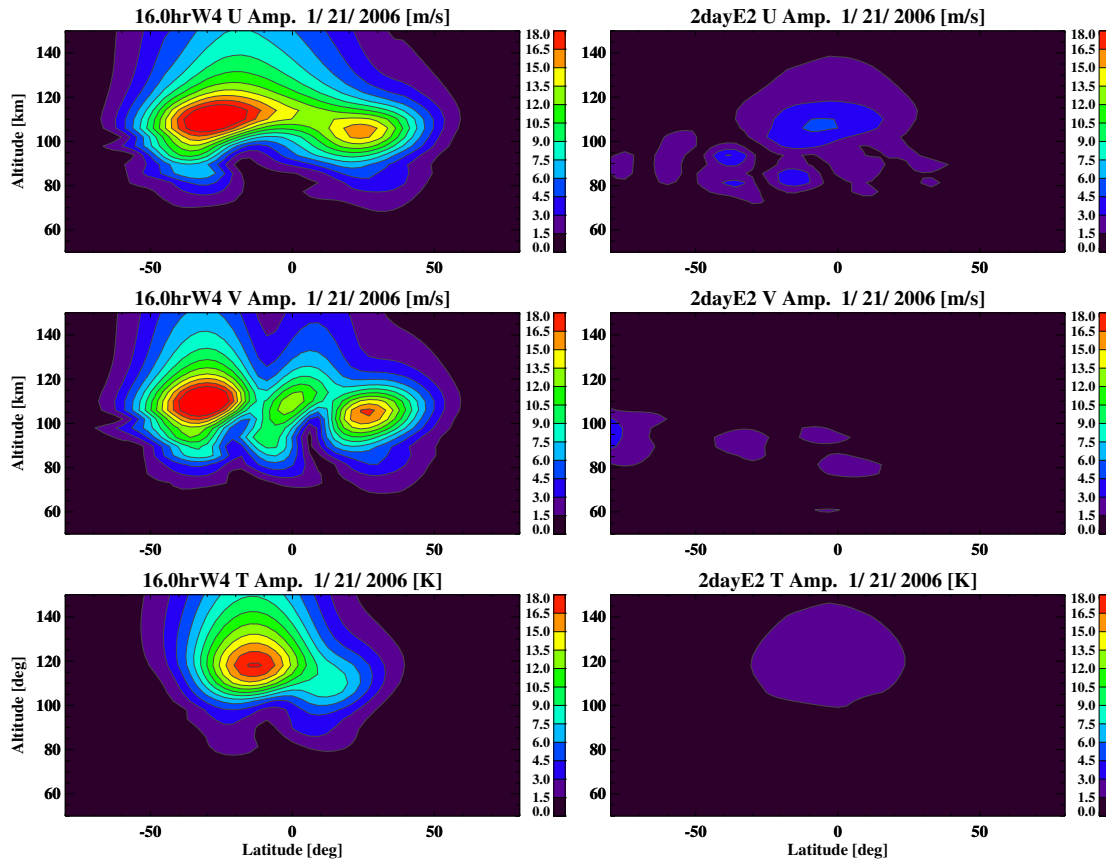


Figure 6.1: Vertical-latitude amplitude structure computed from the linear tidal model centered on January 21st, 2006 for the 16hrW4 zonal wind (upper-left), 16hrW4 meridional wind (middle-left), 16hrW4 temperature (lower-left), 2dayE2 zonal wind (upper-right), 2dayE2 meridional wind (middle-right), and 2dayE2 temperature (lower-right). Nonlinear forcing presented in Chapter 5 are used to force the linear tidal model and compute secondary wave responses.

are much smaller, attaining amplitudes of only about 3-4 K. The altitude of maximum 16hrW4 amplitude is also located slightly higher than the corresponding value for the 2dayE2. Furthermore, moderate 16hrW4 amplitudes are observed throughout the thermosphere to about 200 km whereas the 2dayE2 amplitudes are insignificant above the MLT region.

Secondary wave responses to the nonlinear forcing centered upon January 25, 2009 and January 31, 2010 are displayed in Figures 6.2 and 6.3, respectively, for a multi-year comparison. The aforementioned dates correspond to the peak day of the 2dayW3 amplitude during each year. These results indicate that the magnitude of the secondary wave amplitude significantly varies on

a inter-annual basis. In 2009, maximum 16hrW4 amplitudes of about 12 m/s in the horizontal wind fields and maximum 2dayE2 amplitudes of about 5 m/s in the zonal wind field are observed. Compared to the 2006 response, the 2009 16hrW4 amplitude is about 33% smaller and the 2009 2dayE2 is approximately equal in amplitude. The maximum 2010 16hrW4 amplitudes lie in between the 2006 and 2009 peak values whereas the maximum 2010 2dayE2 amplitude is similar to the values observed during the other years.

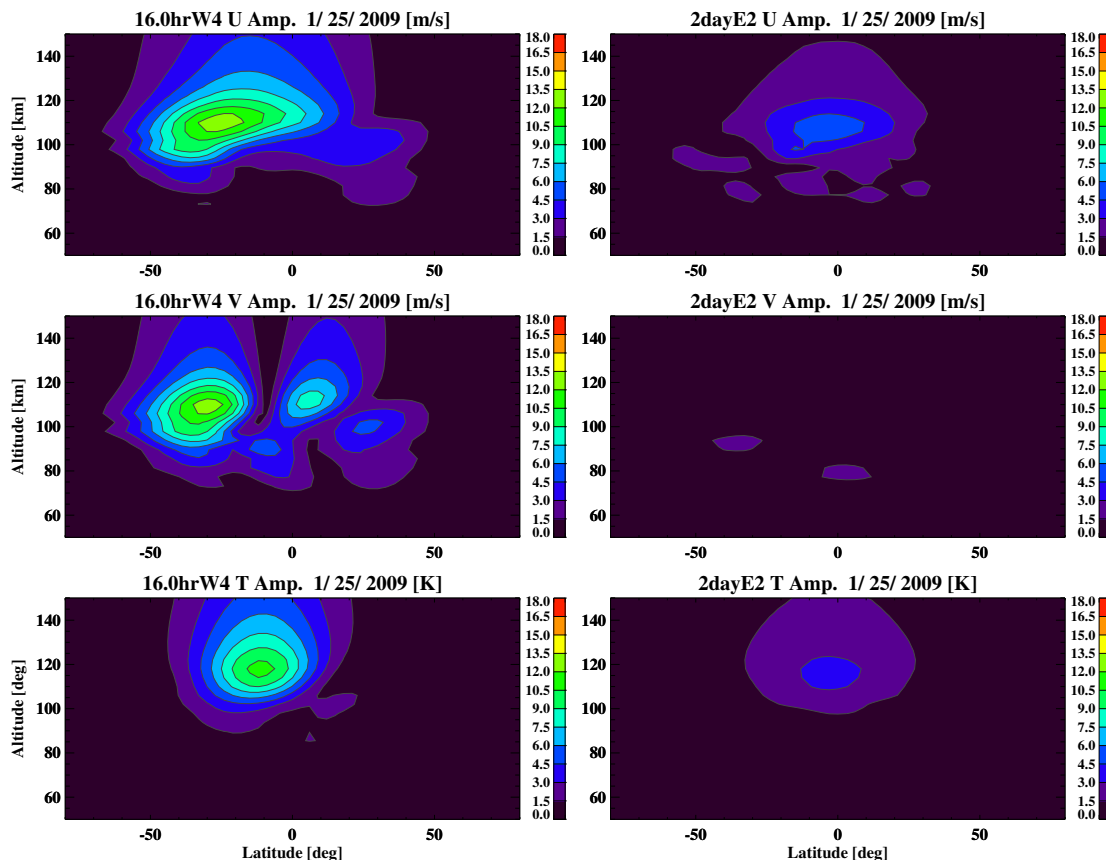


Figure 6.2: Vertical-latitude amplitude structure computed from the linear tidal model centered on January 25th, 2009 for the 16hrW4 zonal wind (upper-left), 16hrW4 meridional wind (middle-left), 16hrW4 temperature (lower-left), 2dayE2 zonal wind (upper-right), 2dayE2 meridional wind (middle-right), and 2dayE2 temperature (lower-right). Nonlinear forcing quantities presented in Chapter 5 are used to force the linear tidal model and compute secondary wave responses.

Additionally, the latitudinal structures of each secondary wave response exhibit inter-annual similarities and disparities. The 16hrW4 response during all three years is concentrated between

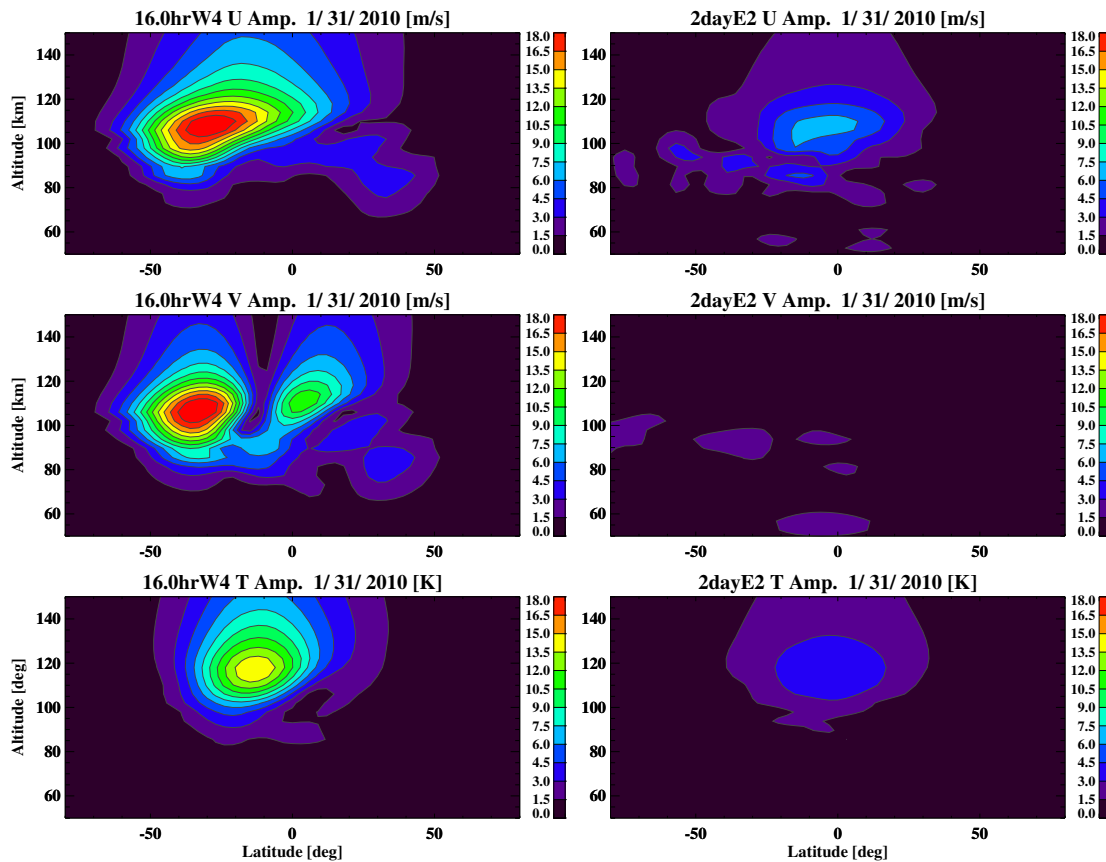


Figure 6.3: Vertical-latitude amplitude structure computed from the linear tidal model centered on January 31st, 2010 for the 16hrW4 zonal wind (upper-left), 16hrW4 meridional wind (middle-left), 16hrW4 temperature (lower-left), 2dayE2 zonal wind (upper-right), 2dayE2 meridional wind (middle-right), and 2dayE2 temperature (lower-right). Nonlinear forcing quantities presented in Chapter 5 are used to force the linear tidal model and compute secondary wave responses.

-50S and 50N in the horizontal wind and temperature fields. Below 100 km, the 16hrW4 amplitude possesses a higher order structure, where order is defined here as the number of amplitude maxima along the latitudinal axis. At higher altitudes, the 16hrW4 amplitude structure transitions to a lower order structure that is predominantly latitudinally symmetric. The most glaring difference among the 16hrW4 responses is the prominence of the 16hrW4 wind at northern latitudes during 2006 and the lack of response within this region during the other years. Similarly, the 2dayE2 responses below 100 km exhibit a high order latitudinal structure, particularly in the Southern Hemisphere. However, the higher order structure below 100 km is more noticeable in the 2006 and

2010 2dayE2 responses than in the 2009 response. Like the 16hrW4 response, the 2dayE2 in all years transitions to a low-order, symmetric structure at higher altitudes.

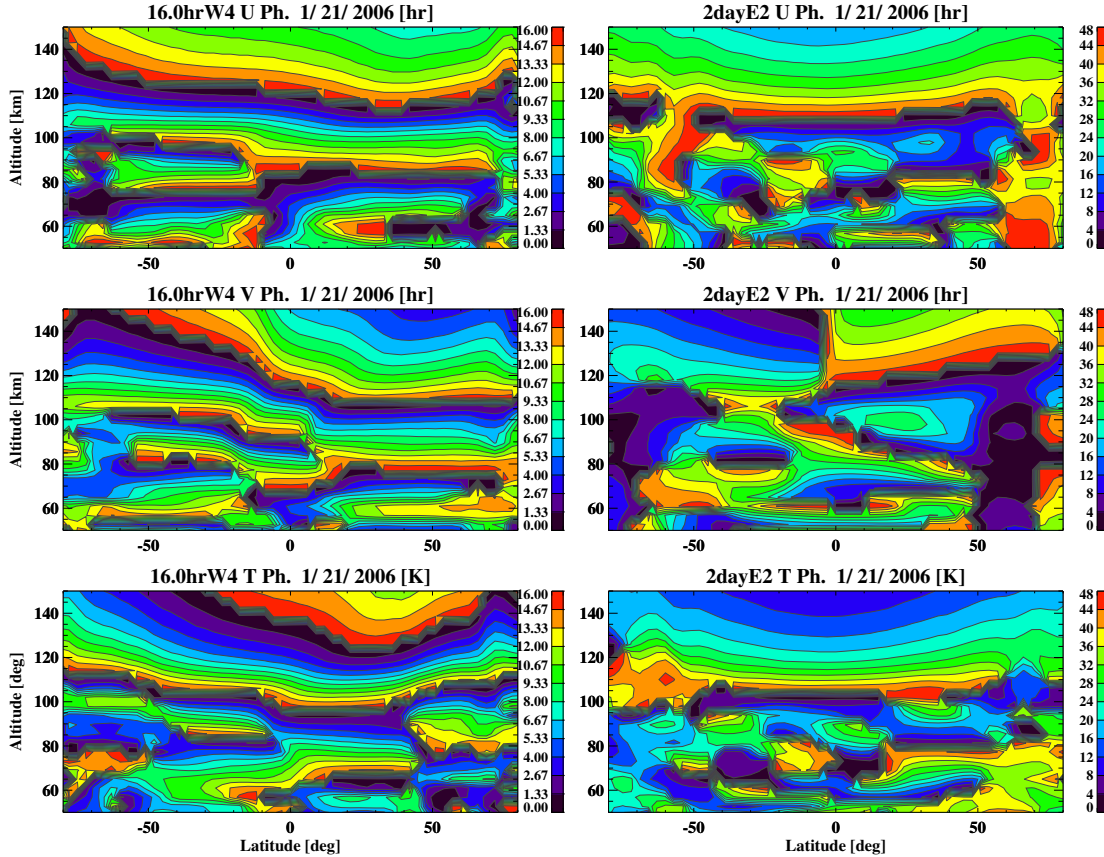


Figure 6.4: Vertical-latitude phase structure computed from the linear tidal model centered on January 21st, 2006 for the 16hrW4 zonal wind (upper-left), 16hrW4 meridional wind (middle-left), 16hrW4 temperature (lower-left), 2dayE2 zonal wind (upper-right), 2dayE2 meridional wind (middle-right), and 2dayE2 temperature (lower-right). Nonlinear forcing quantities presented in Chapter 5 are used to force the linear tidal model and compute secondary wave responses.

The linear model computations for the vertical-latitude structure of the 16hrW4 and 2dayE2 phase during 2006 are presented in Figure 6.4. The phase structure for both secondary waves reveals downward phase progression, which implies upward energy propagation. Below 100 km, the phase structure is mainly antisymmetric with respect to latitude and displays vertical wavelengths that are generally shorter than 30 km. Above 100 km, the phase structure is symmetric and constant with latitude in the zonal wind and temperature fields and antisymmetric in the

meridional wind field. The vertical wavelengths of both secondary waves in the thermosphere also lengthen to about 30-40 km, which is consistent with the lower order Hough mode amplitude structure and explained in more detail in the following section. The results for the secondary wave phase structure observed in 2009 and 2010 are similar to the 2006 results and thus, are only displayed in the Appendix F for reference.

In order to understand the results for the secondary wave responses presented in this section, several numerical experiments with the GSWM are conducted. The outcomes and analysis of these experiments are presented in the following sections (6.2-6.4) and serve to elucidate the relationship between the nonlinear forcing and the secondary wave response.

## 6.2 Dissipation Effects on Secondary Wave Hough Modes

The vertical-latitudinal structure of the 16hrW4 and 2dayE2 secondary waves can be understood by analyzing the dominant Hough modes that comprise each response. In this analysis, each Hough mode is defined as a set containing a unique Hough function, which is a solution to Laplace's tidal equation, and associated zonal and meridional expansion functions. Each mode can either propagate away from its source region or remain evanescent. The first three propagating Hough modes of the 16hrW4 and 2dayE2 secondary waves are displayed in Figure 6.5. The associated U expansion and Hough functions of the first mode of the 16hrW4 wave are characterized by a latitudinally symmetric peak at the equator while the meridional V expansion function for this mode contains two peaks at approximately  $\pm 30^\circ$  that are opposite in phase with each other. The first mode for the 2dayE2 exhibits a similar latitudinal structure to the first mode of the 16hrW4 except with a slightly narrower U expansion function and a broader V expansion function.

Higher order Hough modes are generally characterized by Hough functions that contain more zero-crossings with respect to the latitude. As shown in Figure 6.5, the 2nd Hough function of each secondary wave contains one more zero crossing than the 1st mode and contains two peaks that are antisymmetric in phase. The 3rd Hough function is described by two zero crossings and a latitudinally symmetric structure with maximal peaks located at mid-latitudes. Successive higher

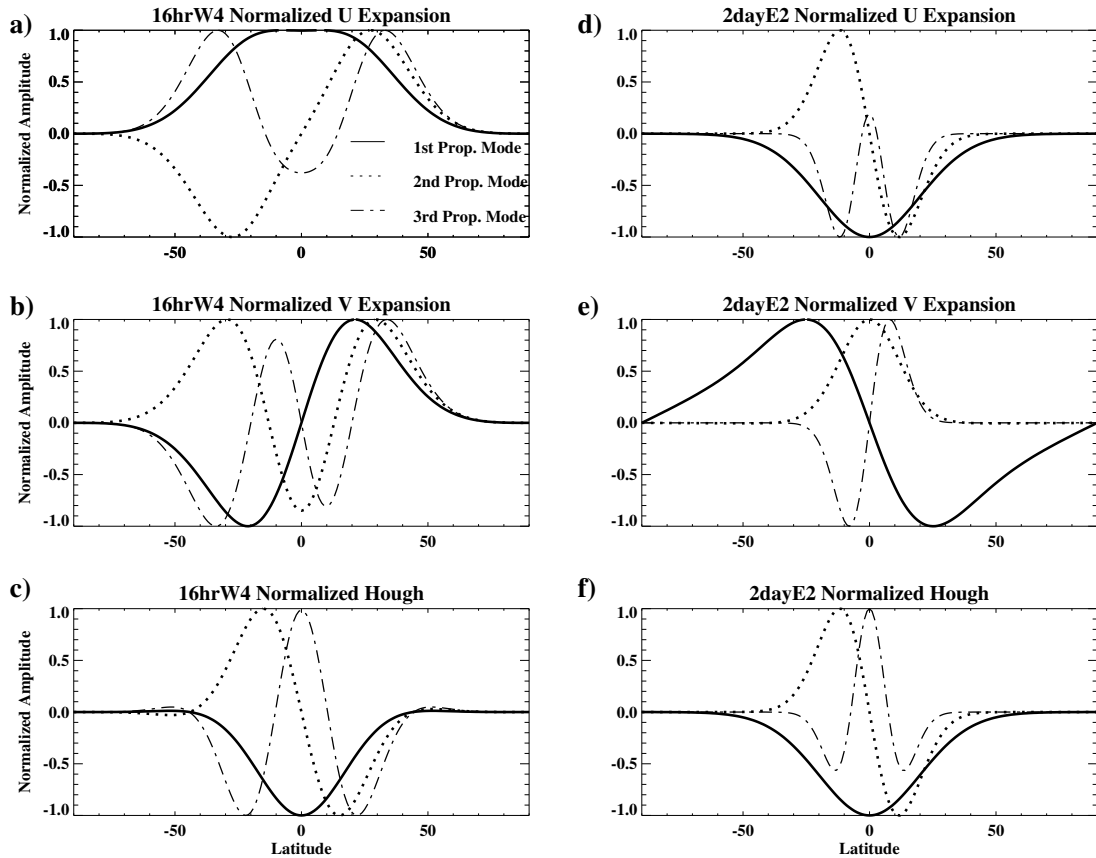


Figure 6.5: Normalized zonal wind, meridional wind expansion functions and Hough functions for the first, second and third propagating modes of the 16hrW4 (a, b, c) and 2dayE2 waves (d, e, f).

order modes, which are not displayed, contain more equatorial crossings and peaks that are located at higher latitudes.

Additionally, each propagating Hough mode is also associated with a vertical wavelength. The lowest order propagating modes generally have the longest vertical wavelength, which generally decrease with increasing mode order. For the 16hrW4, the 1st mode has a vertical wavelength of about 43 km and the 2nd mode is characterized by a wavelength of approximately 30 km. Comparatively, the 2dayE2 possesses shorter vertical wavelengths for each respective mode ( 39 km for 1st mode and 12 km for the 2nd mode).

In order to analyze the dominant Hough modes that comprise each secondary wave response, the functions displayed in Figure 6.5 are least squares fit to the amplitude and phase values for

each secondary wave at each altitude level. The U and V expansion functions are fit to secondary wave values in the zonal wind and meridional wind fields and the Hough functions are fit to the secondary wave temperatures. Hence, a single complex coefficient representing the amplitude and phase of each Hough mode in each field is obtained at every altitude level. The amplitudes of the first 3 modes contained in the each secondary wave temperature response for January 21st, 2006 are displayed in Figure 6.6. The amplitudes of each mode generally increase (decrease) with altitude below (above) 120 km, which follows the overall secondary wave amplitude in temperature.

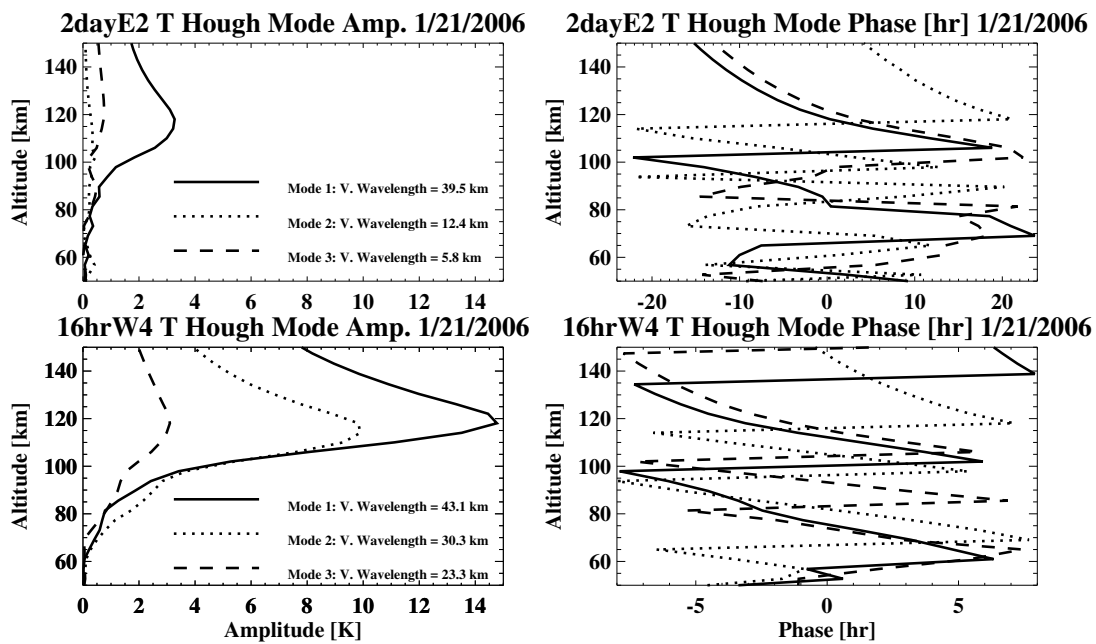


Figure 6.6: 16hrW4 amplitude (lower-left) and phase (lower-right), and 2dayE2 amplitude (upper-left) and phase (upper-right) as a function of altitude for January 21st, 2006. Each Hough mode amplitude was extracted by least squares fitting theoretical Hough mode functions to the overall secondary wave amplitude and phases at each altitude level. Units are in degrees Kelvin.

The plots in Figure 6.6 show that the magnitude of each secondary wave Hough mode is dependent on altitude. Although the 2nd mode of the 16hrW4 is the largest mode at altitudes below 100 km, the 1st mode amplitude of the 16hrW4 grows at the fastest rate and exceeds all other modes at higher altitudes. In contrast, there is no clear significant mode in the 2dayE2 temperature response below 100 km. Above 100 km, the 1st mode is the only mode that significantly increases

and hence, is the dominant mode of the 2dayE2 response. A comparison of this figure to Figure 6.1 shows that the Hough mode amplitudes are consistent with the overall secondary wave response. The 16hrW4 response exhibits a 2nd mode structure below 100 km, which subsequently transitions to a symmetric 1st mode structure at higher altitudes. On the other hand, the 2dayE2 temperature response is insignificant below 100 km and dominated by the 1st propagating Hough mode above this altitude.

The dominance of the lowest order propagating modes in the secondary wave response, particularly in the lower thermosphere, can be explained by the dependence of dissipation on vertical wavelength. For incompressible flow, momentum or thermal dissipation for a linearized perturbation can be modeled by the following equation where  $f'$  is a perturbation field variable and  $\mu$  is atmospheric viscosity (Holton, 2004 [39]).

$$F_{dissipation} = \nabla \cdot (\mu \nabla f') \quad (6.1)$$

The effects of dissipation on a given perturbation can be analyzed by comparing the magnitude of the inertial term ( $\frac{\partial f'}{\partial t}$ ) contained in the linearized momentum equation and the dissipation term described above. An expression representing the ratio of the dissipation force and wave inertial force is derived by making the following simplifications:

- (1) Gradients in the atmospheric field variables are larger in the vertical direction than in the horizontal direction, which allows  $\nabla$  to be written as  $\partial/\partial z$ .
- (2) Each perturbation is propagating in time, longitude and the vertical direction and can be written in the form  $f' = \hat{A}e^{j(s\lambda - \sigma t + \lambda_z z)}$ . Thus,  $\partial/\partial t = \sigma$  and  $\partial/\partial z = 2\pi/\lambda_z$  where  $\lambda_z$  denotes the vertical wavelength and  $\sigma$  represents the wave frequency.

Hence, the ratio of the dissipation to inertial perturbation forces ( $\chi$ ) can be expressed as the following:

$$\chi = \frac{4\pi^2}{\lambda_z^2} \frac{\mu}{\sigma} \quad (6.2)$$

The preceding equation implies that the dissipation effects are inversely correlated with vertical wavelength and wave frequency. As shown in Figure 6.6, the lowest order modes have the longest vertical wavelengths, which suggests that they are less susceptible to dissipation. This tendency can clearly be seen in the secondary wave Hough mode amplitudes. In the lower and middle mesosphere, the dissipation effects on each mode are negligible due to relatively small molecular and eddy diffusion values. At higher altitudes however, the onset of molecular and eddy diffusion begin to induce wavelength-dependent dissipation. Due to their long vertical wavelengths, the 1st propagating Hough mode for each secondary wave is least affected by the effects of dissipation and subsequently, becomes the most dominant mode in the lower thermosphere.

Equation 6.2 also serves to partially explain why the 16hrW4 is much larger than the 2dayE2. Because the 16hrW4 has a higher frequency than the 2dayE2, it is less affected by dissipation. Furthermore, the first 3 propagating Hough modes of the 16hrW4 have vertical wavelengths of greater than 23 km, which allows for some penetration into the lower thermosphere. In contrast, only the 1st mode of the 2dayE2 has a vertical wavelength (39.5 km) greater than 13 km. Consequently, the 1st mode of the 2dayE2 is the only mode that can achieve significant amplitude throughout the mesosphere and lower thermosphere region as depicted in Figure 6.6. Overall, the larger frequency and longer vertical wavelengths associated with the Hough modes of the 16hrW4 decrease the dissipation effects and allow it to vertically penetrate much farther into the atmosphere than the 2dayE2.

Figures 6.7 and 6.8 show the Hough mode amplitudes of each secondary wave during the peak 2dayW3 days of 2009 and 2010, respectively. Similar to the 2006 results, these results show that the lowest order Hough modes are least affected by dissipation and the 16hrW4 more effectively penetrates into the lower thermosphere than the 2dayE2. A comparison of the Hough modes during each year concludes that the 16hrW4 Hough mode amplitudes generally correlate with the overall secondary wave amplitudes. The largest 16hrW4 Hough mode amplitudes are observed during 2006 when the overall 16hrW4 amplitude is largest and the smallest 16hrW4 Hough mode amplitudes are seen during 2009 when the 16hrW4 amplitude is smallest. In contrast, since there

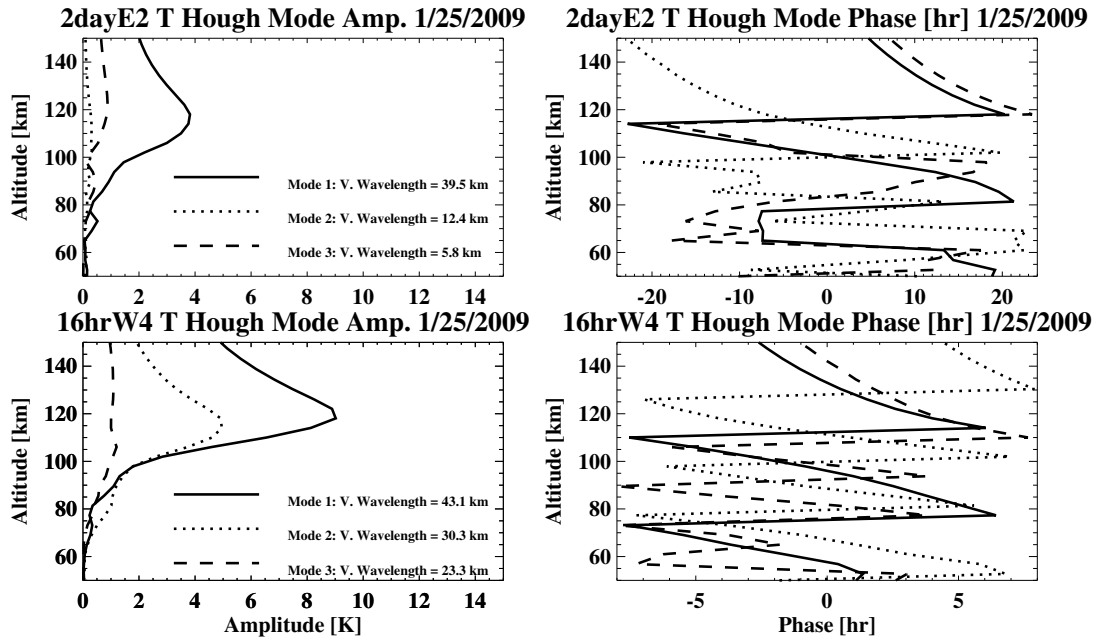


Figure 6.7: 16hrW4 amplitude (lower-left) and phase (lower-right), and 2dayE2 amplitude (upper-left) and phase (upper-right) as a function of altitude. Each Hough mode amplitude was extracted by least squares fitting theoretical Hough mode functions to the overall secondary wave amplitude and phases at each altitude level for January 25th, 2009. Units are in degrees Kelvin.

is minimal difference between the overall 2dayE2 amplitudes (Figure 6.1-6.3), the 2dayE2 Hough mode amplitudes exhibit minimal year-to-year variation.

### 6.3 Efficient Projection of Forcing on Propagating Hough Modes

The relationship between the observed secondary wave responses and the nonlinear forcing is addressed by performing several numerical experiments. To evaluate how efficient the primary modes are excited in the nonlinear interaction process, a numerical experiment is conducted where the momentum and thermal forcing distributions for 2006 displayed in Figure 5.15 are first projected onto the Hough functions and wind expansion functions that define the 1st and 2nd propagating modes of each secondary wave. The thermal forcing mode projections (Figure 6.9) show that the forcing for the 2nd propagating mode is larger than the forcing for the 1st propagating mode for both secondary waves at altitudes above 70 km. Below 70 km, the 1st and 2nd mode forcing for the

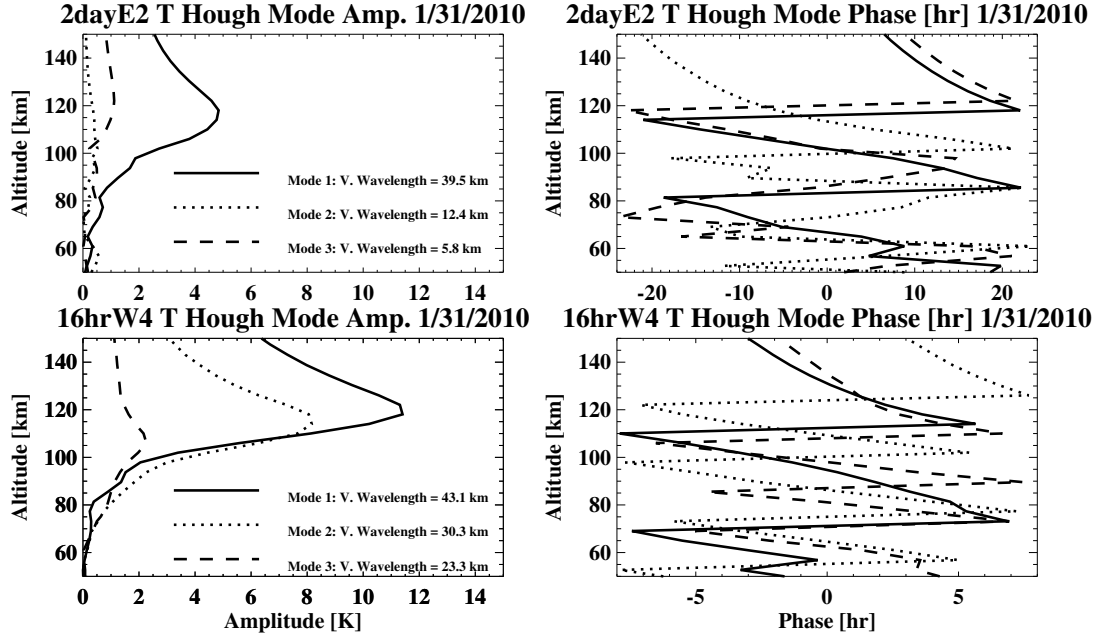


Figure 6.8: 16hrW4 amplitude (lower-left) and phase (lower-right), and 2dayE2 amplitude (upper-left) and phase (upper-right) as a function of altitude for January 31st, 2010. Each Hough mode amplitude was extracted by least squares fitting theoretical Hough mode functions to the overall secondary wave amplitude and phases at each altitude level. Units are in degrees Kelvin.

16hrW4 are close in magnitude while the 2nd mode forcing is still larger than the 1st mode forcing for the 2dayE2. In addition, the magnitude of the 1st mode forcing for the 16hrW4 is greater than the 2dayE2 1st mode forcing.

The forcing projections are consistent with the primary wave amplitudes and nonlinear forcing displayed in Chapter 5. As previously shown, 2dayW3 amplitudes and correspondingly, the nonlinear momentum and thermal forcing generally skew towards higher southern latitudes with increasing altitude. Since higher order modes broadly determine the amplitude structure at higher latitudes, the nonlinear forcing amplitude of both secondary waves subsequently shifts from lower order modes in the lower mesosphere to higher modes in the upper mesosphere. It is also observed that the nonlinear momentum and thermal forcing for the 16hrW4 is concentrated at lower latitudes while the nonlinear forcing for the 2dayE2 extends to higher latitudes. This explains why the thermal forcing projection onto the first mode of the 16hrW4 is larger than the corresponding

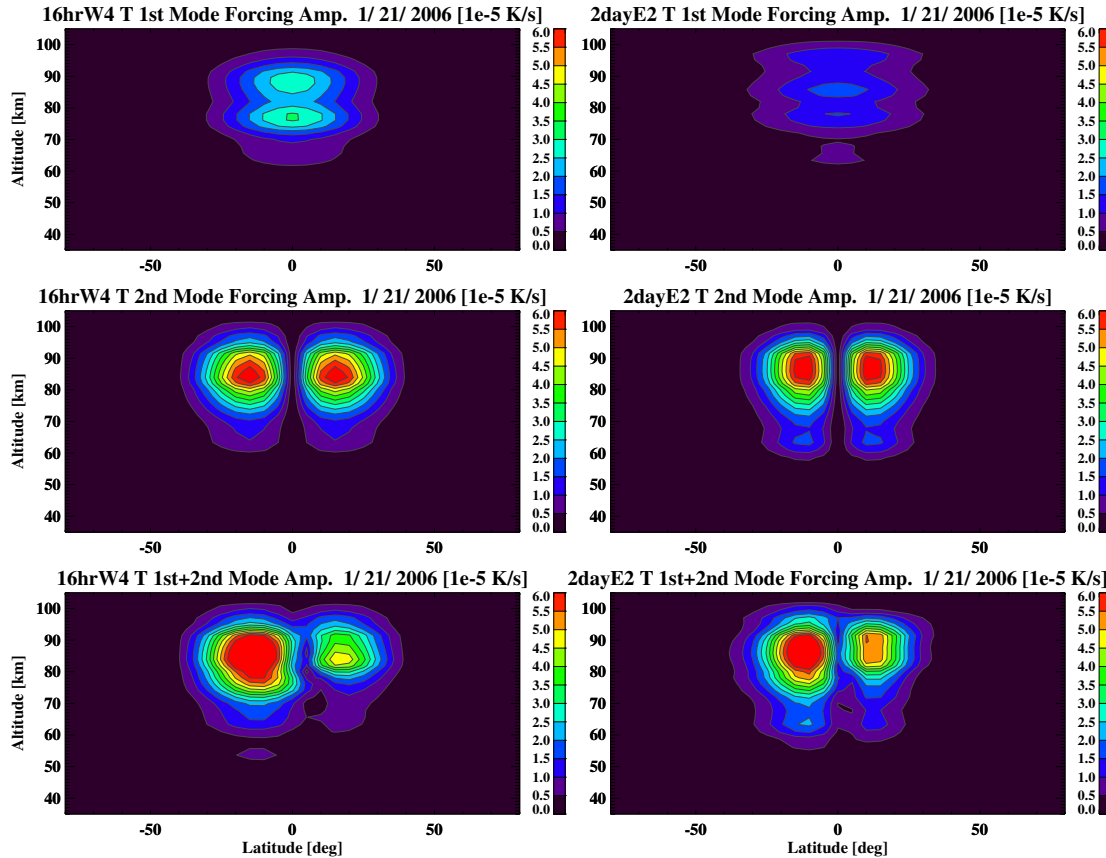


Figure 6.9: Projections of 16hrW4-2dayE2 thermal forcing projected onto the 16hrW4 1st propagating mode (upper-left), 16hrW4 2nd propagating mode (middle-left), 16hrW4 1st and 2nd modes (lower-left), 2dayE2 1st propagating mode (upper-right), 2dayE2 2nd propagating mode (middle-right), and 2dayE2 1st and 2nd modes (lower-right).

projection for the 2dayE2.

Projections of nonlinear momentum and thermal forcing onto the 1st and 2nd modes for each secondary wave are then utilized to force the linearized tidal model and produce a response for each case. Since the 1st mode forcing is greater for the 16hrW4 than the 2dayE2, a larger 1st mode 16hrW4 zonal wind response is observed as shown in Figure 6.10. Furthermore, the superposition of the responses of the 16hrW4 to the 1st and 2nd mode forcing is a good approximation to the overall 16hrW4 response as illustrated in Figure 6.1. This indicates that the majority of the overall 16hrW4 response is determined by the magnitude of the nonlinear forcing projection onto the lowest order propagating modes. In contrast, the 2dayE2 response to the 1st and 2nd mode forcing

only captures portions of the overall 2dayE2 response. These differences, particularly at the high latitudes, further hint that modes other than the 1st and 2nd modes are effectively excited from the nonlinear interaction process and comprise significant portions of the overall 2dayE2 response.

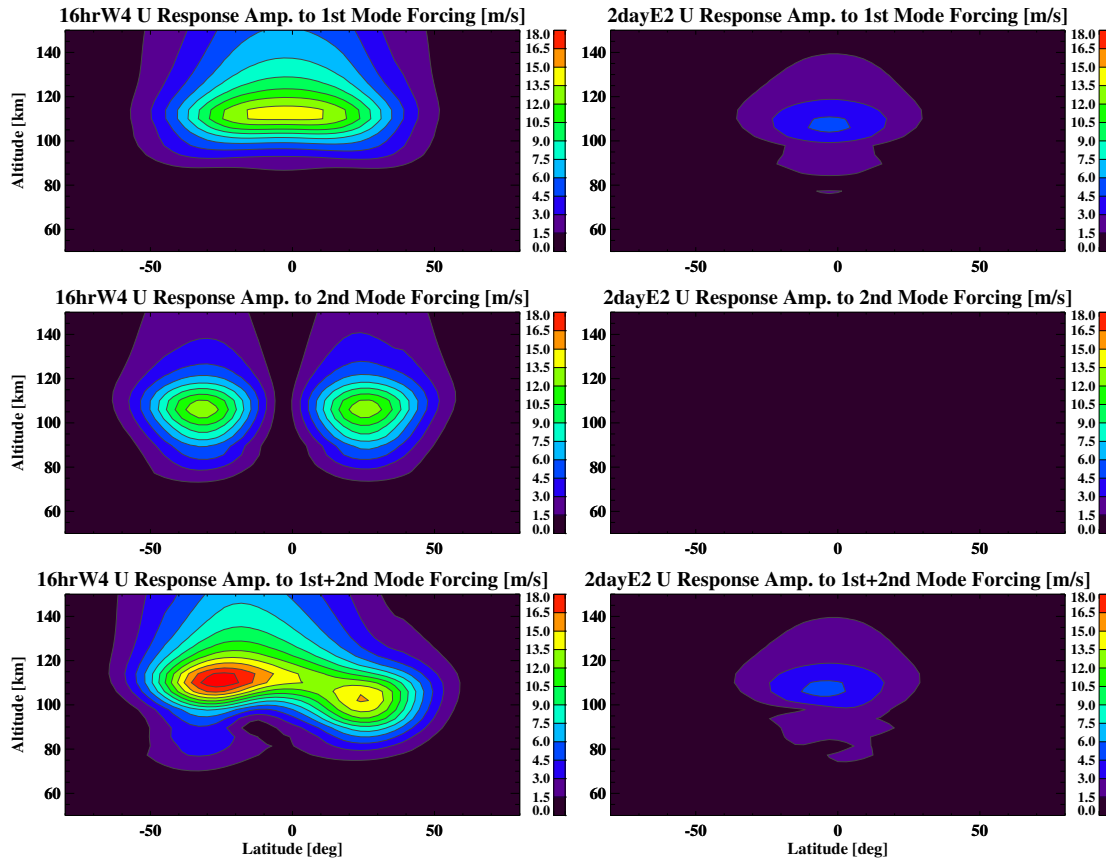


Figure 6.10: Zonal wind response amplitude to the 16hrW4-2dayE2 forcing projected onto the 16hrW4 1st propagating mode (upper-left), 16hrW4 2nd propagating mode (middle-left), 16hrW4 1st and 2nd modes (lower-left), 2dayE2 1st propagating mode (upper-right), 2dayE2 2nd propagating mode (middle-right), and 2dayE2 (lower-right).

The amplitude response to each individual mode forcing also reveal that the response of both secondary waves to the 1st mode forcing is larger than the response to the 2nd mode forcing, especially at higher altitudes in the thermosphere. This is explained by the difference in vertical wavelengths between each mode. The 1st propagating modes are characterized by longer vertical wavelengths than the second order modes and thus, are less susceptible to damping from dissipative forces. Thus, it is expected that the first mode to be more efficiently excited in the atmosphere

than higher order modes.

A full explanation can now be made on why the 16hrW4 is larger than the 2dayE2 for a zero wind background atmosphere. In addition to being less susceptible to dissipation as explained earlier, the 16hrW4 is also more effectively forced from the DW1-2dayW3 interaction. Since the nonlinear forcing for the 16hrW4 is concentrated at lower latitudes than the 2dayE2 forcing, the nonlinear forcing more efficiently projects onto the lowest order modes of the 16hrW4. As shown in this numerical experiment, the lowest order modes mainly determine the majority of the secondary wave response. Consequently, the 16hrW4 possesses a much greater amplitude than the 2dayE2 throughout the zero wind atmosphere. This is a key result of this dissertation since past studies have been unable to explain why one secondary wave may be larger than another within the same nonlinear interaction.

This experiment is also repeated for the 2009 and 2010 cases for comparison. As illustrated in the figures presented in Appendix F, the 1st and 2nd mode projected forcing for the 16hrW4 is smaller in 2009 and 2010 than in 2006, which results in smaller 16hrW4 responses to the Hough mode forcing during these years. In contrast, the 1st mode and 2nd mode forcing for the 2dayE2 for 2009 and 2010 are similar in magnitude to the projected forcing in 2006, leading to similar 2dayE2 responses in all 3 years.

The results of these experiments shown here and Appendix F indicate that inter-annual variability of the secondary wave response in a zero wind atmosphere is mainly dictated by the projection of the forcing onto the lowest order modes, and not necessarily dependent on the overall forcing amplitude. For the 16hrW4 wave, the largest forcing amplitudes (2006) results in the largest 1st and 2nd mode projected forcing and overall wave response. For the 2dayE2 wave, however, the large nonlinear forcing amplitudes observed during 2006 do not as efficiently project onto the 1st and 2nd order Hough modes as during the other years. Consequently, similar 2dayE2 amplitudes are observed in all three years.

## 6.4 Importance of Altitude Location

The numerical experiment presented in this section assesses the sensitivity of the 16hrW4 and 2dayE2 responses to the altitude location of the nonlinear forcing. First, a 15 km altitudinal thick window centered at a particular altitude is applied to the overall momentum and thermal nonlinear forcing. The nonlinear forcing values lying outside of the window are Gaussian-tapered to zero in order to avoid any sharp vertical gradients in the nonlinear forcing. Examples of forcing cases centered around 70 km and 90 km for January 21st, 2006 (Figure 6.11) show that the forcing contained in the upper mesosphere is much greater and generally extends to higher southern latitudes than the forcing contained in the lower mesosphere. These altitude slices of the overall nonlinear forcing are subsequently employed to compute 16hrW4 and 2dayE2 responses in the model.

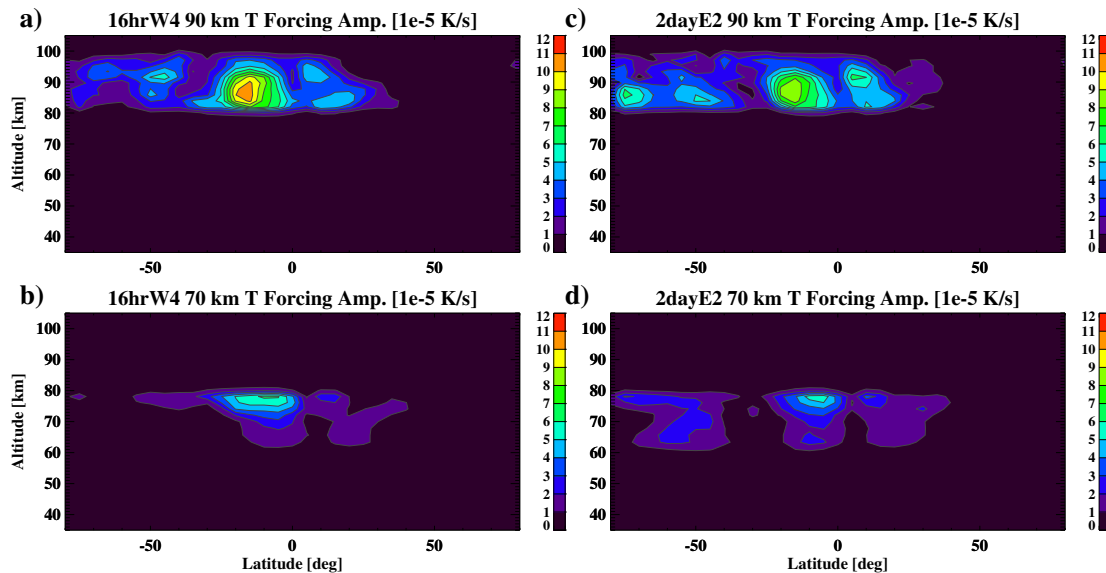


Figure 6.11: 15 km subsections of secondary wave forcing centered at a) 90 km for 16hrW4, b) 70 km for 16hrW4, c) 90 km for 2dayE2 and d) 70 km for 16hrW4 during January 21st, 2006. Each forcing structure is obtained by applying a 15 km altitudinal window centered at 70 km and 90 km to the overall nonlinear forcing displayed in Figure 7. Values which lie outside of the window are Gaussian-tapered to zero.

The results displayed in Figure 6.12 demonstrate that the 16hrW4 and 2dayE2 zonal wind responses to the forcing centered around 70 km are larger than the respective responses to the

forcing centered around 90 km. While this results may seem surprising, it is explained by analyzing the growth rate of each secondary wave with altitude. Because the atmosphere is characterized by exponentially decreasing density, the secondary wave amplitudes approximately increase exponentially with altitude from their source region due to the conservation of kinetic energy. Like most other atmospheric tides and waves, the secondary wave growth rate is halted by dissipative forces that dominate around 100 and 120 km. For the 70 km forcing case, this suggests that each secondary wave exponentially grows for about 50 km before dissipation dominates. In contrast, secondary wave growth for the 90 km forcing case is initialized much closer to the dominant dissipation region. Although larger forcing is contained in the 90 km forcing case due to larger primary wave amplitudes, the vertical growth rate of the forcing is exceeded by the exponential growth rate of the secondary wave response. As a result, the 70 km forcing produces a larger secondary wave responses than the 90 km forcing for this particular nonlinear interaction event.

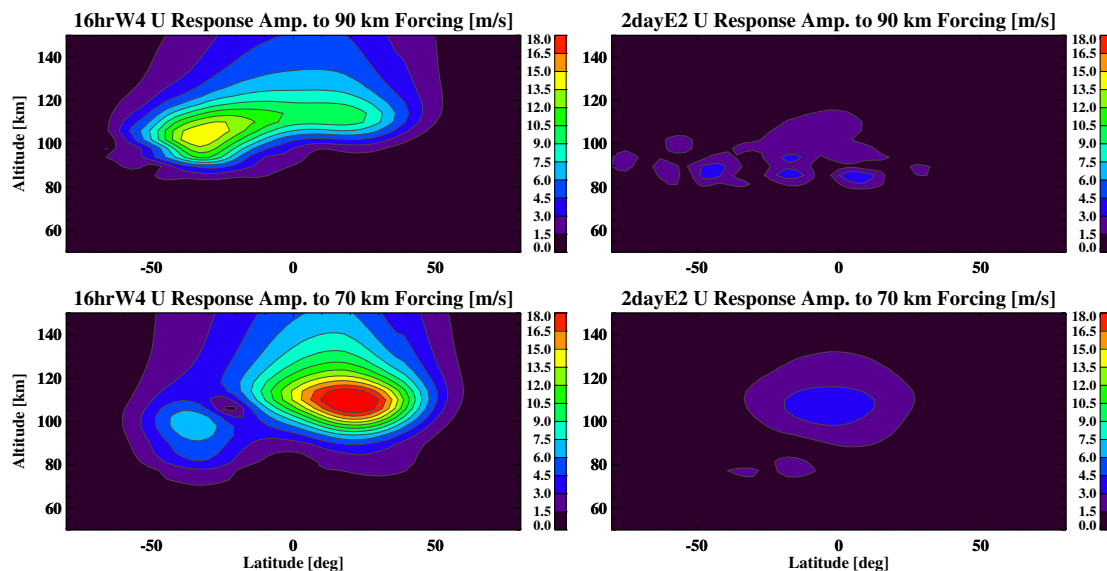


Figure 6.12: Secondary wave zonal wind response to the nonlinear forcing centered at a) 90 km for 16hrW4, b) 70 km for 16hrW4, c) 90 km for 2dayE2 and d) 70 km for 16hrW4 during January 21st, 2006.

Results from this experiment also show that the secondary wave responses to the 70 km forcing are more latitudinally symmetric about the equator than the the responses to the 90 km forcing.

Additionally, the 16hrW4 zonal wind response is most dominant in the low latitude northern hemisphere for the 70 km forcing while the response is more dominant in the mid-latitude southern hemisphere for the 90 km forcing. Because the 70 km forcing is more concentrated near the equator, most of the forcing projects onto the 1st and 2nd propagating modes. Consequently, the responses for each secondary wave to the 70 km forcing is dominated by the lowest order modes. Unlike the secondary wave response to the 70 km forcing, the response to the forcing centered at 90 km is more asymmetric about the equator and spans to higher southern latitudes, indicating the presence of higher order modes. The largest secondary wave amplitudes are located within or near the region of forcing, which originates from considerable momentum and thermal forcing contained in the southern, upper mesosphere where the 2dayW3 amplitude is substantial. However, as demonstrated in Figure 6.12, the higher order components have short vertical wavelengths and are not able to propagate far away from their excitation source while the 1st propagating mode is able to penetrate to higher altitudes in the thermosphere.

This sensitivity study is extended to other altitude locations by sliding the 15 km forcing window from 40 km to 95 km at 5 km intervals and computing the secondary wave response due to the forcing at each altitude. The maximum amplitude in the zonal wind, meridional wind and temperature fields are recorded for each case and secondary wave. From the results displayed in Figure 6.13, the response of the 16hrW4 amplitude during 2006 is observed to be most sensitive to the forcing centered around 70 km. The 2dayE2 in zonal wind and temperature is sensitive to the forcing at 65 km, while the 2dayE2 meridional amplitude is most sensitive to forcing at around 90 km. The sensitivity of both secondary waves to the forcing in the lower mesosphere is mainly due to the sufficient vertical distance between the excitation region and the dissipation region, which allows for exponential growth over a large range. This is a novel result that contradicts the current thinking that nonlinear interactions are most important in interactions between large primary waves. From the analysis presented earlier, it is concluded that the 1st and 2nd order modes are most effectively excited from the lower mesosphere region. The dominant excitation of the 1st propagating mode in the lower mesosphere is further supported by the weak 2dayE2 meridional

wind response in this region. Since the 1st propagating mode of the 2dayE2 is approximated by a Kelvin wave, the meridional wind response is expected to be close to zero (Salby, 1984 [98]). As the forcing transitions to higher altitudes, additional higher order modes are forced in-situ, which causes larger responses in the meridional wind field as well as zonal wind and temperature fields at higher latitudes.

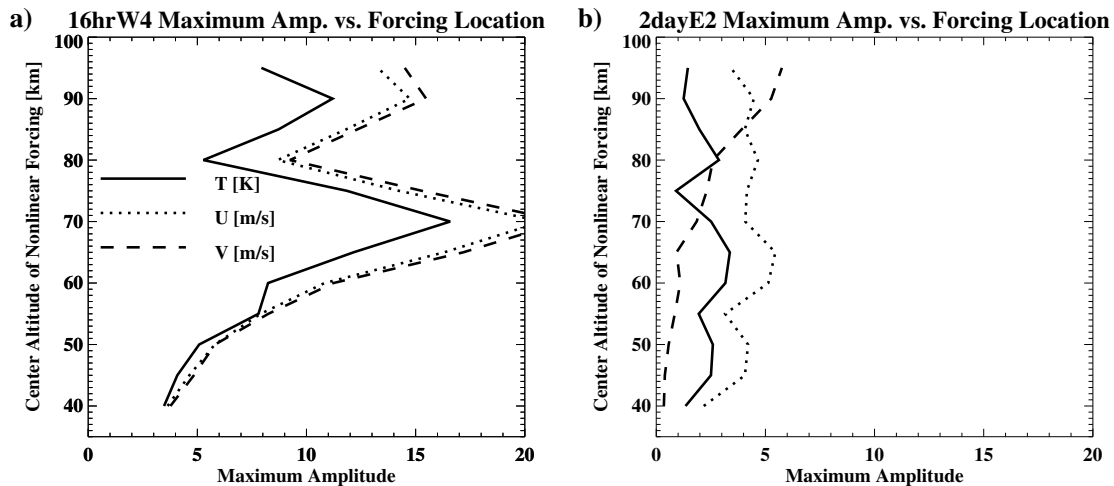


Figure 6.13: Maximum amplitude of the a) 16hrW4 and b) 2dayE2 versus center altitude of the nonlinear forcing subsection during January 21st, 2006. Each nonlinear forcing subsection is obtained by applying the 15 km vertical window.

The sensitivity of the secondary waves to the vertical location of the forcing was also analyzed for the nonlinear interactions during January 2009 and 2010. The results presented in Appendix F show that the 16hrW4 is equally sensitive to the forcing at 70 km and 90 km during 2009 and more sensitive to the forcing located at 90 km during 2010. These results indicate that the response sensitivity to the forcing location varies on an inter-annual basis and is likely due to the year-to-year spatial variations in the forcing structure.

The numerical experimental results presented in this section can also be used to illustrate the role of interference between secondary waves forced at different altitude regions on the overall secondary wave response. Figure 6.14 shows the phase of the 16hrW4 forced from the 70 km and 90 km centered forcing presented in an earlier figure. While the phase relationship between the 16hrW4

responses produces constructive interference in the lower thermosphere at southern latitudes, the phase relationship produces destructive interference in the northern lower thermosphere. As a result, a larger overall 16hrW4 response (Figure 6.1) is observed in the southern hemisphere. Hence, the overall secondary wave response can be viewed as the superposition of independent secondary waves produced from different vertical regions of the atmosphere that constructively or destructively interfere with each other in some manner.

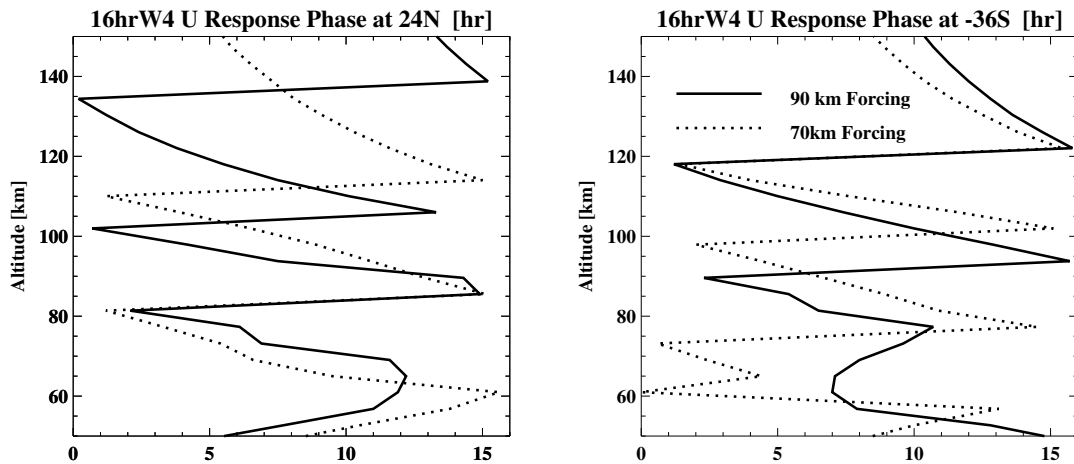


Figure 6.14: Phase of the 16hrW4 response to the nonlinear forcing subsections centered at 70 km (dotted) and 90 km (solid) during January 21st, 2006. The left plot shows the phase at 24N and the right plot shows the phase at 36S.

The main takeaway from these experimental results is that the nonlinear forcing regions with the largest impact on the overall secondary wave response do not necessarily coincide with the regions containing the largest forcing amplitudes. Due to exponential secondary wave growth with altitude, a secondary wave forced at lower altitudes will be larger than a secondary wave generated from identical forcing at a higher altitude. These results provide further indication that the largest secondary waves may not be generated from the largest primary waves in the MLT region.

## 6.5 Impact of Primary Wave Phase on Secondary Wave Response

The results displayed in the previous sections of this chapter indicate that the inter-annual variability in the vertical and latitudinal structure of the primary waves has a large influence on the secondary wave responses. However, variability in the primary wave phase does not have a significant impact on the secondary wave response. In order to demonstrate this claim, the phase of the 2dayW3 during January 21st, 2006 is subtracted by  $\pi/2$  radians at all locations and atmospheric variables to produce a new nonlinear forcing structure. The magnitude of the 2dayW3 phase change is consistent with the year-to-year changes in the 2dayW3 phase observed from NOGAPS-ALPHA. In contrast, the DW1 phase remains constant on a year-to-year basis.

By changing the 2dayW3 phase by  $\pi/2$  radians at all locations and keeping the DW1 phase constant, the nonlinear forcing phase is shifted by the same amount. The amplitude of the nonlinear forcing, however, is not altered. This can be shown simply by examining the nonlinear forcing equations contained in Appendix C. The nonlinear forcing structure produced from shifting the 2dayW3 phase is then employed to produce a new secondary wave response. Figures in Appendix F show that the secondary wave amplitude results produced from this case is almost identical to the original results displayed in Figure 6.1. This observation is expected because the nonlinear forcing amplitude structure has not been altered. As a result, the dominant Hough mode responses comprising the 16hrW4 and 2dayE2 waves remain unchanged. The only significant change in the secondary wave response is observed in the secondary wave phase, which has been shifted by  $\pi/2$  radians. From these results, it is concluded that the inter-annual variability of the secondary wave responses is primarily generated by the primary wave amplitude changes and not primary wave phase changes.

## 6.6 Secondary Wave Response with Background Winds

In the remaining sections of this chapter, secondary wave responses in the presence of realistic background winds and temperatures are examined. The background zonal winds and temperatures

are extracted from hourly NOGAPS-ALPHA reanalysis output by zonally and temporally averaging measurements at each latitude-altitude location over 6 days. The 6-day temporal window is slid one day to produce unique background zonal wind and temperature configuration for each day. Because the NOGAPS-ALPHA model only produces output to approximately 95 km, January climatological values from the NRL MSIS and HWM reanalysis models are utilized at higher altitudes. To minimize the impact of differences between the NOGAPS-ALPHA and climatological models, background winds and temperatures are linearly smoothed between 90 km and 100 km.

Figure 6.15 presents the background zonal wind structure for the peak 2dayW3 day of 2006, 2009 and 2010. Below 90 km in each case, the background zonal wind are westward in the southern hemisphere and reach maximum values of about 100 m/s. In the northern hemisphere below 90 km, the background zonal winds are mainly eastward equatorward of  $50^{\circ}\text{N}$  and westward north of this latitude. Above 90 km, the background winds reverse in the southern hemisphere and become mainly eastward. The summer mesopause reversal in the winds is consistent with past observations and has been attributed to the background filtering of gravity wave momentum deposition (Vincent and Fritts [111]). Due to the dearth of observations above 110 km, the background zonal wind and temperatures within the lower thermosphere and above should only be considered as rough approximations to the values in the real atmosphere.

Although there is a similar general structure in the background zonal winds for all 3 cases, Figure 6.15 reveals slight differences. The largest background wind values are found in the 2006 case, which attain westward winds up to 100 m/s in the southern hemisphere and eastward winds of 55 m/s in the northern hemisphere. The northern hemispheric eastward jet in 2009 is noticeably weaker than the winds displayed in the other years. During 2010, the maximum westward and eastward wind values in the southern and northern hemisphere, respectively, are more comparable in magnitude due to a stronger northern eastward jet and a slightly weaker southern westward jet. While some of these differences is certainly explained by inter-annual variability, other differences may be explained by the different days represented in each case. Generally, the southern westward jet during early January is strong and weakens throughout the month, whereas the opposite is true

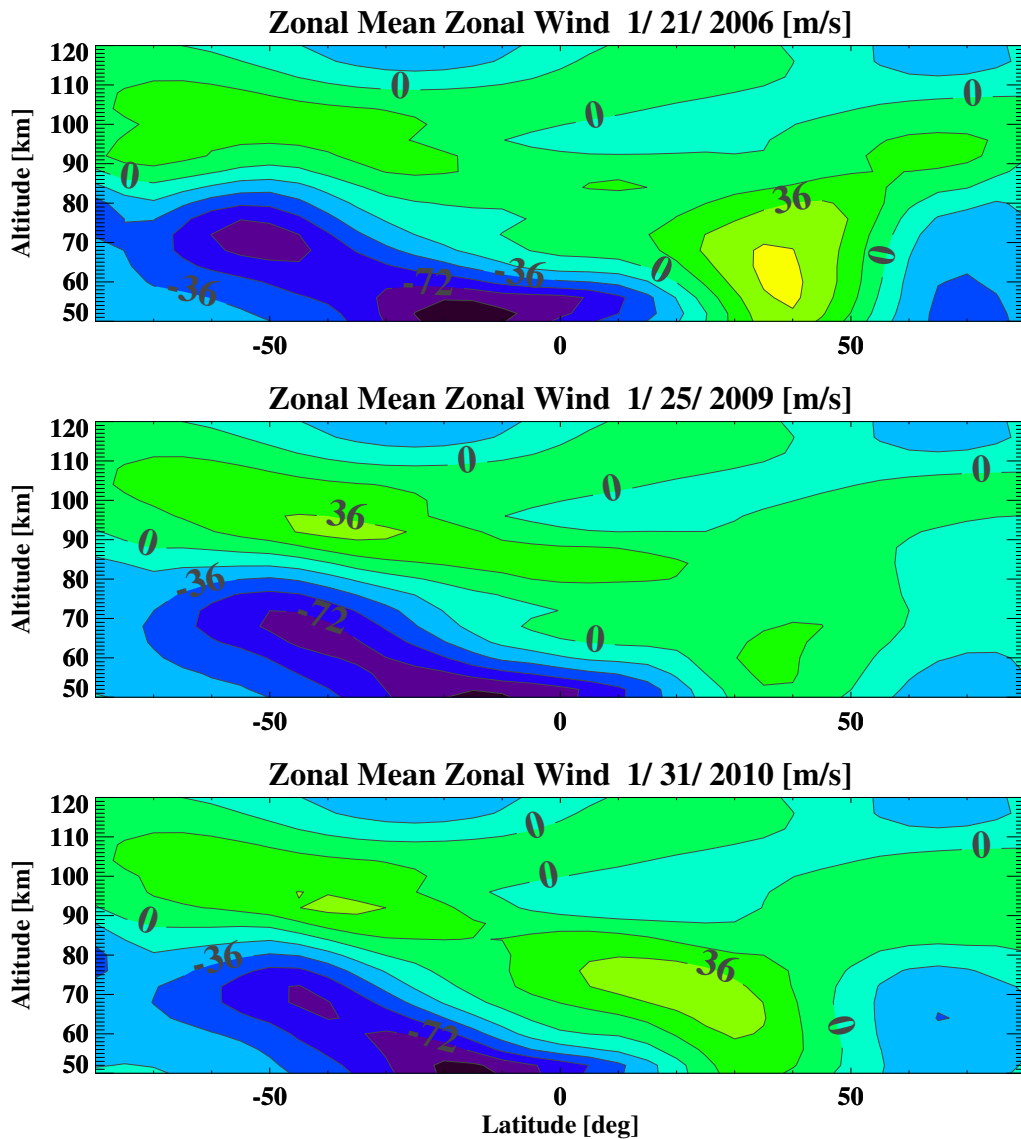


Figure 6.15: Vertical-latitude structure of background zonal wind for January 21st, 2006 (top), January 25th, 2009 (middle), and January 31st, 2010 (bottom). Zonal winds below 95 km are derived from NOGAPS-ALPHA reanalysis output. Monthly climatological values from HWM are used at higher altitudes.

for the northern eastward jet. Thus, it is expected to see more of a balance between the magnitude of the hemispheric jets during late-January, which is observed in the 2010 case.

The background winds (Figure 6.15) and temperatures are implemented in the linear tidal

model in order to compute another set of secondary wave responses. The computed secondary wave responses in the presence of a realistic background are displayed in Figures 6.16 through 6.18. In all three years, the 16hrW4 and 2dayE2 waves increase in amplitude with altitude until about 100 km, which is the location of molecular and eddy diffusion onset. The 16hrW4 amplitude in the zonal and meridional wind fields is generally largest around  $\pm 45^\circ$  latitude and smaller at lower latitudes. In contrast, the 16hrW4 amplitude structure in temperature is skewed towards slightly lower latitudes. In both the wind and temperature fields, the 16hrW4 amplitude is most significant in the northern hemisphere below 90 km and largest at southern latitudes in the thermosphere. Compared to the 16hrW4 response, the 2dayE2 amplitude is weak and only achieves values above 5 m/s in certain locations. The 2dayE2 response is mainly confined to southern latitudes in the MLT region and shows little evidence of propagation to higher altitudes.

The secondary wave responses also show some inter-annual differences. Unlike in other years, the 2006 16hrW4 response in the horizontal wind fields has a significant presence at northern latitudes in the MLT region and reaches maximum values of about 11 m/s. While the 16hrW4 during 2009 and 2010 is small in the northern hemisphere, the 16hrW4 during these years achieves comparable values to the 2006 16hrW4 in the southern hemisphere above 100 km. The major inter-annual differences in the 2dayE2 responses are observed in the amplitude magnitudes. Larger 2dayE2 amplitudes are observed during 2006 and 2010 than during 2009.

A comparison of the results presented in this section to the secondary wave responses in a zero background zonal wind configuration (Section 6.1) highlights the impact of the background zonal wind on the spatial structure and magnitude of the secondary wave response. The maximum 16hrW4 amplitude has been reduced by about 40-50% from the zero wind case in all three years. The largest reductions in the 16hrW4 amplitude are observed at low latitudes where the wave is almost non-existent in the non-zero background wind case. In contrast, the inclusion of non-zero background winds slightly enhance the 2dayE2 response, particularly at southern latitudes in the MLT region. However, the 2dayE2 response is still much smaller than the 16hrW4 response.

The impacts of the background winds on the magnitude of the secondary wave responses

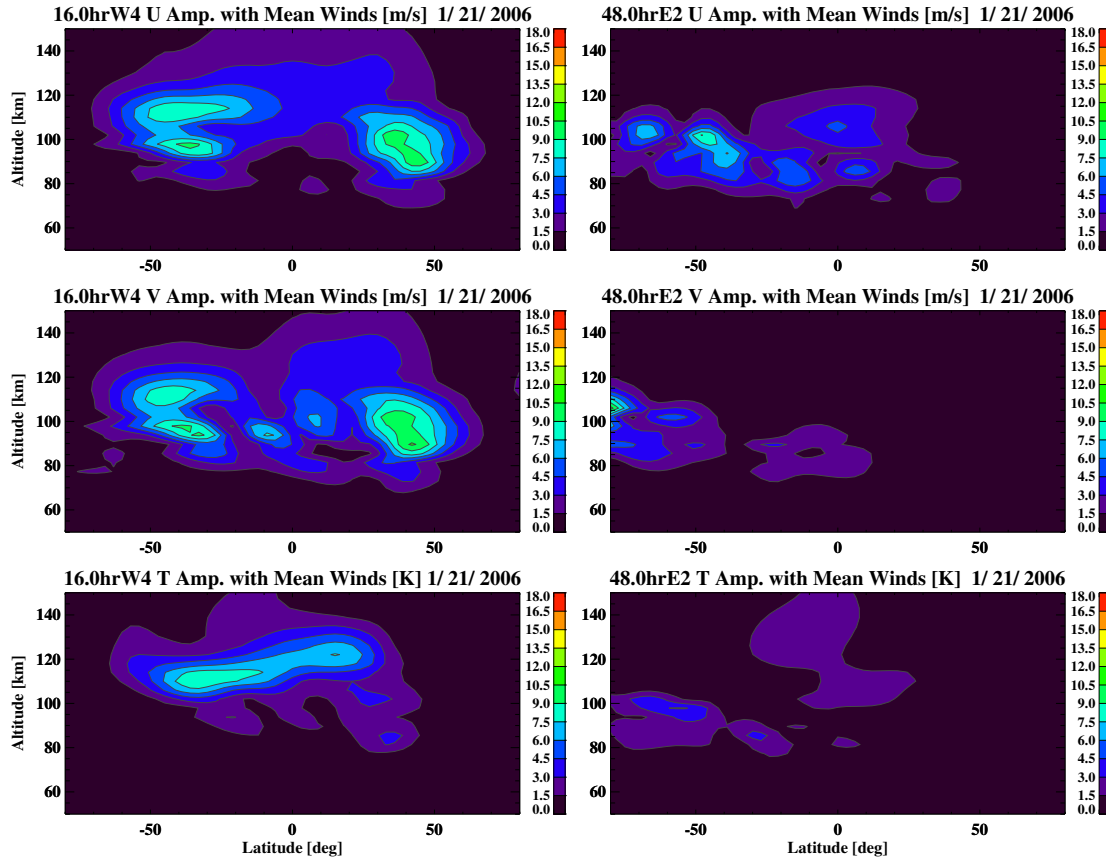


Figure 6.16: Vertical-latitude amplitude structure computed from the linear tidal model with background winds centered on January 21st, 2006 for the 16hrW4 zonal wind (upper-left), 16hrW4 meridional wind (middle-left), 16hrW4 temperature (lower-left), 2dayE2 zonal wind (upper-right), 2dayE2 meridional wind (middle-right), and 2dayE2 temperature (lower-right). Nonlinear forcing presented in Chapter 5 are used to force the linear tidal model and compute secondary wave responses.

are elucidated here by examining the Hough modes that comprise each response. The first 3 propagating modes for the non-zero background wind 2006 secondary wave response are presented in Figure 6.19 while corresponding results for 2009 and 2010 are presented in Appendix F. The results reveal that the first 3 modes of the 16hrW4 response have been reduced from the zero wind case although the altitude of maximum for each mode is unchanged. The decrease in each mode can be partially explained by “mode coupling” (Forbes, 1982 [11]). As a consequence of the 16hrW4 amplitude being shifted from low latitudes to middle latitudes by the background winds,

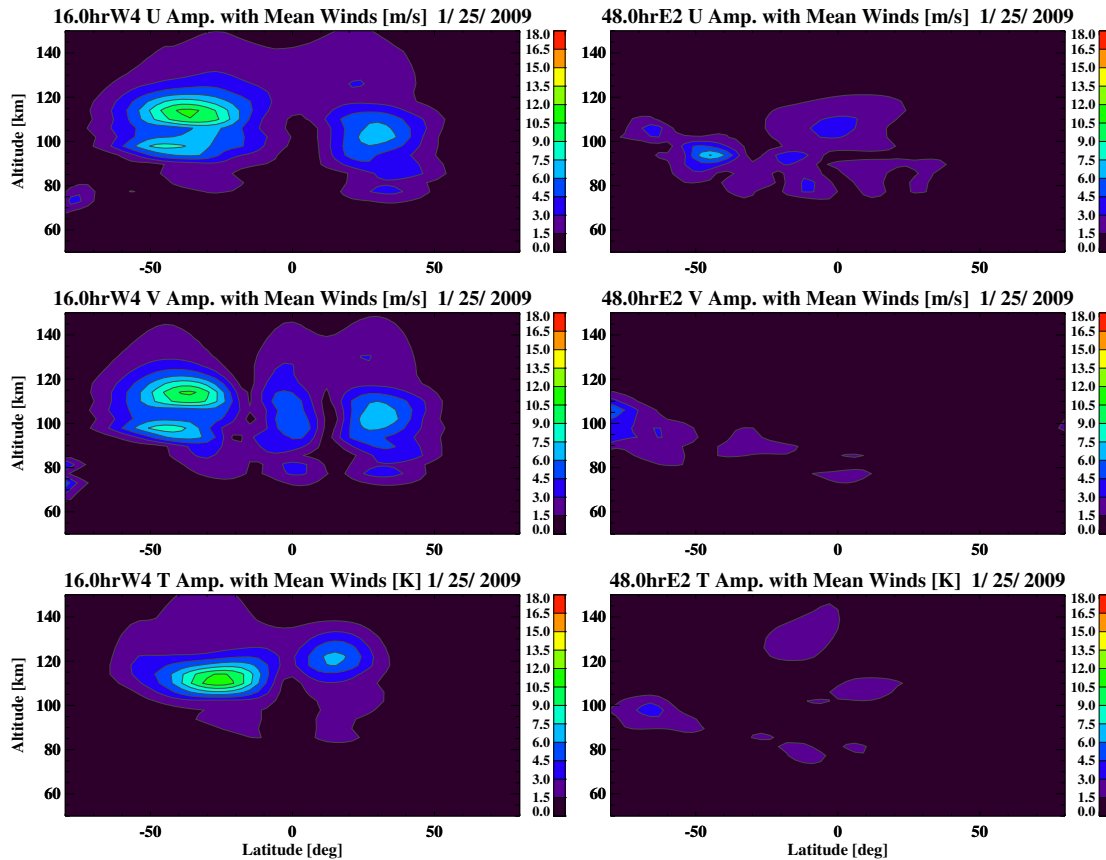


Figure 6.17: Vertical-latitude amplitude structure computed from the linear tidal model with background winds centered on January 25th, 2009 for the 16hrW4 zonal wind (upper-left), 16hrW4 meridional wind (middle-left), 16hrW4 temperature (lower-left), 2dayE2 zonal wind (upper-right), 2dayE2 meridional wind (middle-right), and 2dayE2 temperature (lower-right). Nonlinear forcing presented in Chapter 5 are used to force the linear tidal model and compute secondary wave responses.

the magnitude of the lowest order Hough modes are reduced. The energy present in the lowest order modes for the zero background wind case is coupled to higher order modes in the non-zero background case. Because the background winds are strongest in magnitude in the mesosphere, the majority of the “mode coupling” occurs in this region. However, higher order modes are not likely to effectively propagate vertically due to their associated vertical wavelengths as explained in previous sections. Consequently, the 16hrW4 response above 100 km is still primarily composed of the first 3 propagating modes, which have been decreased due to the background winds at lower

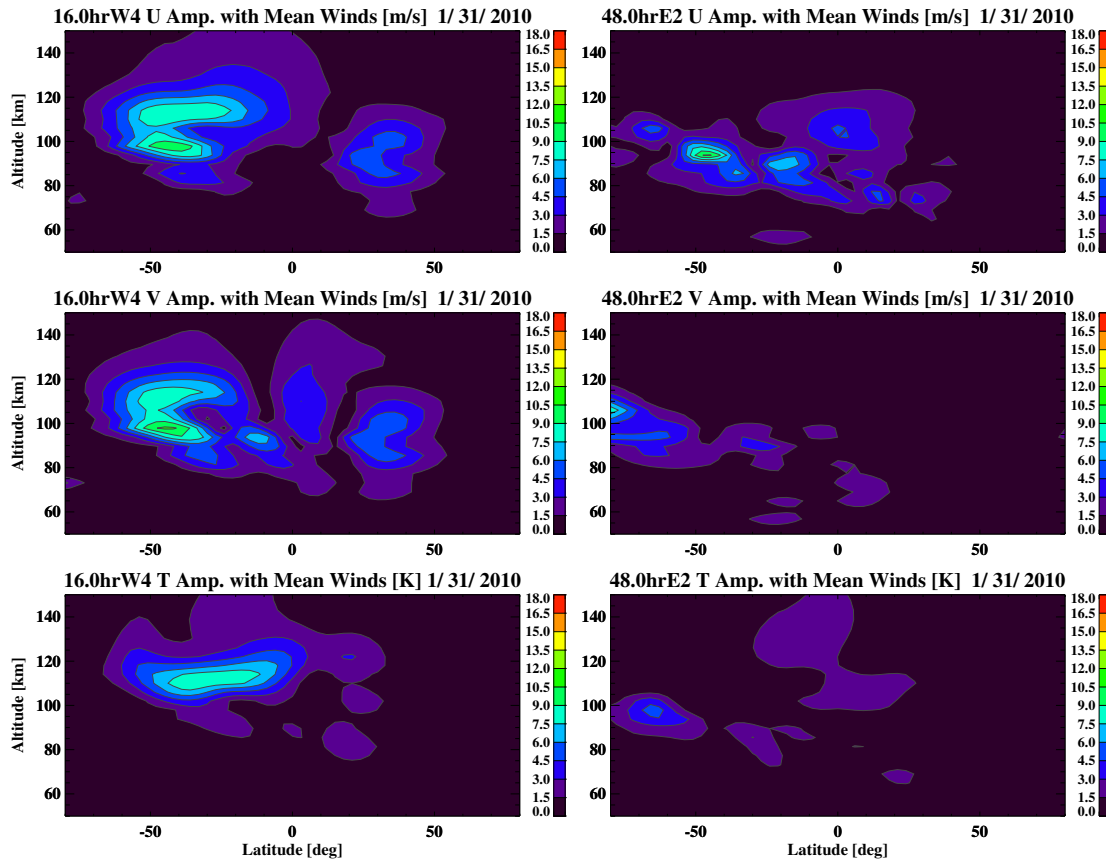


Figure 6.18: Vertical-latitude amplitude structure computed from the linear tidal model with background winds centered on January 31st, 2010 for the 16hrW4 zonal wind (upper-left), 16hrW4 meridional wind (middle-left), 16hrW4 temperature (lower-left), 2dayE2 zonal wind (upper-right), 2dayE2 meridional wind (middle-right), and 2dayE2 temperature (lower-right). Nonlinear forcing presented in Chapter 5 are used to force the linear tidal model and compute secondary wave responses.

altitudes. The final result is a decrease in the overall 16hrW4 response.

Similarly, the first 3 Hough modes for the 2dayE2 are slightly reduced by the inclusion of non-zero background winds, which leads to a decrease in the 2dayE2 response above the MLT region from the zero wind case. Unlike the 16hrW4 response however, the in-situ modes play a larger role in determining the overall 2dayE2 response. These in-situ modes are enhanced at southern latitudes due to background winds. Consequently, a slightly larger 2dayE2 response is observed at southern latitudes in the MLT region due to the inclusion of non-zero background winds.

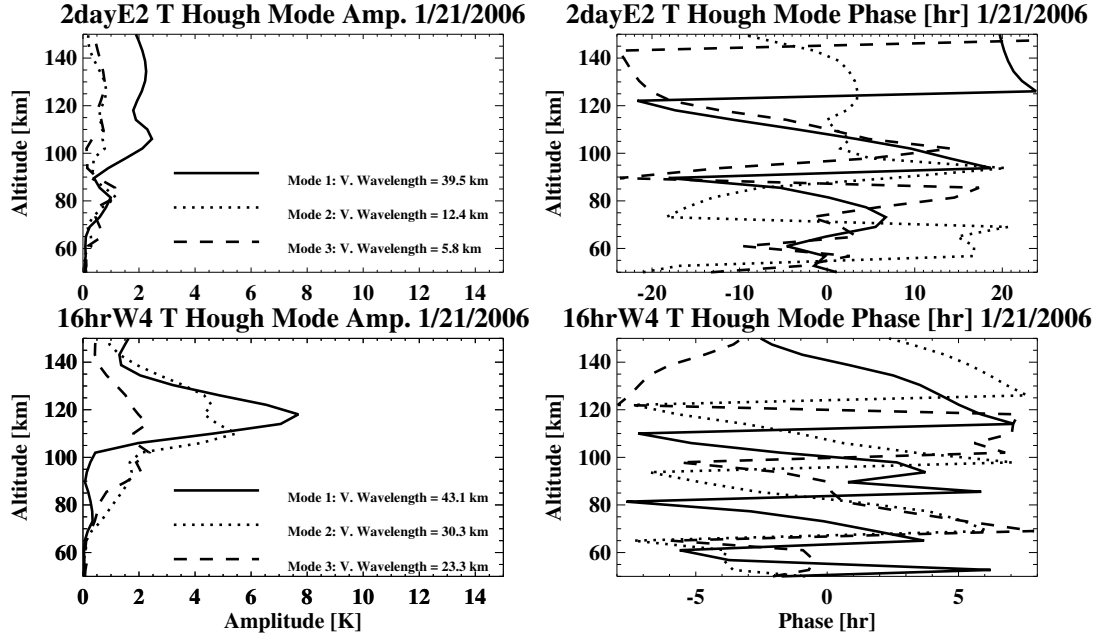


Figure 6.19: 16hrW4 amplitude (lower-left) and phase (lower-right), and 2dayE2 amplitude (upper-left) and phase (upper-right) as a function of altitude for January 21st, 2006 under the non-zero background winds specified by NOGAPS-ALPHA. Each Hough mode amplitude was extracted by least squares fitting theoretical Hough mode functions to the overall secondary wave amplitude and phases at each altitude level. Units are in degrees Kelvin.

## 6.7 Shape Function

The observed effects of the background winds on the spatial structure of the secondary waves are explained in this section by examining the linearized perturbation momentum equations for a non-zero zonal wind and viscous background atmosphere denoted by variable  $U$ :

$$i\sigma_D u' - [f + \zeta] v' + \left[ \frac{\partial U}{\partial z} + \frac{U}{a} \right] = F_{Pressgrad,x} + F_{fric,x} + F_{other,x} \quad (6.3)$$

$$i\sigma_D v' - [\hat{f}] u' = F_{Pressgrad,y} + F_{fric,y} + F_{other,y} \quad (6.4)$$

In Equations 6.3 and 6.4, the leading coefficients of the perturbation horizontal wind variables ( $u'$  and  $v'$ ) are simplified in terms of  $\sigma_D$ ,  $f$ ,  $\hat{f}$  and  $\zeta$  defined below in order to demonstrate the effects

of a zonal wind configuration on perturbation motion. Expressions  $\sigma_D$ ,  $f$ ,  $\hat{f}$  and  $\zeta$  are displayed by the following:

$$\sigma_D = \sigma + \frac{sU}{a \cos \phi} \quad (6.5)$$

$$\zeta = -\frac{1}{a \cos \phi} \frac{\partial}{\partial \phi} (U \cos \phi) \quad (6.6)$$

$$\hat{f} = f + \frac{2U \tan \phi}{a} \quad (6.7)$$

The variable denoted by  $\sigma_D$  represents the Doppler-shifted frequency of a tidal or planetary wave. For westward propagating waves ( $s < 0$ ), eastward background zonal winds ( $U > 0$ ) have the effect of decreasing the intrinsic wave frequency while the intrinsic frequency of eastward propagating waves ( $s > 0$ ) is increased in westward background zonal winds ( $U < 0$ ). Relative atmospheric vorticity is denoted by  $\zeta$ , which is dependent on the latitudinal gradient of the zonal wind. A non-zero latitudinal gradient of the background wind resulting in non-zero relative vorticity acts to alter the effectiveness of the Coriolis force ( $f$ ). For example, a positive gradient in the background winds in the northern hemisphere ( $f > 0$ ) decreases the magnitude of the leading coefficient of  $v'$  in Equation 6.3, which represents a decrease in the effective Coriolis force.

The impacts of the background winds on the latitudinal structure of a given wave may be encapsulated by the following expression derived by Ortland and Alexander ([72]):

$$\Delta = \frac{(\sigma_D^2 - (f + \zeta)\hat{f})}{4\Omega^2} \quad (6.8)$$

The preceding function is referred to as the shape function. Larger  $\Delta$ , which is a function of latitude, implies an enhanced wave response whereas smaller  $\Delta$  indicates suppressed wave response. Equation 6.8 demonstrates that a certain wave response is augmented by either increasing the Doppler-shifted frequency or decreasing the effective Coriolis force. It should be noted that a similar result to Ortland and Alexander, 2005 [72] can be obtained through a different procedure

by assuming equations of motion for an atmosphere described by constant Coriolis force with latitude (f-plane approximation). This method is described in detail in Forbes and Hagan, 1988 [16].

The shape function allows the effects of the background winds on the secondary wave response to be examined. Figure 6.20 displays the shape function for both the non-zero and zero background wind cases with the normalized 16hrW4 temperature amplitude at selected altitudes. The zero wind shape function is positive between  $\pm 50^\circ$  latitude and negative at other latitudes due to increasing Coriolis force moving away from the equator. The structure of the zero wind shape function indicates a large 16hrW4 response at low latitudes and evanescent response at high latitudes. These characteristics match the results for the 16hrW4 response for the zero background case shown presented earlier in section 6.1.

The introduction of the realistic background wind structure alters the shape function at each altitude. Below 85 km, the background zonal winds are mainly eastward in the northern hemisphere and westward in the southern hemisphere. Consequently, a greater Doppler-shifted frequency and shape function for the 16hrW4 are observed in the northern hemisphere than the southern hemisphere in the mesosphere. As a result of this background wind structure, the 16hrW4 amplitude is enhanced at mid-northern latitudes below 85 km, which can be observed in Figure 6.20. At higher altitudes, the peak of the shape function shifts from the northern to southern hemisphere as the background zonal winds reverse in each hemisphere. Thus, the 16hrW4 becomes most dominant in the southern hemisphere above 100 km. In contrast to the 16hrW4 results, the 2dayE2 wave is greatest at southern latitudes below 100 km (not shown) because of the westward background winds below. The 2dayE2 at higher altitudes is insignificant due to the factors discussed earlier in the chapter.

## 6.8 Mean Wind Effects on the Nonlinear Forcing Projection Responses

In order to fully understand the effects of mean winds on the secondary wave response, the numerical experiments conducted for a zero wind background atmosphere presented earlier

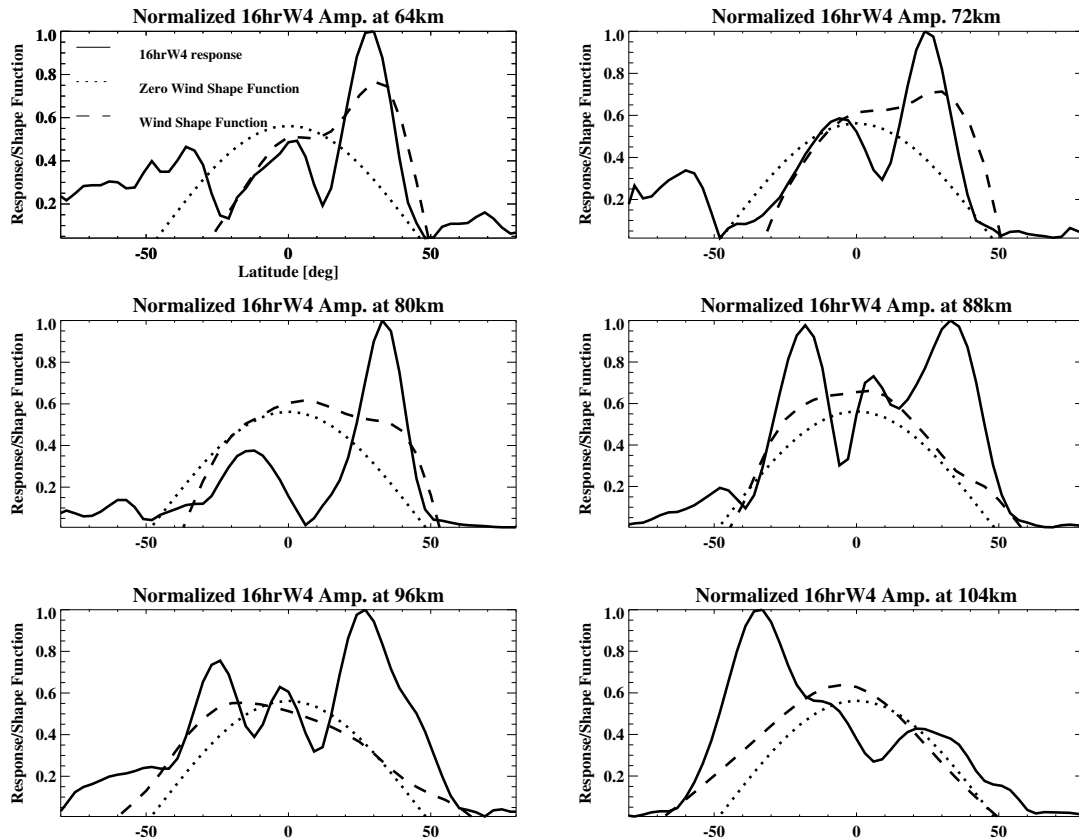


Figure 6.20: Effects of background winds on the shape function and 16hrW4 amplitude as a function of latitude at selected altitudes: 64 km (top-left), 72 km (top-right), 80 km (middle-left), 88 km (middle-right), 96 km (bottom-left), 104 km (bottom-right). The dotted line refers to the shape-function in a zero-background wind atmosphere. The dashed line represents the shape-function in a non-zero background wind atmosphere specified by NOGAPS-ALPHA. The solid line represents the normalized 16hrW4 amplitude response.

are repeated for the non-zero background wind case. Figure 6.21 presents the secondary wave response under the realistic background winds to the nonlinear forcing projected onto the first two propagating Hough modes. Unlike in the zero background wind case, the 16hrW4 response to the 1st mode forcing deviates from the classical Hough mode latitudinal structure. This result indicates the presence of mode coupling where the background winds are coupling the 1st mode response to higher order modes. From another perspective, the background winds shift the 1st mode response toward the northern hemisphere in the mesosphere and the southern hemisphere in the lower thermosphere, which correspond to the changes in the Doppler shifted frequency and shape function.

Similarly, the 16hrW4 response to the 2nd mode forcing is not characterized by the latitudinal structure of the 2nd Hough mode. The background winds cause the 16hrW4 2nd mode response to slightly skew towards the southern hemisphere between 90 and 110 km. At higher altitudes, the 16hrW4 2nd mode response becomes more symmetrical about the equator. The combination of the two 16hrW4 responses results in a structure that resembles the overall response (6.16), which indicates that the majority of the 16hrW4 response is still determined by the projection of the forcing onto the lowest order Hough modes. Hence, it is concluded the projected forcing onto the lowest order modes is still most effective at generating the most efficiently propagating 16hrW4 modes, which mainly determine the overall 16hrW4 response in the lower thermosphere and above.

Unlike the 16hrW4 response, the 2dayE2 responses to the Hough mode projected forcing are miniscule and does not resemble the overall 2dayE2 response shown in Figure 6.16. This is expected because as shown in the zero wind results, the 2dayE2 is mainly composed of evanescent modes at southern latitudes instead of the lower order propagating modes. By comparing the zero wind and non-zero wind results for the 2dayE2, it is observed the westward winds in the southern mesosphere slightly amplify the 2dayE2 evanescent modes in the MLT region, but does not lead to coupling to lower order, propagating modes.

Figure 6.22 presents the secondary wave response to 15 km sections of the forcing centered at 70 km and 90 km under a non-zero background wind configuration. Similar to the zero wind

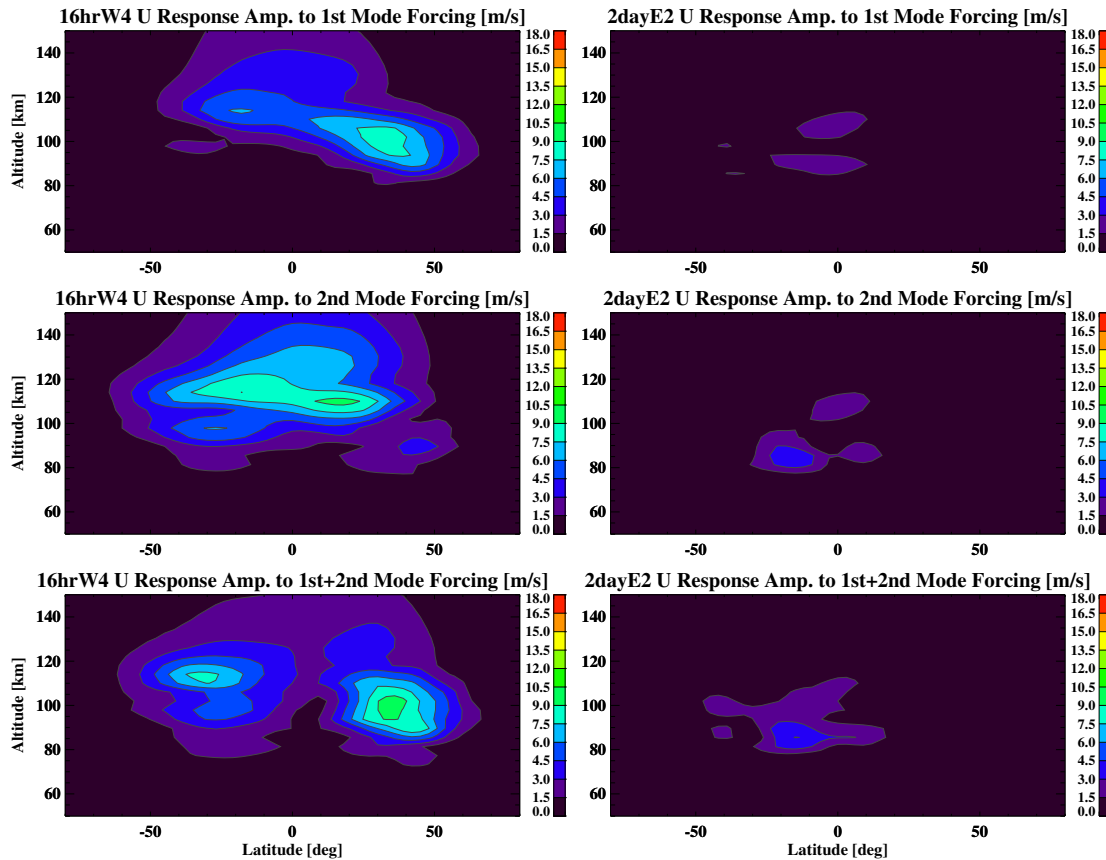


Figure 6.21: Zonal wind response amplitude to the 16hrW4-2dayE2 forcing projected onto the 16hrW4 1st propagating mode (upper-left), 16hrW4 2nd propagating mode (middle-left), 16hrW4 1st and 2nd modes (lower-left), 2dayE2 1st propagating mode (upper-right), 2dayE2 2nd propagating mode (middle-right), and 2dayE2 (lower-right). Background winds were used in the numerical simulation.

case, the 16hrW4 response to the 70 km is significant throughout the mesosphere and thermosphere region due to exponential wave growth. It can be observed that the 70 km forcing gives rise to the majority of the 16hrW4 response in the northern MLT region, which is caused by the eastward background winds present in the region. In contrast to the 16hrW4 response to the 70 km forcing, the vertical-latitude structure of the 16hrW4 wave response to the 90 km forcing does not deviate much from the zero wind case. The 16hrW4 response to the 90 km forcing is remains skewed towards the southern hemisphere between 100 km and 120 km and latitudinally symmetric at higher altitudes in the thermosphere. Since the background winds above 100 km are relatively

small in magnitude, the 16hrW4 response is only mildly impacted by the background winds. The most noticeable difference from the zero background wind case is a slight increase in the 16hrW4 amplitude, which is set up by a small eastward jet in the southern hemisphere at around 100 km.

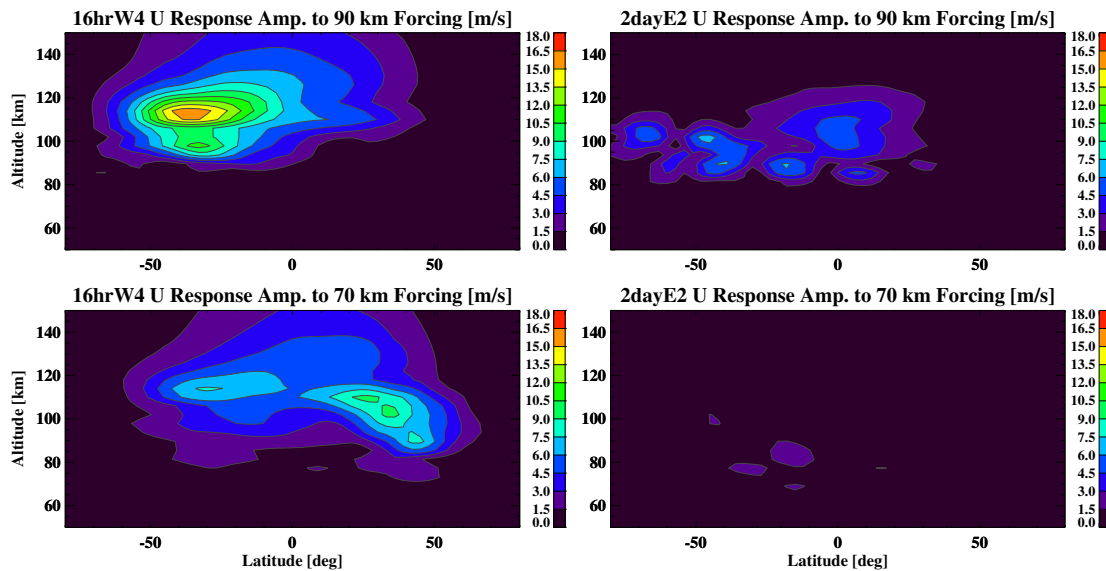


Figure 6.22: Secondary wave zonal wind response to the nonlinear forcing centered at a) 90 km for 16hrW4, b) 70 km for 16hrW4, c) 90 km for 2dayE2 and d) 70 km for 16hrW4 during January 21st, 2006. Background winds from NOGAPS-ALPHA were used in the numerical simulations.

Similar to the 16hrW4 results, the background winds have a larger impact on the 2dayE2 response to the 70 km forcing than the 90 km forcing. The 2dayE2 response to the 70 km forcing has almost been eliminated by the introduction of the background winds, which is mainly caused by mode coupling of the 1st propagating mode to higher order modes with smaller vertical wavelengths. Since the 2dayE2 response to the 70 km is primarily dependent on the efficient vertical propagation to the lower thermosphere, the effect of mode coupling to higher modes induced by the background winds is to significantly decrease the 2dayE2 response. In contrast, the background winds are smaller above 90 km, which results in minimal impact on the 2dayE2 response to the 90 km forcing. Like the zero wind case, the 2dayE2 response to 90 km forcing is mostly composed of evanescent modes that do not propagate far from the forcing region.

## 6.9 Time Evolution

To assess the time evolution of the secondary wave response, the linear model runs are repeated for each day in 2006, 2009 and 2010 from day of year DOY 7 through DOY 40. Six-day averages of nonlinear forcing, background winds and background temperatures centered on each day are used to compute secondary wave responses within the model.

Figure 6.23 displays the amplitude of the 16hrW4 and 2dayE2 waves at 90 km during January 2006. The largest 16hrW4 amplitudes during 2006 are observed before DOY 10 and around DOY 21 while slightly smaller amplitudes are present in between these days. The 16hrW4 decreases rapidly after DOY 25 and becomes insignificant after DOY 30. The 2dayE2 response during 2006 exhibits a similar temporal evolution although the maximum amplitudes are smaller than the 16hrW4 values. However, the temporal evolution of the secondary waves vary greatly on an inter-annual basis. During 2009, the secondary wave responses are brief, only achieving amplitudes greater than 5 K for a few days in mid-January. The 2010 secondary wave responses are more significant for a longer timespan than the 2009 secondary waves, but do not last as long as the 2006 secondary waves. Furthermore, the 2010 secondary waves peak at a later date than either the 2006 or 2009 secondary waves responses.

The temporal evolution of the secondary wave responses during each year exhibits a strong correlation with the temporal evolution of the nonlinear forcing. As presented and explained in Chapter 5, the momentum and thermal forcing for the 16hrW4 and 2dayE2 during 2006 5.19 are significant for several weeks in January, which is primarily a result of a long duration 2dayW3 event. Since the nonlinear forcing is the main factor in determining the secondary wave response, the secondary wave responses exhibits a similar temporal structure. During 2009, the nonlinear forcing lasts for only a few days, which produces the brief secondary waves responses presented in this section. Finally, the nonlinear forcing during 2010 achieves its greatest values at a later date, which results in the secondary waves peaking in early February instead of mid-to-late January.

However, the results also reveal that the temporal evolution of the secondary wave responses

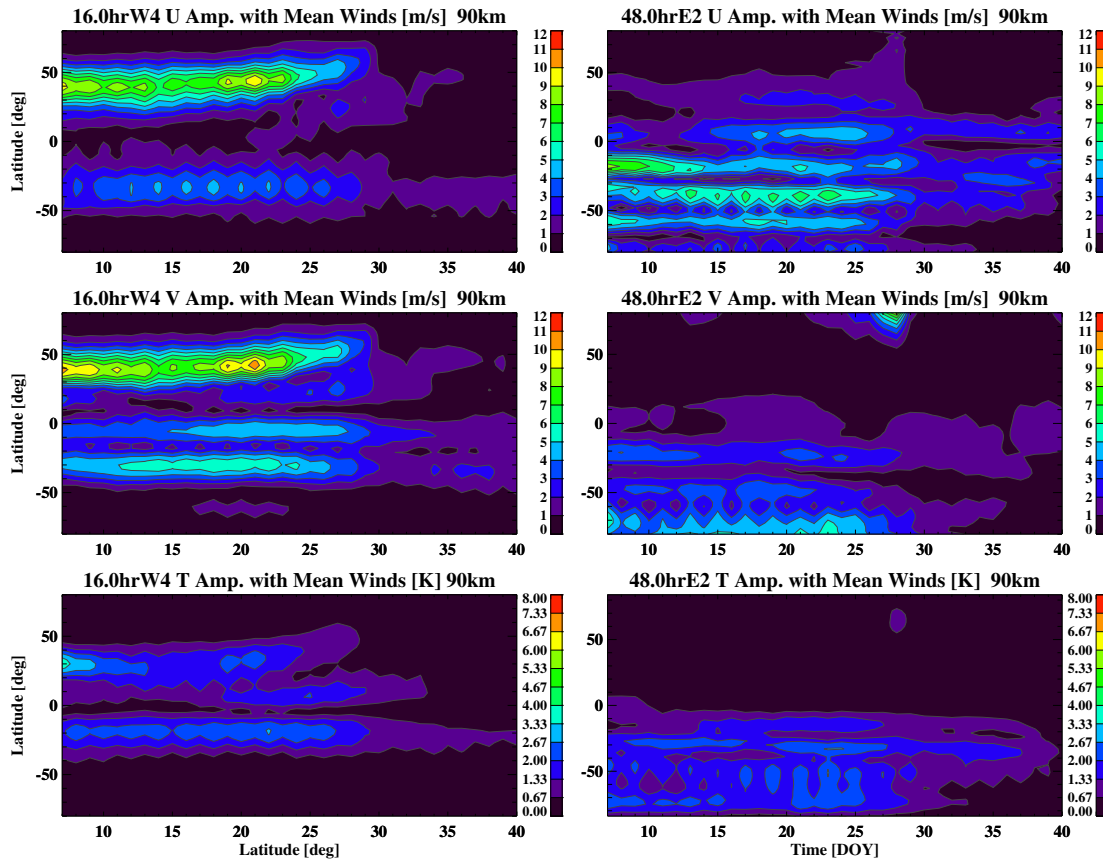


Figure 6.23: Temporal-latitude amplitude structure at 90 km during 2006 for 16hrW4 zonal wind (top-left), 16hrW4 meridional wind (middle-left), 16hrW4 temperature (bottom-left), 2dayE2 zonal wind (top-right), 2dayE2 meridional wind (middle-right), and 2dayE2 temperature (bottom-right). Secondary wave responses were computed with non-zero background winds.

occasionally deviates from the temporal structure of the nonlinear forcing. A perfect linear correlation between the secondary wave forcing and response temporal structures cannot be achieved primarily because the secondary wave response depends on the combination of forcing from three different fields (zonal momentum, meridional momentum and thermal), which are characterized by slightly different temporal and spatial structures. For instance, the 2006 momentum and thermal forcing for the 16hrW4 wave at 70 km (Figure 5.19) possesses a consistent latitudinal structure with time until about DOY 27. After this day, the latitudinal structure of the zonal momentum and thermal forcing of the 16hrW4 skews towards the northern hemisphere while the meridional forcing latitudinal structure remains constant. Although the maximum values of the 16hrW4 forcing does

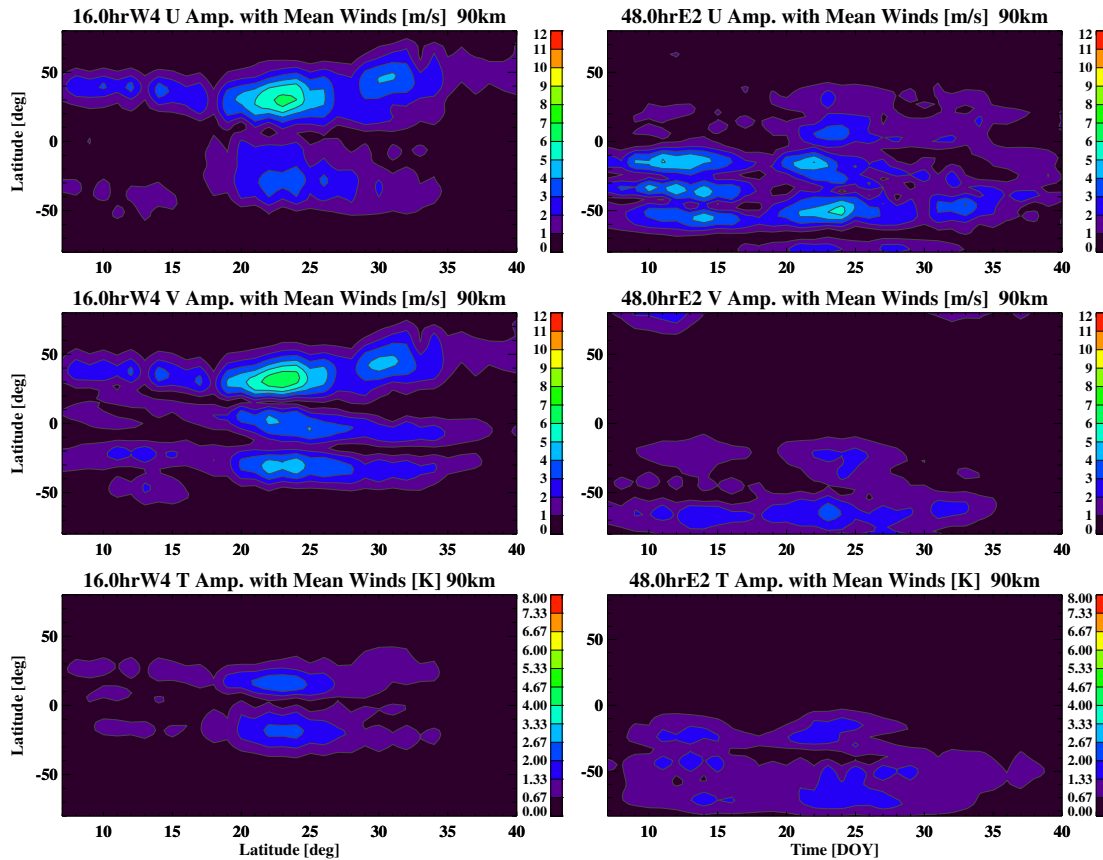


Figure 6.24: Temporal-latitude amplitude structure at 90 km during 2009 for 16hrW4 zonal wind (top-left), 16hrW4 meridional wind (middle-left), 16hrW4 temperature (bottom-left), 2dayE2 zonal wind (top-right), 2dayE2 meridional wind (middle-right), and 2dayE2 temperature (bottom-right). Secondary wave responses were computed with non-zero background winds.

not change during this day, the 16hrW4 response amplitude decreases rapidly in response to the changes in the zonal momentum and thermal forcing spatial structures. As explained previously in this chapter, the secondary wave response is determined by the projection of the forcing onto Hough modes. Thus, a change in the latitudinal structure of the forcing can modify the projection onto the wave Hough modes and subsequently, alter the magnitude of the secondary wave response.

The background winds have the primary effect of determining the spatial structure of the secondary wave responses. As shown in Figure 6.26, the background zonal winds in the mesosphere are generally eastward in the northern hemisphere and westward in the southern hemisphere. The eastward jet in the northern mesosphere is strong during the early portion of January, and subse-

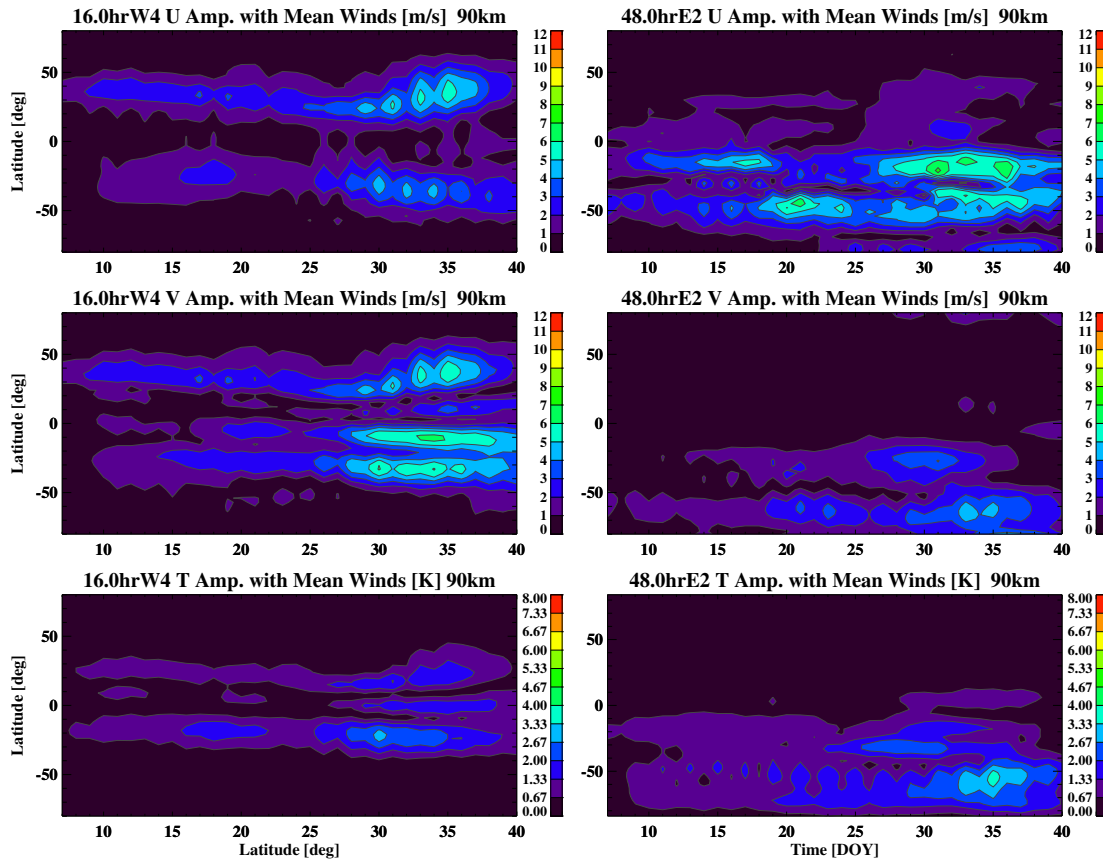


Figure 6.25: Temporal-latitude amplitude structure at 90 km during 2010 for 16hrW4 zonal wind (top-left), 16hrW4 meridional wind (middle-left), 16hrW4 temperature (bottom-left), 2dayE2 zonal wind (top-right), 2dayE2 meridional wind (middle-right), and 2dayE2 temperature (bottom-right). Secondary wave responses were computed with non-zero background winds.

quently weakens during the middle of the month. This reversal in the northern hemisphere eastward jet is associated with sudden stratospheric warming (SSW) events, which affects the background circulation in the upper stratosphere and lower mesosphere at mid-to-high latitudes in the northern hemisphere, and present in observations during 2006, 2009 and 2010 (Coy et al., 2009 [10]; Goncharenko et al., 2010 [22]; Goncharenko et al., 2013 [23]). After the weakening of the eastward jet, the background winds in the northern hemisphere increase again and veer towards higher latitudes. In the southern hemisphere, a strong westward jet dominates during the early portion of January and decreases throughout the month.

A comparison of the secondary wave response to the background winds demonstrates the

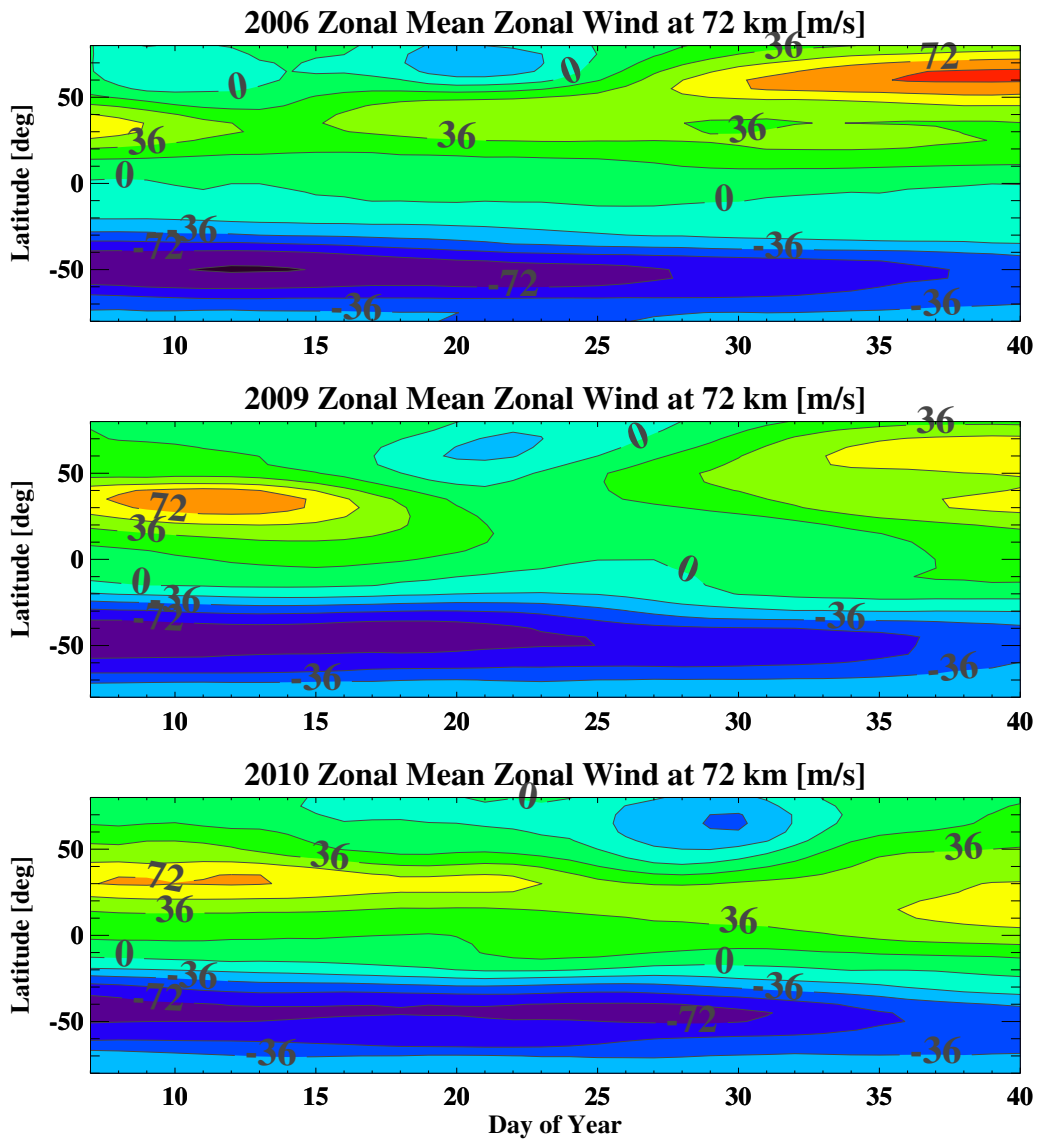


Figure 6.26: Temporal-latitude background zonal wind structure at 72 km during January 2006 (top), 2009 (middle), and 2010 (bottom).

considerable influence of the background winds on secondary wave spatial structure. The 16hrW4 response at 90 km is largest around 45°N during the early portion of January 2006 and 2009 because the eastward winds in the northern mesosphere are more favorable for westward wave propagation. During the latter portion of January 2006 and 2009, the eastward wind jet veers towards higher

latitudes which causes the 16hrW4 response to also skew in that direction. The 2010 16hrW4 wave is characterized by a more latitudinally symmetric structure than the 16hrW4 during the other years. Since the 16hrW4 wave during 2010 reaches its peak during the early portion of February, the wave travels through a weaker westward jet in the southern hemisphere, which is more conducive to wave propagation. As a result, there is significant 16hrW4 in the southern hemisphere in addition to the northern hemisphere.

In contrast, the 2dayE2 response is largest in the southern hemisphere partly due to the westward background winds in that region. However, because the 2dayE2 response mainly consists of in-situ forced modes instead of propagating modes forced at lower altitudes, the 2dayE2 response is still largest in the southern hemisphere even without the presence of background winds. This was demonstrated earlier in the chapter by comparing the 2dayE2 results with and without the inclusion of background winds in the model. The main effect of the background winds on the 2dayE2 response is to slightly enhance the response in the southern hemisphere and reduce the wave amplitude in other regions.

## 6.10 Comparison to NOGAPS

A comparison between the 16hrW4 and 2dayE2 responses in the linear model and the corresponding responses in the NOGAPS-ALPHA is performed to provide validation of the results presented in this chapter. Since the NOGAPS-ALPHA model assimilates observational data, it is expected to accurately represent the secondary wave behavior. A comparison of the NOGAPS-ALPHA secondary waves to observations from TIMED-SABER presented earlier in this dissertation provides evidence that the secondary waves within the reanalysis model are indeed an accurate portrayal of reality. Furthermore, a recent study performed by Lieberman et al., 2016 [48] showed that the NOGAPS-ALPHA results for the 2dayE2 and 16hrW4 waves compared favorably with ground-based observations. Thus, it is concluded that the secondary waves contained within NOGAPS-ALPHA are physically accurate.

Figure 6.27 shows the comparison of the 2006 results during the peak day of the 2dayW3 for

altitudes where NOGAPS-ALPHA output is provided (up to 95 km). The plots reveal that the linear tidal model results (with NOGAPS-ALPHA background winds and temperatures) capture the majority of the large scale features the 16hrW4 vertical-latitudinal structure contained within NOGAPS-ALPHA. The 16hrW4 structure in both models exhibit a larger response in the northern hemisphere and differ in maximum amplitude by only about 1-2 m/s. The large scale features of the 2dayE2 above 80 km in the NOGAPS-ALPHA model shown in Figure 6.27 are also contained within the linear model results. At lower altitudes however, the 2dayE2 in NOGAPS-ALPHA displays larger amplitudes.

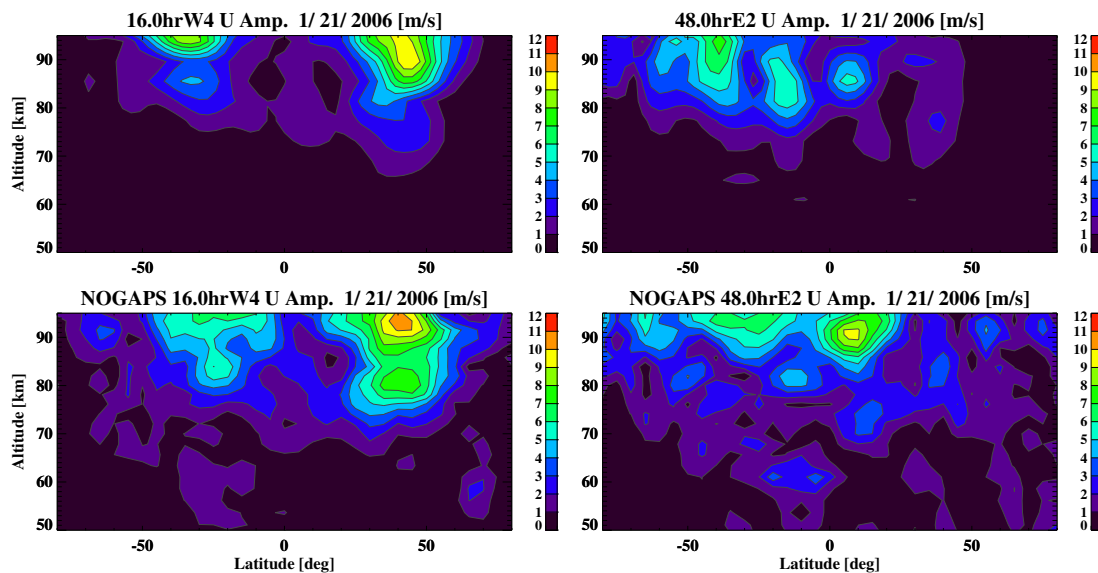


Figure 6.27: Vertical-latitudinal amplitude structure on January 21st, 2006 for the linear model 16hrW4 zonal wind (top-left), NOGAPS-ALPHA 16hrW4 zonal wind (bottom-left), linear model 2dayE2 zonal wind (top-right), and NOGAPS-ALPHA 2dayE2 zonal wind (bottom-right).

The temporal-latitudinal structures of each secondary wave at 90 km computed from each model are juxtaposed in Figure 6.28. The 16hrW4 response in both models are similar in structure, exhibiting the largest amplitudes in the northern hemisphere at approximately  $45^{\circ}\text{N}$ . Both models compute smaller responses in the opposite hemisphere at  $45^{\circ}\text{S}$ . The major differences between the 16hrW4 responses in each model are observed after DOY 28. During these days, the NOGAPS-ALPHA 16hrW4 response exhibits amplitudes of about 6-7 m/s in the northern hemisphere while

the response within the linear tidal model is nonexistent. In contrast, there is less agreement between the 2dayE2 temporal-latitudinal structures computed using each model. Although both models compute similar amplitude values in the southern hemisphere, the NOGAPS-ALPHA 2dayE2 response displays much larger amplitudes near the equator.

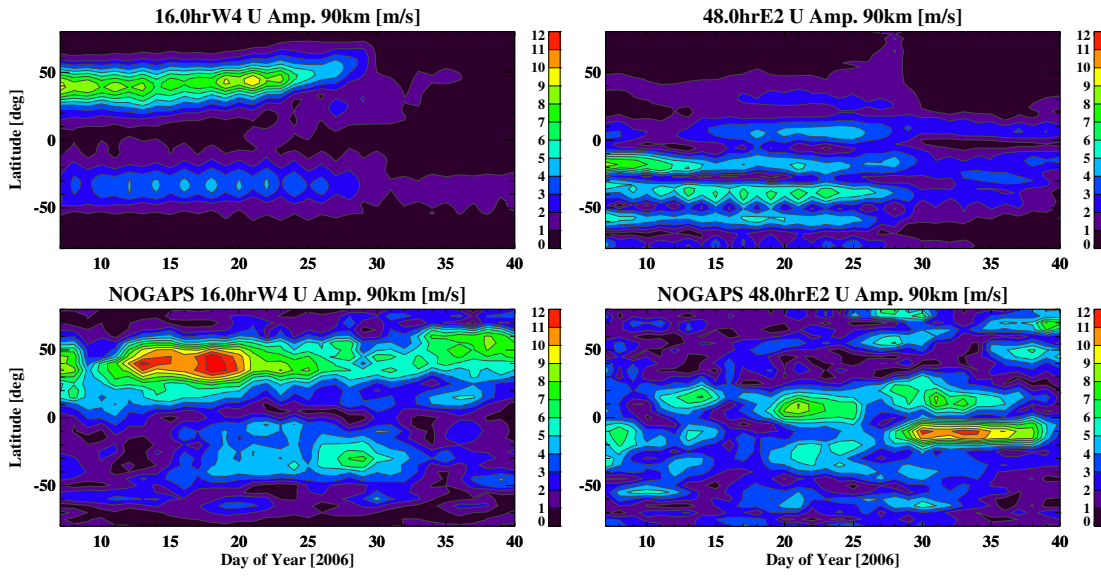


Figure 6.28: Temporal-latitudinal amplitude structure at 90 km for the linear model 16hrW4 zonal wind (top-left), NOGAPS-ALPHA 16hrW4 zonal wind (bottom-left), linear model 2dayE2 zonal wind (top-right), and NOGAPS-ALPHA 2dayE2 zonal wind (bottom-right).

The comparison between the NOGAPS-ALPHA and linear model secondary wave results can be utilized to assess the significance of nonlinear wave-wave interaction as a wave source. The general agreement between the 16hrW4 responses in both models indicate that the major source of this wave is the nonlinear interaction between the 2dayW3 and DW1. In contrast, the larger 2dayE2 amplitudes observed in the NOGAPS-ALPHA than in the linear model suggests that other mechanisms may assume a role in generating this wave. Other than nonlinear wave-wave interaction, a likely source for the 2dayE2 is the polar night jet instability (Manney et al., 1993 [58]), which has been studied in models and observations. Since the first propagating mode of the 2dayE2 behaves like a Kelvin wave, tropical convection in the troposphere may possibly generate the 2dayE2 wave in the MLT equatorial region. The Kelvin wave maximizes in the zonal wind field

at the equator as observed in NOGAPS-ALPHA, which indicates tropical convection is a possible source of the 2dayE2. However, more work needs to be conducted to validate this theory.

Finally, the comparison presented in this section highlights the role of a linear model in studying the potential transmission of secondary wave effects to higher altitudes in the ionosphere-thermosphere system. Unlike NOGAPS-ALPHA and current observational data sets, the linear model can capture the secondary wave structure at higher altitudes in the thermosphere system. The general agreement between the NOGAPS-ALPHA and linear model secondary wave results below 95 km provides support that the linear model accurately simulates secondary wave dynamic behavior in the MLT region and may correctly predict the secondary wave response in the thermosphere. However, complete validation of the secondary wave response in the middle thermosphere is not currently possible due to the lack of reanalysis and observational data sets that cover this region. Nevertheless, the linear model results provided in this chapter are still valuable to the atmospheric-space weather coupling research field because they provide the most clear evidence of secondary wave propagation to the upper atmosphere to date. The results discussed in this chapter have shown that the 16hrW4 may effectively propagate into the lower thermosphere due to its long vertical wavelength and efficient forcing structure while the 2dayE2 shows weak activity above 100 km due to its short vertical wavelength. Since the lower thermosphere is coupled to the ionosphere through driving of the E-region dynamo region (Immel et al., 2006 [42]), the effects of the 16hrW4 may be transmitted to even higher altitudes. Future work is necessary to elucidate the effects of the 16hrW4 wave on the entire SAIR.

## Chapter 7

### NONLINEAR INTERACTION BETWEEN QUASI-TWO DAY WAVE AND MIGRATING SEMIDIURNAL TIDE

The observational and modelling results presented thus far in this dissertation have focused on the generation of secondary waves from the nonlinear interaction between the 2dayW3 and DW1. These results have led to a better understanding of the factors that govern the manifestation of secondary waves within the space-atmosphere interaction region. With the nonlinear interaction between the 2dayW3 and DW1 now elucidated, the final portion of this thesis shifts its focus to the 2dayW3 interaction with the migrating semidiurnal tide (SW2) in order to provide a broader context of global-scale wave-wave interaction. The results contained in this chapter show that the interaction between the 2dayW3 and SW2 leads to much larger secondary waves in the thermosphere than 2dayW3-DW1 interaction, and thus, serves as a prime example of space-atmosphere vertical coupling.

#### 7.1 Introduction

Along with the migrating diurnal tide (DW1), the migrating semidiurnal tide (SW2) is one of the principal periodic responses of the atmosphere to solar heating. The SW2 is primarily forced by water vapor absorption of infrared radiation in the troposphere and ozone absorption of ultraviolet radiation in the stratosphere (Forbes and Garrett, 1978 [14]). It propagates westward with a period of 12 hours and zonal wavenumber 2 and is, hence, sun-synchronous. Although the SW2 is forced in the lower portions of the atmosphere, it propagates vertically with increasing

amplitude and becomes one of the largest tidal components in the MLT region. Additionally, SW2 has the capability of propagating farther into the thermosphere than DW1 due to its long vertical wavelength.

The nonlinear interaction between the 2dayW3 and SW2 has been speculated in past studies (Manson and Meek, [60]; Beard et al., 1999 [3]; Moulden and Forbes, 2014 [66]), but has not received much recent attention. In a study conducted by Beard et al. ([3]), meridional winds derived from a ground-based meteor radar at approximately 53° N were analyzed to present evidence of 2dayW3-SW2 interaction. As shown in Figure 7.1, the periodogram revealed dominant spectral peaks at periods of 2 and 0.5 days, which correspond to the 2dayW3 and SW2 respectively. Smaller peaks at 16 and 9.6 hours were also observed from the data, which were surmised to represent the 9.6hrW5 and 16hrE1 secondary waves produced from 2dayW3-SW2 interaction. However, this study conducted by Beard et al., 1999 [3] and other past studies have not clearly explained the process of manifestation of the secondary waves generated from 2dayW3-SW2 interaction and its potential impacts on atmospheric vertical coupling.

Like the 2dayW3-DW1 interaction, the 2dayW3-SW2 nonlinear interaction is examined in this chapter through a combination of numerical models. NOGAPS-ALPHA reanalysis output is utilized to extract observationally-based estimates of the SW2 and 2dayW3 throughout the stratosphere and mesosphere. Primary wave estimates are subsequently used to compute the nonlinear forcing for the 9.6hrW5 and 16hrE1 secondary waves. Finally, the nonlinear forcing is implemented within a linear tidal model to compute and analyze secondary wave responses.

## 7.2 SW2-2dayW3 Amplitudes

Similar to the extraction of DW1 and 2dayW3 estimates, amplitude and phase estimates at each altitude and latitude grid point for the SW2 are extracted from NOGAPS-ALPHA through a 2-dimensional FFT of temperature and horizontal wind data over a 6-day temporal window. The 6-day window is slid forward by one day to obtain SW2 estimates from day of year 7 to day of year 40. Estimates for the SW2 are only obtained up to approximately 95-100 km due to the upper

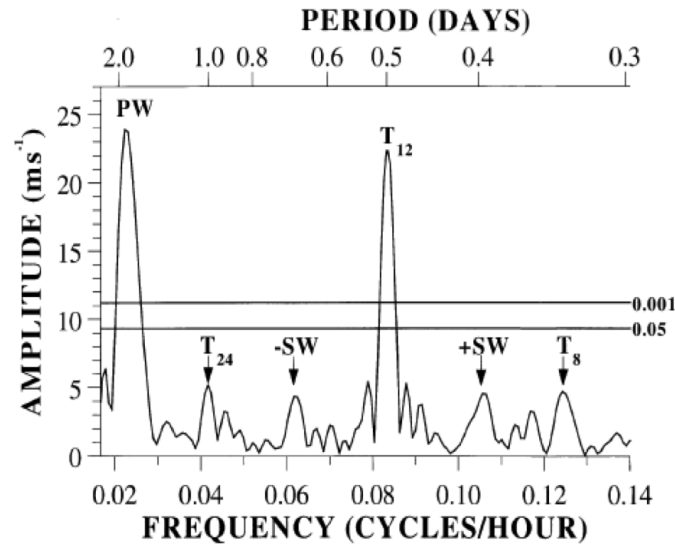


Figure 7.1: Periodogram of meridional wind derived from a ground-based meteor radar at  $53^{\circ}$  M. Primary peaks are observed at 2 days and 12 hours, which correspond to the 2dayW3 and SW2 waves. Sideband peaks likely correspond to secondary waves generated from nonlinear interaction. Figure adapted from Beard et al., 1999 [3].

boundary of the model.

Amplitude estimates for the SW2 centered around January 21st, 2006 in the zonal wind, meridional wind and temperature fields are displayed in Figure 7.2 along with the 2dayW3 estimates. The results reveal that that the SW2 amplitude during the January timeframe in all three fields increases with altitude and reaches a maximum near the model upper boundary. The SW2 structure is highly asymmetric, exhibiting larger amplitudes in the northern hemisphere than in the southern hemisphere. In the zonal and horizontal wind fields, the SW2 peaks at around  $60^{\circ}$  N and attains maximum values of about 30-40 m/s. In contrast, the SW2 amplitude in temperature reaches maximum values of about 8 K at approximately  $40^{\circ}$  N.

The SW2 phase estimates centered around the same date are displayed in Figure 7.3. The phase results suggest primarily downward phase progression, particularly in the northern hemisphere, which is consistent with the wave source existing at lower altitudes in the troposphere and stratosphere. A vertical wavelength of approximately 40-50 km can also be observed in the results.

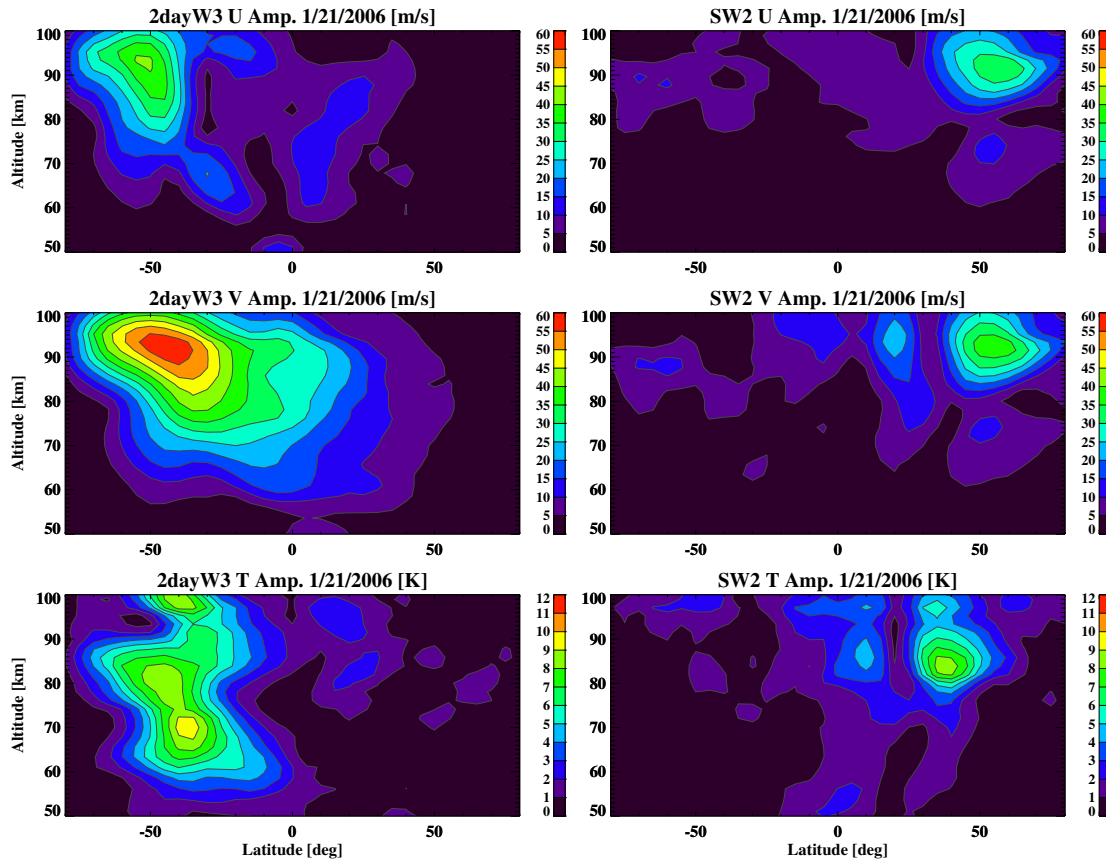


Figure 7.2: Amplitude of the 2dayW3 and SW2 as a function of latitude and altitude during January 2006. Estimates for the zonal wind field are shown on top, meridional wind in the middle and temperature on the bottom.

By comparing the results presented here for the SW2 amplitude and vertical wavelength to the SW2 Hough modes computed from classical tidal theory, it can be concluded that SW2 structure is dominated by the (2, 4) and (2, 5) modes. The (2, 4) and (2, 5) modes are characterized by latitudinal structures that contain primary amplitude peaks at around  $\pm 35\text{-}40^\circ$  and vertical wavelengths of 53.8 km and 41.0 km respectively. These modes contrast the lower order Hough modes for the SW2, which are characterized by primary amplitude peaks at lower latitudes and longer vertical wavelengths.

Figure 7.4 presents the temporal-latitudinal amplitude structure of the SW2 over January-February 2006 at 90 km. NOGAPS-ALPHA estimates for the 2dayW3 are also juxtaposed with

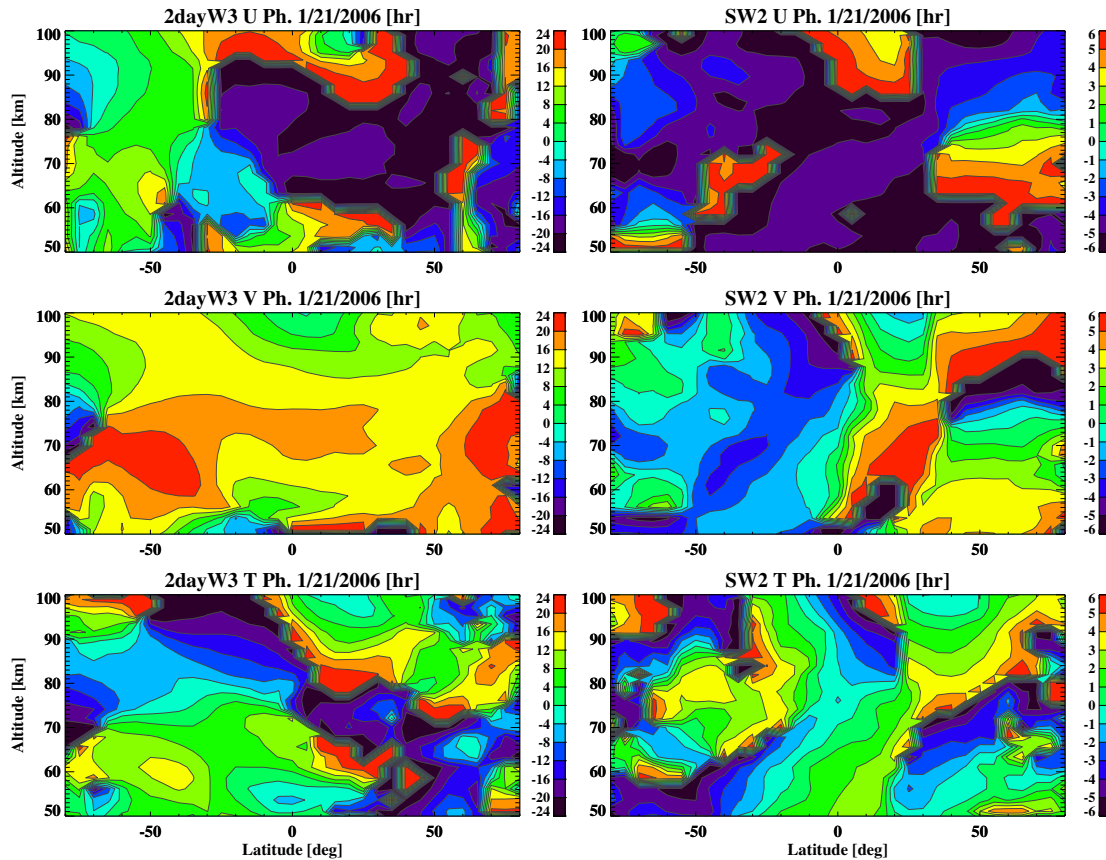


Figure 7.3: Phase in hours of the 2dayW3 and SW2 as a function of latitude and altitude during January 2006. Estimates for the zonal wind field are shown on top, meridional wind in the middle and temperature on the bottom.

the SW estimates on the figure for comparison. The results for the SW2 reveal short-term tidal enhancements around January 8th, January 21st, and February 2nd, but an explanation for this observation has not been explored. Moreover, unlike with the DW1-2dayW3 interaction, a clear anti-correlation between the 2dayW3 and the SW2 is not observed in the NOGAPS-ALPHA results, which indicates that the 2dayW3 is affecting the SW2 amplitude through other dynamic mechanisms, if at all. Since the effects of the 2dayW3 on the short-term variability of the SW2 has not been investigated by any study to date and is beyond the scope of this dissertation, further detail is not provided here.

Due to the lack of short-term (less than 60 day) observations of the SW2 on a global-scale, the

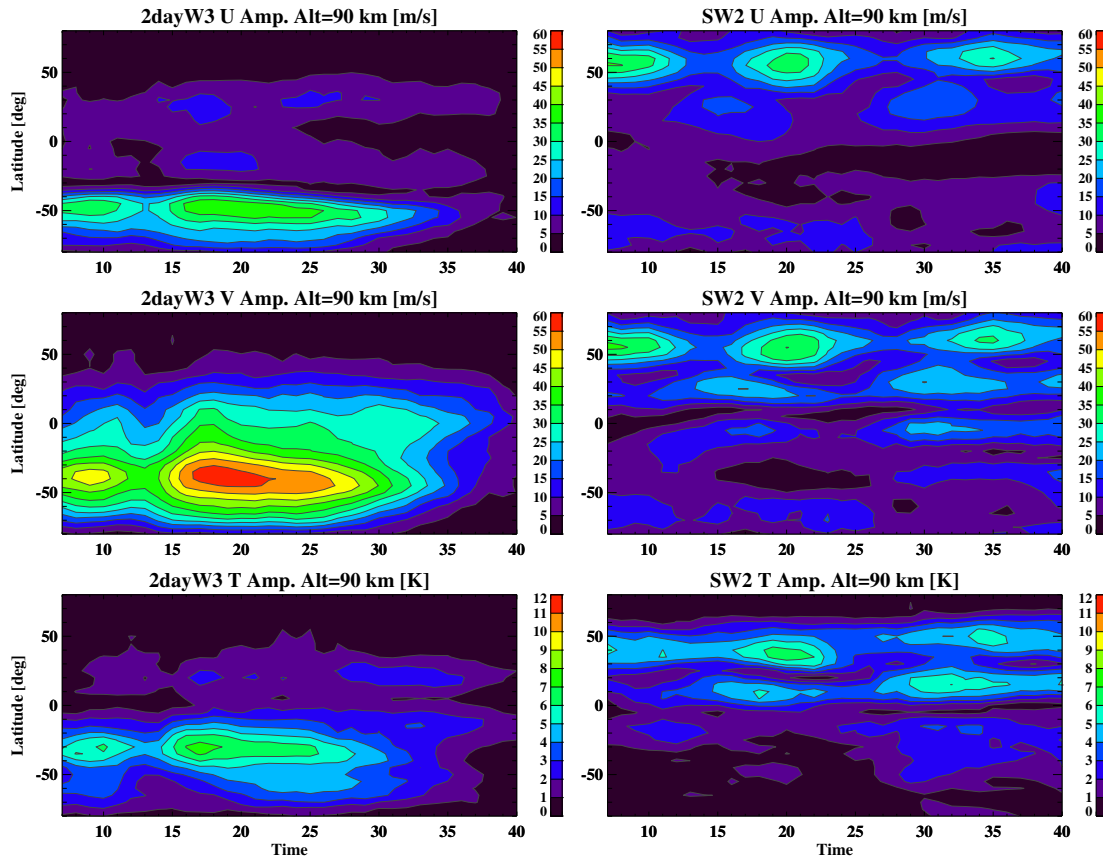


Figure 7.4: Amplitude of the 2dayW3 and SW2 as a function of time and latitude at 90 km during January 2006. Estimates for the zonal wind field are shown on top, meridional wind in the middle and temperature on the bottom.

SW2 estimates obtained from NOGAPS-ALPHA has yet to be validated. Instead of developing a new technique to produce short-term global estimates of the SW2, validation is provided here for the SW2 observed in NOGAPS-ALPHA by comparing the dissertation results to past studies which extracted tidal estimates from satellite observations over one yaw cycle (Zhang et al., 2006 [120]; Pancheva et al., 2009 [80]; Wu et al., 2011 [117]). Although the estimates obtained from these past studies represent averages over monthly periods, a comparison with these results can help determine the plausibility of the NOGAPS-ALPHA estimates.

The study by Pancheva et al., 2009 [80] examined the SW2 in the MLT region by applying a least squares method to SABER temperatures over a 60-day yaw cycle. Similar to NOGAPS-

ALPHA, they observed the largest SW2 amplitudes in the northern hemisphere during January 2006 with maximum values of about 7-8 K at around 90 km and 40°N. Much smaller amplitudes of about 0-2 K were found at 90 km in the southern hemisphere during this time, which matches the NOGAPS-ALPHA results. They also observed the SW2 vertical wavelength to be approximately 35 km, which is slightly lower than what is observed in NOGAPS-ALPHA. It should also be noted that the study extracted SW2 estimates from SABER temperatures up to 120 km in altitude and found the SW2 to maximize at around 110 km. This indicates that the NOGAPS-ALPHA model is unable to capture the entire vertical structure of the SW2 and hence, does not account for the secondary wave forcing that may exist in the lower thermosphere. However, the majority of the secondary wave forcing is still expected to exist below the NOGAPS-ALPHA upper boundary because as shown in the previous chapters, the 2dayW3 amplitude maximizes around 90-95 km and decreases above that altitude.

The SW2 horizontal wind estimates extracted from NOGAPS-ALPHA may also be compared to Wu et al., 2011 [117], which examined the SW2 from TIDI wind observations from 2002-2009. Similar to Pancheva et al., 2009, Wu et al., 2011 used a 60-day sliding window to cover a diurnal range in local time and extract the SW2 with minimal aliasing. Their results showed that the SW2 is much larger in the northern hemisphere than the southern hemisphere and peaks around 60°, which agrees with the NOGAPS-ALPHA results. They observed maximum zonal and meridional wind amplitude values of about 40 m/s in the northern hemisphere at 95 km. Furthermore, their phase estimates indicated that the SW2 is described by a vertical wavelength of approximately 30-35 km during December solstice 2005, which is comparable to the SW2 vertical wavelength observed in NOGAPS-ALPHA several weeks later.

The approximate agreement between the SW2 extracted from NOGAPS-ALPHA and past global satellite observations provide confidence that the SW2 estimates presented here are an accurate representation of reality. Although the short-term evolution of the SW2 observed in NOGAPS-ALPHA cannot be verified, these estimates should still serve the purpose of understanding the generation of secondary waves from 2dayW3-SW2 interaction and comparing to the 2dayW3-DW1

interaction products.

### 7.3 Nonlinear Forcing

The 2dayW3 and SW2 estimates extracted from NOGAPS-ALPHA allows for the computation of zonal momentum, meridional momentum and thermal forcing for the 9.6hrW5 and 16hrE1 secondary waves. The vertical-latitudinal structure of the nonlinear forcing amplitude are presented in Figure 7.5 while the forcing phase structure can be found in Appendix F. As expected, the momentum and thermal forcing for each secondary wave increases with altitude throughout the mesosphere and attains maximum values around 90-95 km, which is where the primary wave amplitudes are largest. Overall, there are slight differences between the forcing amplitude structures of each secondary wave. The meridional forcing amplitude for the 9.6hrW5 is concentrated at low-to-mid latitudes whereas the meridional forcing amplitude for the 16hrE1 is mainly concentrated at high southern latitudes poleward of 50°S. However, the zonal momentum and thermal forcing for the 9.6hrW5 and 16hrE1 are quite similar in that both wave forcing structures exhibit generally high latitude zonal forcing and low latitude thermal forcing.

A comparison of the nonlinear forcing presented in Figure 7.5 to the forcing amplitude values for the 16hrW4 and 2dayE2 secondary waves (Figure 5.15) concludes the 9.6hrW5 and 16hrE1 forcing amplitudes to be smaller in overall magnitude. As shown in Chapter 5, the 16hrW4 and 2dayE2 meridional forcing amplitude displayed maximum values of approximately  $3.6 \times 10^{-4} \text{ m/s}^2$ , which is about 10-25% greater than the maximum forcing amplitude values of the 9.6hrW5 and 16hrE1 secondary waves. Additionally, the 16hrW4 and 2dayE2 secondary wave forcing is much greater at altitudes below 80 km than the respective forcing for the 9.6hrW4 and 16hrE1 waves. The smaller forcing amplitudes observed for the 9.6hrW5 and 16hrE1 secondary waves is explained by the differences between the DW1 and SW2 amplitude structures. During January 2006, the DW1 amplitude structure is characterized by mainly low latitude peaks that are primarily symmetric about the equator. In comparison, the SW2 amplitude structure displays the largest values at mid-to-high latitudes in the northern hemisphere. As a result, the DW1 amplitude structure possesses

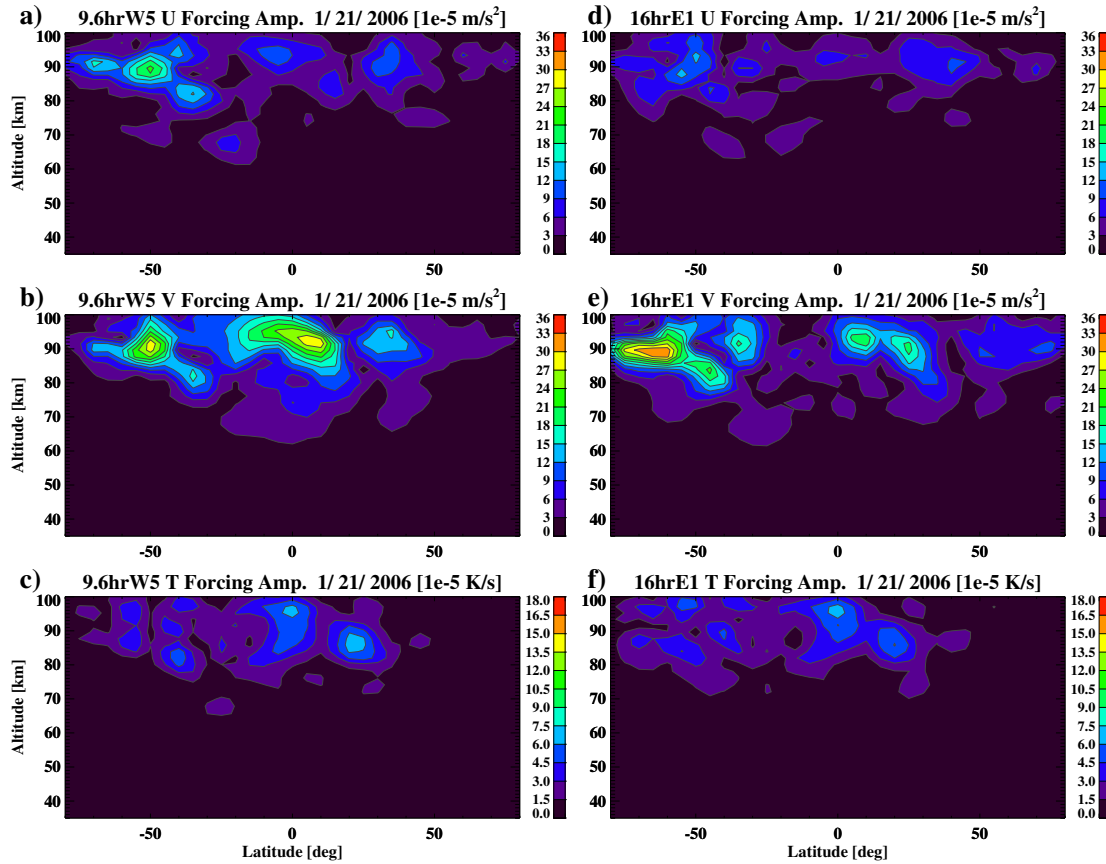


Figure 7.5: Vertical-latitude amplitude structure centered at January 21, 2006 for a) 9.6hrW5 zonal momentum forcing, b) 9.6hrW5 meridional momentum forcing, c) 9.6hrW5 thermal forcing, d) 16.0hrE1 zonal momentum forcing, e) 16.0hrE1 meridional momentum forcing, and f) 16.0hrE1 thermal forcing. Nonlinear forcing amplitude is derived from primary wave amplitude and phase estimates shown in the previous section.

a larger overlap with the 2dayW3, which is most dominant middle southern latitudes and almost non-existent at high latitudes in the northern hemisphere. This leads to larger nonlinear forcing values due to advection for the 16hrW4 and 2dayE2 waves than the 9.6hrW5 and 16hrE1 waves.

An intriguing question is whether the smaller nonlinear forcing for the 9.6hrW5 and 16hrE1 secondary waves leads to smaller secondary wave responses. Although the magnitude of the nonlinear forcing does indeed play a role in determining the secondary wave response, other factors such as secondary wave frequency and wavelength are at least as equally important. This question is investigated in the remaining portion of this chapter, which presents results for the 9.6hrW5 and

16hrE1 secondary wave responses obtained from the linear tidal model.

## 7.4 Secondary Wave Responses

The nonlinear forcing values produced from the interaction between the 2dayW3 and SW2 are utilized to compute secondary wave responses in a linear tidal model. Figure 7.6 shows the vertical-latitude amplitude structures of the 9.6hrW5 and 16hrE1 secondary waves for a background atmosphere described by zero zonal mean wind and an equatorial temperature profile obtained from the MSIS model. The results for this case reveal that the 9.6hrW5 amplitude increases rapidly in the MLT region between 80 km and 120 km. At 120 km, the 9.6hrW5 reaches its maximum amplitude of approximately 36 m/s in zonal wind, 30 m/s in meridional wind and 36 K in temperature. The 9.6hrW5 gradually decreases with altitude above 120 km although moderate amplitude values are still observed at 200 km. The model results also demonstrate that the 9.6hrW5 latitudinal structure is predominantly described by two peaks in the zonal wind and temperature fields at around  $30^\circ$  N/S and 3 peaks in the meridional field at  $40^\circ$ S,  $0^\circ$ , and  $40^\circ$ N. Slightly larger 9.6hrW5 amplitude values are observed in the northern hemisphere.

Like the 9.6hrW5, the 16hrE1 wave is only significantly large at altitudes above 80 km. However, the 16hrE1 amplitudes are much smaller than the 9.6hrW5, attaining maximum values of only 7 K in temperature and 8 m/s in meridional wind. Furthermore, unlike the 9.6hrW5 wave, the 16hrE1 wave amplitude is approximately constant with altitude within the thermosphere region. The 16hrE1 features a latitudinal structure described by two dominant peaks at around  $40$ - $45^\circ$  N/S in the zonal wind and temperature fields and one dominant peak at the equator. Higher order latitudinal structures can be observed between 80 and 100 km in both the horizontal and meridional wind fields.

The vertical-latitude phase structures for the 16hrE1 and 9.6hrE1 waves are displayed in Figure 7.7. The 9.6hrW5 phase values exhibit a primarily asymmetric latitudinal structure in the zonal wind and temperature fields and a symmetric structure in the meridional wind field. Additionally, the 9.6hrW5 meridional wind phase values near the equator are out-of-phase with the

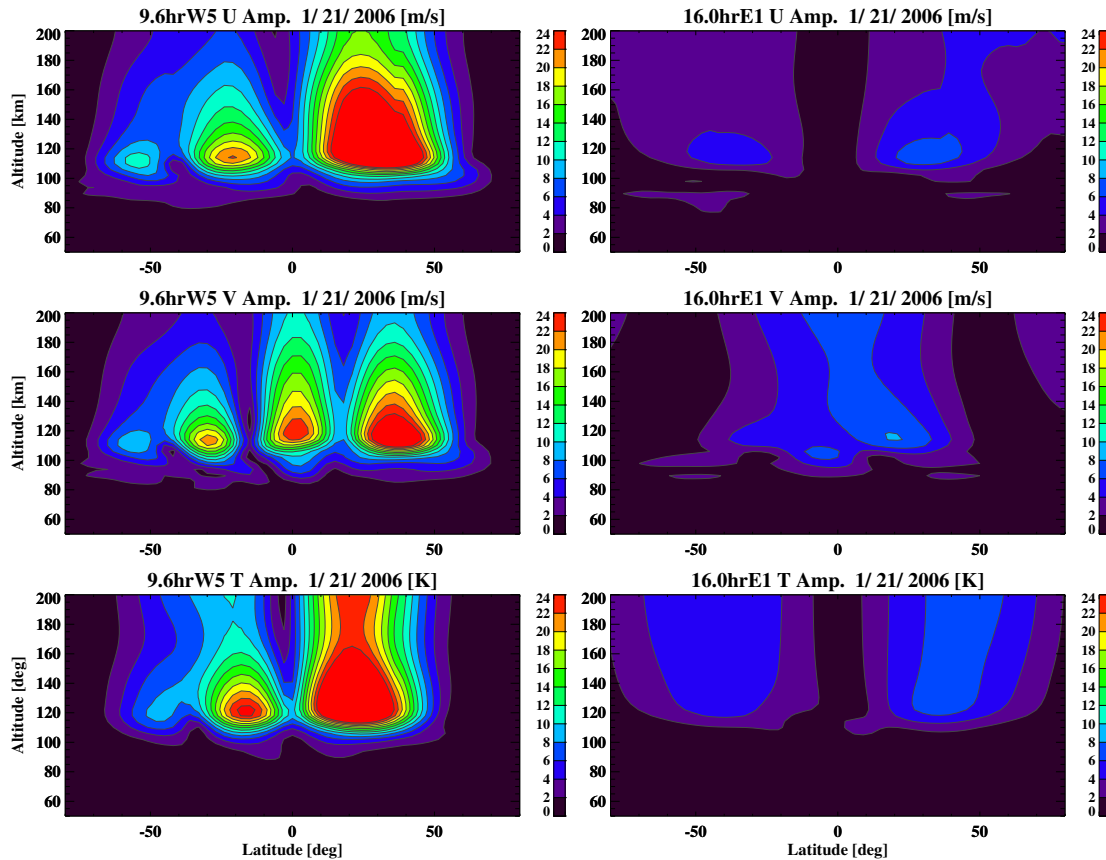


Figure 7.6: Vertical-latitude amplitude structure computed from the linear tidal model centered on January 21st, 2006 for the 9.6hrW5 zonal wind (upper-left), 9.6hrW5 meridional wind (middle-left), 9.6hrW5 temperature (lower-left), 16.0hrE1 zonal wind (upper-right), 16.0hrE1 meridional wind (middle-right), and 16.0hrE1 temperature (lower-right). Background winds are set to zero and background temperatures are set to equatorial values from NOGAPS-ALPHA.

phase values at higher latitudes. The 16hrE1 phase structure is similar to the 9.6hrW5 phase structure in that it is also described by latitudinal asymmetry in the temperature and zonal wind fields and latitudinal symmetry in the meridional wind field. Differences from the 9.6hrW5 latitudinal phase structure are noticeable in the meridional wind field where the 16hrE1 is described by near constant phase with latitude between  $60^{\circ}\text{S}$  and  $60^{\circ}\text{N}$  and anti-phase regions at higher latitudes.

The downward phase progression with altitude observed for the 9.6hrW5 and 16hrE1 throughout the thermosphere in Figure 7.7 implies that both waves are propagating upward and away from the nonlinear forcing source at a lower altitude region as expected. From the vertical phase progres-

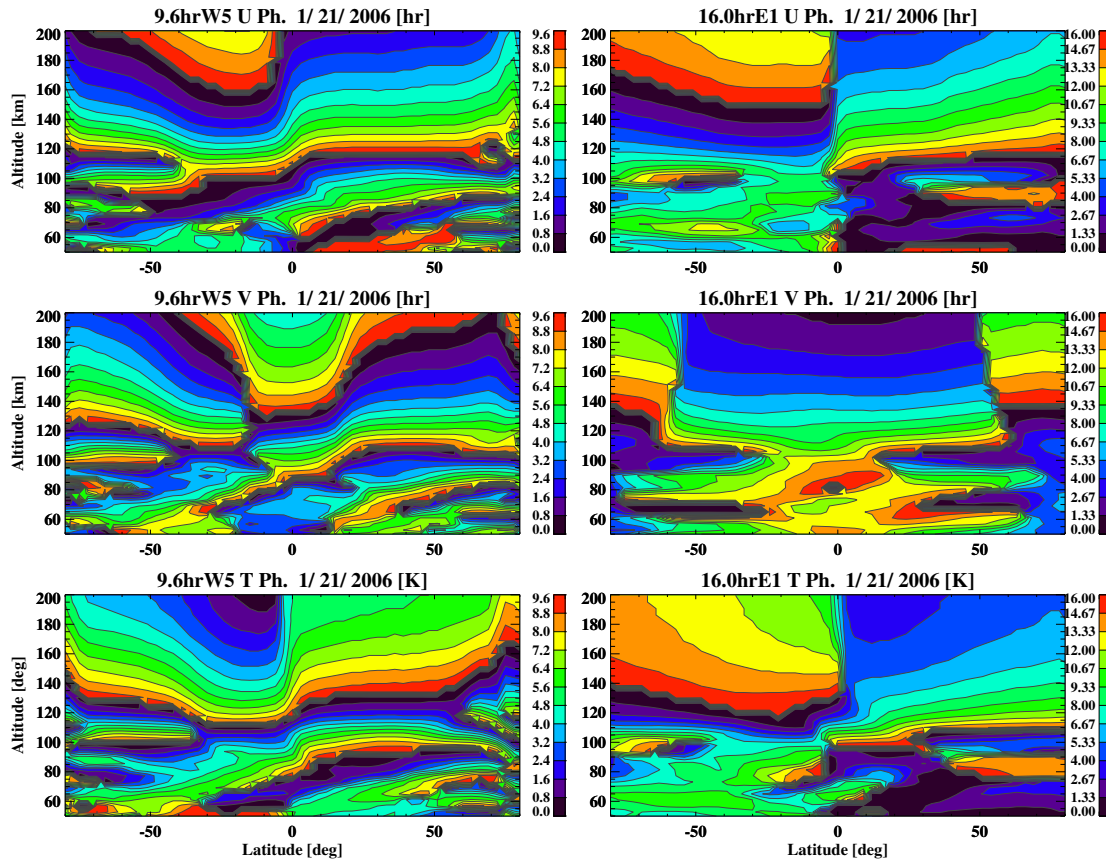


Figure 7.7: Vertical-latitude phase structure computed from the linear tidal model centered on January 21st, 2006 for the 9.6hrW5 zonal wind (upper-left), 9.6hrW5 meridional wind (middle-left), 9.6hrW5 temperature (lower-left), 16.0hrE1 zonal wind (upper-right), 16.0hrE1 meridional wind (middle-right), and 16.0hrE1 temperature (lower-right). Nonlinear forcing quantities presented in Chapter 5 are used to force the linear tidal model and compute secondary wave responses. Background winds are set to zero and background temperatures are set to equatorial values from NOGAPS-ALPHA.

sion with altitude, it can be estimated that the 9.6hrW5 has a vertical wavelength of about 50-60 km in the lower thermosphere and longer vertical wavelengths at higher altitudes. In contrast, the 16hrE1 is characterized by a much longer vertical wavelength of about 160 km. Since the 9.6hrW5 and 16hrE1 vertical wavelengths are long compared to other propagating, global-scale waves, it is expected that dissipation effects for these waves are small, which allows for further penetration into the thermosphere region. This prediction is supported by the significantly large secondary wave amplitude values in the middle thermosphere (Figure 7.6).

Like the secondary waves arising from DW1-2dayW3 interaction, the secondary wave responses presented here can be best explained by invoking Hough modes predicted from classical tidal theory. The normalized latitudinal structures of the first 3 propagating modes of the 9.6hrW5 and 16hrE1 waves are plotted in Figure 7.8. The first propagating mode of the 9.6hrW5 is described by one symmetric peak at the equator in the temperature and zonal wind fields and two asymmetric peaks at  $20^{\circ}\text{N/S}$  in the meridional wind field. In contrast, the first propagating mode of the 16hrE1 contains asymmetric peaks at  $30^{\circ}\text{N/S}$  in the zonal wind and temperature fields and a dominant symmetric equatorial peak in meridional wind. Each successive order Hough mode is generally characterized contains by more zero-crossings along the latitude axis and dominant peaks that move closer to towards the poles.

The numerical experiments with the 2dayW3-DW1 interaction presented in Chapter 5 showed that the projection of nonlinear forcing onto the secondary wave Hough modes assume a key role in determining the secondary wave response. Figure 7.9 displays the meridional momentum forcing projections onto the first three propagating modes of the 9.6hrW5 and 16hrE1 secondary waves. For the 9.6hrW5, the nonlinear forcing most efficiently projects onto the 2nd propagating mode between 80 and 100 km and the 3rd propagating Hough mode between 70 and 80 km. The efficient projection onto the 2nd propagating mode of the 9.6hrW5 can be observed in the meridional momentum forcing presented in Figure 7.5, which, similar to the 2nd propagating mode, is characterized by an equatorial peak and two additional peaks at mid-latitudes. Overall, the 16hrE1 nonlinear forcing does not as efficiently project onto the first 3 propagating modes as the 9.6hrW5 forcing, especially for the first two modes. This can be explained by the differences between the latitudinal distributions of nonlinear forcing for each secondary wave. The 16hrE1 nonlinear forcing is concentrated at higher latitudes than the 9.6hrW5 forcing and consequently, does not as efficiently project onto the lowest order modes, which are most dominant at low latitudes.

The relationship between the nonlinear forcing Hough mode projection and the overall secondary response can be discerned by examining the Hough modes contained within the each response. Figure 7.10 shows the amplitude of the first 3 propagating modes for the 9.6hrW5 and

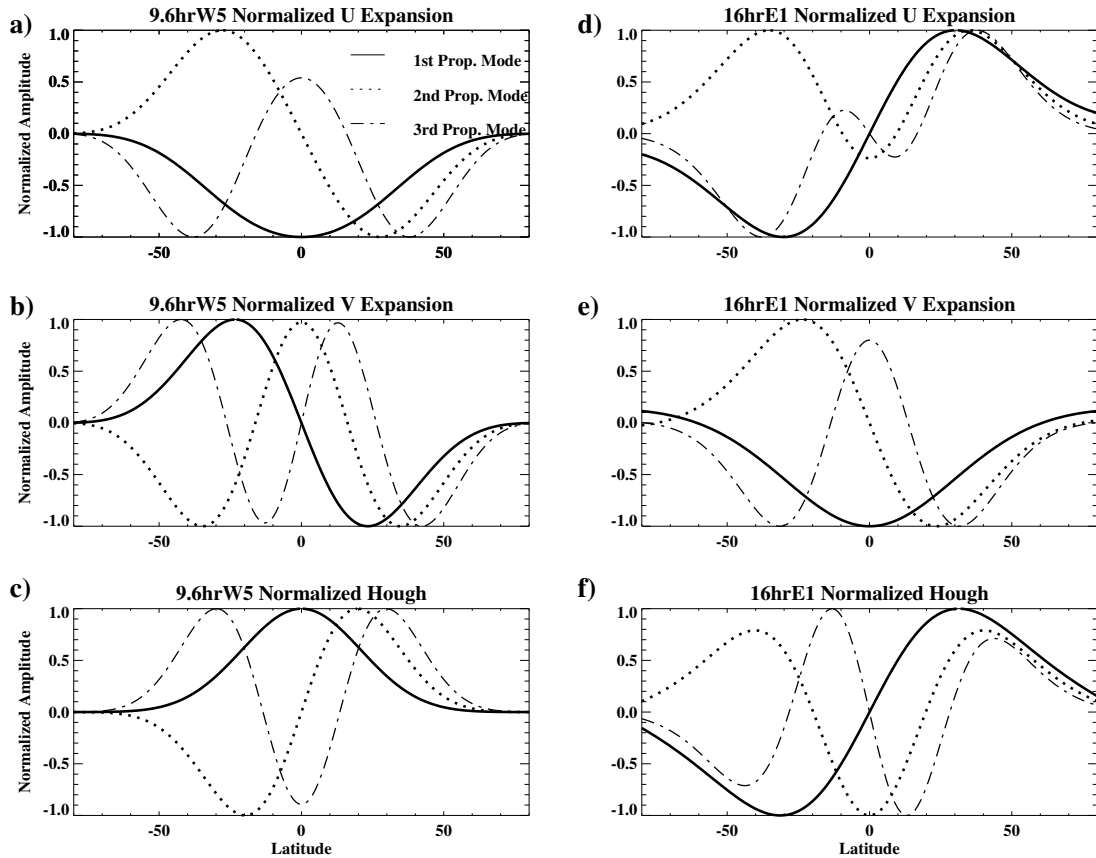


Figure 7.8: Normalized zonal wind, meridional wind expansion functions and Hough functions for the first, second and third propagating modes of the 9.6hrW5 (a, b, c) and 16.0hrE1 waves (d, e, f).

16.0hrE1 waves. As explained in Chapter 6, the amplitude of each Hough mode is determined by least squares projecting the overall secondary wave response onto the latitudinal structures of each mode. The Hough mode projections reveal that the 9.6hrW5 response is primarily composed of the 2nd propagating mode, followed by the 1st and 3rd propagating modes. These results demonstrate that the efficient projection of forcing onto the 2nd propagating mode combined with a long vertical wavelength (61 km) allow it to propagate into the thermosphere with significant amplitude. Although the 3rd mode forcing for the 9.6hrW5 is approximately equivalent to the 1st mode forcing, the 1st mode is the second largest component of the response in the thermosphere. This is explained by the long vertical wavelength of the 1st mode (83 km) compared to the 3rd mode (49

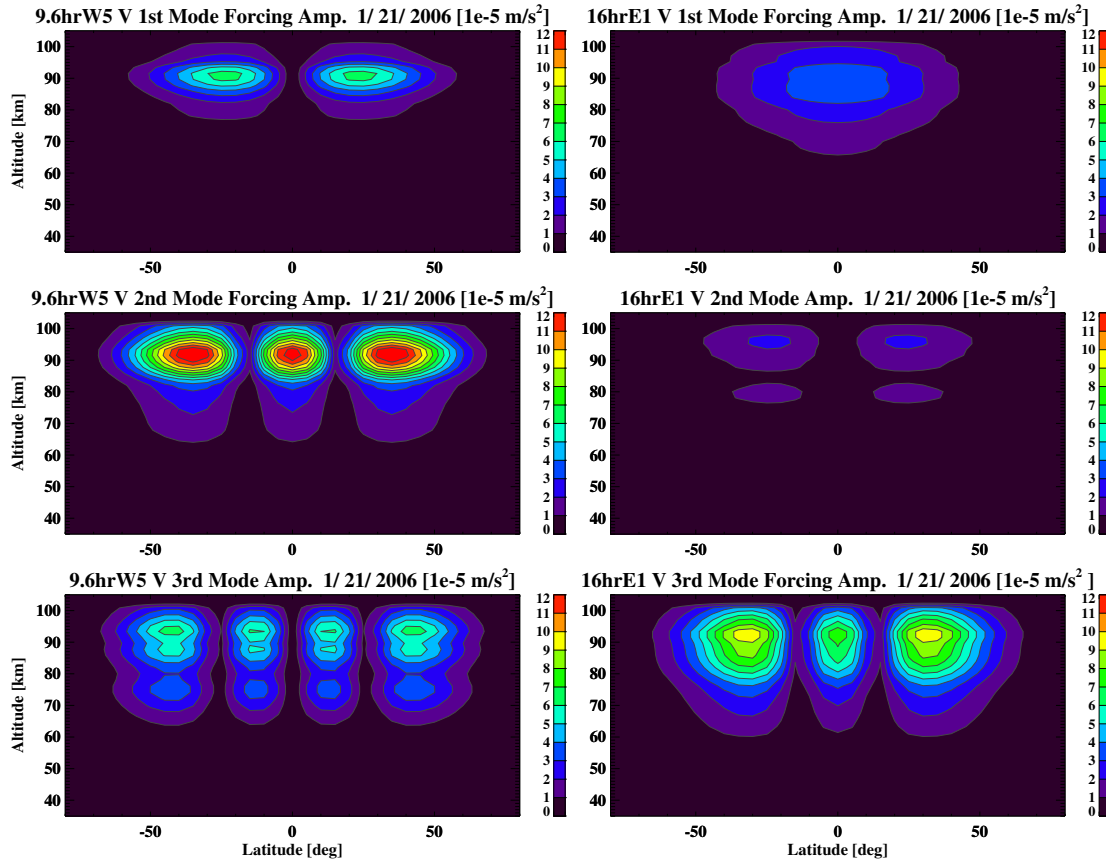


Figure 7.9: Projections of 16hrW4-2dayE2 meridional momentum forcing projected onto the 9.6hrW5 1st propagating mode (upper-left), 9.6hrW5 2nd propagating mode (middle-left), 9.6hrW 3rd propagating mode (lower-left), 16.0hrE1 1st propagating mode (upper-right), 16.0hrE1 2nd propagating mode (middle-right), and 16.0hrE1 3rd propagating mode (lower-right).

km), which means the 1st mode is less susceptible to dissipation in the lower thermosphere than the 3rd mode.

For the 16hrE1 response, the 1st propagating mode is largest even though the forcing more efficiently projects onto the 3rd propagating mode. The lack of correlation between the 16.0hrE1 forcing Hough mode projection and Hough mode response is explained by the vertical wavelengths of each mode. Since the 3rd propagating mode of the 16hrE1 has a relatively short vertical wavelength (35 km), it is severely impacted by dissipation effects in the MLT region. Thus, the 3rd propagating mode is unable to grow in amplitude with altitude in the thermosphere. The 1st propagating mode of the 16hrE1 mode in contrast has a long vertical wavelength (165 km), which allows it to penetrate

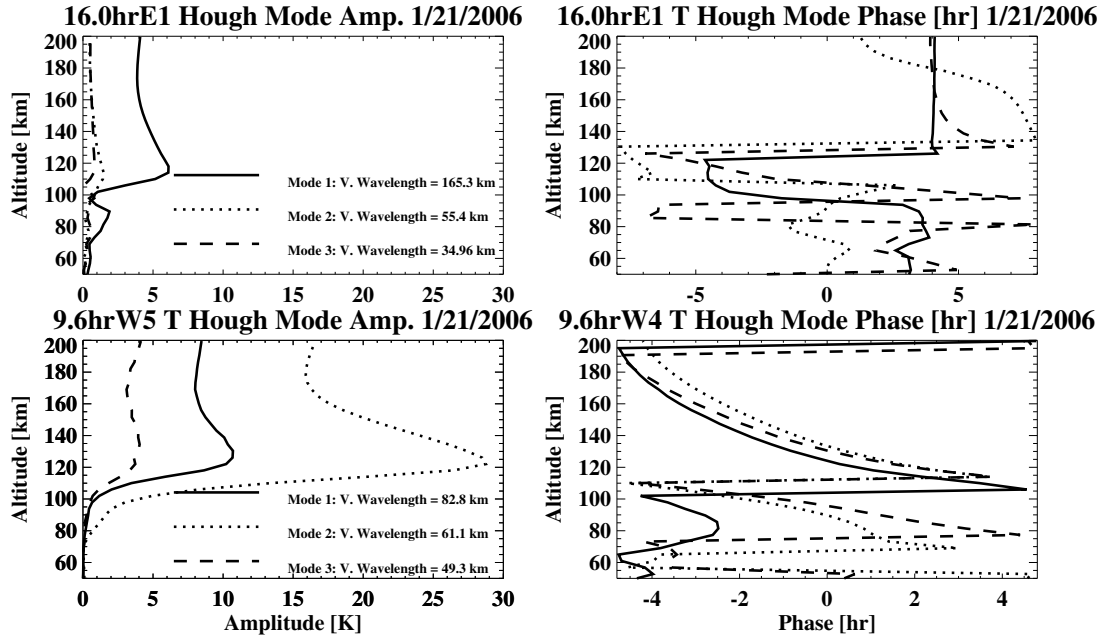


Figure 7.10: 9.6hrW5 amplitude (lower-left) and phase (lower-right), and 16.0hrE1 amplitude (upper-left) and phase (upper-right) as a function of altitude for January 21st, 2006. Each Hough mode amplitude was extracted by least squares fitting theoretical Hough mode functions to the overall secondary wave amplitude and phases at each altitude level. Units are in degrees Kelvin.

far into the thermosphere despite having a smaller forcing. Overall, the Hough modes contained within the 16hrE1 response are much smaller in amplitude than the modes for the 9.6hrW5 mainly due to the less efficient projection of the forcing onto these modes. Because the majority of the secondary wave response is determined by the magnitude of the first several propagating modes as concluded in Chapter 6, the overall 16hrE1 response is much smaller than the 9.6hrW5 response.

A comparison between the 16hrE1 and 9.6hrW5 waves generated from 2dayW3-SW2 interaction and the 16.0hrW4 and 2dayE2 waves generated from 2dayW3-DW1 interaction presented in the previous chapter reveal stark differences. At altitudes below 90 km in a zero wind background atmosphere, the 16hrW4 and 2dayE2 attain moderate amplitudes of approximately 9 K and 4 K, respectively, while the 16hrE1 and 9.6hrW5 waves are negligible. Above 100 km however, the 9.6hrW5 and 16hrE1 are generally larger and extend much farther into the thermosphere than the waves generated from 2dayW3-DW1 interaction. These results obtained from the linear tidal model

can be explained by a combination of the nonlinear forcing and the vertical wavelengths of each secondary wave. The nonlinear forcing values for the 16hrW4 and 2dayE2 waves are mainly greater at all altitudes in the MLT region, resulting in larger amplitudes within this region. However, the vertical wavelengths of the principal propagating Hough modes of the 16hrW4 and 2dayE2 waves ( $\lambda_z < 45$  km) are much shorter than the corresponding values for the 16hrE1 and 9.6hrW5 waves ( $\lambda_z > 60$  km). As a result, the majority of the 16hrW4 and 2dayE2 waves are damped out by 120 km whereas the 9.6hrW5 and 16hrE1 waves are able to penetrate to much greater altitudes.

The secondary wave responses generated from the 2dayW3-SW2 interaction are finally computed for a non-zero wind background atmosphere obtained from NOGAPS-ALPHA to obtain a more realistic picture. Figure 7.11 displays the vertical-latitudinal structure of the 9.6hrW5 and 16hrE1 amplitude during January 21st, 2006. A comparison to the zero wind background wind results reveals only slight differences in the general latitudinal structure of each secondary wave and mainly occur at altitudes below 100 km. It is observed that the 16hrE1 amplitude in the horizontal wind fields are enhanced by about 8 m/s at mid-southern latitudes in the MLT region, which is explained by favorable eastward wave propagation in a westward wind background atmosphere. Analogously, the 9.6hrW5 is marginally enhanced in the northern MLT region due to favorable westward wave propagation in a eastward background atmosphere.

In the thermosphere, the general latitudinal structure of each wave is similar to the zero background case, but the maximum amplitude values have changed. For the 9.6hrW5, the maximum amplitude values have decreased from about 36 m/s in zonal wind for the zero wind case to about 26 m/s for the non-zero wind case. In contrast, the maximum amplitude for the 16.0hrE1 has increased by about 10 m/s in the horizontal wind fields from the zero wind case. As explained in detail in the previous chapter, these results indicate the presence of mode coupling. In the case of the 9.6hrW5, the background winds in the mesosphere likely alter the latitudinal structure of the wave such that some of the energy contained within the lowest order propagating Hough modes is transferred to higher order modes. Since higher order modes, which are associated with shorter vertical wavelengths, are less likely to penetrate past the lower thermosphere due to dissipation,

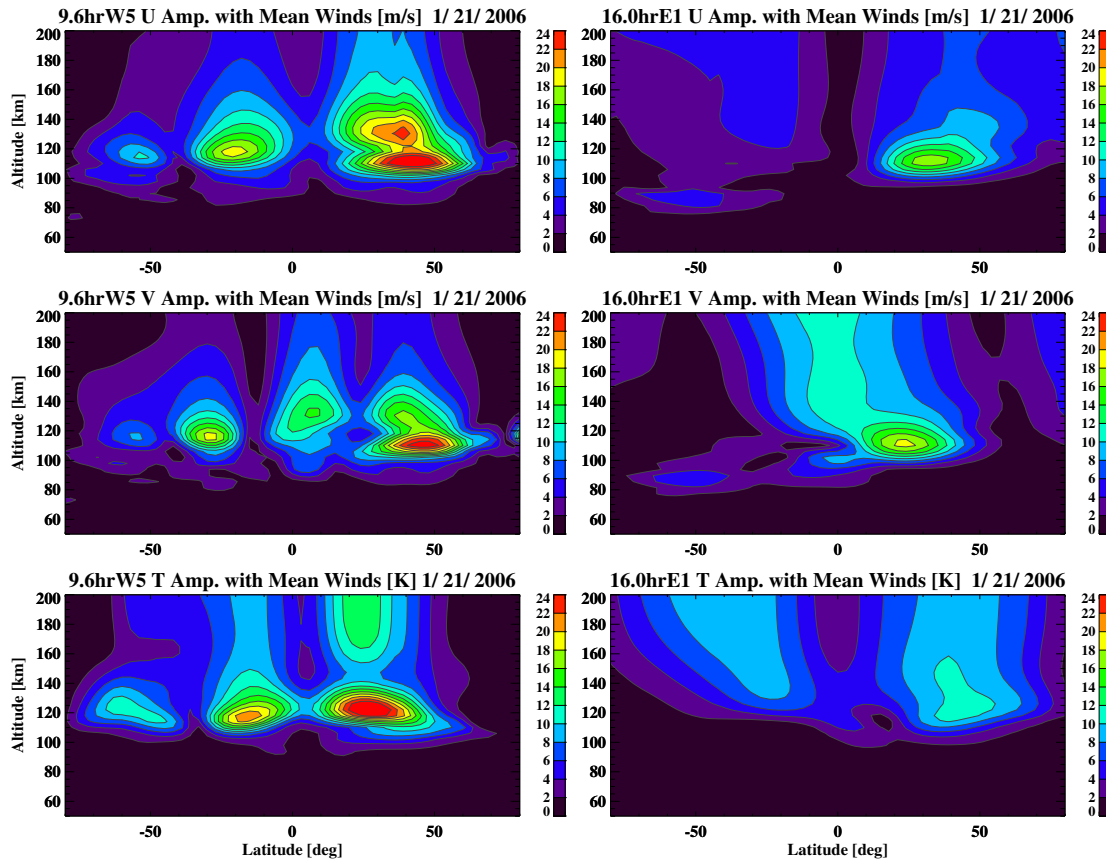


Figure 7.11: Vertical-latitude amplitude structure computed from the linear tidal model with background winds centered on January 21st, 2006 for the 9.6hrW5 zonal wind (upper-left), 9.6hrW5 meridional wind (middle-left), 9.6hrW5 temperature (lower-left), 16hrE1 zonal wind (upper-right), 16hrE1 meridional wind (middle-right), and 16hrE1 temperature (lower-right). Background winds and temperatures are extracted from NOGAPS-ALPHA.

secondary wave responses containing a higher proportion of high order propagating Hough modes are smaller in the thermosphere. The case of the 16hrE1 likely indicates an enhancement of the 1st propagating Hough mode by the background wind structure, which has a long vertical wavelength of 165 km. As a result, the 16hrE1 is enhanced in the presence of the background wind.

The amplitude and phase of the 9.6hrW5 and 16hrE1 waves are also computed for the January 2009 and 2010 cases to demonstrate the inter-annual variability of the secondary wave responses. Similar the 2006 results, the secondary wave responses for the January 2009 and 2010 are computed by using NOGAPS-derived 2dayW3 and SW2 nonlinear forcing estimates. The vertical-latitude

structure of the January 2009 and 2010 amplitude responses, displayed in Figures 7.12 and 7.13, reveal much smaller secondary amplitudes than the 2006 case. For the 2009 case, the 9.6hrW5 attains maximum amplitudes of only 16 m/s in horizontal wind (26 m/s in 2006) and 14 K (26 K in 2006) in temperature whereas the 16.0hrE1 reaches maximum amplitudes of 6 m/s in horizontal wind (18 m/s in 2006) and 4 K in temperature (10 K in 2006). Similar maximum amplitude values are also observed during January 2010.

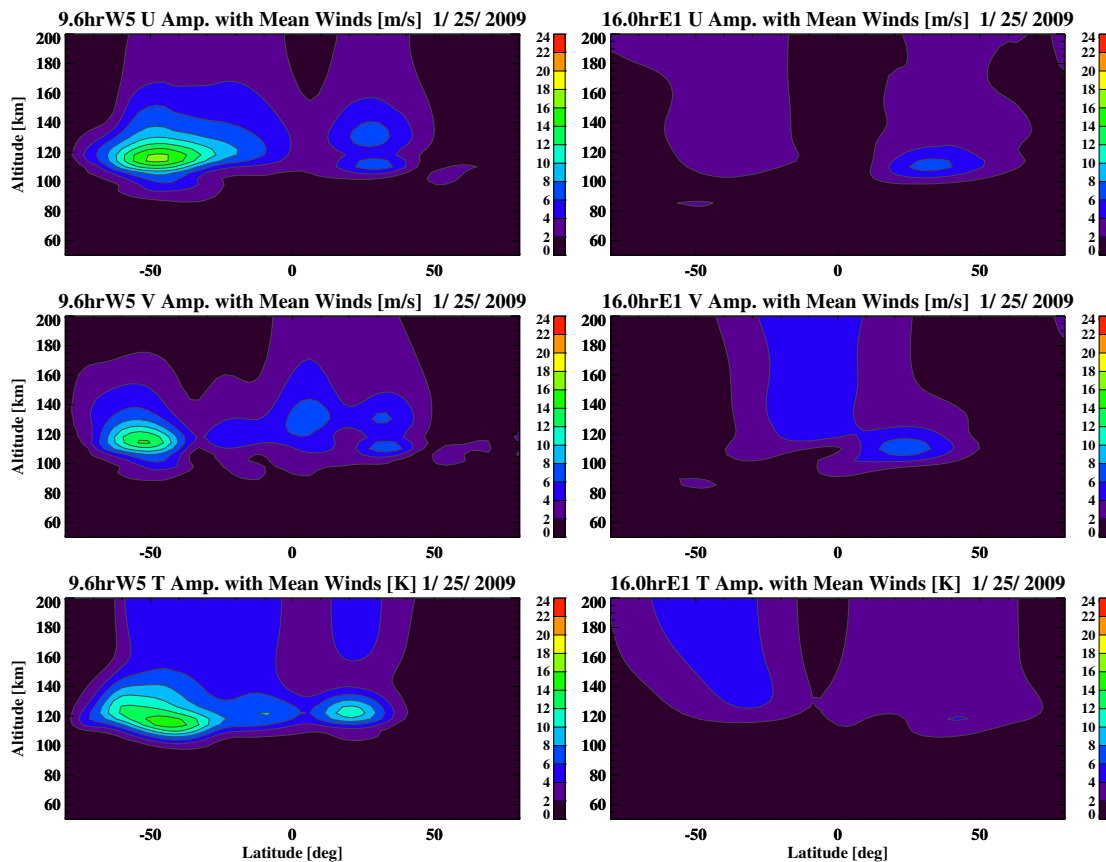


Figure 7.12: Vertical-latitude amplitude structure computed from the linear tidal model with background winds centered on January 25th, 2009 for the 9.6hrW5 zonal wind (upper-left), 9.6hrW5 meridional wind (middle-left), 9.6hrW5 temperature (lower-left), 16.0hrE1 zonal wind (upper-right), 16.0hrE1 meridional wind (middle-right), and 16.0hrE1 temperature (lower-right). Background winds and temperatures are extracted from NOGAPS-ALPHA.

Common and varying features in the latitudinal structure of the secondary waves among the 3 cases are also observed. While the 2006 9.6hrW5 response is characterized by a dominant

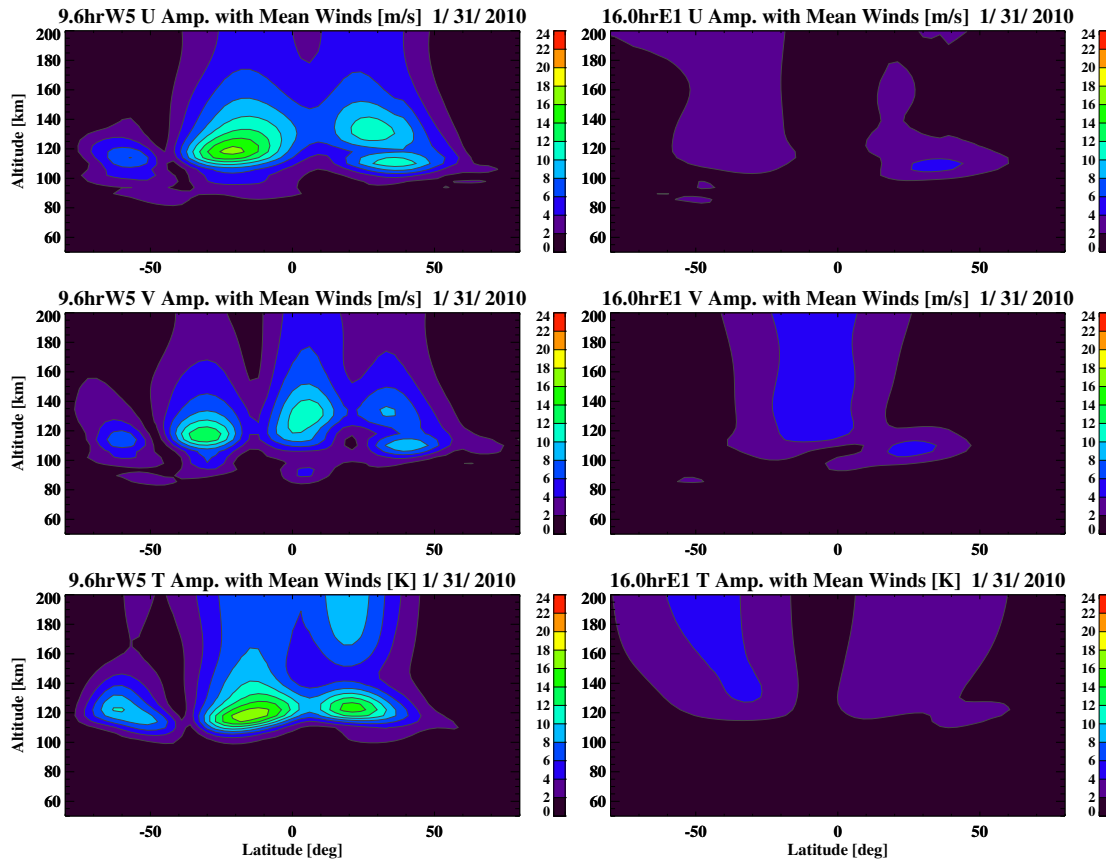


Figure 7.13: Vertical-latitude amplitude structure computed from the linear tidal model with background winds centered on January 25th, 2010 for the 9.6hrW5 zonal wind (upper-left), 9.6hrW5 meridional wind (middle-left), 9.6hrW5 temperature (lower-left), 16.0hrE1 zonal wind (upper-right), 16.0hrE1 meridional wind (middle-right), and 16.0hrE1 temperature (lower-right). Background winds and temperatures are extracted from NOGAPS-ALPHA.

2nd propagating mode structure peaking at mid-northern latitudes, the 2009 9.6hrW5 structure is mainly confined to southern latitudes, maximizing at around  $50^{\circ}\text{S}$ . On the other hand, the latitudinal structure of the 2010 9.6hrW5 response resembles the 2006 case. The latitudinal structures of the 16hrE1 are similar for all 3 years, each displaying a 1st propagating Hough mode structure with two peaks in zonal wind and temperature and one equatorial peak in meridional wind.

The large inter-annual variability observed among 2006, 2009 and 2010 9.6hrW5 and 16.0hrE1 responses is explained by the variability in the primary wave amplitudes. As shown in Figure 7.2, the SW2 during 2006 is largest in the northern hemisphere with maximum amplitudes of about

35 m/s in meridional wind and 8 K in temperature. By comparison, the SW2 amplitudes during the other years are much smaller (Appendix F), reaching amplitudes of only 12 m/s in meridional wind for the 2009 case and approximately 16 m/s in meridional wind for the 2010 case. The combination of large SW2 and 2dayW3 amplitudes during 2006 results in the largest nonlinear forcing amplitudes out of the 3 years. Consequently, it is expected to observe the largest secondary wave amplitudes in the thermosphere during 2006 as shown in this chapter.

Overall, the results contained in this chapter not only provide a broader context on the generation of global-scale, secondary waves in the upper atmosphere, but they also serve as a prime example of the impacts of nonlinear interactions on the space-atmosphere interaction region (SAIR). The direct penetration the 9.6hrW5 and 16.0hrE1 into the middle thermosphere and the E-region ionosphere implies that they may be able to affect the SAIR at even higher altitudes through mechanisms such as the neutral wind driven dynamo and alteration of neutral composition near the turbopause although the latter mechanism is more important for longer period waves (Nguyen and Palo, 2014 [70]). However, it is still necessary to validate the secondary wave response, particularly above 100 km, before assertions can be made about the magnitude of impact on the SAIR. The general agreement between the 9.6hrW5 and 16.0hrE1 responses computed from the linear tidal model and the NOGAPS-ALPHA (Figure 7.14) provides some confidence that the secondary wave responses presented here are accurate. While the secondary waves in the upper mesosphere may be representative of reality, the responses in the lower thermosphere may not be due to the lack of knowledge of the true background wind configuration. Since the background zonal wind has an impact on the secondary wave structure, more accurate background winds are important for studies of wave propagation into the ionosphere-thermosphere system. Future observations of the ionosphere-thermosphere from ground-based instruments such as incoherent scatter radar or satellites such as Ionospheric Connection Explorer (currently planned launch in 2017) are required to determine the true impact of the secondary waves on the complete SAIR. Despite these uncertainties, the modeling results contained within this chapter and the rest of the dissertation raises compelling questions about the impact of nonlinear interactions on the total

variability of the SAIR.

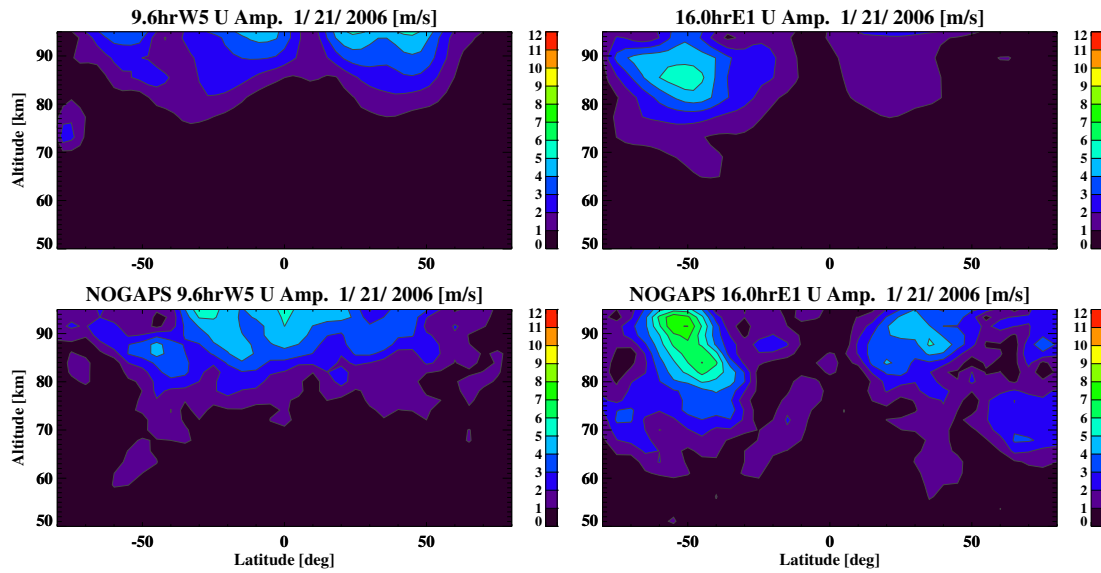


Figure 7.14: Vertical-latitude amplitude structure during January 21st, 2006 for the linear model 9.6hrW5 zonal wind (top-left), NOGAPS-ALPHA 9.6hrW5 zonal wind (bottom-left), linear model 16.0hrE1 zonal wind (top-right), and NOGAPS-ALPHA 16.0hrE1 zonal wind (bottom-right).

## Chapter 8

### CONCLUSIONS

#### 8.1 Summary

The dissertation has investigated the manifestation of secondary waves arising from nonlinear interaction between global-scale atmospheric tides and planetary waves in the space-atmosphere interaction region (SAIR). The majority of the work specifically focused on the nonlinear interaction between the quasi two-day wave (2dayW3) and the migrating diurnal tide (DW1), which theoretically produces the 2dayE2 and 16hrW4 secondary waves.

First, observationally-based evidence of secondary waves arising from this interaction was extracted by applying the Fast Fournier Synoptic Mapping (FFSM) technique to temperature data sets from the TIMED-SABER and Aura MLS satellite instruments. The major findings from this portion of the dissertation are summarized as follows:

- (1) Unlike methods utilized in previous studies, the FFSM technique applied to near sun-synchronous observations of the atmosphere was demonstrated to produce estimates for the 2dayE2 secondary wave that are not aliased by other spectral phenomenon within the Nyquist sampling limit. Aliasing contributions to the 2dayE2 from outside of the Nyquist limits are likely to be solely caused by secondary wave products arising from nonlinear interaction between the 2dayW3 and migrating atmospheric tides. Hence, it is concluded that FFSM-derived estimates for the 2dayE2 are representative of secondary wave production.

- (2) Estimates of the 2dayE2 wave derived from six years of TIMED-SABER and Aura MLS observations revealed that the largest secondary wave amplitudes are not coincident with the largest primary wave amplitudes (2dayW3, DW1). This result suggests that secondary waves are likely forced from nonlinear interaction in one region of the atmosphere and then propagate into other vertical and latitudinal regions, which contrasts past assertions regarding this mechanism. The observational results also revealed that the secondary waves are only significant above 80 km and grow in amplitude at higher altitudes. Comparison with results derived from the NOGAPS-ALPHA reanalysis produced similar conclusions.

The remaining portion of the dissertation concentrated on numerical experiments with a linearized tidal model to understand the factors that govern the secondary wave response in the SAIR. In order to derive observationally-accurate secondary wave forcing driven by nonlinear wave-wave advection, estimates for each primary wave were derived from hourly NOGAPS-ALPHA reanalysis model output. The derived forcing was then implemented in a linearized tidal model, modified from the Global Scale Wave Model (GSWM), to produce secondary wave responses under different conditions. From the modeling results, it is concluded that the secondary wave response is mainly dependent on the following factors:

- (1) **Wave propagation characteristics:** Each secondary wave can be decomposed into Hough modes that define the wave spatial structure and propagation characteristics. Numerical experiments demonstrated that secondary wave responses whose lowest order propagating modes are associated with long vertical wavelengths are less affected by dissipation forces in the mesosphere-lower thermosphere. Thus, secondary waves possessing long vertical wavelength can penetrate farther into the SAIR and attain large amplitudes. Experiments examining the 2dayW3-DW1 interaction revealed that the 16hrW4 is less affected by dissipation than 2dayE2 due to longer vertical wavelengths and subsequently, larger throughout the lower thermosphere. Additional experiments demonstrated that the 9.6hrW5 and 16hrE1 waves arising from the interaction between the 2dayW3 and migrating

semidiurnal tide (SW2) are capable of penetrating even farther into thermosphere than the 16hrW4 or 2dayE2 waves due to their long vertical wavelengths.

- (2) **Latitudinal structure of the forcing:** The latitudinal structure of the nonlinear forcing determines how efficient each Hough mode in each secondary wave is excited and consequently has a large impact on the spatial structure and magnitude of the secondary wave response. Although the maximum forcing for the 16hrW4 and 2dayE2 are approximately equal, the low-latitude structure of the 16hrW4 forcing is more effective at exciting propagating Hough modes, which results in exponential wave growth with height. In contrast, the 2dayE2 forcing mainly generated modes that were either trapped or characterized by short vertical wavelengths, leading to a small response above the forcing region. Furthermore, the magnitude and spatial structure of the forcing greatly varies on an inter-annual basis due to changes in the interacting primary waves and was discovered to be a dominant driver of inter-annual variability observed in the secondary wave response.
- (3) **Vertical location of the forcing:** Additional experiments showed that the most impactful portion of the forcing on the response is not necessarily located in the upper mesosphere and lower thermosphere where the primary waves and subsequently, forcing are largest. In some instances, smaller forcing contained in the lower mesosphere results in equally large secondary waves as larger forcing contained at higher altitudes due to exponential wave growth with altitude and large dissipation forces present at the top of the mesosphere.
- (4) **Background winds:** Finally, the background winds structure was found to influence the latitudinal structure of the secondary waves. Westward (eastward) propagating secondary waves are more prominent in the presence of a eastward (westward) background wind structure.

## 8.2 Discussion and Future Work

Past studies have often assumed that tidal/planetary wave interactions occurred when two large primary waves propagate into the same region and produce coincident secondary wave responses. A core result of this dissertation has dispelled these assumptions and elucidated the manifestation process of secondary waves. It has been shown through both observations and numerical modeling that secondary waves can propagate away from the nonlinear interaction region and thus, achieve significant amplitude in regions where neither primary waves are present. The modeling results have also shown that the largest secondary waves are not necessarily produced by the largest primary waves. Although the SW2 is smaller than the DW1, the SW2 interaction with the 2dayW3 produces more significant secondary waves throughout most of the SAIR due to the factors listed above and explained throughout this dissertation.

The results of this dissertation immediately raise questions on how much impact these secondary waves have on the entirety of the SAIR. While the dissertation results have suggested that the secondary waves may attain moderate amplitudes in the SAIR, a complete validation of the response in the thermosphere has not yet been achieved. Future validation may be conducted with observational datasets from ground-based radar and/or space satellites such as ICON. In addition, secondary wave effects on ionospheric variability have also not been investigated. Studies of the impacts of nonlinear interaction on the ionosphere may be more effectively carried out with general circulation models such as the NCAR TIME-GCM or TIE-GCM, which, unlike linearized tidal models, are able to simulate the effects of ion-neutral coupling.

The impacts of nonlinear interactions between other atmospheric tides and planetary waves can also be more effectively investigated after the conduction of this dissertation. Past studies (Truskowski et al., 2014 [108]) have suggested that certain atmospheric tides within the SAIR are more likely to be generated from nonlinear interaction than other tides. Explanation and support of these past assertions can be given by the conclusions made in this dissertation. For example, past studies have shown that the SW3 and SW1 tidal components are amplified in the mesosphere

and lower thermosphere during sudden stratospheric warming events (Angelats i Coll and Forbes, 2002 [1], Chang et al., 2009 [6], Pedatella and Forbes, 2010 [82]; Truskowski et al., 2014 [108]). These studies have suggested that the SW3/SW1 amplification during these events are caused by the nonlinear interaction between SW2 and the stationary planetary wave 1. By conducting this dissertation, the large SW1 and SW3 responses can now be explained by the long vertical wavelengths of each secondary wave and a nonlinear interaction region that is situated at lower altitudes. The factors governing the secondary wave response can be utilized to investigate other nonlinear interactions in order to determine the dominant secondary waves within the SAIR and improve our understanding of the pathways through which atmosphere-space weather coupling can occur.

## Bibliography

- [1] M. Angelats i Coll and J. M. Forbes. Nonlinear interactions in the upper atmosphere: The  $s = 1$  and  $s = 3$  nonmigrating semidiurnal tides. Journal of Geophysical Research: Space Physics, 107(A8), 2002.
- [2] E. V. Appleton. Two anomalies in the ionosphere. Nature, 157, 1946.
- [3] A. Beard, N. Mitchell, P. Williams, and M. Kunitake. Non-linear interactions between tides and planetary waves resulting in periodic tidal variability. Journal of Atmospheric and Solar-Terrestrial Physics, 61(5):363 – 376, 1999.
- [4] M. D. Burrage, M. E. Hagan, W. R. Skinner, D. L. Wu, and P. B. Hays. Long-term variability in the solar diurnal tide observed by hrdi and simulated by the gswm. Geophysical Research Letters, 22(19):2641–2644, 1995.
- [5] CEDAR. Cedar the new dimension, strategic vision for the national science foundation, June 2011.
- [6] L. C. Chang, S. E. Palo, and H.-L. Liu. Short-term variation of the  $s = 1$  nonmigrating semidiurnal tide during the 2002 stratospheric sudden warming. Journal of Geophysical Research, 114, 2009.
- [7] L. C. Chang, S. E. Palo, and H.-L. Liu. Short-term variability in the migrating diurnal tide caused by interactions with the quasi 2 day wave. Journal of Geophysical Research: Atmospheres, 116(D12), 2011.
- [8] S. Chapman and R. S. Lindzen. Atmospheric Tides: thermal and gravitational, volume 15. Springer Science, 1970.
- [9] R. Clark and J. Bergin. Bispectral analysis of mesosphere winds. Journal of Atmospheric and Solar-Terrestrial Physics, 59(6):629 – 639, 1997. A selection of papers presented at The IUGG XXI General Assembly on Large-Scale Structure, Dynamics and Aeronomy of the Upper Atmosphere.
- [10] L. Coy, S. D. Eckermann, and K. W. Hoppel. Planetary wave breaking and tropospheric forcing as seen in the stratospheric sudden warming of 2006. Journal of Atmospheric Science, 66:495–507, 2006.
- [11] J. M. Forbes. Atmospheric tides: 1. model description and results for the solar diurnal component. Journal of Geophysical Research: Space Physics, 87(A7):5222–5240, 1982.

- [12] J. M. Forbes. Tidal and planetary waves. The upper mesosphere and lower thermosphere: a review of experiment and theory, pages 67–87, 1995.
- [13] J. M. Forbes. Planetary waves in the thermosphere-ionosphere system. J. Geomag. Geoelectr., 48:91–98, 1996.
- [14] J. M. Forbes and H. B. Garrett. Thermal excitation of atmospheric tides due to insolation absorption by o<sub>3</sub> and h<sub>2</sub>o. Geophysical Research Letters, 5(12):1013–1016, 1978.
- [15] J. M. Forbes and M. E. Hagan. Tides in the joint presence of friction and rotation: An f plane approximation. Journal of Geophysical Research: Space Physics, 84(A3):803–810, 1979.
- [16] J. M. Forbes and M. E. Hagan. Diurnal propagating tide in the presence of mean winds and dissipation : a numerical investigation. Planetary and Space Science, 36(6):579 – 590, 1988.
- [17] J. M. Forbes, M. Kilpatrick, D. Fritts, A. H. Manson, and R. A. Vincent. Zonal mean and tidal dynamics from space: an empirical examination of aliasing and sampling issues. Annales Geophysicae, 15:1158–1164, 1997.
- [18] J. M. Forbes, J. Russell, S. Miyahara, X. Zhang, S. Palo, M. Mlynczak, C. J. Mertens, and M. E. Hagan. Troposphere-thermosphere tidal coupling as measured by the saber instrument on timed during july–september 2002. Journal of Geophysical Research: Space Physics, 111(A10), 2006.
- [19] J. M. Forbes and R. A. Vincent. Effects of mean winds and dissipation on the diurnal propagating tide: An analytic approach. Planetary and Space Science, 37(2):197 – 209, 1989.
- [20] R. R. Garcia, D. R. Marsh, D. E. Kinnison, B. A. Boville, and F. Sassi. Simulation of secular trends in the middle atmosphere. Journal of Geophysical Research, 112(D09301), 2007.
- [21] R. R. Garcia and S. Solomon. The effect of breaking gravity waves on the dynamics and chemical composition of the mesosphere and lower thermosphere. Journal of Geophysical Research: Atmospheres, 90(D2):3850–3868, 1985.
- [22] L. P. Goncharenko, A. J. Coster, J. L. Chau, and C. E. Valladares. Impact of sudden stratospheric warmings on equatorial ionization anomaly. Journal of Geophysical Research: Space Physics, 115(A10), 2010.
- [23] L. P. Goncharenko, V. W. Hsu, C. G. M. Brum, S.-R. Zhang, and J. T. Fentzke. Wave signatures in the midlatitude ionosphere during a sudden stratospheric warming of january 2010. Journal of Geophysical Research: Space Physics, 118(1), 2010.
- [24] G. Groves. Hough components of ozone heating. Journal of Atmospheric and Terrestrial Physics, 44(2):111 – 121, 1982.
- [25] S.-Y. Gu, T. Li, X. Dou, Q. Wu, M. G. Mlynczak, and J. M. Russell. Observations of quasi-two-day wave by timed/saber and timed/tidi. Journal of Geophysical Research: Atmospheres, 118(4):1624–1639, 2013.
- [26] M. E. Hagan and J. M. Forbes. Migrating and nonmigrating diurnal tides in the middle and upper atmosphere excited by tropospheric latent heat release. Journal of Geophysical Research: Atmospheres, 107(D24), 2002.

- [27] M. E. Hagan, J. M. Forbes, and F. Vial. Numerical investigation of the propagation of the quasi-two-day wave into the lower thermosphere. Journal of Geophysical Research: Atmospheres, 98(D12):23193–23205, 1993.
- [28] M. E. Hagan, J. M. Forbes, and F. Vial. On modeling migrating solar tides. Geophysical Research Letters, 22(8):893–896, 1995.
- [29] M. E. Hagan, A. Maute, and R. G. Roble. Tropospheric tidal effects on the middle and upper atmosphere. Journal of Geophysical Research: Space Physics, 114(A1), 2009.
- [30] K. Hamilton. Latent heat release as a possible forcing mechanism for atmospheric tides. Monthly Weather Review, 109(1):3–17, 1981.
- [31] T. J. Harris and R. A. Vincent. The quasi-two day wave observed in the equatorial middle atmosphere. Journal of Geophysical Research, 98, 1993.
- [32] Y. Hayashi. Space-time spectral analysis and its applications to atmospheric waves. J. Meteor. Soc. Japan, 60:156–171, 1982.
- [33] A. E. Hedin. Extension of the msis thermosphere model into the middle and lower atmosphere. Journal of Geophysical Research, 96:7657–7688, 1991.
- [34] C. O. Hines. Internal gravity waves at ionospheric heights. Can. J. Phys., 38:1441–1481, 1960.
- [35] I. Hirota. Excitation of planetary rossby waves in the winter stratosphere by periodic forcing. J. Meteor. Soc. Japan, 49:439–449, 1971.
- [36] M. H. Hitchman and C. B. Leovy. Evolution of the zonal mean state in the equatorial middle atmosphere during october 1978-may 1979. Journal of the Atmospheric Sciences, 43(24):3159–3175, 1986.
- [37] M. H. Hitchman and C. B. Leovy. Quasi-stationary zonally asymmetric circulations in the equatorial lower mesosphere. Journal of the Atmospheric Sciences, 44(16):2219–2236, 1987.
- [38] J. R. Holton. The Dynamic Meteorology of the Stratosphere and Mesosphere. American Meteorological Society, Boston, MA, 1975.
- [39] J. R. Holton. An Introduction to Dynamic Meteorology. Elsevier Academic Press, 4th edition, 2004.
- [40] K. W. Hoppel, N. L. Baker, L. Coy, S. D. Eckermann, J. P. McCormack, G. E. Nedoluha, and E. Siskind. Assimilation of stratospheric and mesospheric temperatures from mls and saber into a global nwp model. Atmospheric Chemistry and Physics, 8:6103–6116, 2008.
- [41] S. S. Hough. On the application of harmonic analysis to the dynamical theory of tides, part i. on laplace’s ‘oscillations of the first species’, and on the dynamics of ocean currents’. Phil. Trans. Roy. Soc., A189:201–257, 1897.
- [42] T. J. Immel, E. Sagawa, S. L. England, S. B. Henderson, M. E. Hagan, S. B. Mende, H. U. Frey, C. M. Swenson, and L. J. Paxton. The control of equatorial ionospheric morphology by atmospheric tides. Geophysical Research Letters, 33, 2006.

- [43] E. e. a. Kalnay. The ncep/ncar 50-year reanalysis project. Bull. Am. Meteorol. Soc., 79:437–471, 1996.
- [44] T. L. Killeen, Q. Wu, S. C. Solomon, D. A. Ortland, W. R. Skinner, R. J. Niciejewski, and D. A. Gell. Timed doppler interferometer: Overview and recent results. Journal of Geophysical Research, 111(A10S01), 2006.
- [45] J. M. Leonard, J. M. Forbes, and G. H. Born. Impact of tidal density variability on orbital and reentry predictions. Space Weather, 10(S12003), 2012.
- [46] R. S. Lieberman. Eliassen-palm fluxes of the 2-day wave. Journal of the Atmospheric Sciences, 56(16):2846–2861, 1999.
- [47] R. S. Lieberman and D. Riggin. High resolution doppler imager observations of kelvin waves in the equatorial mesosphere and lower thermosphere. Journal of Geophysical Research: Atmospheres, 102(D22):26117–26130, 1997.
- [48] R. S. Lieberman, D. M. Riggin, V. Nguyen, S. E. Palo, D. E. Siskind, N. J. Mitchell, G. Strober, S. Wilhelm, and N. J. Livesey. Global observations of two-day wave coupling to the diurnal tide. Journal of Geophysical Research, 2016.
- [49] R. S. Lieberman, D. M. Riggin, D. A. Ortland, S. W. Nesbitt, and R. A. Vincent. Variability of mesospheric diurnal tides and tropospheric diurnal heating during 1997–1998. Journal of Geophysical Research: Atmospheres, 112(D20), 2007.
- [50] R. S. Lieberman, D. M. Riggin, D. A. Ortland, J. Oberheide, and D. E. Siskind. Global observations and modeling of nonmigrating diurnal tides generated by tide-planetary wave interactions. Journal of Geophysical Research: Atmospheres, 120(22), 2015.
- [51] V. Limpasuvan and D. L. Wu. Two-day wave observations of uars microwave limb sounder mesospheric water vapor and temperature. Journal of Geophysical Research, 108(D10), 2003.
- [52] R. Lindzen and H.-L. Kuo. A reliable method for the numerical integration of a large class of ordinary and partial differential equations. In Mon. Wea. Rev. Citeseer, 1969.
- [53] R. S. Lindzen and S.-S. Hong. Effects of mean winds and horizontal temperature gradients on solar and lunar semidiurnal tides in the atmosphere. Journal of the Atmospheric Sciences, 31(5):1421–1446, 1974.
- [54] R. S. Lindzen and D. J. Mckenzie. Tidal theory with newtonian cooling. Pure and Applied Geophysics, 66(1):90–96, 1967.
- [55] N. J. Livesey, W. G. Read, L. Froidevaux, A. Lambert, G. L. Manney, H. C. Pumphrey, M. L. Santee, M. J. Schwartz, S. Wang, R. E. Cofield, D. T. Cuddy, R. A. Fuller, R. F. Jarnot, J. H. Jiang, B. W. Knosp, P. C. Stek, P. A. Wagner, and D. L. Wu. Earth Observing System (EOS) Aura Microwave Limb Sounder (MLS) Version 3.3 Level 2 Data Quality and Description Document. Jet Propulsion Laboratory.
- [56] R. A. Madden. Further evidence of traveling planetary waves. Journal of the Atmospheric Sciences, 35, 1979.

- [57] R. A. Madden and P. Julian. Further evidence of global-scale 5-day pressure waves. Journal of the Atmospheric Sciences, 29:1464–1469, 1972.
- [58] G. L. Manney and W. J. Randel. Instability at the winter stratopause: A mechanism for the 4-day wave. Journal of the Atmospheric Sciences, 50(23), 1993.
- [59] A. Manson and C. Meek. Winds and tidal oscillations in the upper middle atmosphere at saskatoon ( $52^{\circ}\text{n}$ ,  $107^{\circ}\text{w}$ ,  $l = 4.3$ ) during the year june 1982–may 1983. Planetary and Space Science, 32(9):1087 – 1099, 1984.
- [60] A. Manson and C. Meek. Long period (8–20 h) wind oscillations in the upper middle atmosphere at saskatoon ( $52^{\circ}\text{n}$ ): Evidence for non-linear tidal effects. Planetary and Space Science, 38(11):1431 – 1441, 1990.
- [61] H. G. Mayr and J. G. Mengel. Interannual variations of the diurnal tide in the mesosphere generated by the quasi-biennial oscillation. Journal of Geophysical Research: Atmospheres, 110(D10), 2005.
- [62] J. P. McCormack, L. Coy, and K. W. Hoppel. Evolution of the quasi 2-day wave during january 2006. Journal of Geophysical Research, 114(D20115), 2009.
- [63] J. P. McCormack, S. D. Eckermann, K. W. Hoppel, and R. A. Vincent. Amplification of the quasi-two day wave through nonlinear interaction with the migrating diurnal tide. Geophysical Research Letters, 37(16), 2010.
- [64] C. McLandress. The seasonal variation of the propagating diurnal tide in the mesosphere and lower thermosphere. part ii: The role of tidal heating and zonal mean winds. Journal of the Atmospheric Sciences, 59(6):907–922, 2002.
- [65] N. J. Mitchell, P. J. S. Williams, A. G. Beard, G. R. Buesnel, and H. G. Muller. Nonlinear planetary/tidal wave interactions in the lower thermosphere observed by meteor radar. Annales Geophysicae, 14:364–366, 1996.
- [66] Y. Moudeden and J. M. Forbes. Quasi-two-day wave structure, interannual variability, and tidal interactions during 2002-2011 decade. Journal of Geophysical Research: Atmospheres, 119:2241–2260, 2014.
- [67] P. J. Mukhtarov, D. Pancheva, and B. Andonov. Global structure and seasonal and interannual variability of the migrating diurnal tide seen in the saber/timed temperatures between 20 and 120 km. Journal of Geophysical Research, 114(A02309), 2009.
- [68] H. G. Muller. Long period meteor wind oscillations. Phil. Trans. Roy. Soc., 271:585–598, 1972.
- [69] V. Nguyen and S. Palo. Technique to produce daily estimates of the migrating diurnal tide using timed/saber and {EOS} aura/mls. Journal of Atmospheric and Solar-Terrestrial Physics, 105–106(0):39 – 53, 2013.
- [70] V. Nguyen and S. Palo. Transmission of planetary wave effects to the upper atmosphere through eddy diffusion modulation. Journal of Atmospheric and Solar-Terrestrial Physics, 117(0):1 – 6, 2014.

- [71] P. J. Olver and C. Shakiban. Applied Linear Algebra. Pearson, 2005.
- [72] D. A. Ortland. Generalized hough modes: The structure of damped global-scale waves propagating on a mean flow with horizontal and vertical shear. Journal of the Atmospheric Sciences, 62(8):2674–2683, 2005.
- [73] D. A. Ortland. A study of the global structure of the migrating diurnal tide using generalized hough modes. Journal of the Atmospheric Sciences, 62(8):2684–2702, 2005.
- [74] D. A. Ortland. Determining daily zonal mean, tidal, and stationary wave structures in the mesosphere and lower thermosphere from saber temperature measurements. in preparation.
- [75] S. E. Palo. Analysis of the Equatorial Semiannual Oscillation and Quasi Two-Day Wave in the Mesosphere and Lower Thermosphere Using a Spectral Model and Data Collected with the Christmas Island Radar Systems. PhD thesis, University of Colorado at Boulder, 1994.
- [76] S. E. Palo, J. M. Forbes, X. Zhang, J. M. Russell, and M. G. Mlynczak. An eastward propagating two-day wave: Evidence for nonlinear planetary wave and tidal coupling in the mesosphere and lower thermosphere. Geophysical Research Letters, 34(7), 2007.
- [77] S. E. Palo, R. G. Roble, and M. E. Hagan. Middle atmosphere effects of the quasi-two-day wave determined from a general circulation model. Earth, planets and space, 51(7-8):629–647, 1999.
- [78] D. Pancheva, C. Haldoupis, C. E. Meek, A. H. Manson, and N. J. Mitchell. Evidence of a role for modulated atmospheric tides in the dependence of sporadic e layers on planetary waves. Journal of Geophysical Research: Space Physics, 108(A5), 2003.
- [79] D. Pancheva and P. Mukhtarov. Variability of mesospheric dynamics observed at yambol (42.5°n, 26.6°e) by meteor radar. Journal of Atmospheric and Terrestrial Physics, 56(10):1271 – 1278, 1994.
- [80] D. Pancheva, P. J. Mukhtarov, H. Middleton, and H. G. Muller. Variability of the semidiurnal tide due to fluctuations in solar activity and total ozone. Journal of Atmospheric and Solar-Terrestrial Physics, 65:1–19, 2009.
- [81] D. V. Pancheva. Quasi-2-day wave and tidal variability observed over ascension island during january/february 2003. Journal of Atmospheric and Solar-Terrestrial Physics, 68(3–5):390 – 407, 2006. Vertical Coupling in the Atmosphere/Ionosphere System 2nd IAGA/ICMA Workshop on Vertical Coupling in the Atmosphere/Ionosphere System, Bath, UK, 12 - 15 July, 2004.
- [82] N. M. Pedatella and J. M. Forbes. Evidence for stratosphere sudden warming-ionosphere coupling due to vertically propagating tide. Geophysical Research Letters, 37(L11104), 2010.
- [83] N. M. Pedatella and J. M. Forbes. The quasi 2 day wave and spatial-temporal variability of the oh emission and ionosphere. Journal of Geophysical Research: Space Physics, 117(A1), 2012.
- [84] N. M. Pedatella, M. E. Hagan, and A. Maute. The comparative importance of de3, se2, and spw4 on the generation of wavenumber-4 longitude structures in the low-latitude ionosphere during september equinox. Geophysical Research Letters, 39(19), 2012.

- [85] N. M. Pedatella, H.-L. Liu, and M. E. Hagan. Day-to-day migrating and nonmigrating tidal variability due to the six-day planetary wave. Journal of Geophysical Research: Space Physics, 117(A6), 2012.
- [86] A. R. Plumb. Baroclinic instability of the summer mesosphere: a mechanism for the quasi-two-day wave? Journal of the Atmospheric Sciences, 40(1):262–270, 1983.
- [87] A. Pogoreltsev. Numerical simulation of secondary planetary waves arising from the nonlinear interaction of the normal atmospheric modes. Physics and Chemistry of the Earth, Part C: Solar, Terrestrial & Planetary Science, 26(6):395 – 403, 2001.
- [88] W. J. Randel. The evaluation of winds from geopotential height data in the stratosphere. Journal of the Atmospheric Sciences, 44(20):3097–3120, 1987.
- [89] W. J. Randel. Observations of the 2-day wave in nmc stratospheric analyses. Journal of Atmospheric Science, 51:306–313, 1994.
- [90] E. E. Remsberg, B. T. Marshall, M. Garcia-Comas, D. Krueger, G. S. Lingenfelter, J. Martin-Torres, M. G. Mlynczak, J. M. Russell, A. K. Smith, Y. Zhao, C. Brown, L. L. Gordley, M. J. Lopez-Gonzalez, M. Lopez-Puertas, C.-Y. She, M. J. Taylor, and R. E. Thompson. Assessment of the quality of the version 1.07 temperature-versus-pressure profiles of the middle atmosphere from timed/saber. Journal of Geophysical Research: Atmospheres, 113(D17), 2008.
- [91] A. D. Richmond. Energy relations of atmospheric tides and their significance to approximate methods of solutions for tides with dissipative forces. Journal of the Atmospheric Sciences, 32(980), 1975.
- [92] D. C. Riggin, D. M. and Fritts, T. Tsuda, T. Nakamura, and R. A. Vincent. Radar observations of a 3-day kelvin wave in the equatorial mesosphere. Journal of Geophysical Research, 102:26141–26157, 1997.
- [93] C. D. Rodgers and A. J. Prata. Evidence for a traveling two-day wave in the middle atmosphere. Journal of Geophysical Research: Oceans, 86(C10):9661–9664, 1981.
- [94] R. Russell. Layers of earth’s atmosphere, September 2010.
- [95] M. L. Salby. The 2-day wave in the middle atmosphere: Observations and theory. Journal of Geophysical Research: Oceans (1978–2012), 86(C10):9654–9660, 1981.
- [96] M. L. Salby. Rossby normal modes in nonuniform background configurations. part i: Simple fields. Journal of the Atmospheric Sciences, 38(9):1803–1826, 1981.
- [97] M. L. Salby. Sampling theory for asynoptic satellite observations. part i: Space-time spectra, resolution, and aliasing. Journal of the Atmospheric Sciences, 39(11):2577–2600, 1982.
- [98] M. L. Salby. Survey of planetary-scale traveling waves: The state of theory and observations. Reviews of Geophysics, 22(2):209–236, 1984.
- [99] M. L. Salby and P. F. Callaghan. Seasonal amplification of the 2-day wave: Relationship between normal mode and instability. Journal of the Atmospheric Sciences, 58(14):1858–1869, 2001.

- [100] M. L. Salby, D. L. Hartmann, P. L. Bailey, and J. C. Gille. Evidence for equatorial kelvin modes in nimbus-7 lims. Journal of Atmospheric Science, 41:220–235, 1984.
- [101] F. Sassi, R. Garcia, B. A. Boville, and H.-L. Liu. On temperature inversions and the mesospheric surf zone. Journal of Geophysical Research, 107(D19), 2002.
- [102] M. J. Schwartz, A. Lambert, G. L. Manney, W. G. Read, N. J. Livesey, L. Froidevaux, C. O. Ao, P. F. Bernath, C. D. Boone, R. E. Cofield, W. H. Daffer, B. J. Drouin, E. J. Fetzer, R. A. Fuller, R. F. Jarnot, J. H. Jiang, Y. B. Jiang, B. W. Knosp, K. Krüger, J.-L. F. Li, M. G. Mlynczak, S. Pawson, J. M. Russell, M. L. Santee, W. V. Snyder, P. C. Stek, R. P. Thurstans, A. M. Tompkins, P. A. Wagner, K. A. Walker, J. W. Waters, and D. L. Wu. Validation of the aura microwave limb sounder temperature and geopotential height measurements. Journal of Geophysical Research: Atmospheres, 113(D15), 2008.
- [103] M. Siebert. Atmospheric tides. Advances in Geophysics, 7(105), 1961.
- [104] A. A. Svoboda, J. M. Forbes, and S. Miyahara. A space-based climatology of diurnal {MLT} tidal winds, temperatures and densities from {UARS} wind measurements. Journal of Atmospheric and Solar-Terrestrial Physics, 67(16):1533 – 1543, 2005.
- [105] E. R. Talaat and R. S. Lieberman. Nonmigrating diurnal tides in mesospheric and lower-thermospheric winds and temperatures. Journal of the Atmospheric Sciences, 56(24):4073–4087, 1999.
- [106] J. D. Tarpley. The ionospheric wind dynamo-ii solar tides. Planetary and Space Science, 18:1091–1103, 1970.
- [107] H. Teitelbaum and F. Vial. On tidal variability induced by nonlinear interaction with planetary waves. Journal of Geophysical Research: Space Physics, 96(A8):14169–14178, 1991.
- [108] A. O. Truskowski, J. M. Forbes, X. Zhang, and S. E. Palo. New perspectives on thermosphere tides: 1. lower thermosphere spectra and seasonal-latitudinal structures. Earth, Planets and Space, 66(136), 2014.
- [109] T. Tsuda and S. Kato. Diurnal non-migrating tides excited by differential heating due to land-sea distribution. J. Meteor. Soc. Japan, 67:43–54, 1989.
- [110] V. M. Tunbridge, D. J. Sandford, and N. J. Mitchell. Zonal wave numbers of the summertime 2 day planetary wave observed in the mesosphere by eos aura microwave limb sounder. Journal of Geophysical Research: Atmospheres, 116(D11), 2011.
- [111] R. A. Vincent and D. C. Fritts. A climatology of gravity wave motions in the mesopause region. Journal of the Atmospheric Sciences, 44(4), 1986.
- [112] R. L. Walterscheid, J. G. Devore, and S. V. Venkateswaran. Influence of mean zonal motion and meridional temperature gradients on the solar semidiurnal atmospheric tide: A revised spectral study with improved heating rates. Journal of the Atmospheric Sciences, 37(2):455–470, 1980.
- [113] C. R. Williams and S. K. Avery. Diurnal nonmigrating tidal oscillations forced by deep convective clouds. Journal of Geophysical Research: Atmospheres, 101(D2):4079–4091, 1996.

- [114] D. L. Wu. A least squares method for spectral analysis of space-time series. Journal of the Atmospheric Sciences, 52(20):3501–3511, 1995.
- [115] D. L. Wu, E. F. Fishbein, W. G. Read, and J. W. Waters. Excitation and evolution of the quasi-2-day wave observed in uars/mls temperature measurements. Journal of the Atmospheric Sciences, 53:728–738, 1996.
- [116] D. L. Wu, P. B. Hays, W. R. Skinner, A. R. Marshall, M. D. Burrage, R. S. Lieberman, and D. A. Ortland. Observations of the quasi 2-day wave from the high resolution doppler imager on uars. Geophysical Research Letters, 20(24):2853–2856, 1993.
- [117] Q. Wu, D. A. Ortland, S. C. Solomon, W. R. Skinner, and R. J. Niciejewski. Global distribution, seasonal, and inter-annual variations of mesospheric semidiurnal tide observed by timed tidi. Journal of Atmospheric and Solar-Terrestrial Physics, 73:2482–2502, 2011.
- [118] J. Xu, A. K. Smith, W. Yuan, H.-L. Liu, Q. Wu, M. G. Mlynczak, and J. M. Russell. Global structure and long-term variations of zonal mean temperature observed by timed/saber. Journal of Geophysical Research, 112(D24106), 2007.
- [119] X. Zhang, J. M. Forbes, and M. E. Hagan. Longitudinal variation of tides in the mlt region: 1. tides driven by tropospheric net radiative heating. Journal of Geophysical Research: Space Physics, 115(A6), 2010.
- [120] X. Zhang, J. M. Forbes, M. E. Hagan, J. M. Russell, S. E. Palo, C. J. Mertens, and M. G. Mlynczak. Monthly tidal temperatures 20–120 km from timed/saber. Journal of Geophysical Research: Space Physics, 111(A10), 2006.

## Appendix A

### GLOSSARY

$u$	Zonal wind velocity
$v$	Meridional wind velocity
$w$	Vertical wind velocity
$T$	Temperature
$p$	Pressure
$\Phi$	Geopotential height
$\rho$	Density
$\Omega$	Rotation rate of Earth
$s$	Zonal Wavenumber where positive is eastward
$\sigma$	Frequency in cycles per day
$\omega$	Wave frequency in arbitrary units
$\phi$	Latitude
$\lambda$	Longitude
$J$	Diabatic Heating
$R$	Specific gas constant
$\vartheta$	Thermal dissipation
$c_v$	Specific heat at constant volume
$\theta$	Wave Phase
$a$	Radius of the Earth

## Appendix B

### WAVE NOMENCLATURE

Zonal wavenumbers ( $s$ ) are defined such that westward (eastward) propagating waves have negative (positive) zonal wavenumbers. Additionally, each atmospheric tide or planetary wave in this dissertation is represented in shorthand notation by the following convention: [(period)(propagation direction)( $|s|$ )] where period is ‘D’ for diurnal, ‘S’ for semidiurnal or otherwise written out explicitly, propagation direction is ‘W’ for westward or ‘E’ for eastward, and  $|s|$  is the absolute value zonal wavenumber. Waves commonly referred to in this dissertation are displayed as follows:

**DW1**: Migrating Diurnal Tide

**SW2**: Migrating Semidiurnal Tide

**2dayE2**: 2 day period, eastward propagating with zonal wavenumber 2

**16hrW4**: 16 hour period, westward propagating with zonal wavenumber 4

**16hrE1**: 16 hour period, eastward propagating with zonal wavenumber 1

**9.6hrW5**: 9.6 hour period, westward propagating with zonal wavenumber 5

**QTDW** or **2-dayW3**: Quasi two-day wave

Each planetary wave and atmospheric tide is often composed of a summation of orthogonal Hough modes predicted by classical tidal theory. In this dissertation, Hough modes are denoted by ( $|s|$ ,  $n$ ) where  $n$  is the meridional index representing the number of latitudinal nodes in the Northern or Southern Hemisphere. Positive ‘ $n$ ’ refers to propagating Hough modes while negative ‘ $n$ ’ represents trapped modes. For example, the DW1 (1, 1) mode refers to the propagating Hough mode with meridional index 1 for the DW1.

## Appendix C

### DERIVATION OF NONLINEAR FORCING

- (1) Nonlinear forcing terms for secondary waves originate from primary wave-wave advection terms and other products of first order perturbations. To derive the forcing originating from wave-wave advection, each perturbation variable is decomposed into the summation of two primary waves ( $f' = f'_1 + f'_2$ ). Perturbation velocities are also assumed to be mainly in the horizontal direction ( $w=0$ ). Hence, the wave-wave advection term for an arbitrary field variable,  $f$ , can be expanded as follows.

$$\begin{aligned} \vec{u}' \cdot \nabla f' = & u'_1 \frac{\partial}{a \cos \phi \partial \lambda} f'_2 + u'_2 \frac{\partial}{a \cos \phi \partial \lambda} f'_1 + u'_1 \frac{\partial}{a \cos \phi \partial \lambda} f'_1 + u'_2 \frac{\partial}{a \cos \phi \partial \lambda} f'_2 + \\ & v'_1 \frac{\partial}{a \partial \phi} f'_2 + v'_2 \frac{\partial}{a \partial \phi} f'_1 + v'_1 \frac{\partial}{a \partial \phi} f'_1 + v'_2 \frac{\partial}{a \partial \phi} f'_2 \quad (\text{C.1}) \end{aligned}$$

- (2) Each term on the right hand side of Equation C.1 is expanded by assuming perturbation solutions in the form  $\hat{f} \cos(s\lambda - \omega t + \theta_f)$ ,  $\hat{u} \cos(s\lambda - \omega t + \theta_u)$ , and  $\hat{v} \cos(s\lambda - \omega t + \theta_v)$  where  $\hat{f}$ ,  $\hat{u}$  and  $\hat{v}$  represent real-valued amplitude values and  $\theta_f$ ,  $\theta_u$  and  $\theta_v$  are the phase values of each wave.

$$\begin{aligned} u'_1 \frac{\partial}{a \cos \phi \partial \lambda} f'_2 &= \frac{1}{a \cos \phi} [\hat{u}_1 \cos(s_1 \lambda - \omega_1 t + \theta_{u1})] \frac{\partial}{\partial \lambda} [\hat{f}_2 \cos(s_2 \lambda - \omega_2 t + \theta_{f2})] \\ &= \frac{1}{a \cos \phi} \hat{u}_1 \hat{f}_2 [\cos(s_1 \lambda - \omega_1 t + \theta_{u1})] [-s_2 \sin(s_2 \lambda - \omega_2 t + \theta_{f2})] \\ &= \frac{-s_2}{a \cos \phi} \hat{u}_1 \hat{f}_2 \left[ \frac{1}{2} \sin((s_1 + s_2)\lambda - (\omega_1 + \omega_2)t + (\theta_{u1} + \theta_{f2})) \right. \\ &\quad \left. + \frac{1}{2} \sin((s_2 - s_1)\lambda - (\omega_2 - \omega_1)t + (\theta_{f2} - \theta_{u1})) \right] \quad (\text{C.2}) \end{aligned}$$

$$u'_2 \frac{\partial}{a \cos \phi \partial \lambda} f'_1 = \frac{-s_1}{a \cos \phi} \hat{u}_2 \hat{f}_1 \left[ \frac{1}{2} \sin((s_1 + s_2)\lambda - (\omega_1 + \omega_2)t + (\theta_{f_1} + \theta_{u_2})) - \frac{1}{2} \sin((s_2 - s_1)\lambda - (\omega_2 - \omega_1)t + (\theta_{u_2} - \theta_{f_1})) \right] \quad (\text{C.3})$$

$$u'_1 \frac{\partial}{a \cos \phi \partial \lambda} f'_1 = \frac{-s_1}{a \cos \phi} \hat{u}_1 \hat{f}_1 \left[ \frac{1}{2} \sin((2s_1)\lambda - (2\omega_1)t + (\theta_{u_1} + \theta_{f_1})) + \frac{1}{2} \sin(\theta_{f_1} - \theta_{u_1}) \right] \quad (\text{C.4})$$

$$u'_2 \frac{\partial}{a \cos \phi \partial \lambda} f'_2 = \frac{-s_2}{a \cos \phi} \hat{u}_2 \hat{f}_2 \left[ \frac{1}{2} \sin((2s_2)\lambda - (2\omega_2)t + (\theta_{u_2} + \theta_{f_2})) + \frac{1}{2} \sin(\theta_{f_2} - \theta_{u_2}) \right] \quad (\text{C.5})$$

$$v'_1 \frac{\partial}{a \partial \phi} f'_2 = \frac{1}{a} \frac{\partial \hat{f}_2}{\partial \phi} \hat{v}_1 \left[ \frac{1}{2} \cos((s_1 + s_2)\lambda - (\omega_1 + \omega_2)t + (\theta_{v_1} + \theta_{f_2})) + \frac{1}{2} \cos((s_2 - s_1)\lambda - (\omega_2 - \omega_1)t + (\theta_{f_2} - \theta_{v_1})) \right] \quad (\text{C.6})$$

$$v'_2 \frac{\partial}{a \partial \phi} f'_1 = \frac{1}{a} \frac{\partial \hat{f}_1}{\partial \phi} \hat{v}_2 \left[ \frac{1}{2} \cos((s_1 + s_2)\lambda - (\omega_1 + \omega_2)t + (\theta_{f_1} + \theta_{v_2})) + \frac{1}{2} \cos((s_2 - s_1)\lambda - (\omega_2 - \omega_1)t + (\theta_{v_2} - \theta_{f_1})) \right] \quad (\text{C.7})$$

$$v'_1 \frac{\partial}{a \partial \phi} f'_1 = \frac{1}{a} \frac{\partial \hat{f}_1}{\partial \phi} \hat{v}_1 \left[ \frac{1}{2} \cos((2s_1)\lambda - (2\omega_1)t + (\theta_{v_1} + \theta_{f_1})) + \frac{1}{2} \cos(\theta_{f_1} - \theta_{v_1}) \right] \quad (\text{C.8})$$

$$v'_2 \frac{\partial}{a \partial \phi} f'_2 = \frac{1}{a} \frac{\partial \hat{f}_2}{\partial \phi} \hat{v}_2 \left[ \frac{1}{2} \cos((2s_2)\lambda - (2\omega_2)t + (\theta_{f_2} + \theta_{v_2})) + \frac{1}{2} \cos(\theta_{f_2} - \theta_{v_2}) \right] \quad (\text{C.9})$$

- (3) By grouping together terms of same frequency and wavenumber in Equations C.2-C.10, the advection term can be written as a sum of the difference, sum, self-interaction waves and a DC term.

$$\vec{u} \cdot \nabla f = [\vec{u} \cdot \nabla f]_{[(s_1+s_2),(\omega_1+\omega_2)]} + [\vec{u} \cdot \nabla f]_{[(s_2-s_1),(\omega_2-\omega_1)]} + [\vec{u} \cdot \nabla f]_{[(2s_1),(2\omega_1)]} + [\vec{u} \cdot \nabla f]_{[(2s_2),(2\omega_2)]} + DC \quad (C.10)$$

- (4) According to Teitelbaum and Vial [107] and other studies, only the sum and difference waves are important. The nonlinear advection terms forcing the sum and difference waves are expanded here.

$$\begin{aligned} [\vec{u} \cdot \nabla f]_{[(s_1+s_2),(\omega_1+\omega_2)]} &= \frac{1}{2} \left[ \frac{1}{a} \frac{\partial \hat{f}_2}{\partial \phi} \hat{v}_1 \right] \cos((s_1 + s_2)\lambda - (\omega_1 + \omega_2)t + (\theta_{v1} + \theta_{f2})) \\ &+ \frac{1}{2} \left[ \frac{1}{a} \frac{\partial \hat{f}_1}{\partial \phi} \hat{v}_2 \right] \cos((s_1 + s_2)\lambda - (\omega_1 + \omega_2)t + (\theta_{f1} + \theta_{v2})) \\ &- \frac{1}{2} \left[ \frac{s_2}{a \cos \phi} \hat{u}_1 \hat{f}_2 \right] \sin((s_1 + s_2)\lambda - (\omega_1 + \omega_2)t + (\theta_{u1} + \theta_{f2})) \\ &- \frac{1}{2} \left[ \frac{s_1}{a \cos \phi} \hat{u}_2 \hat{f}_1 \right] \sin((s_1 + s_2)\lambda - (\omega_1 + \omega_2)t + (\theta_{f1} + \theta_{u2})) \\ &= A_1 \cos((s_1 + s_2)\lambda - (\omega_1 + \omega_2)t + \theta_{A1}) \\ &+ A_2 \cos((s_1 + s_2)\lambda - (\omega_1 + \omega_2)t + \theta_{A2}) \\ &+ A_3 \sin((s_1 + s_2)\lambda - (\omega_1 + \omega_2)t + \theta_{A3}) \\ &+ A_4 \sin((s_1 + s_2)\lambda - (\omega_1 + \omega_2)t + \theta_{A4}) \end{aligned} \quad (C.11)$$

where

$$\begin{aligned} A_1 &= \frac{1}{2} \left[ \frac{1}{a} \frac{\partial \hat{f}_2}{\partial \phi} \hat{v}_1 \right] \\ A_2 &= \frac{1}{2} \left[ \frac{1}{a} \frac{\partial \hat{f}_1}{\partial \phi} \hat{v}_2 \right] \\ A_3 &= -\frac{1}{2} \left[ \frac{s_2}{a \cos \phi} \hat{u}_1 \hat{f}_2 \right] \\ A_4 &= -\frac{1}{2} \left[ \frac{s_1}{a \cos \phi} \hat{u}_2 \hat{f}_1 \right] \end{aligned}$$

$$\theta_{A1} = \theta_{v1} + \theta_{f2}$$

$$\theta_{A2} = \theta_{f1} + \theta_{v2}$$

$$\theta_{A3} = \theta_{u1} + \theta_{f2}$$

$$\theta_{A4} = \theta_{f1} + \theta_{u2}$$

$$\begin{aligned}
[\vec{u} \cdot \nabla u]_{[(s_2-s_1),(\omega_2-\omega_1)]} &= \frac{1}{2} \left[ \frac{1}{a} \frac{\partial \hat{f}_2}{\partial \phi} \hat{v}_1 \right] \cos((s_2 - s_1)\lambda - (\omega_2 - \omega_1)t + (\theta_{f2} - \theta_{v1})) \\
&+ \frac{1}{2} \left[ \frac{1}{a} \frac{\partial \hat{f}_1}{\partial \phi} \hat{v}_2 \right] \cos((s_2 - s_1)\lambda - (\omega_2 - \omega_1)t + (\theta_{v2} - \theta_{f1})) \\
&- \frac{1}{2} \left[ \frac{s_2}{a \cos \phi} \hat{u}_1 \hat{f}_2 \right] \sin((s_2 - s_1)\lambda - (\omega_2 - \omega_1)t + (\theta_{f2} - \theta_{u1})) \\
&+ \frac{1}{2} \left[ \frac{s_1}{a \cos \phi} \hat{u}_2 \hat{f}_1 \right] \sin((s_2 - s_1)\lambda - (\omega_2 - \omega_1)t + (\theta_{u2} - \theta_{f1})) \\
&= B_1 \cos((s_2 - s_1)\lambda - (\omega_2 - \omega_1)t + \theta_{B1}) \\
&+ B_2 \cos((s_2 - s_1)\lambda - (\omega_2 - \omega_1)t + \theta_{B2}) \\
&+ B_3 \sin((s_2 - s_2)\lambda - (\omega_2 - \omega_1)t + \theta_{B3}) \\
&+ B_4 \sin((s_2 - s_2)\lambda - (\omega_2 - \omega_1)t + \theta_{B4}) \tag{C.12}
\end{aligned}$$

where

$$\begin{aligned}
B_1 &= \frac{1}{2} \left[ \frac{1}{a} \frac{\partial \hat{f}_2}{\partial \phi} \hat{v}_1 \right] \\
B_2 &= \frac{1}{2} \left[ \frac{1}{a} \frac{\partial \hat{f}_1}{\partial \phi} \hat{v}_2 \right] \\
B_3 &= -\frac{1}{2} \left[ \frac{s_2}{a \cos \phi} \hat{u}_1 \hat{f}_2 \right] \\
B_4 &= \frac{1}{2} \left[ \frac{s_1}{a \cos \phi} \hat{u}_2 \hat{f}_1 \right]
\end{aligned}$$

$$\theta_{B1} = \theta_{f2} - \theta_{v1}$$

$$\theta_{B2} = \theta_{v2} - \theta_{f1}$$

$$\theta_{B3} = \theta_{f2} - \theta_{u1}$$

$$\theta_{B4} = \theta_{u2} - \theta_{f1}$$

- (5) Equations C.11-C.12 consist of sine and cosine waves with the same frequency and wavenumber, but varying amplitude and phase. The following step adds the sine and cosine waves in Equation C.11 using complex trigonometric identities (Equation C.13-C.14) to obtain a single cosine wave for the sum wave (Equation C.14), representing the nonlinear advection forcing for the sum wave.

$$X \cos(s\lambda - \omega t + \theta) = \frac{1}{2}(X \cos(\theta) + jX \sin(\theta))e^{j(s\lambda - \omega t)} + \frac{1}{2}(X \cos(\theta) - jX \sin(\theta))e^{-j(s\lambda - \omega t)} \quad (\text{C.13})$$

$$X \sin(s\lambda - \omega t + \theta) = -\frac{j}{2}(X \cos(\theta) + jX \sin(\theta))e^{j(s\lambda - \omega t)} + \frac{j}{2}(X \cos(\theta) - jX \sin(\theta))e^{-j(s\lambda - \omega t)} \quad (\text{C.14})$$

$$[\vec{u} \cdot \nabla f]_{[(s_1+s_2),(\omega_1+\omega_2)]} = Amp_{sum} \cos((s_1 + s_2)\lambda - (\omega_1 + \omega_2)t + Ph_{sum}) \quad (\text{C.15})$$

$$Amp_{sum} = [(A_1 \cos(\theta_{A1}) + A_2 \cos(\theta_{A2}) + A_3 \sin(\theta_{A3}) + A_4 \sin(\theta_{A4}))^2 + (A_1 \sin(\theta_{A1}) + A_2 \sin(\theta_{A2}) - A_3 \cos(\theta_{A3}) - A_4 \cos(\theta_{A4}))^2]^{1/2} \quad (\text{C.16})$$

$$Ph_{sum} = \tan^{-1} \left( \frac{A_1 \sin(\theta_{A1}) + A_2 \sin(\theta_{A2}) - A_3 \cos(\theta_{A3}) - A_4 \cos(\theta_{A4})}{A_1 \cos(\theta_{A1}) + A_2 \cos(\theta_{A2}) + A_3 \sin(\theta_{A3}) + A_4 \sin(\theta_{A4})} \right) \quad (\text{C.17})$$

- (6) Similarly, Equation C.12 simplified to obtain the nonlinear advection forcing for the difference wave.

$$[\vec{u} \cdot \nabla f]_{[(s_2-s_1),(\omega_2-\omega_1)]} = Amp_{diff} \cos((s_1 + s_2)\lambda - (\omega_1 + \omega_2)t + Ph_{diff}) \quad (C.18)$$

where

$$\begin{aligned} Amp_{diff} &= [(B_1 \cos(\theta_{B1}) + B_2 \cos(\theta_{B2}) + B_3 \sin(\theta_{B3}) + B_4 \sin(\theta_{B4}))^2 \\ &+ (B_1 \sin(\theta_{B1}) + B_2 \sin(\theta_{B2}) - B_3 \cos(\theta_{B3}) - B_4 \cos(\theta_{B4}))^2]^{1/2} \quad (C.19) \end{aligned}$$

$$Ph_{diff} = \tan^{-1} \left( \frac{B_1 \sin(\theta_{B1}) + B_2 \sin(\theta_{B2}) - B_3 \cos(\theta_{B3}) - B_4 \cos(\theta_{B4})}{B_1 \cos(\theta_{B1}) + B_2 \cos(\theta_{B2}) + B_3 \sin(\theta_{B3}) + B_4 \sin(\theta_{B4})} \right) \quad (C.20)$$

## Appendix D

### FAST FOURIER SYNOPTIC MAPPING DETAILS

An outline of the Fast Fourier Synoptic Mapping procedure is provided along with additional aliasing tests.

#### D.1 FFSM Procedure

Note: To accommodate Salby [97] notation, ‘m’ here represents zonal wavenumber while ‘s’ represents the along orbit coordinate direction.

- (1) Sort data into orbit, latitude, altitude, ascending/descending bins. The observed longitudes and times are related to each other by

$$\lambda_{dj} = \lambda_{d0} - c_0\tau_0j \quad (\text{D.1})$$

$$\lambda_{aj} = \lambda_{a0} - c_0\tau_0j \quad (\text{D.2})$$

$$t_{dj} = t_{d0} - \tau_0j \quad (\text{D.3})$$

$$t_{aj} = \lambda_{a0} - \tau_0j \quad (\text{D.4})$$

where  $j=0\dots J-1$ ,  $J$  is the total number of orbits used in the analysis,  $c_0$  is the magnitude of the zonal speed of the satellite in rad/day,  $\tau_0$  is the orbital period, and  $\lambda_{d0}$ ,  $\lambda_{a0}$ ,  $t_{d0}$ , and  $t_{a0}$  are the starting descending longitude, ascending longitude, descending time, and ascending time for the sequence. From these equations, it is shown that  $\lambda$  is not independent of time and thus, separate temporal and zonal transforms cannot be performed.

- (2) The remaining steps are performed for data contained in each altitude and latitude bin.
- (3) Calculate orbital parameters: average time change between orbits ( $\Delta t$ ), average longitude change between orbits ( $\Delta \lambda$ ), average time between ascending and descending points on the same orbit ( $\Delta t_{ad}$ ), and average longitude change between ascending and descending points on the same orbit ( $\Delta \lambda_{ad}$ ).

$$\Delta \lambda = \langle \lambda_{j-1} - \lambda_j \rangle \quad (\text{D.5})$$

$$\Delta t = \langle t_{j-1} - t_j \rangle \quad (\text{D.6})$$

$$\Delta \lambda_{ad} = \langle \lambda_{dj} - \lambda_{aj} \rangle \quad (\text{D.7})$$

$$\Delta t_{ad} = \langle t_{dj} - t_{aj} \rangle \quad (\text{D.8})$$

- (4) Rotate the data from  $(t, \lambda)$  coordinates into a coordinate system defined by  $s$  (along orbit) and  $r$  (perpendicular to  $s$ ). The magnitude of the zonal speed of the satellite,  $c_0$  determines the rotation angle between the  $[t, \lambda]$  axes and  $[s, r]$  axes. The zonal speed of the satellite and the rotation angle ( $\alpha$ ) of the coordinate system is calculated by

$$c_0 = |d\lambda/dt| \quad (\text{D.9})$$

$$\alpha = \tan^{-1}\left(\frac{dt}{d\lambda}\right) = \tan^{-1}\left(\frac{1}{c_0}\right) \quad (\text{D.10})$$

The relationships between the coordinate systems are defined by:

$$\lambda = s \cos \alpha + r \sin \alpha \quad (\text{D.11})$$

$$t = -s \sin \alpha + r \cos \alpha \quad (\text{D.12})$$

$$s = \lambda \cos \alpha - t \sin \alpha = \frac{|c_0| \lambda - t}{\sqrt{1 + c_0^2}} \quad (\text{D.13})$$

$$r = \lambda \sin \alpha + t \cos \alpha = \frac{\lambda + |c_0| t}{\sqrt{1 + c_0^2}} \quad (\text{D.14})$$

- (5) The ascending and descending data series have unique r-values. The r-values can be found given a  $(\lambda, t)$  pair for each series and rotating the pair into  $(s, r)$  coordinates using the above equations. Please note that ‘s’ is NOT representative of zonal wavenumber here. These values denoted  $r_a$  and  $r_d$  can be expressed as

$$r_a = \lambda_{a0} \sin \alpha + t_{a0} \cos \alpha \quad (\text{D.15})$$

$$r_d = \lambda_{d0} \sin \alpha + t_{d0} \cos \alpha \quad (\text{D.16})$$

- (6) The transformed coordinate (s) decreases with time so it is desirable to reverse the series. After this is done, the J-1 term becomes the first term of the series and must be accounted for as an offset after performing the Fourier Transform. The s-coordinates of the J-1 term in the ascending and descending series are derived by rotating the last  $(\lambda, t)$  coordinate in each series to the  $(s, r)$  frame.

$$s_{d0} = (\lambda_{d0} - c_0 \tau_0 (J - 1)) \cos \alpha - (t_{d0} + \tau_0 (J - 1)) \sin \alpha \quad (\text{D.17})$$

$$s_{a0} = (\lambda_{a0} - c_0 \tau_0 (J - 1)) \cos \alpha - (t_{a0} + \tau_0 (J - 1)) \sin \alpha \quad (\text{D.18})$$

- (7) Perform separate DFTs of the time-reversed ascending and descending data series. The frequencies corresponding to the spectral values of each transform are denoted by  $k_s$ .
- (8) According to Salby, only two possible waves correspond to any value of  $k_s$ :  $(k_s, k_{r-})$  and  $(k_s, k_{r+})$ . These pairs exist because waves of different wavenumber and frequency can be Doppler shifted to the same observed frequency due to the satellite’s motion relative to the earth given by

$$F_0 = |\sigma + m| \quad (\text{D.19})$$

where  $F_0$  is the observed frequency in cycles per day,  $m$  is the zonal wavenumber, and  $\sigma$  is the actual wave frequency in cycles per day. Thus, there are two possible  $(\sigma, m)$  pairs for each observed frequency  $F_0$  within the satellite Nyquist limits.

Salby [1982] showed that the r-coordinates of the two wave pairs corresponding to any value of  $k_s$  due to the satellite's motion relative to the earth are

$$k_{r-} = -k_s|c_0| + m(1 + c_0^2)^{0.5} \quad (\text{D.20})$$

$$k_{r+} = -k_s|c_0| + (m + 1)(1 + c_0^2)^{0.5} \quad (\text{D.21})$$

- (9) Adjust the phase of the two 1-D Fourier transforms using the offsets in the s-coordinate shown in Equations D.17-D.18.

$$\Psi'_a = \Psi_a e^{-ik_s s_{a0}} \quad (\text{D.22})$$

$$\Psi'_d = \Psi_d e^{-ik_s s_{d0}} \quad (\text{D.23})$$

- (10) For a given  $k_s$ , a system of two equations for the ascending and descending FFTs with two unknowns consisting of the wave pairs is formed. By solving the wave pairs,  $\Psi(k_s, k_{r-})$  and  $\Psi(k_s, k_{r+})$ , for each  $k_s$ , all spectra are solved within the Nyquist limits.

$$\Psi(k_s, k_{r-})e^{ik_{r-}r_d} + \Psi(k_s, k_{r+})e^{ik_{r+}r_d} = \Psi'(k_s, r_d) \quad (\text{D.24})$$

$$\Psi(k_s, k_{r-})e^{ik_{r-}r_a} + \Psi(k_s, k_{r+})e^{ik_{r+}r_a} = \Psi'(k_s, r_a) \quad (\text{D.25})$$

Solve for  $\Psi(k_s, k_{r-})$  and  $\Psi(k_s, k_{r+})$

$$\Psi(k_s, k_{r-}) = \frac{\Psi''_a - \Psi''_d e^{-i\Delta\lambda_{ad}}}{1 - e^{-i\Delta\lambda_{ad}}} \quad (\text{D.26})$$

$$\Psi(k_s, k_{r+}) = \frac{[\Psi''_d - \Psi''_a]e^{-ir_d/\sin\alpha}}{-[1 - e^{-i\Delta\lambda_{ad}}]} \quad (\text{D.27})$$

where

$$\Psi''_d = \Psi'_d e^{-ik_{r-}r_d} \quad (\text{D.28})$$

$$\Psi''_a = \Psi'_a e^{-ik_{r-}r_a} \quad (\text{D.29})$$

$$e^{-i\Delta\lambda'_{ad}} = \frac{e^{ik_{r+}r_a} e^{ik_{r-}r_d}}{e^{ik_{r-}r_a} e^{ik_{r+}r_d}} \quad (\text{D.30})$$

$\Delta\lambda'_{ad} = \Delta\lambda + |c_0|\Delta t_{ad}$  and is the instantaneous separation between ascending and descending transversals around a latitude circle, i.e., if the ascending and descending observations were made simultaneously.

- (11) The complex conjugate of the computed spectra are simply rotated back into the frequency-wavenumber spectrum by using D.11-D.14 to obtain the full spectrum within the Nyquist limits.

## D.2 Additional Aliasing Tests for Least Squares and FFSSM methods

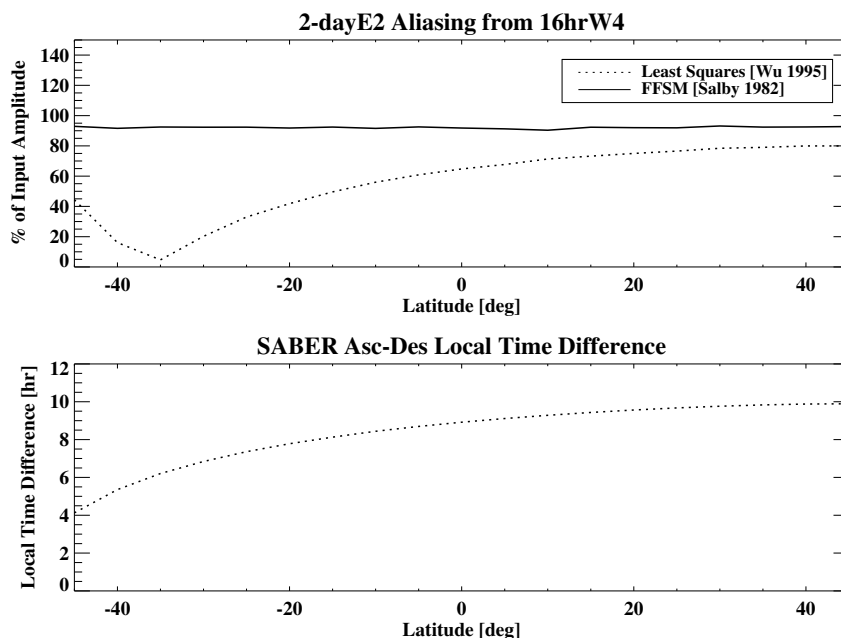


Figure D.1: A comparison of the 2dayE2 amplitude estimated when only the 16hrW4 wave is present using SABER ascending/descending sampling for the traditional least squares method and the FFSSM-least squares method used in this dissertation. The top plot shows the estimated amplitude of the 2dayE2 in terms of the percent 16hrW4 amplitude as a function of latitude. The bottom plot shows the difference between the ascending and descending local times as a function of latitude.

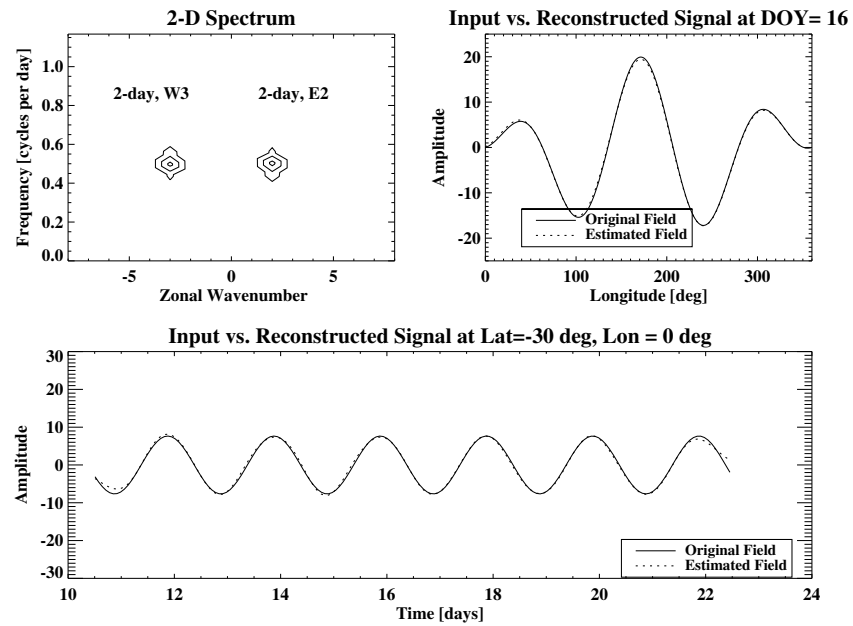


Figure D.2: Reconstruction of a westward-propagating sinusoid described by a period of 2 days, zonal wavenumber 3 and amplitude of 10 K from FFSM spectral coefficients obtained for MLS time/longitude sampling of the equator over 12 days. The top left plot shows the FFSM frequency-wavenumber spectrum. The top right plot compares the FFSM reconstructed signal (dashed) to the true sinusoid signal (solid) at constant time and the bottom plot compares the signals at constant longitude.

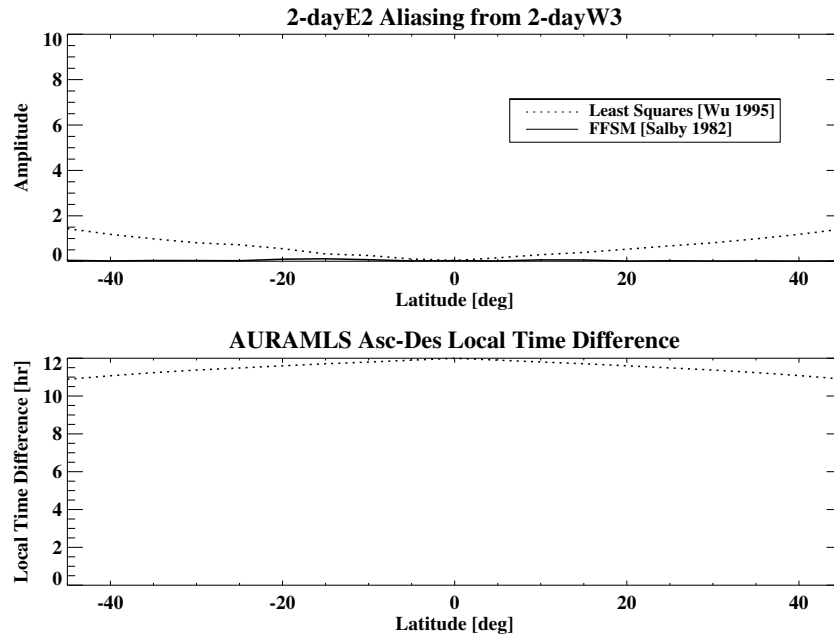


Figure D.3: Same as Figure D.1 except with 2dayW3 wave and MLS sampling.

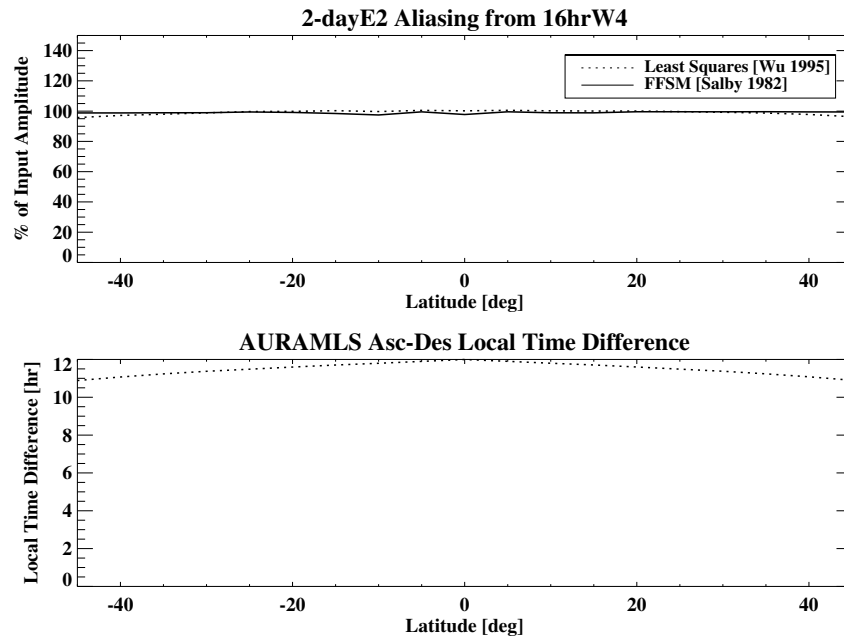


Figure D.4: Same as Figure D.1 except with 16hrW4 wave and MLS sampling.

## Appendix E

### SUPPLEMENTAL FIGURES: PRIMARY WAVES AND NONLINEAR FORCING

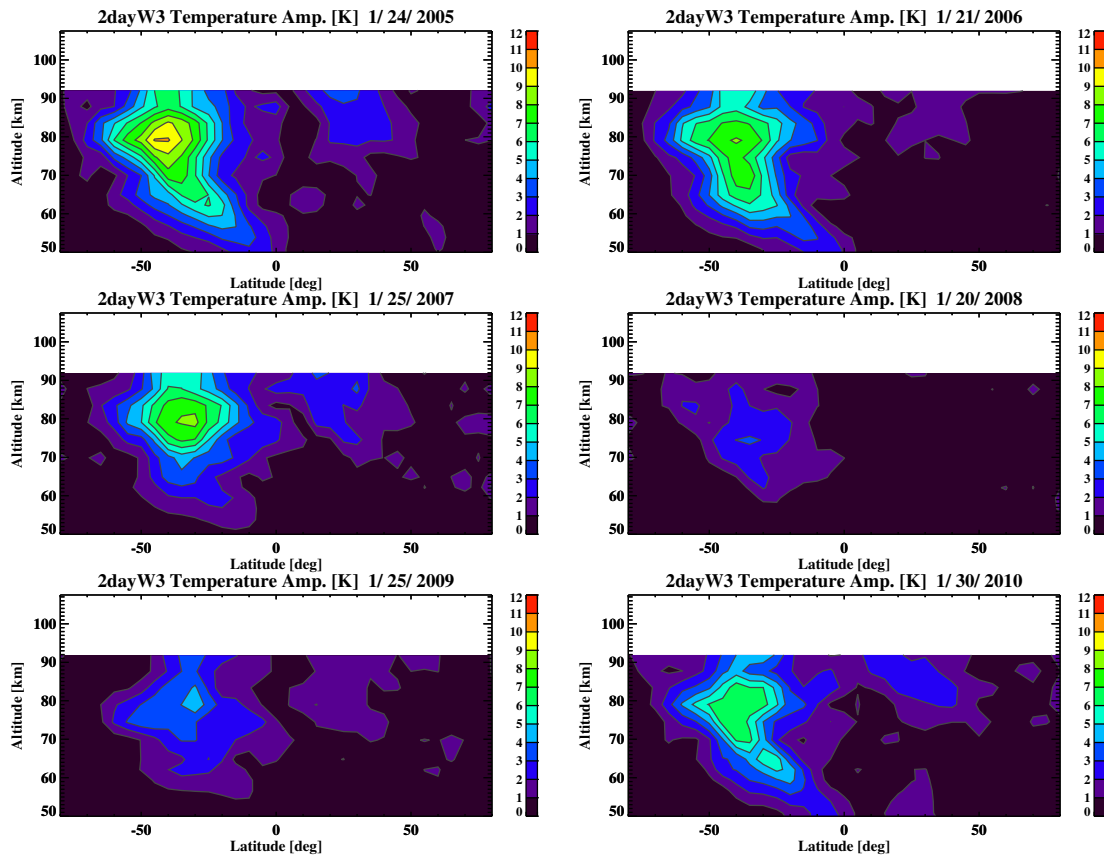


Figure E.1: MLS temperature amplitude of the 2dayW3 as a function of latitude and altitude for 2005, 2006, 2007, 2008, 2009 and 2010. Units are in K. Amplitude was extracted by applying FFSM method.

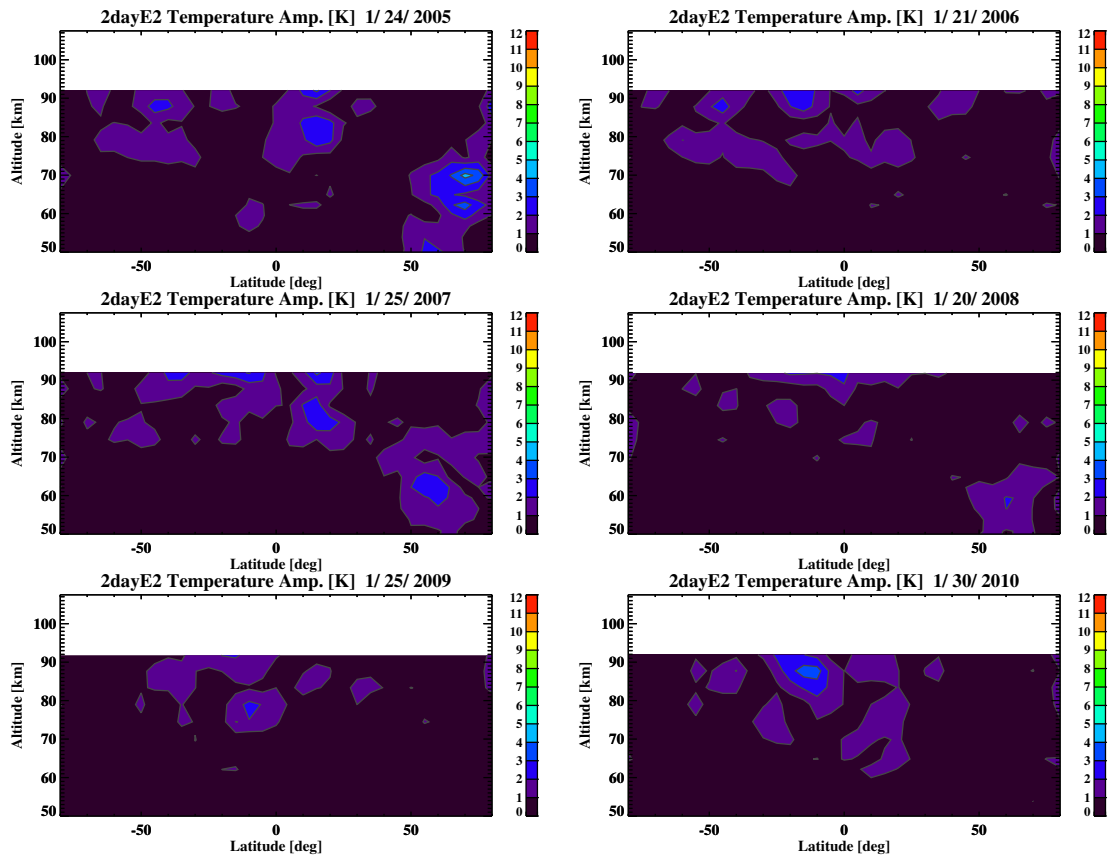


Figure E.2: MLS temperature amplitude of the 2dayE2 as a function of latitude and altitude for 2005, 2006, 2007, 2008, 2009, and 2010. Due to limitations in vertical range, MLS cannot observed large 2dayE2 amplitudes, which are larger above 90 km. Amplitude was extracted by applying FFMS method.

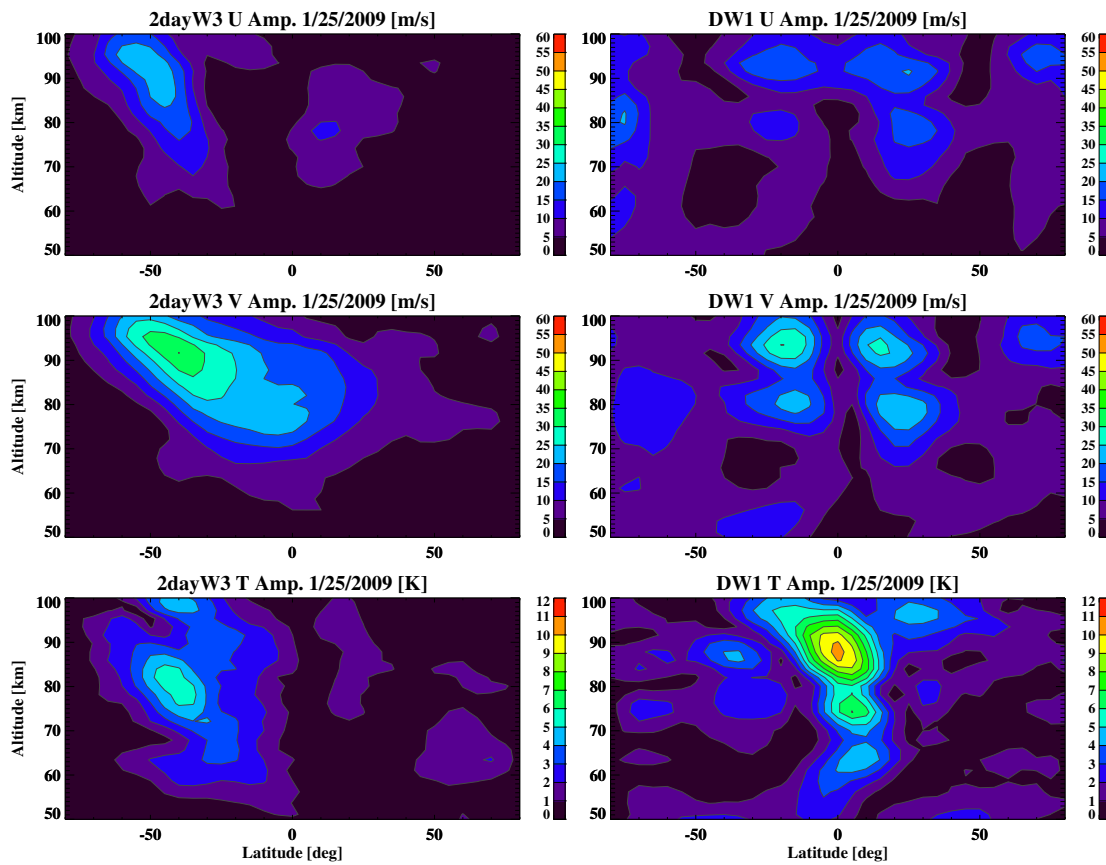


Figure E.3: NOGAPS-ALPHA amplitude of the 2dayW3 and DW1 as a function of latitude and altitude during 2010. Estimates for the zonal wind field are shown on top, meridional wind in the middle and temperature on the bottom.

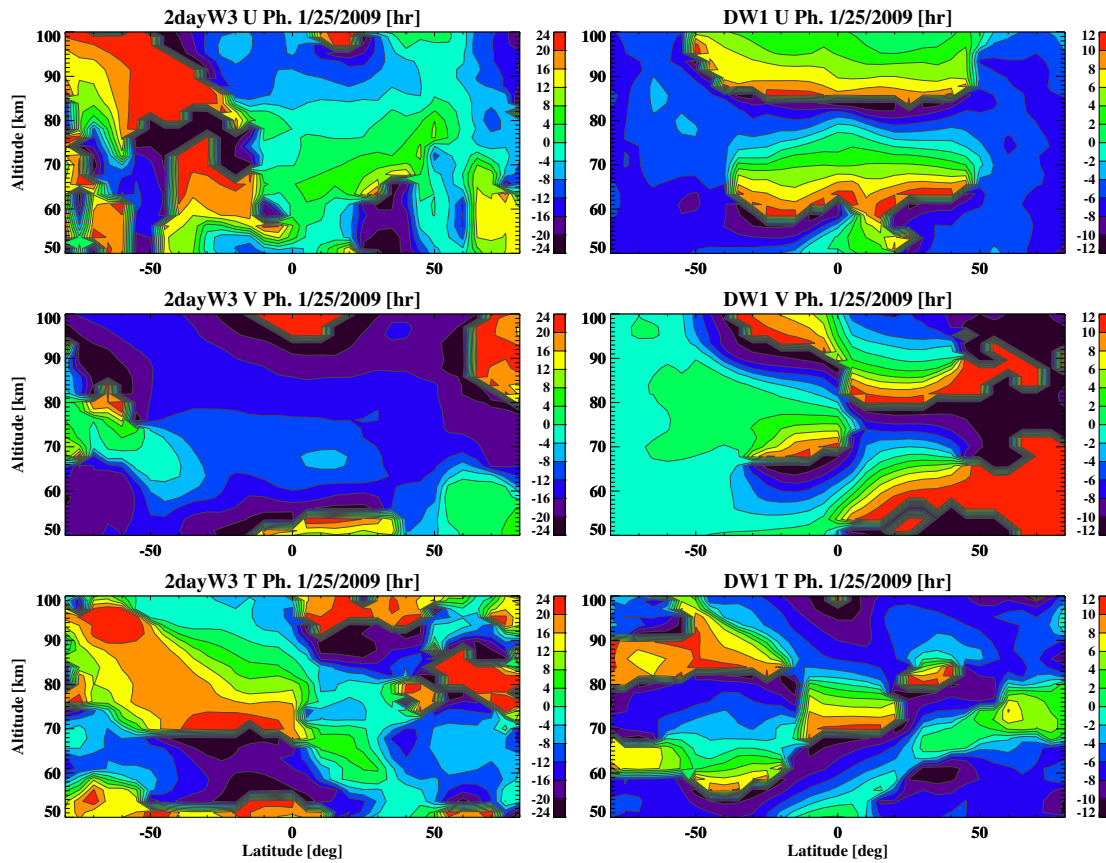


Figure E.4: NOGAPS-ALPHA phase of the 2dayW3 and DW1 as a function of latitude and altitude during 2009. Estimates for the zonal wind field are shown on top, meridional wind in the middle and temperature on the bottom.

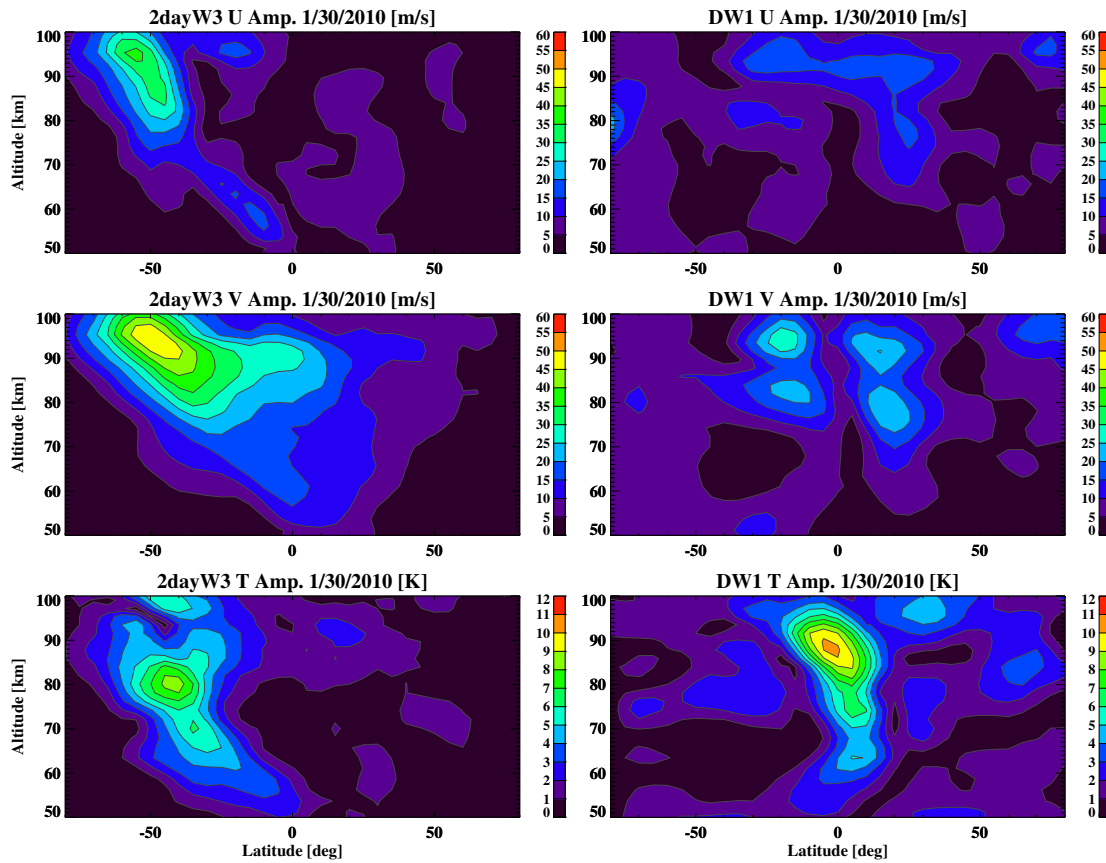


Figure E.5: NOGAPS-ALPHA amplitude of the 2dayW3 and DW1 as a function of latitude and altitude during 2010. Estimates for the zonal wind field are shown on top, meridional wind in the middle and temperature on the bottom.

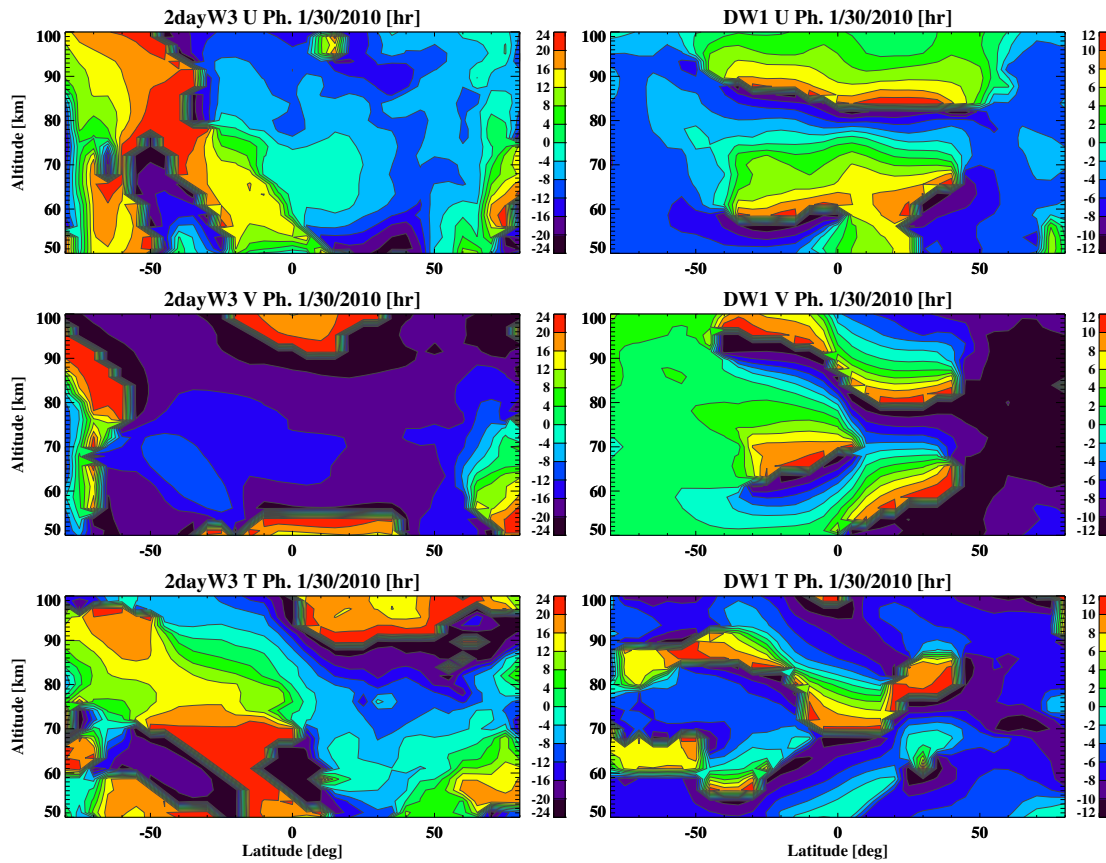


Figure E.6: NOGAPS-ALPHA phase of the 2dayW3 and DW1 as a function of latitude and altitude during 2009. Estimates for the zonal wind field are shown on top, meridional wind in the middle and temperature on the bottom.

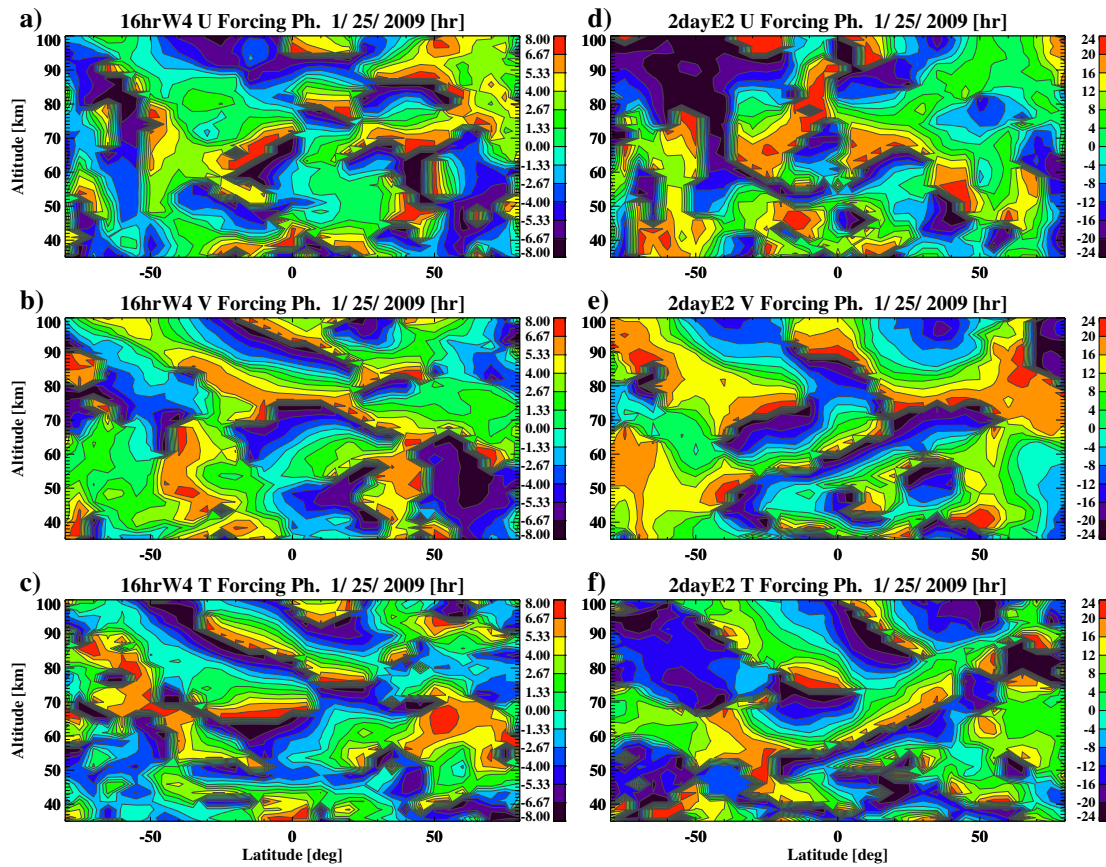


Figure E.7: Vertical-latitude phase structure centered at January 25, 2009 for a) 16hrW4 zonal momentum forcing, b) 16hrW4 meridional momentum forcing, c) 16hrW4 thermal forcing, d) 2dayE2 zonal momentum forcing, e) 2dayE2 meridional momentum forcing, and f) 2dayE2 thermal forcing. Nonlinear forcing phase is derived from NOGAPS-ALPHA primary wave amplitude and phase estimates.

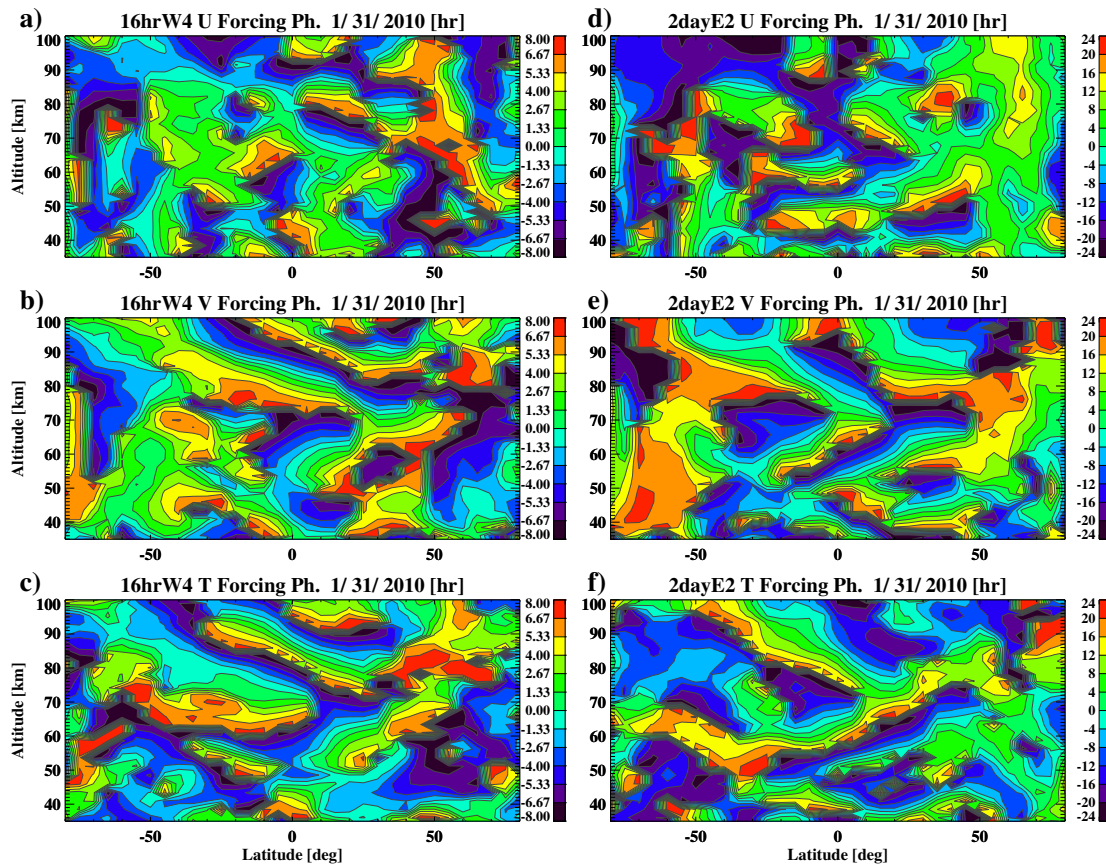


Figure E.8: Vertical-latitude phase structure centered at January 30, 2010 for a) 16hrW4 zonal momentum forcing, b) 16hrW4 meridional momentum forcing, c) 16hrW4 thermal forcing, d) 2dayE2 zonal momentum forcing, e) 2dayE2 meridional momentum forcing, and f) 2dayE2 thermal forcing. Nonlinear forcing phase is derived from NOGAPS-ALPHA primary wave amplitude and phase estimates.

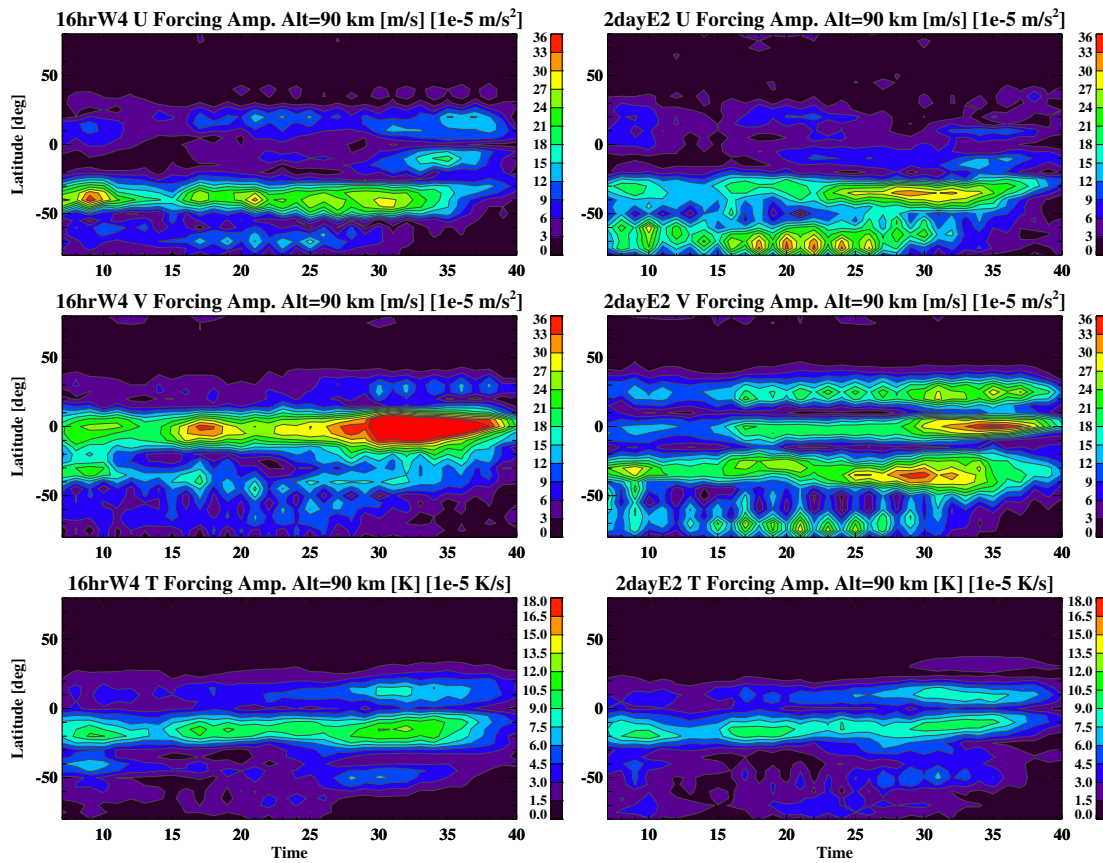


Figure E.9: Temporal-latitude amplitude structure at 90 km during 2006 for a) 16hrW4 zonal momentum forcing, b) 16hrW4 meridional momentum forcing, c) 16hrW4 thermal forcing, d) 2dayE2 zonal momentum forcing, e) 2dayE2 meridional momentum forcing, and f) 2dayE2 thermal forcing. Nonlinear forcing amplitude is derived from NOGAPS-ALPHA primary wave amplitude and phase estimates.

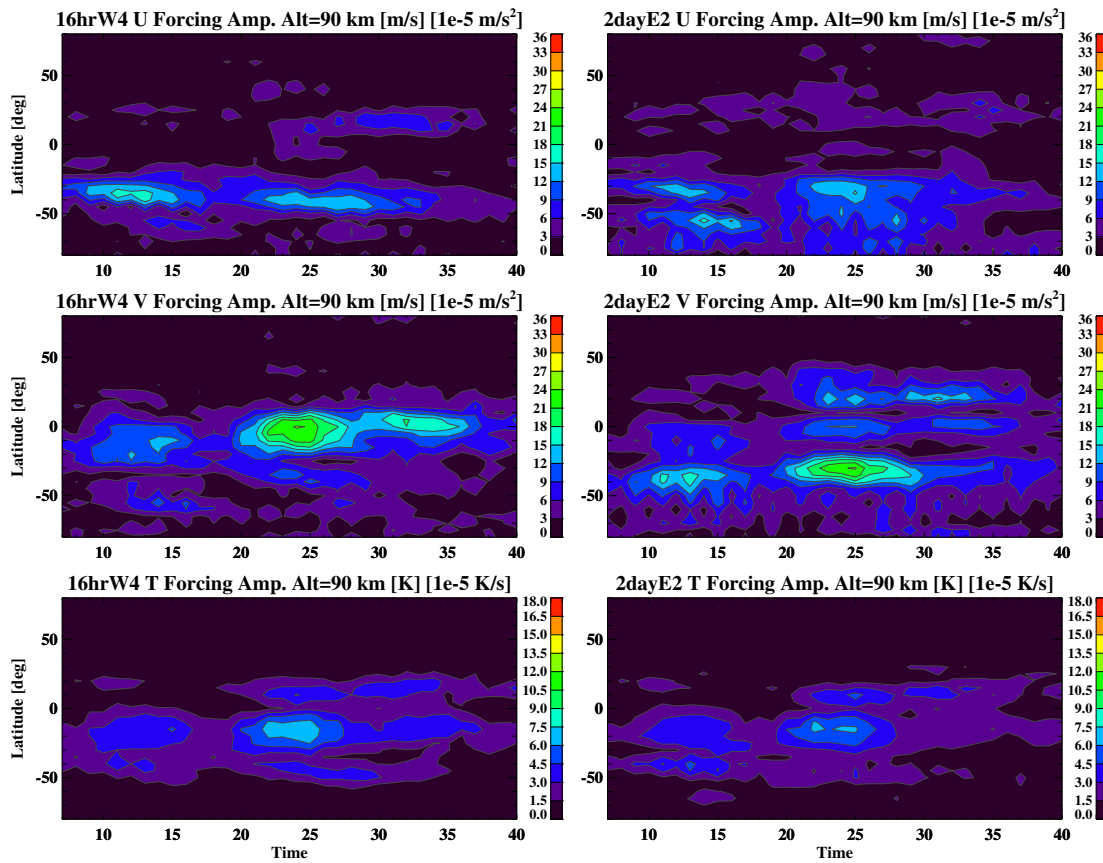


Figure E.10: Temporal-latitude amplitude structure at 90 km during 2009 for a) 16hrW4 zonal momentum forcing, b) 16hrW4 meridional momentum forcing, c) 16hrW4 thermal forcing, d) 2dayE2 zonal momentum forcing, e) 2dayE2 meridional momentum forcing, and f) 2dayE2 thermal forcing. Nonlinear forcing amplitude is derived from NOGAPS-ALPHA primary wave amplitude and phase estimates.

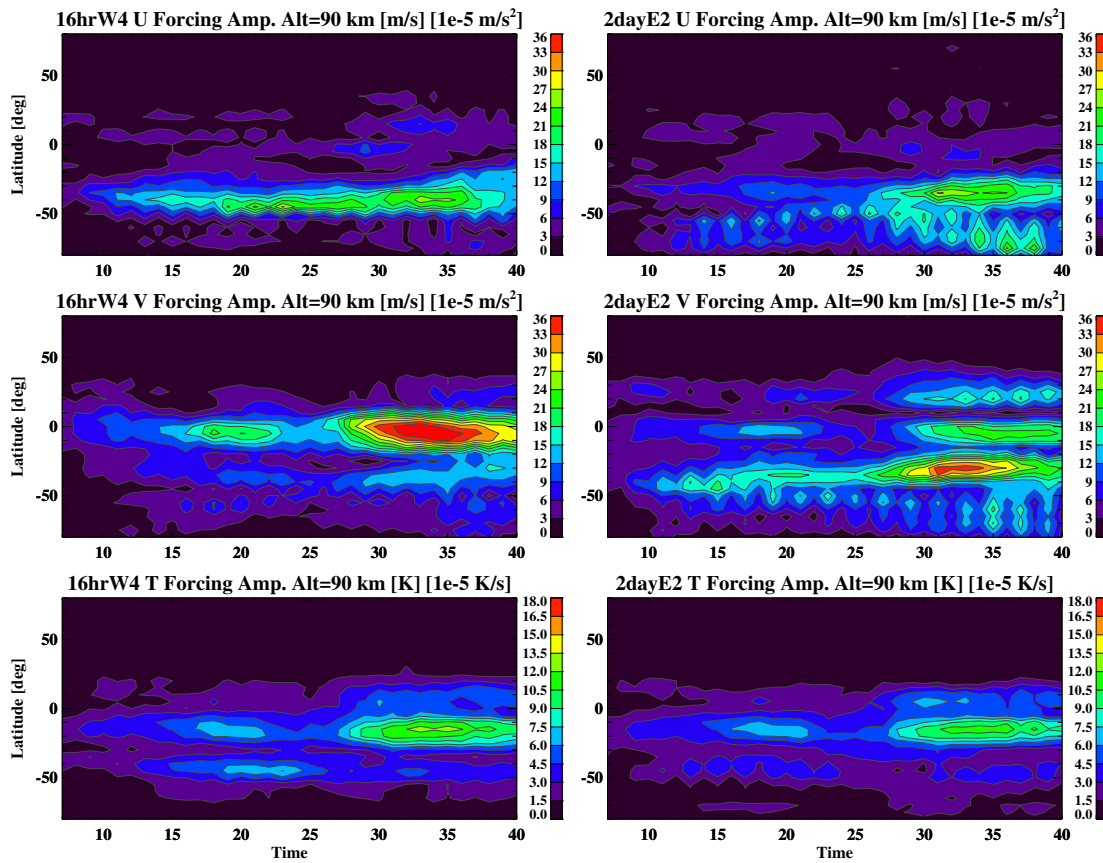


Figure E.11: Temporal-latitude amplitude structure at 90 km during 2010 for a) 16hrW4 zonal momentum forcing, b) 16hrW4 meridional momentum forcing, c) 16hrW4 thermal forcing, d) 2dayE2 zonal momentum forcing, e) 2dayE2 meridional momentum forcing, and f) 2dayE2 thermal forcing. Nonlinear forcing amplitude is derived from NOGAPS-ALPHA primary wave amplitude and phase estimates.

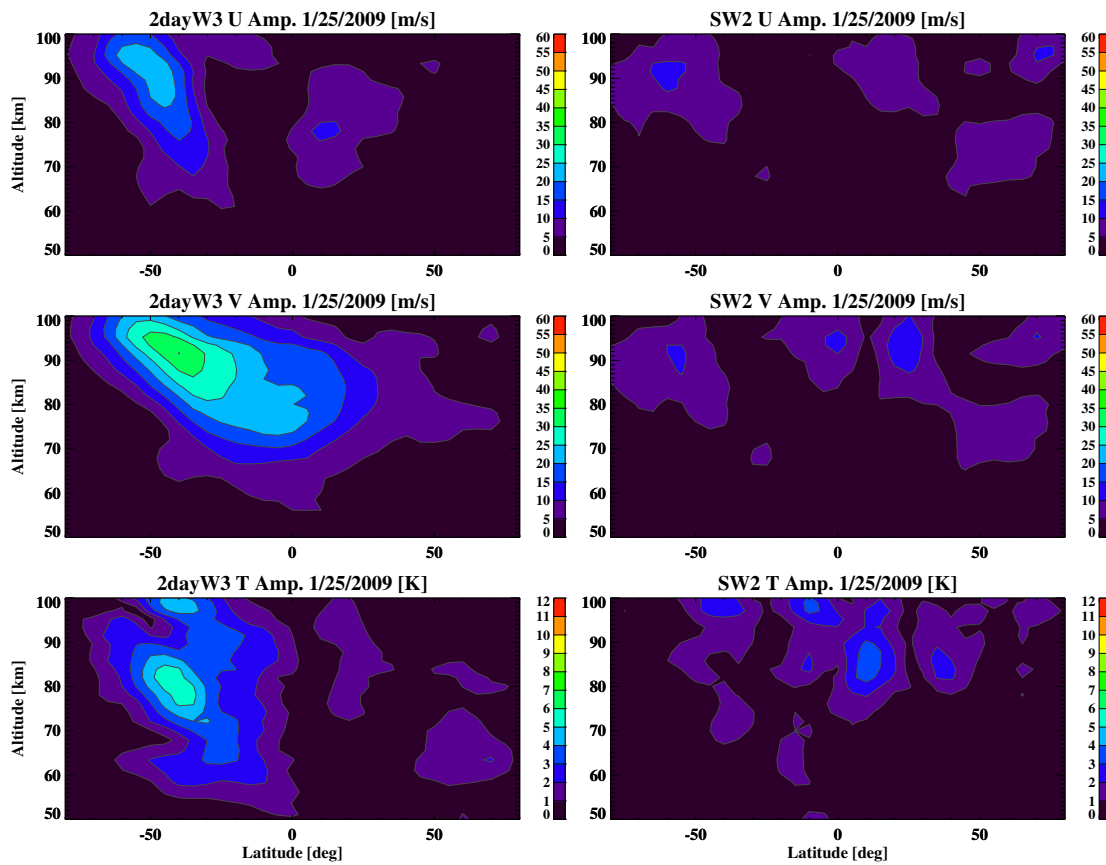


Figure E.12: NOGAPS-ALPHA amplitude of the 2dayW3 and SW2 as a function of latitude and altitude during 2009. Estimates for the zonal wind field are shown on top, meridional wind in the middle and temperature on the bottom.

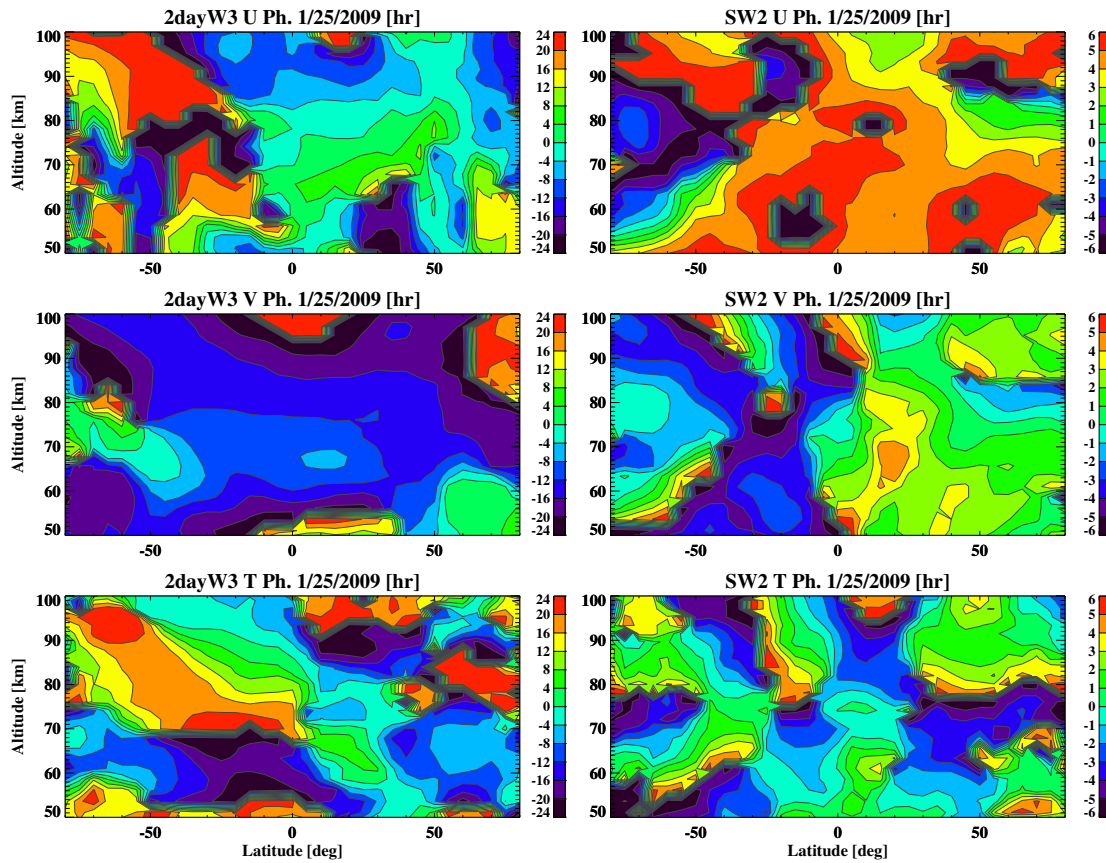


Figure E.13: NOGAPS-ALPHA phase of the 2dayW3 and SW2 as a function of latitude and altitude during 2009. Estimates for the zonal wind field are shown on top, meridional wind in the middle and temperature on the bottom.

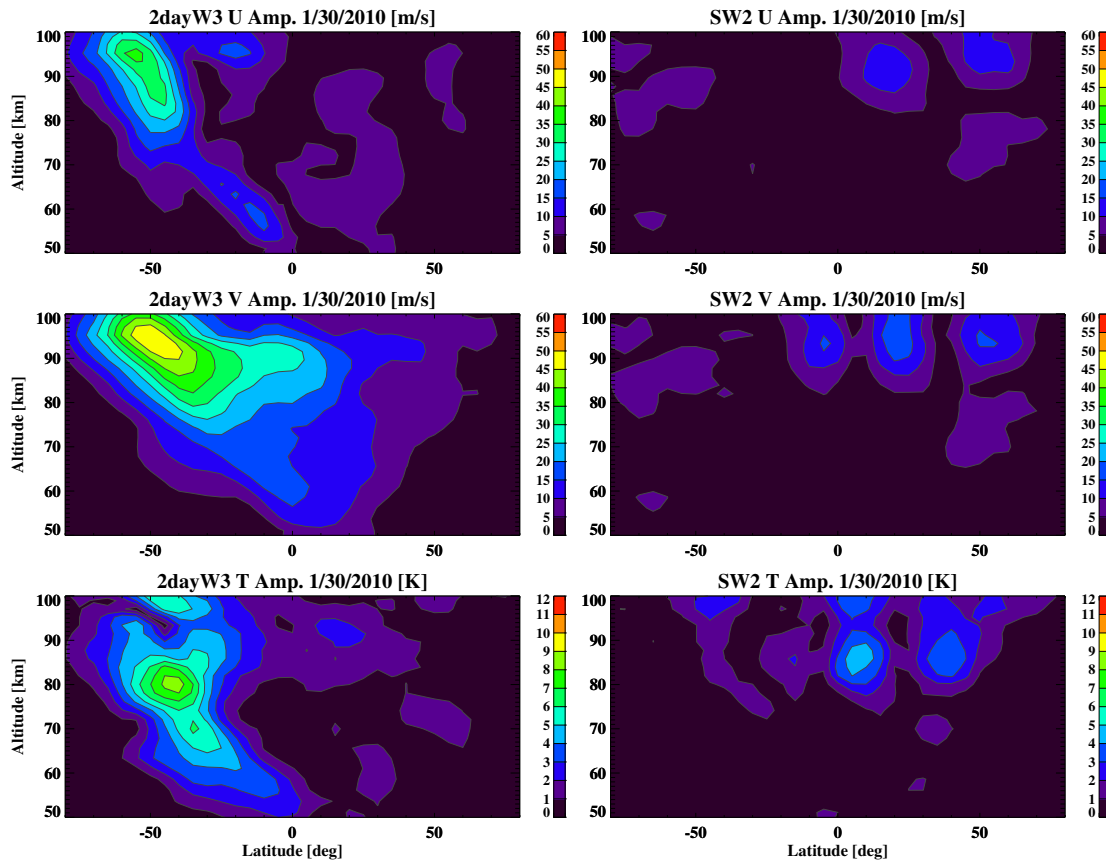


Figure E.14: NOGAPS-ALPHA amplitude of the 2dayW3 and SW2 as a function of latitude and altitude during 2009. Estimates for the zonal wind field are shown on top, meridional wind in the middle and temperature on the bottom.

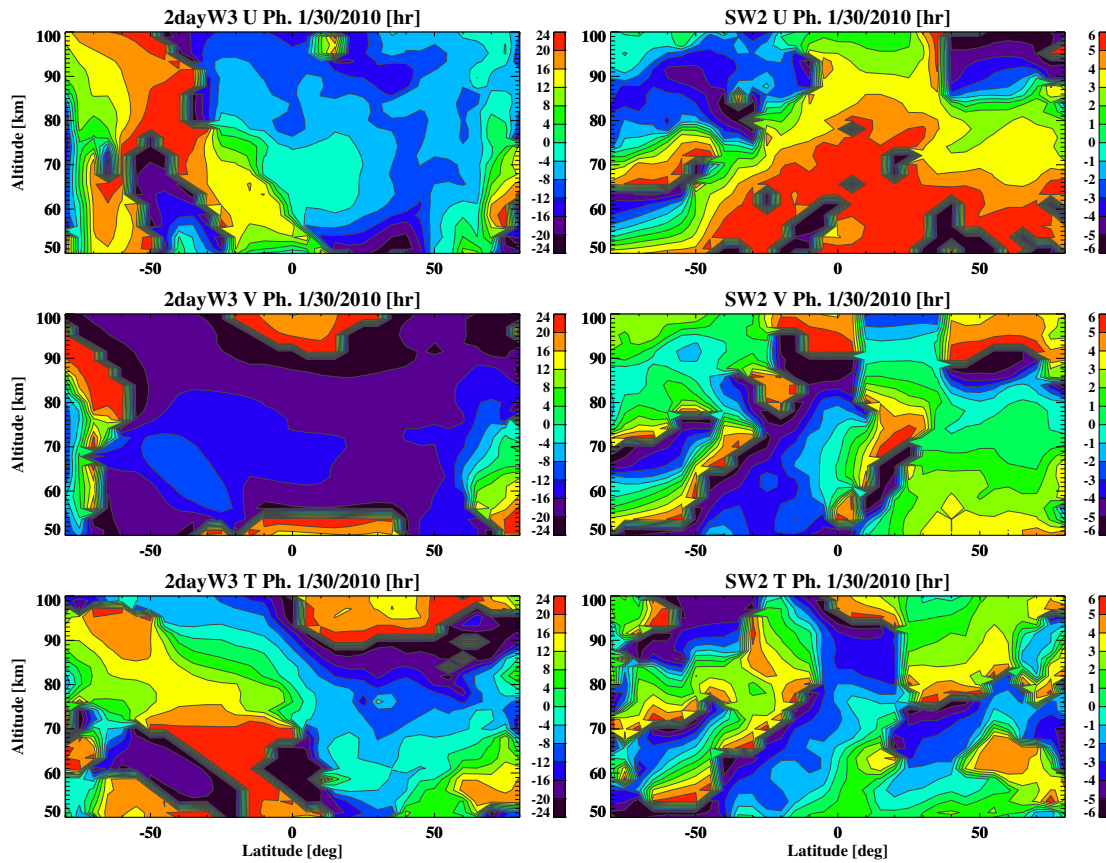


Figure E.15: NOGAPS phase of the 2dayW3 and SW2 as a function of latitude and altitude during 2009. Estimates for the zonal wind field are shown on top, meridional wind in the middle and temperature on the bottom.

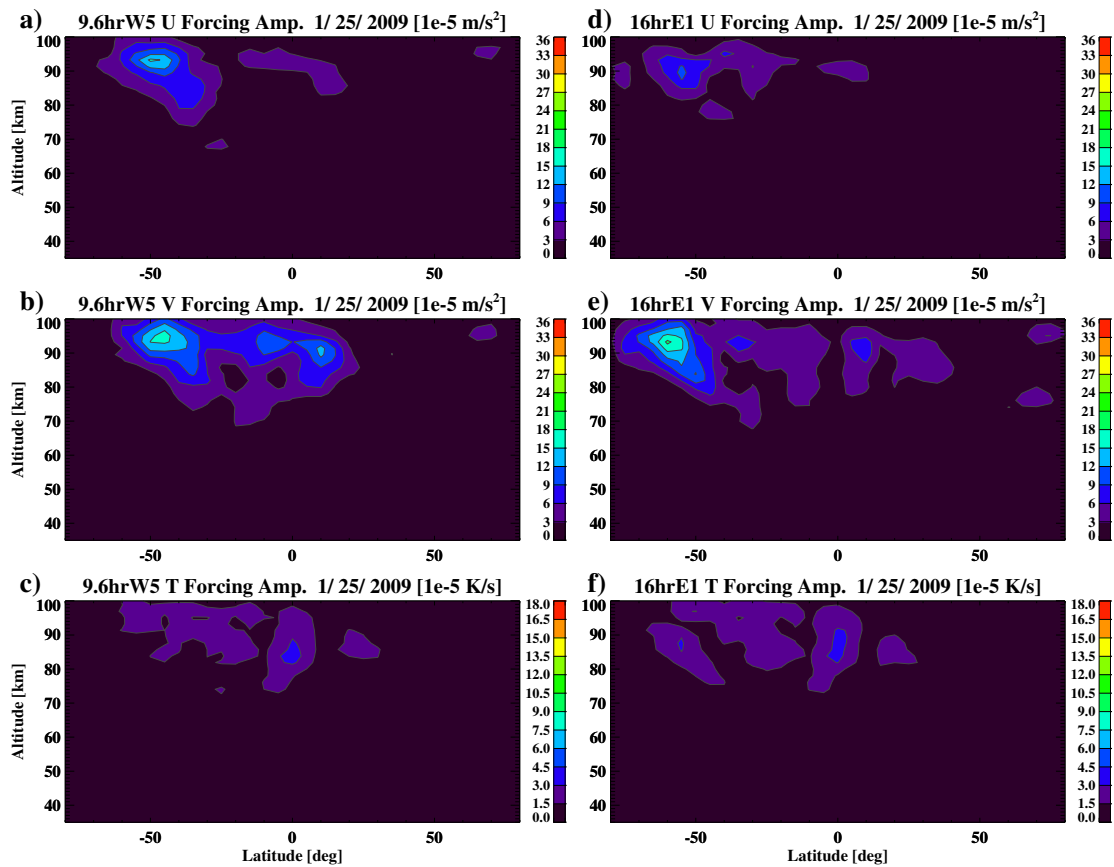


Figure E.16: Vertical-latitude forcing amplitude structure centered at January 25, 2009 for a) 9.6hrW5 zonal momentum forcing, b) 9.6hrW5 meridional momentum forcing, c) 9.6hrW5 thermal forcing, d) 16hrE1 zonal momentum forcing, e) 16hrE1 meridional momentum forcing, and f) 16hrE1 thermal forcing.

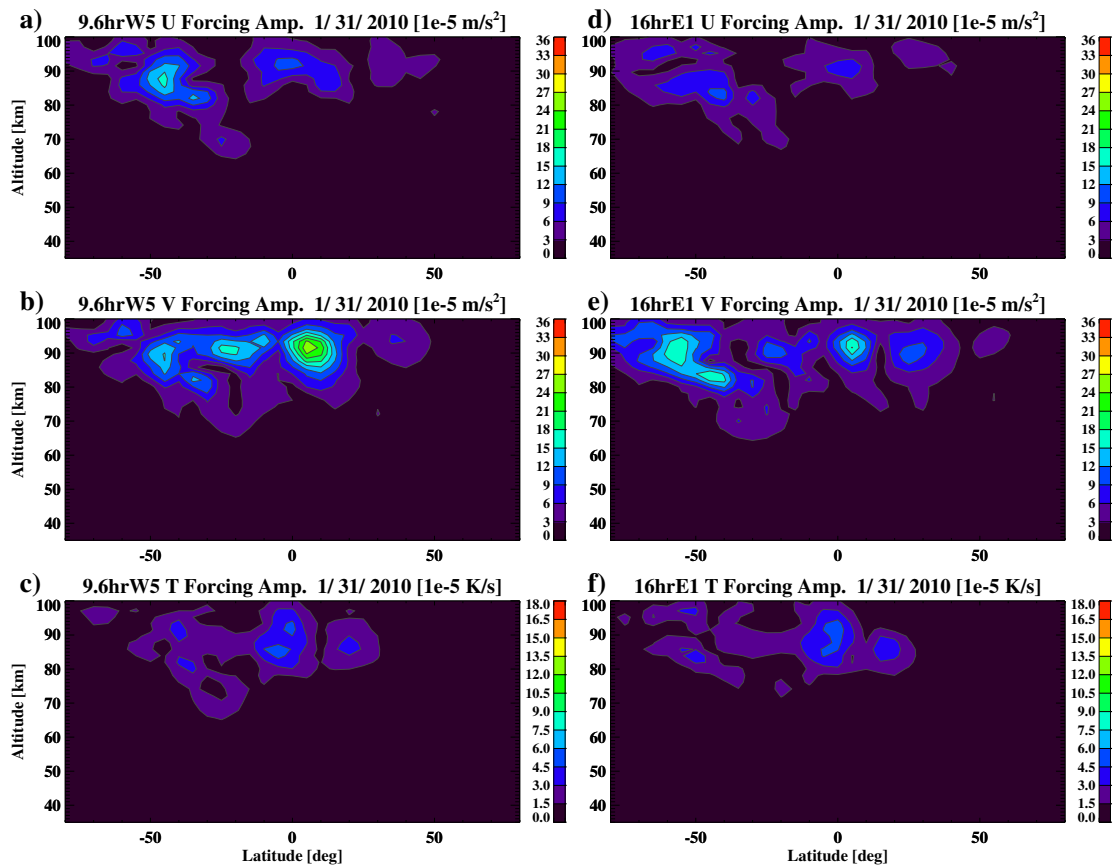


Figure E.17: Vertical-latitude forcing amplitude structure centered at January 31st, 2010 for a) 9.6hrW5 zonal momentum forcing, b) 9.6hrW5 meridional momentum forcing, c) 9.6hrW5 thermal forcing, d) 16hrE1 zonal momentum forcing, e) 16hrE1 meridional momentum forcing, and f) 16hrE1 thermal forcing.

## Appendix F

### SUPPLEMENTAL FIGURES: SECONDARY WAVES COMPUTED FROM THE LINEAR TIDAL MODEL

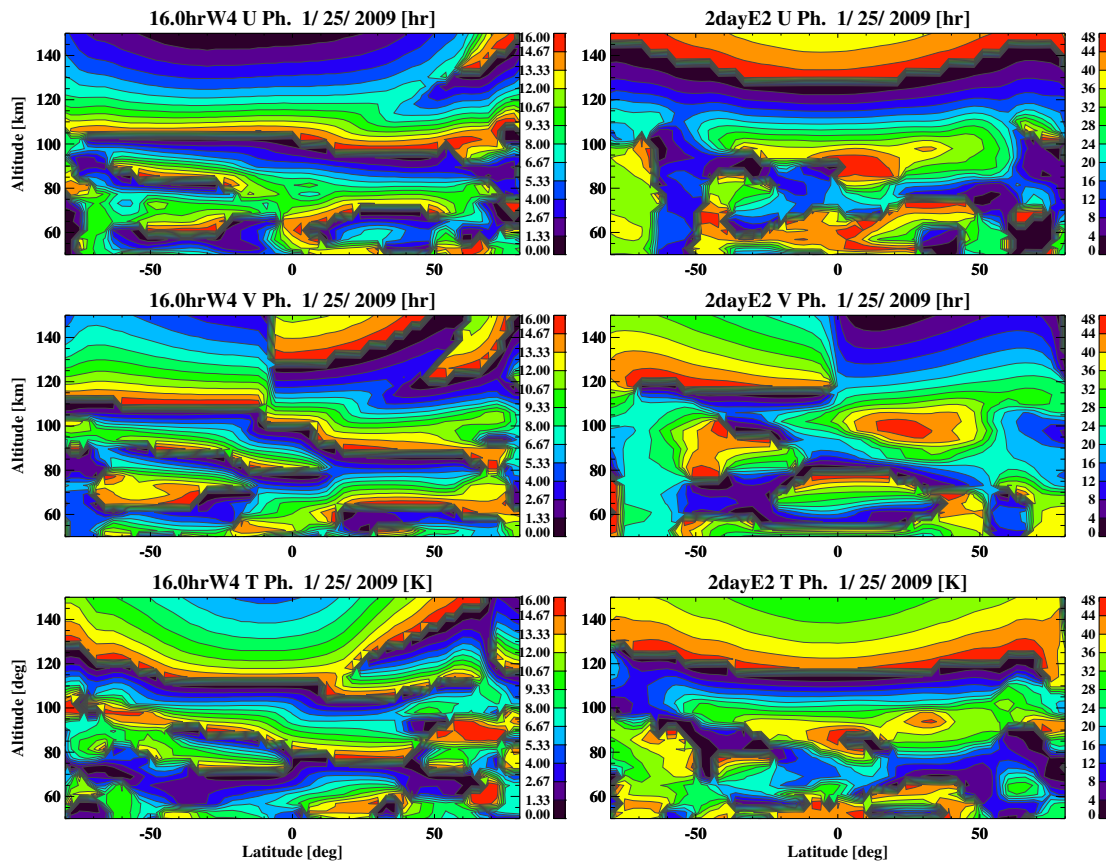


Figure F.1: Vertical-latitude phase structure computed from the linear tidal model centered on January 25th, 2009 for the 16hrW4 zonal wind (upper-left), 16hrW4 meridional wind (middle-left), 16hrW4 temperature (lower-left), 2dayE2 zonal wind (upper-right), 2dayE2 meridional wind (middle-right), and 2dayE2 temperature (lower-right). Zero background winds and equatorial temperatures were used in this case.

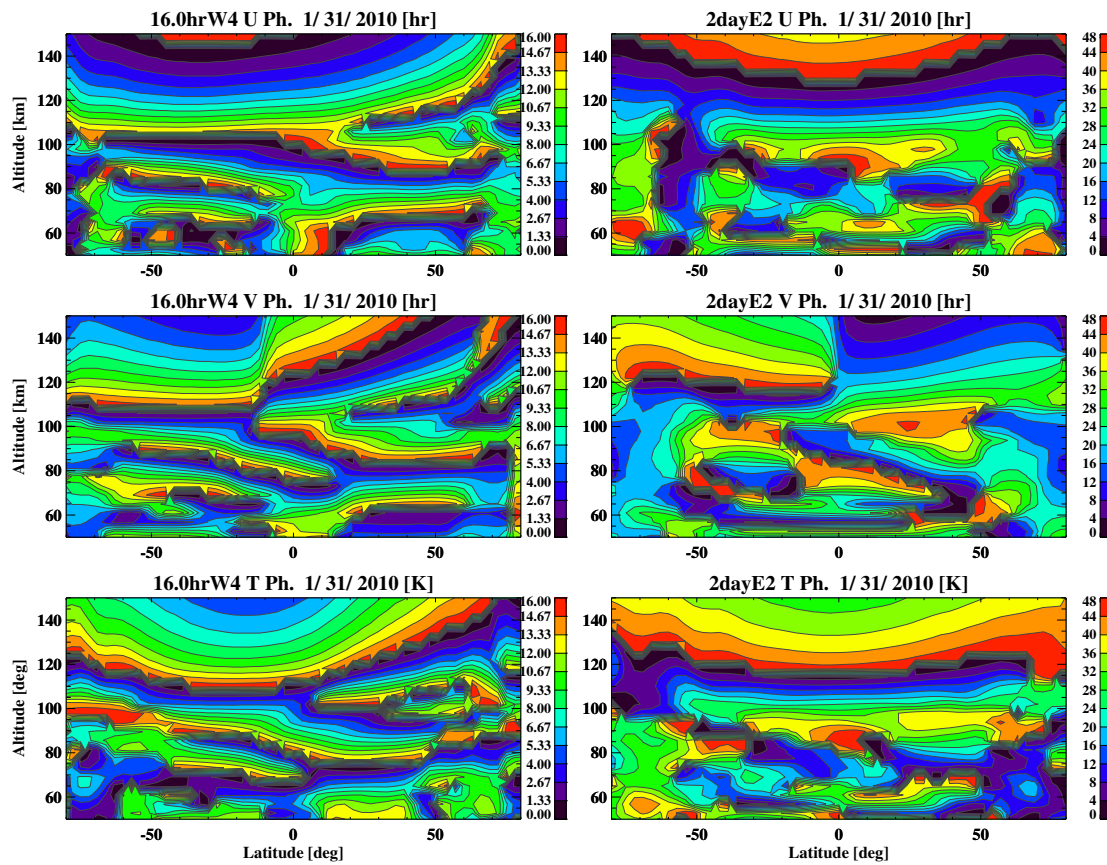


Figure F.2: Vertical-latitude phase structure computed from the linear tidal model centered on January 31st, 2010 for the 16hrW4 zonal wind (upper-left), 16hrW4 meridional wind (middle-left), 16hrW4 temperature (lower-left), 2dayE2 zonal wind (upper-right), 2dayE2 meridional wind (middle-right), and 2dayE2 temperature (lower-right). Zero background winds and equatorial temperatures were used.

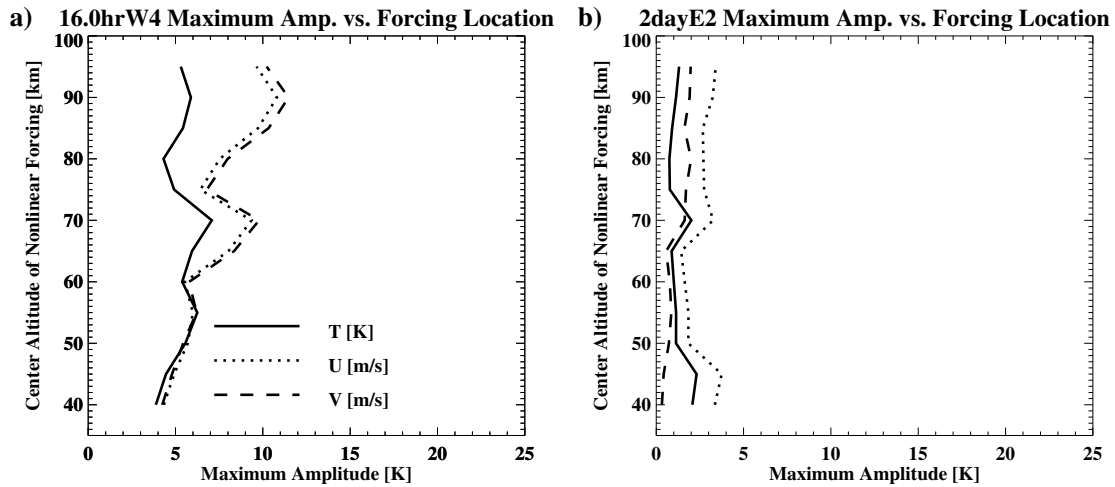


Figure F.3: Maximum amplitude of the a) 16hrW4 and b) 2dayE2 versus center altitude of the nonlinear forcing subsection during January 25th, 2009. Each nonlinear forcing subsection is obtained by applying the 15 km vertical window.

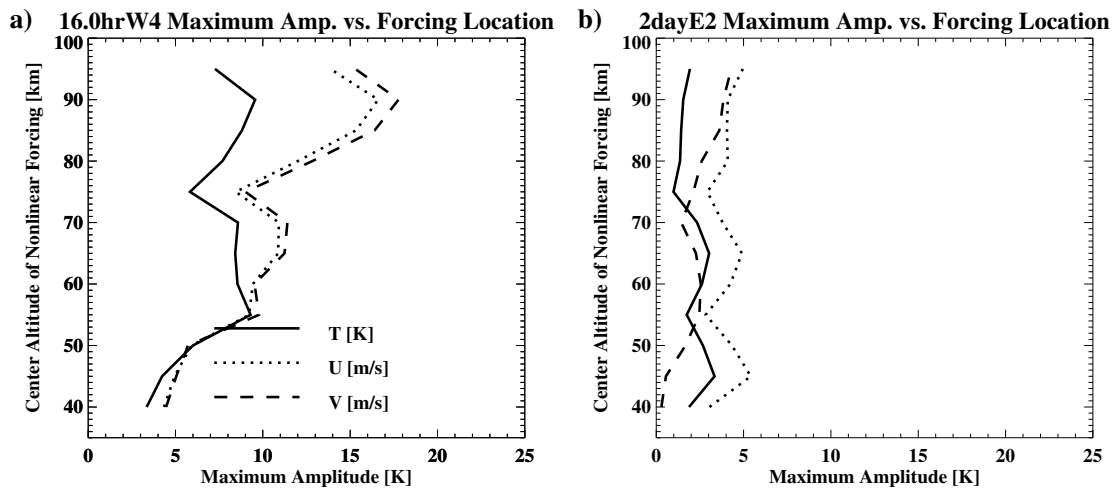


Figure F.4: Maximum amplitude of the a) 16hrW4 and b) 2dayE2 versus center altitude of the nonlinear forcing subsection during January 31st, 2010. Each nonlinear forcing subsection is obtained by applying the 15 km vertical window.

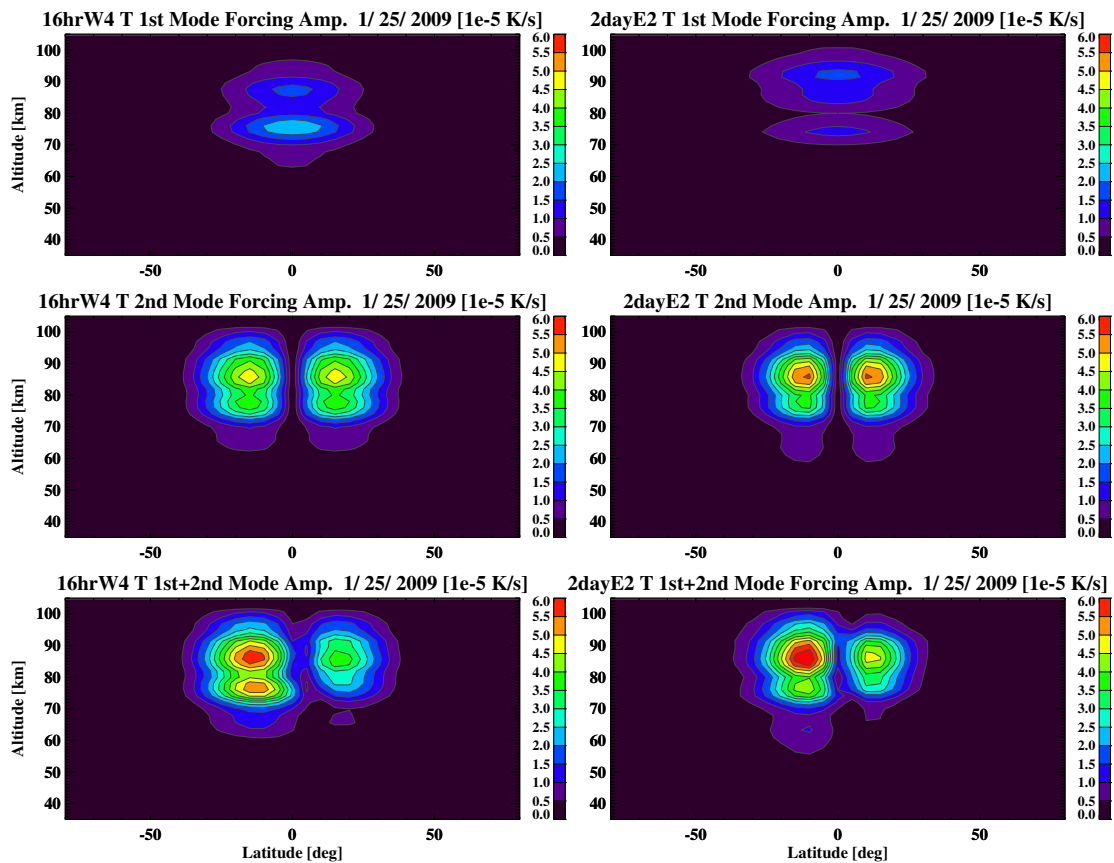


Figure F.5: Projections of 16hrW4-2dayE2 thermal forcing during 2009 projected onto the 16hrW4 1st propagating mode (upper-left), 16hrW4 2nd propagating mode (middle-left), 16hrW4 1st and 2nd modes (lower-left), 2dayE2 1st propagating mode (upper-right), 2dayE2 2nd propagating mode (middle-right), and 2dayE2 1st and 2nd modes (lower-right).

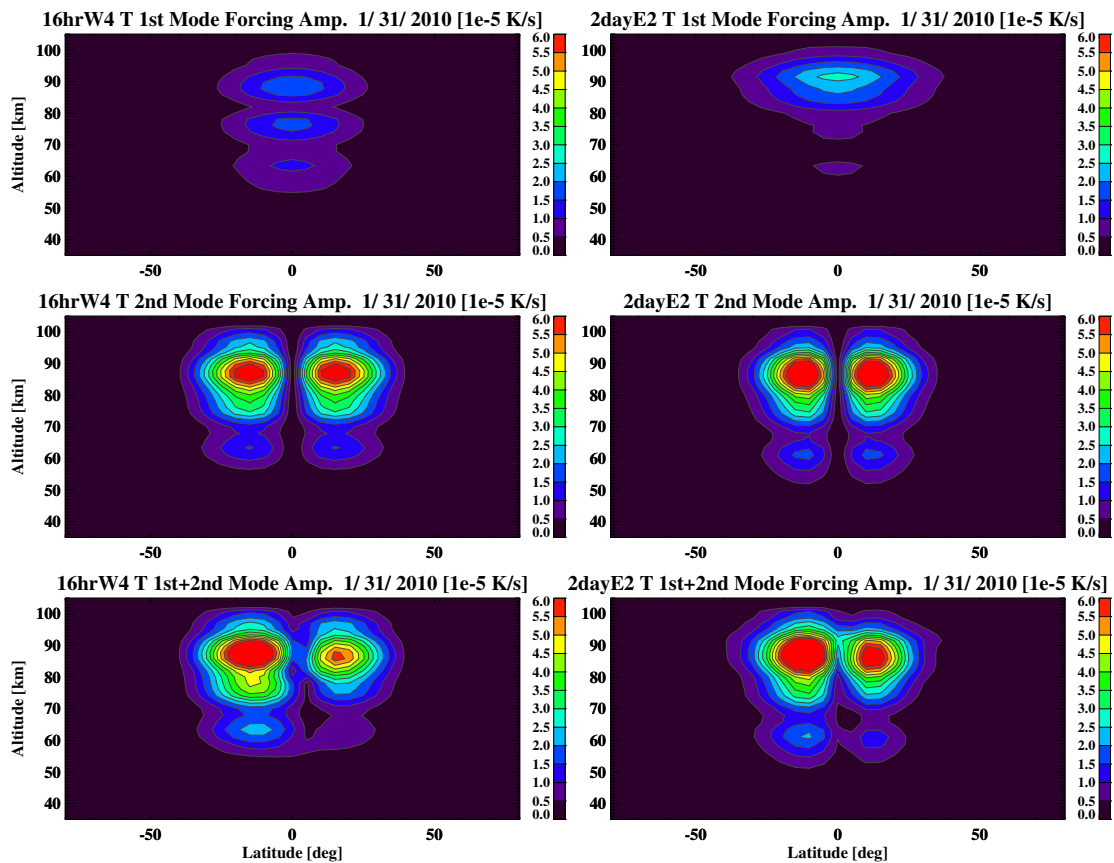


Figure F.6: Projections of 16hrW4-2dayE2 thermal forcing during 2010 projected onto the 16hrW4 1st propagating mode (upper-left), 16hrW4 2nd propagating mode (middle-left), 16hrW4 1st and 2nd modes (lower-left), 2dayE2 1st propagating mode (upper-right), 2dayE2 2nd propagating mode (middle-right), and 2dayE2 1st and 2nd modes (lower-right).

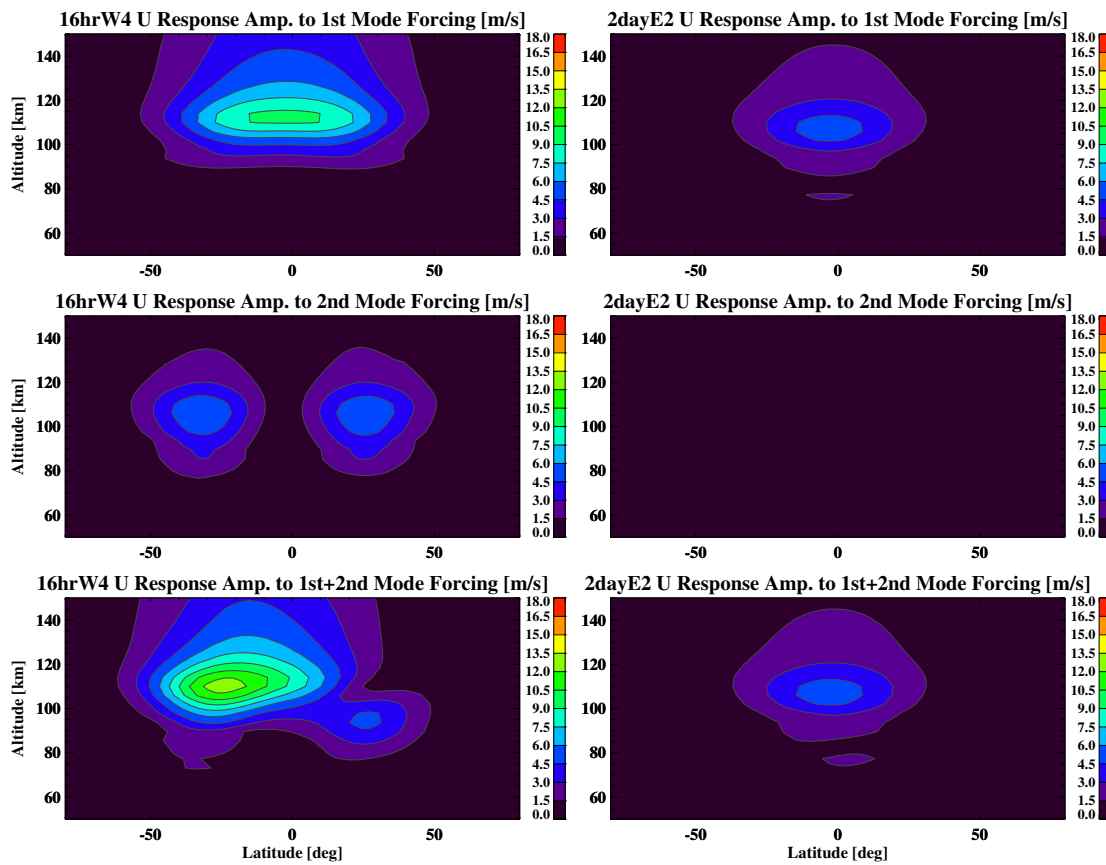


Figure F.7: Zonal wind response amplitude to the 16hrW4-2dayE2 forcing during 2009 projected onto the 16hrW4 1st propagating mode (upper-left), 16hrW4 2nd propagating mode (middle-left), 16hrW4 1st and 2nd modes (lower-left), 2dayE2 1st propagating mode (upper-right), 2dayE2 2nd propagating mode (middle-right), and 2dayE2 (lower-right). Zero background winds and equatorial temperatures were used.

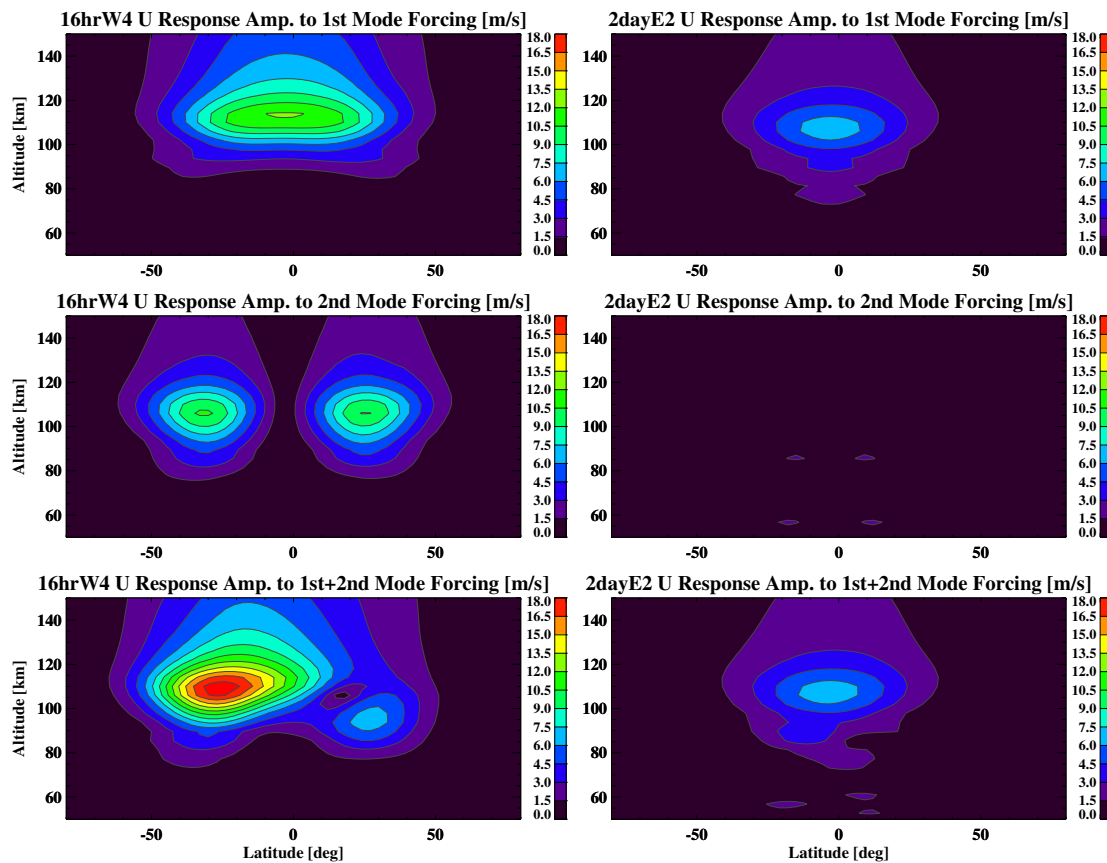


Figure F.8: Zonal wind response amplitude to the 16hrW4-2dayE2 forcing during 2010 projected onto the 16hrW4 1st propagating mode (upper-left), 16hrW4 2nd propagating mode (middle-left), 16hrW4 1st and 2nd modes (lower-left), 2dayE2 1st propagating mode (upper-right), 2dayE2 2nd propagating mode (middle-right), and 2dayE2 (lower-right). Zero background winds and equatorial temperatures were used.

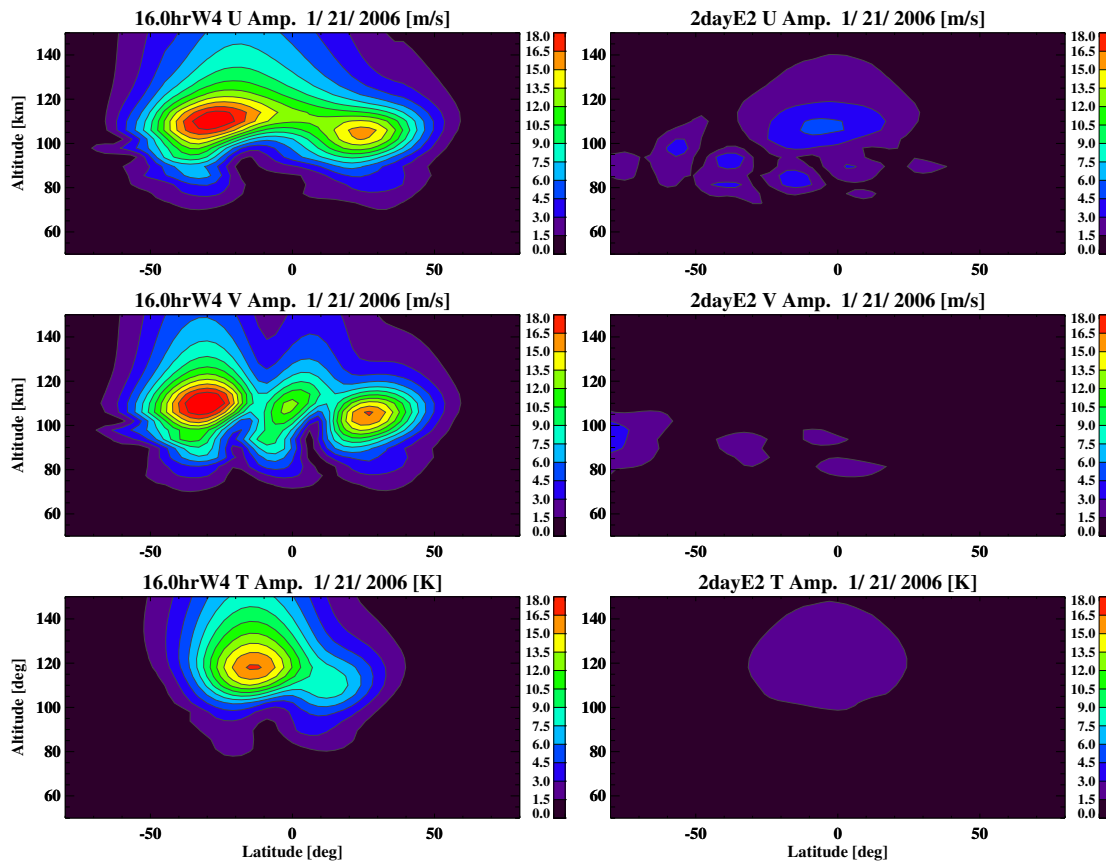


Figure F.9: Vertical-latitude amplitude structure computed from the linear tidal model centered on January 21st, 2006 for the 16hrW4 zonal wind (upper-left), 16hrW4 meridional wind (middle-left), 16hrW4 temperature (lower-left), 2dayE2 zonal wind (upper-right), 2dayE2 meridional wind (middle-right), and 2dayE2 temperature (lower-right). Nonlinear forcing derived from 2dayW3 phase shifted by  $\pi/2$  radians is used to force the linear tidal model and compute secondary wave responses. Response is almost identical to non-shifted 2dayW3, which demonstrates that primary wave phase is not a main factor governing the secondary wave response.

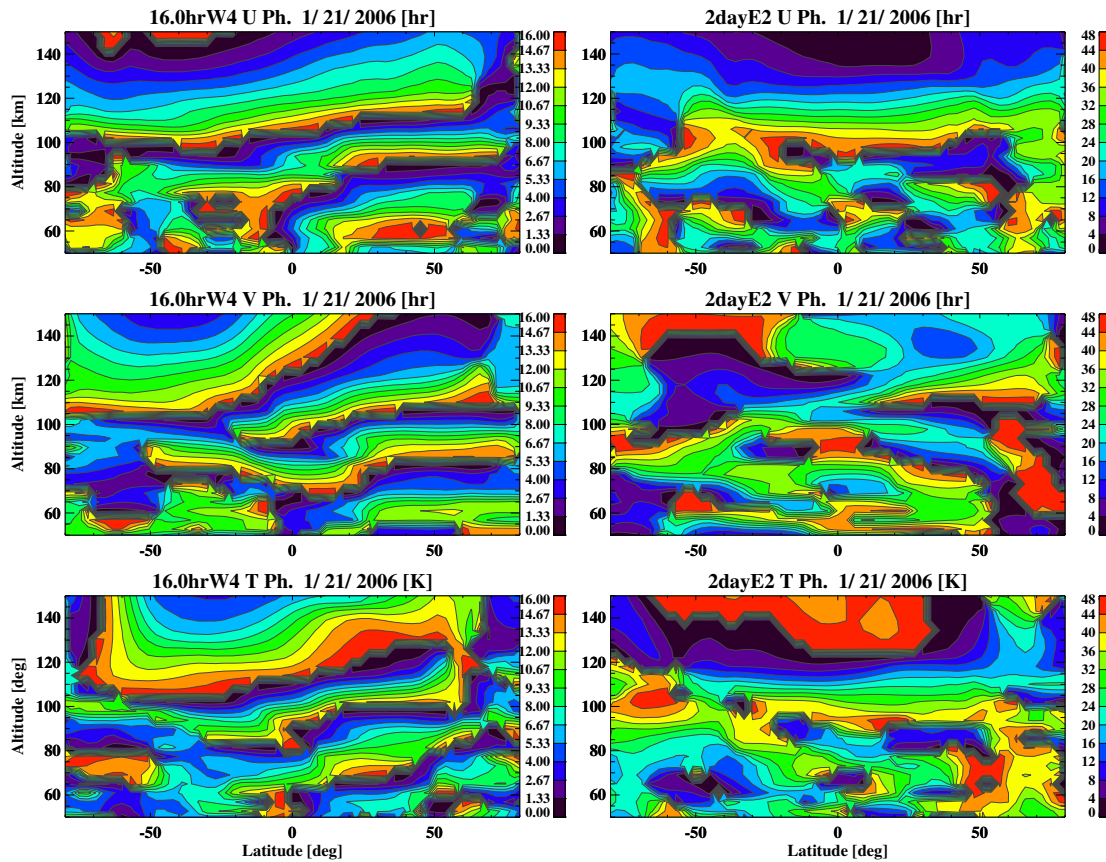


Figure F.10: Vertical-latitude phase structure computed from the linear tidal model centered on January 21st, 2006 for the 16hrW4 zonal wind (upper-left), 16hrW4 meridional wind (middle-left), 16hrW4 temperature (lower-left), 2dayE2 zonal wind (upper-right), 2dayE2 meridional wind (middle-right), and 2dayE2 temperature (lower-right). Nonlinear forcing quantities presented in Chapter 5 are used to force the linear tidal model and compute secondary wave responses. Non-zero background winds were used in this case.

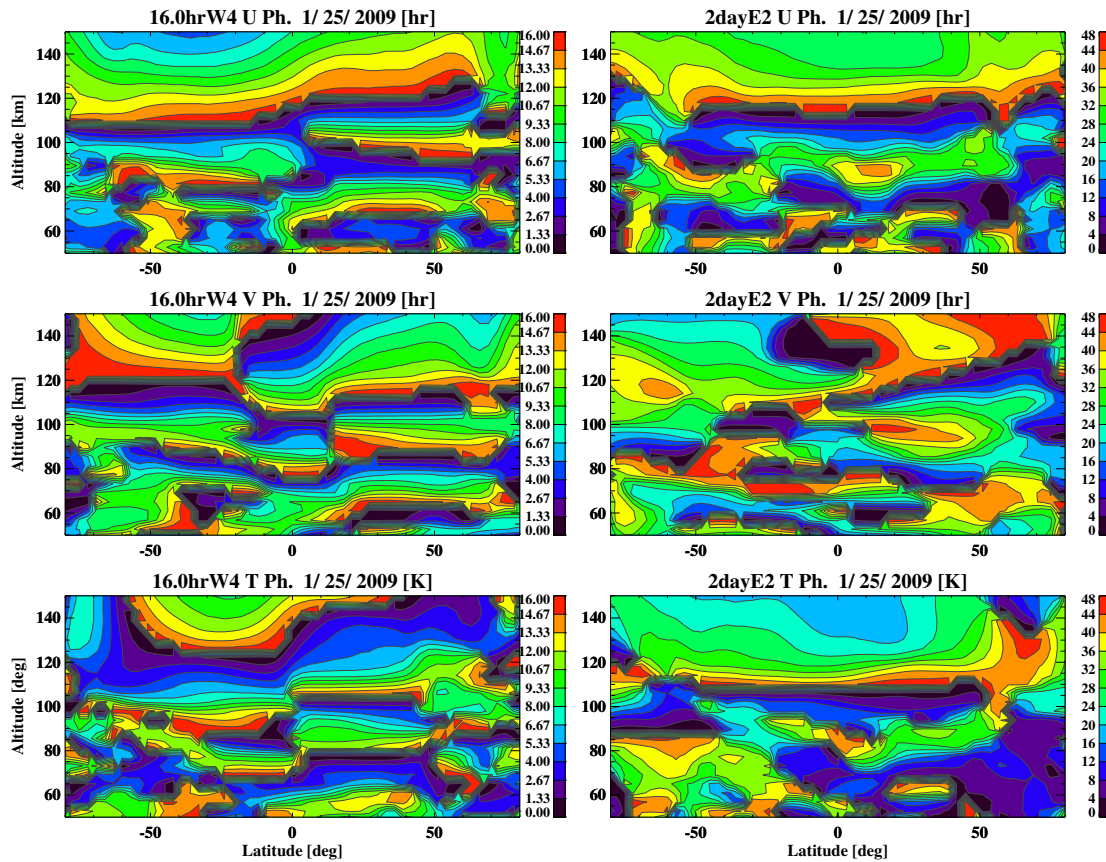


Figure F.11: Vertical-latitudinal phase structure computed from the linear tidal model centered on January 25th, 2009 for the 16hrW4 zonal wind (upper-left), 16hrW4 meridional wind (middle-left), 16hrW4 temperature (lower-left), 2dayE2 zonal wind (upper-right), 2dayE2 meridional wind (middle-right), and 2dayE2 temperature (lower-right). Nonlinear forcing quantities presented in Chapter 5 are used to force the linear tidal model and compute secondary wave responses. Non-zero background winds were used in this case.

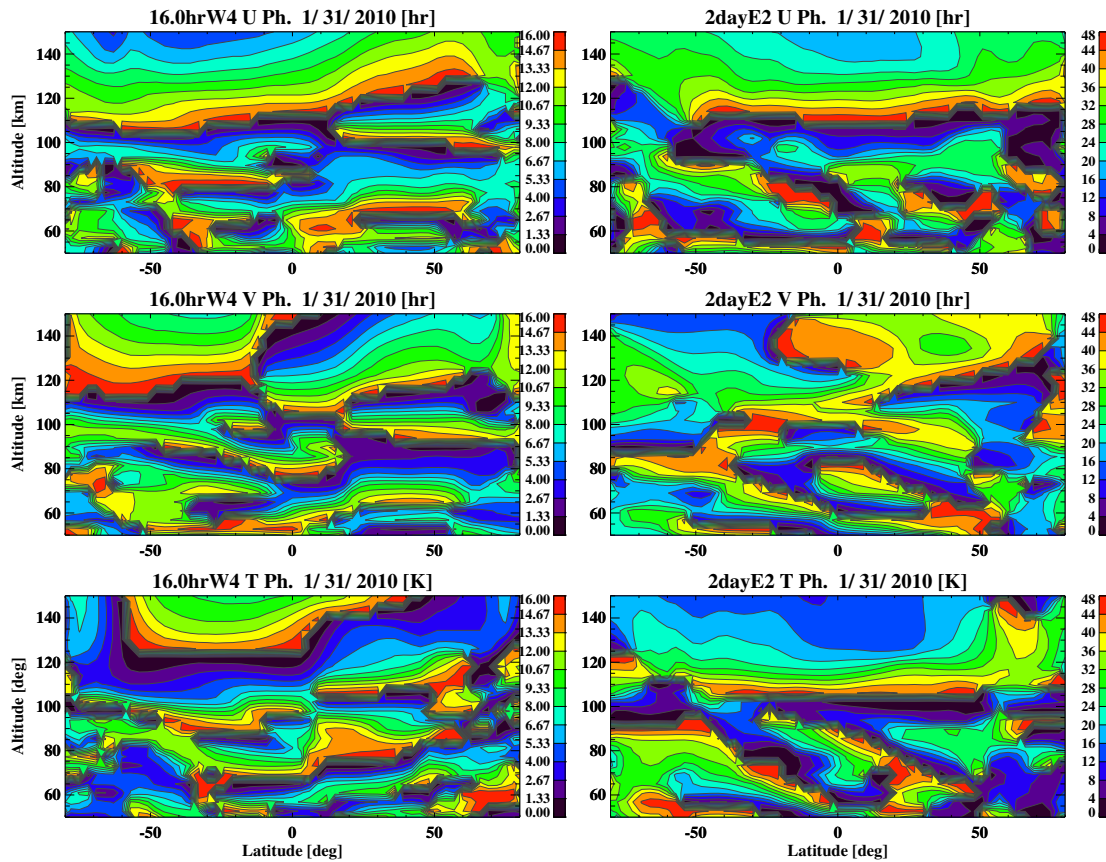


Figure F.12: Vertical-latitude phase structure computed from the linear tidal model centered on January 31st, 2010 for the 16hrW4 zonal wind (upper-left), 16hrW4 meridional wind (middle-left), 16hrW4 temperature (lower-left), 2dayE2 zonal wind (upper-right), 2dayE2 meridional wind (middle-right), and 2dayE2 temperature (lower-right). Nonlinear forcing quantities presented in Chapter 5 are used to force the linear tidal model and compute secondary wave responses. Non-zero background winds were used in this case.

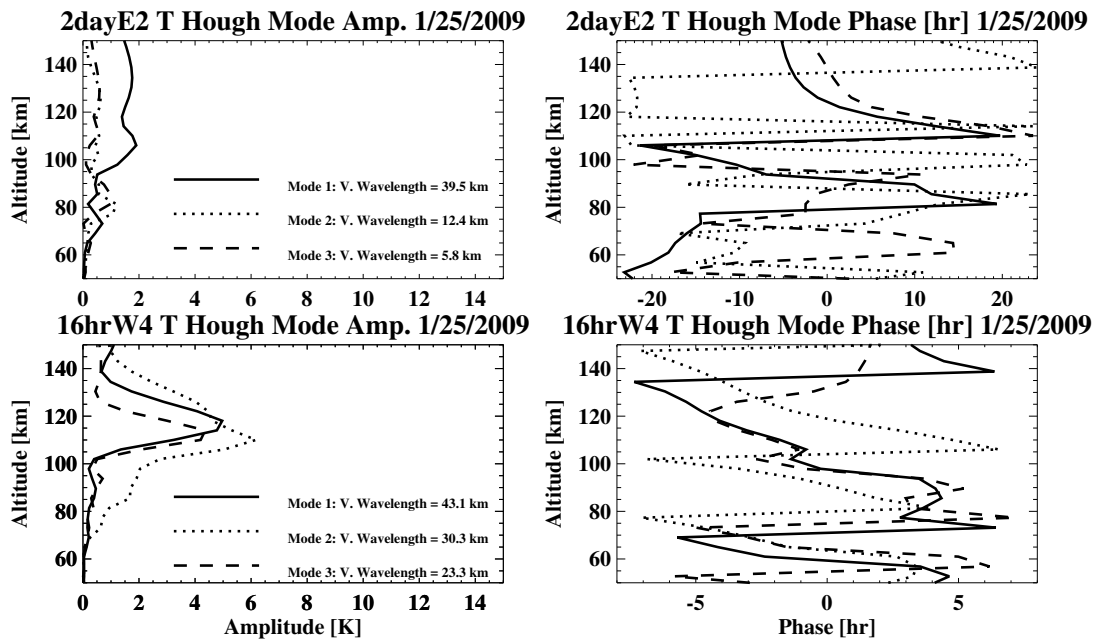


Figure F.13: 16hrW4 amplitude (lower-left) and phase (lower-right), and 2dayE2 amplitude (upper-left) and phase (upper-right) as a function of altitude for January 25th, 2009 under the non-zero background winds specified by NOGAPS-ALPHA. Each Hough mode amplitude was extracted by least squares fitting theoretical Hough mode functions to the overall secondary wave amplitude and phases at each altitude level. Units are in degrees Kelvin.

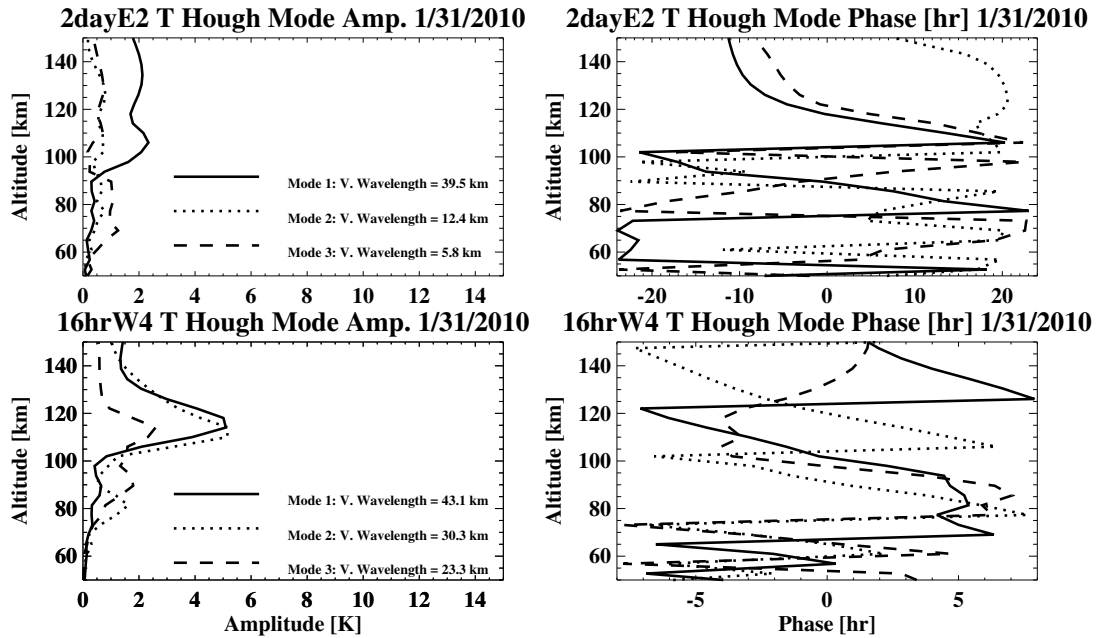


Figure F.14: 16hrW4 amplitude (lower-left) and phase (lower-right), and 2dayE2 amplitude (upper-left) and phase (upper-right) as a function of altitude for January 31st, 2010 under the non-zero background winds specified by NOGAPS-ALPHA. Each Hough mode amplitude was extracted by least squares fitting theoretical Hough mode functions to the overall secondary wave amplitude and phases at each altitude level. Units are in degrees Kelvin.

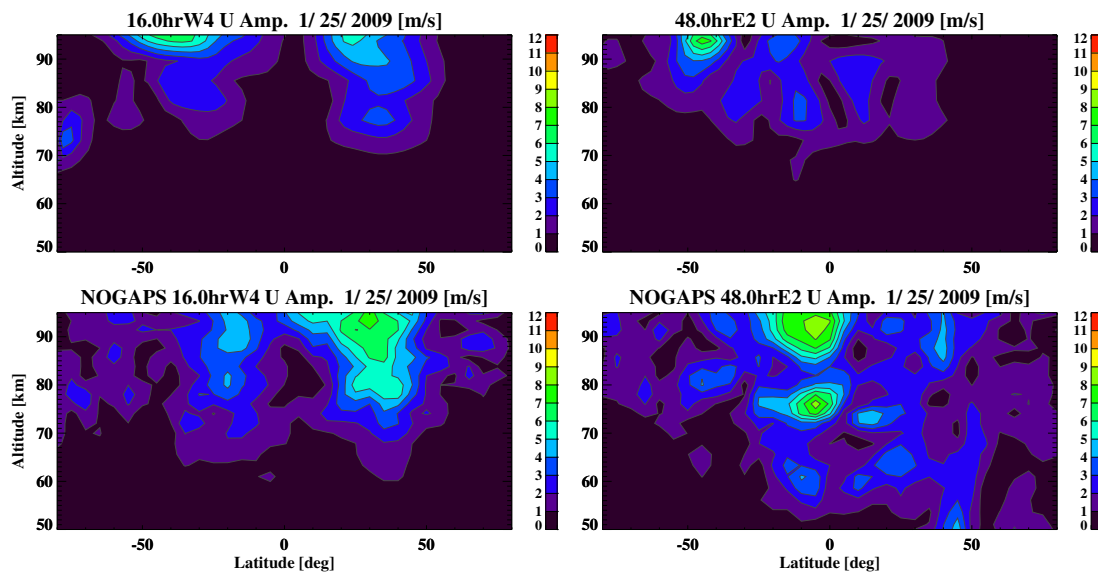


Figure F.15: Vertical-latitude amplitude structure during January 25th, 2009 for the linear model 16hrW4 zonal wind (top-left), NOGAPS-ALPHA 16hrW4 zonal wind (bottom-left), linear model 2dayE2 zonal wind (top-right), and NOGAPS-ALPHA 2dayE2 zonal wind (bottom-right).

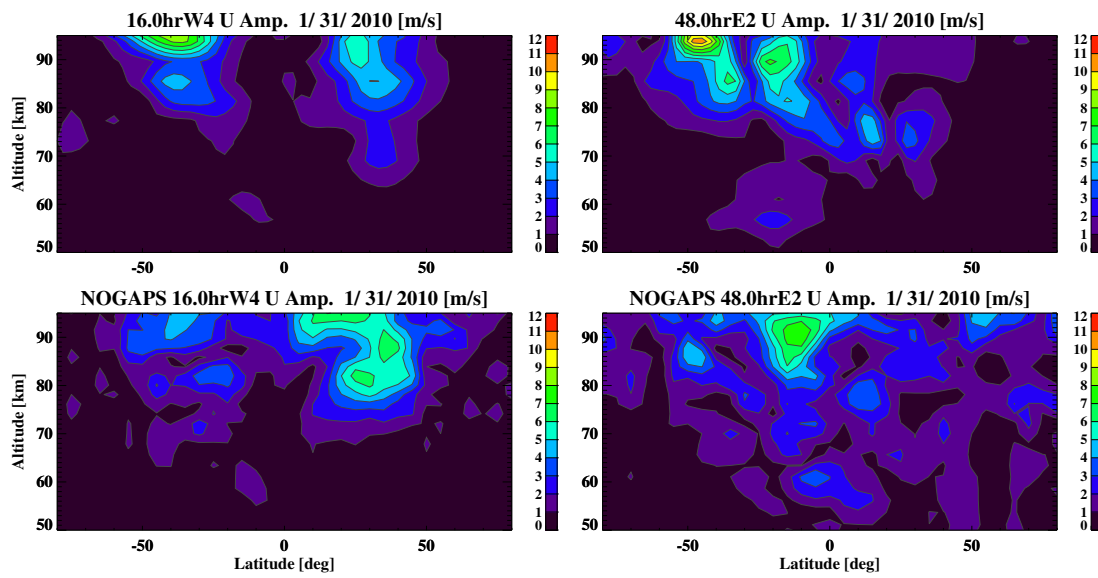


Figure F.16: Vertical-latitude amplitude structure during January 31st, 2010 for the linear model 16hrW4 zonal wind (top-left), NOGAPS-ALPHA 16hrW4 zonal wind (bottom-left), linear model 2dayE2 zonal wind (top-right), and NOGAPS-ALPHA 2dayE2 zonal wind (bottom-right).